The University Of Sheffield.

An investigation of microstructures of as-welded, heat treated, and laser clad thick section electron beam welded pressure vessels

By

Mohammed Noori Ridha Al-Husseini

A thesis submitted for the degree of Doctor of Philosophy

The University of Sheffield

Department of Materials Science and Engineering

July 2020

STATEMENT OF ORIGINALITY

I hereby declare that I have conducted, completed the research work and written the thesis entitled (An investigation of microstructures of as-welded, heat-treated, and laser clad thick section electron beam welded pressure vessels) embodies the results of the work.

They were carried out solely by the candidate as a requirement of the PhD degree at The University of Sheffield. It has not been submitted anywhere for any award. The candidate has made acknowledgement of the support of others and has referred to work carried out in collaboration with other people.

Mohammed Noori Al-Husseini	23-07-2020
Student name	Date

Professor Bradley P Wynne	23-07-2020
Supervisor name	Date

Abstract

A key element of many nations' future baseline energy supply is nuclear fission. A critical component of a civil nuclear reactor is the Reactor Pressure Vessel (RPV). The RPV is exposed to high pressure and high temperature as well as neutron irradiation and other harsh conditions, such as transmutation. The vast majority of RPVs currently in-service use low alloy steel grade SA508 Gr.3 (Mn–Mo–Ni) or its international equivalent. There is, however, a drive to run at higher pressures and temperatures for future nuclear reactors, which requires higher RPV wall thicknesses than currently operating. This has led to the development of SA508 Gr.4N (Ni-Mo-Cr). The new alloy has higher specifications in hardenability, toughness, and strength, which has allowed an increase in the design thickness of the reactor wall to in excess of 200mm, increasing the efficiency, power, and lifespan of the nuclear reactor to well over 50 years.

A major problem going to larger size RPVs will be their manufacture. It is unlikely that they will be able to be manufactured in one forming operation. This means some level of fabrication will be required, i.e., most likely welding. Conventional welding, such as submerged arc welding or metal inert gas welding, can be costly and requires significant levels of inspection and often requires many hours of reworking. In this research, a novel welding technology, Reduced Pressure Electron Beam Welding (RPEBW), is evaluated for its potential to weld thick sections of RPVs in one pass.

Furthermore, the use of laser clad 308L stainless steel to protect the internal surface of the RPV is also evaluated. It was imperative that these two evaluations were done in parallel, as after welding a Quality Heat Treatment (QHT) must be undertaken to restore the weld material to required properties. Thus, it was essential to understand how the cladding performed during this heat treatment.

The results showed that RPEBW could be used to produce a high integrity weld, in a single pass with very little evidence of defects. On welding, the hardness and Charpy impact toughness are significantly changed from the base material, hardness is higher, and toughness is lower, and the microstructure showed the classic weld and heat affected zones. On QHT at a temperature of 860 ℃ and holding time for 8 hours, the microstructure became much more homogenous, while the tensile and Charpy impact properties were close to base material QHT

properties. This suggests the RPEBW and QHT route offers a feasible fabrication route for the manufacture of RPVs.

Laser cladding was also successful, producing a uniform, defect free layer of 308L stainless steel that had a contiguous bond with the base SA508 Gr.4N (Ni-Mo-Cr) material. The microstructure of the cladding had uniform grain size, but there was a very thin heat affected zone in the base material in the as-cladded condition. On QHT there was no evidence of any significant change in cladding morphology, suggesting that the RPEBW followed by laser cladding followed by QHT appears to be a valid manufacturing route.

Acknowledgements

Firstly, I would like to express my profound thanks to Professor Bradley P Wynne supervisors for his supervision, guidance and encouragement throughout my PhD study. Secondly, I would like to thank Professor Eric J Palmiere for his remarks and support for me during my studies.

Besides, I want to thank all the technical staff in the Department of Materials Science and Engineering for helping me to carry out my experimental work and providing laboratory facilities, especially, Neil Hind, Tes Monaghan, Dean Haylock and Mike Bell.

I want to express my thanks to the Ministry of Higher Education and Scientific Research in Iraq and its representative in the United Kingdom, the Iraqi Cultural Attaché. I am also appreciative to the University of Technology in Baghdad for supported and giving me this opportunity to obtain a PhD.

Many thanks to my friends in the group, Nassar, Sameer, Haidar, Alaa, Raghdan, and Afaan for their friendship, comments, and helpful advice throughout the PhD study.

Finally, I would like to express my gratitude and appreciation to my family (mother, and my siblings) for their encouragement and supporting during the study. I wish all the mercy to my father, who taught and encouraged me in all my life.

Contents

List of Figures

List of Tables

Nomenclature

A	Austenite solidification mode
AF	Austenite Ferrite solidification mode
AISI	American Iron and Steel Institute
ASTM	American Society for Testing and Materials
BCC	Body Centered Cubic
BM	Base Metal
BS	British Standard
CCT	Continuous Cooling Transformation
CAD	Computer Aided Design
D/W	Depth to Width Ratio
EBW	Electron Beam Welding
EDM	Electrical Discharged Machining
F	Ferrite
FA	Ferrite Austenite
FCC	Face centered Cubic
FN	Ferrite Number
FZ	Fusion Zone
FTTU	Fast Thermal Treatment Unit
HAGB	High Angle Grain Boundarie
HT	Heat treatment
HAZ	Heat Affected Zone
HCP	Hexagonal Closed Pack
IHT	Intercritical Heat Treatment
LC	Laser Cladding
LB	Lower Bainite
L	Low carbon stainless steel grade
LBW	Laser Beam Welding
Ms	Martensite Start Temperature
Mf	Martensite Finish Temperature
NAMRC	Nuclear Advanced Manufacturing Research Centre
PWHT	Post Weld Heat Treatment
P	Pearlite
PH	Precipitation Hardened
QHT	Quality Heat Treatment
Q/V	Heat input per unit length
RPEBW	Reduced Pressure Electron Beam Welding
RPV	Reactor Pressure Vessel
R	Solidification rate
R_{C1}	Critical growth rate
R_{C2}	Higher growth rate
SA	Steel Alloy
SEM	Scanning Electron Microscopy
TMC	Thermomechanical Compression
TWI	The Welding Institute
VH	Vickers Hardness
UB	Upper Bainite
UTS	Ultimate Tensile Strength
WRC	Welding Research Council
X Ray	Radiographic Inspection
Wt%	Weight Percentage
YS	Yield Strength

Chapter 1 / Introduction

1.1 Introduction:

The construction of new nuclear fission power stations across the world is signposted to significantly increase, owing to many world-wide demands, e.g. Kyoto and Paris agreements and state level legislation, for a reduction in carbon emissions. This is further compounded by energy use forecasts expecting an increase in consumption by up to 50% by 2030 and the possibility of doubling by 2050 [1,2,3].

Therefore, it is vital to maximise the potential of the nuclear energy industry by increasing the capacity, power, and efficiency of nuclear reactors. A critical component of a nuclear reactor is the reactor pressure vessel (RPV). RPVs have many different functions depending on the type of reactor design, example functions include: 1. carry the nuclear reactor coolant, which is used to remove the heat from the core of the nuclear reactor by transferring it to generate electricity, 2. shroud the core to stabilise the nuclear reactions, and 3. contain the nuclear fuel, Figure 1 shows an example RPV scheme. This, in turn, places the RPV under ultra-extreme conditions of high pressure and high temperature, combined with neutron irradiation and possibly even transmutation. Furthermore, next generation nuclear power stations are expected to have larger RPVs to enhance efficiency, thus it has become necessary to improve the RPV by enhancing its microstructure and mechanical properties [4,5].

As a general rule, RPVs are manufactured from a one-piece forging using steels such as SA508 Gr.3 Mn-Mo-Ni low alloy steel (or its international equivalents). However, future generation reactors will be expected to have increased capacity, efficiency and increased lifetime than current ones operating, meaning RPVs will need to be manufactured in sizes larger than most forging companies can make in a single piece. For this reason, RPVs will need to be fabricated from multiple sections, which will require welding to produce the final component. This, however, will not solve all problems, particularly the impact of increased RPV thickness, where the hardenability of SA508 Gr.3 is already being stretched. A more recent material SA508 Gr.4N Ni-Mo-Cr low alloy steel has been suggested as an alternative that has higher

hardenability, which would enable the development of size and specifications of the reactor currently being suggested [6].

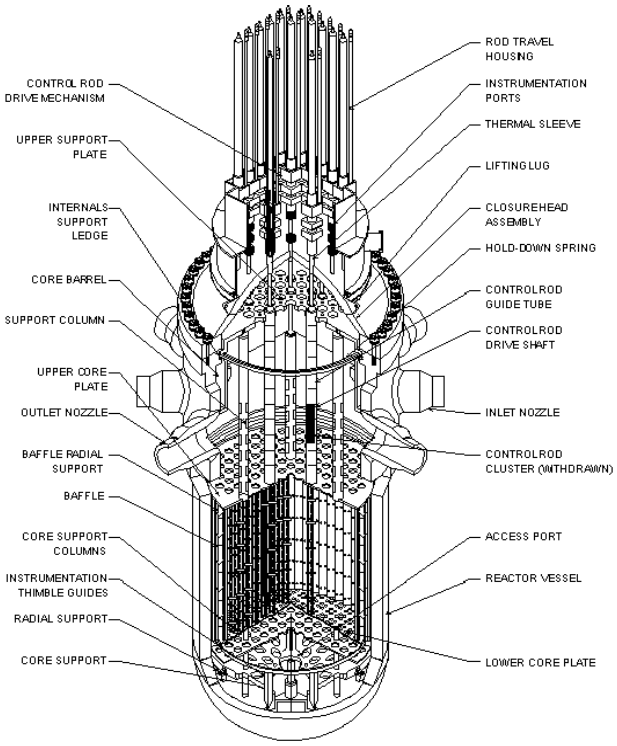

Figure 1: Scheme of the reactor pressure vessel [5].

If fabrication of RPVs is the only option, then conventional welding techniques will not be feasible. The RPV thickness will be in excess of 200 mm meaning that conventional welding techniques will require multiple passes leading to excessive reheating of the base material and the likelihood of a significant level of defects, which cannot be tolerated in a structurally critical RPV. Only laser and electron beam welding with their high-power intensity will be feasible in such circumstances. Realistically, however, only Electron Beam Welding (EBW) with its high depth to width penetration is feasible for 200 mm welding. Unfortunately, however, EBW requires welding to be undertaken in a vacuum like pressure, which for the RPV would require a very large chamber. However, recently The Welding Institute (TWI) have developed reduced pressure EBW (RPEBW) that can be undertaken outside a fully enclosed chamber, enabling the possibility of fabricating large components using EBW [7,8].

In this work, the potential for 200 mm thick RPVs to be fabricated using RPEBW and SA508 Gr.4N is explored, with the investigation concentrating on weld microstructure and its integrity,

the effect of quality heat treatment on mechanical properties and microstructure, and the effect of cladding processes on the near surface microstructures.

1.2 Project Objectives

2. Study as-welded microstructures and mechanical properties in 200 mm thick welds of SA508 Gr.4N using RPEBW

3. Study the effect of heat treatment on the microstructure and mechanical properties of as-welded SA508 Gr.4N.

4. Develop a heat treatment route for the as-welded material to produce the desired mechanical properties such as hardness, toughness and tensile properties in line with current specifications of as-forged material.

5. Investigate the microstructure and the effect of heat treatment on laser clad material to understand and improve the microstructure and mechanical properties of the cladded layers.

1.3 Thesis outline

Chapter 2

The chapter will include all the literature base that has been put forward by previous researchers, including the alloys that are used in RPVs. An overview of the heat treatments and mechanical specifications such as strength, hardenability, toughness and hardness will also be given. This is then followed by an analysis of electron beam welding and laser cladding.

Chapter 3

This chapter explains the experiments which were used in this research and describes the designs of the heat treatments used. The chapter also describes details of the specimen preparation for analysis of microstructure and properties.

Chapter 4

Describes the results and discussion of the 200 mm thickness welding results using RPEBW with the alloy SA508 Gr4N. This includes a detailed analysis of the microstructure and properties in the as-welded stated and in the heat-treated state.

Chapter 5

The chapter presents and discusses the results for laser cladding operation, which is used to protect the internal surface of the RPV from the extreme harsh conditions it experiences. This includes a detailed analysis of the microstructure and properties in the as-cladded state and in the heat-treated state,

Chapter 6

This chapter summarises all the results obtained in the welding and laser processes. An overview of the essential points that contributed to the development of the welding area regarding the microstructure specifications and mechanical properties are presented.

Chapter 7

Suggested ideas for future work are presented in this chapter.

Chapter 2 / Literature Review

2.1 Introduction

In this chapter, an overview of the background literature to support the research undertaken in this work is presented. There is an overview of the basics of steels and a review of the microstructure of the focus steel of this research, namely SA508 grade 4N and a comparison with the previous generation alloy SA508 grade 3. This is followed by a comprehensive review of welding, with a particular emphasis on electron beam welding and reduced pressure electron beam welding. The effects of heat treatment on microstructure and properties are then presented. The laser cladding process is then explained, including an overview of the fundamentals of laser cladding operations, along with a review of the mechanical properties and microstructures of the cladding area.

2.2 Microstructure of steel

The basis of steel is iron, which an allotropic material, i.e., at one atmosphere pressure it takes on different crystal structures, known as phases, at different temperatures. At temperatures below 912ºC iron has a body centred crystal (bcc) structure known as α–ferrite, between 912ºC and below 1394ºC the crystal structure is face centred cubic (fcc) and is known as gamma (γ)-iron and from 1394ºC to the melting temperature the crystal structure reverts back to bcc and is known as δ–ferrite. Each of the iron phases have different levels of carbon solubility, notably both ferrite phases have limited solubility of carbon, meaning that beyond a relatively small addition of carbon the material decomposes into ferrite plus a carbon rich phase, as demonstrated in the binary Fe-C equilibrium phase diagram presented in Figure 2.1 [9,10,11]. In contrast, the austenite phase has a much larger solubility of carbon, with a maximum solubility of 2.14 wt% at 1147ºC. This unique combination of having high carbon solubility at high temperatures and low solubility at room temperature means that steels have the ability to be heat treated. At very slow cooling rates from austenite the phases formed are equilibrium α–ferrite and a carbon rich intermetallic phase, Fe_3C, known as cementite. It is worth noting that any austenite remaining at 727ºC has 0.76wt% carbon, which upon further cooling will

decompose into a morphology of lamellar α–ferrite and Fe_3C, which has an appearance similar to mother of pearl and is known as pearlite. With increasing cooling rate, the distance carbon can diffuse is reduced, resulting in finer and finer pearlitic structures. Thus, a combination of high temperature heat treatment and applications of different cooling rates therefore enables phase morphology (known as microstructure) to be manipulated to produce a different combination of desired properties [12,13,14,15]. At even higher cooling rates diffusion-controlled phase transformations are not possible and non-equilibrium phases are formed, notably Bainite and martensite. In the case of martensite, the crystal structure is body centred tetragonal (bct) formed by a shear mechanism that maintains all the carbon in solution, however; owing to the body centred nature of the crystal structure the crystal lattice is elastically strained by the carbon lying within its structure. This leads to a material that is incredibly strong but brittle. More detailed descriptions of these microstructures and Bainite are presented below [16,17,18].

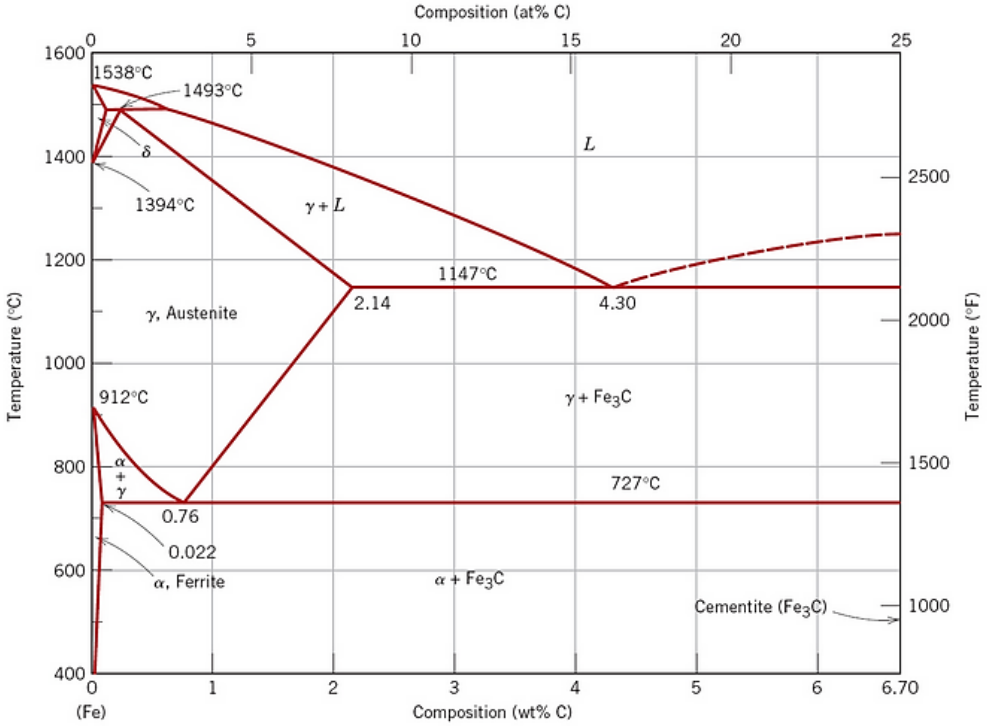

Figure 2.1: The equilibrium diagram of binary Fe-C [10].

2.2.1 Ferrite

Ferrite is the equilibrium phase of iron below 912 °C at one atmosphere pressure. It has a bcc crystal structure and has low solubility of carbon. As a general rule, the morphology of ferrite, upon transformation from austenite, is a function of cooling rate and chemical composition. Equilibrium pro-eutectoid ferrite, for example, can have morphologies ranging from polygonal ferrite, whereas non-equilibrium forms include quasi polyogonal ferrite, widmanstatten side plate ferrite, and acicular ferrite [19,20,21,22]. These structures of ferrite directly affect the mechanical specification of steel, such as toughness. For example, a reduction in propagation of cleavage cracks is produced due to the acicular ferrite microstructure, with its high variation in local orientation [23,24].

2.2.2 Martensite

Martensite is formed in carbon steel when quenching (fast cooling rates) from austenite. Due to the high cooling rate, the carbon atoms do not have enough time to diffuse outside the structure, which means it cannot gain sufficient carbon to form the cementite phase. The Austenite has a face-centred cubic structure which then transforms into a new form with a highly strained body-centred tetragonal structure called martensite which has a high quantity of carbon [25,26].

The martensite reaction typically begins under 250°C and is known as the martensite start temperature (Ms). The reaction is a thermal and further transformation can only continue with a reduction in temperature with 100% martensite forming at the martensite finish temperature (Mf). Furthermore, as there is no long-range diffusion during the formation of martensite the composition of the martensite is the same as the composition of the primary austenite [27,28,29]. As a general rule, the carbon content level determines the structure and specifications of the martensite. If the carbon content is low, martensite takes on a lath morphology, which consists of bundles of narrow flat plates that appear side by side. Whilst for higher carbon content narrow flat plates appear individually more than as bundles [30,31].

2.2.3 Bainite

Bainite consists of ferrite and cementite in a non-lamellar structure forming as a result of Austenite decomposition after continuous cooling in the temperature range of 250–550 °C, the temperature between fine pearlite formation and the start of the martensite formation. In general, the Bainite structure is formed at relatively high cooling rates and is often categorised into two forms: upper Bainite and lower Bainite [32,33,34,35].

Upper Bainite: The microstructure of upper Bainite is in the form of a sheaf shape and consists of cementite within a feathered structure of ferrite laths that are almost carbon-free, or not exceeding the ratio <0.03%. It forms in the temperature range between 400-550°C with the ferrite laths nucleating at austenite grain boundaries. Carbon then diffuses into the surrounding austentite, leading to carbon rich regions that form carbide at the interface between the newly formed ferrite lath and surrounding austenite (see Figure 2.2) [32].

Lower Bainite: The structure of lower Bainite is has a more plate-like form than upper Bainite, which again nucleates at the austenite grain boundaries at temperatures between 250 and 400 °C. In this instance, a small amount of carbon diffusion only can occur, leading to much thinner inter plate carbide thicknesses. This also leads to super saturation of the ferrite plates with carbon, eventually leading to precipitation of carbides within the ferrite plates, as illustrated in Figure 2.2 [32].

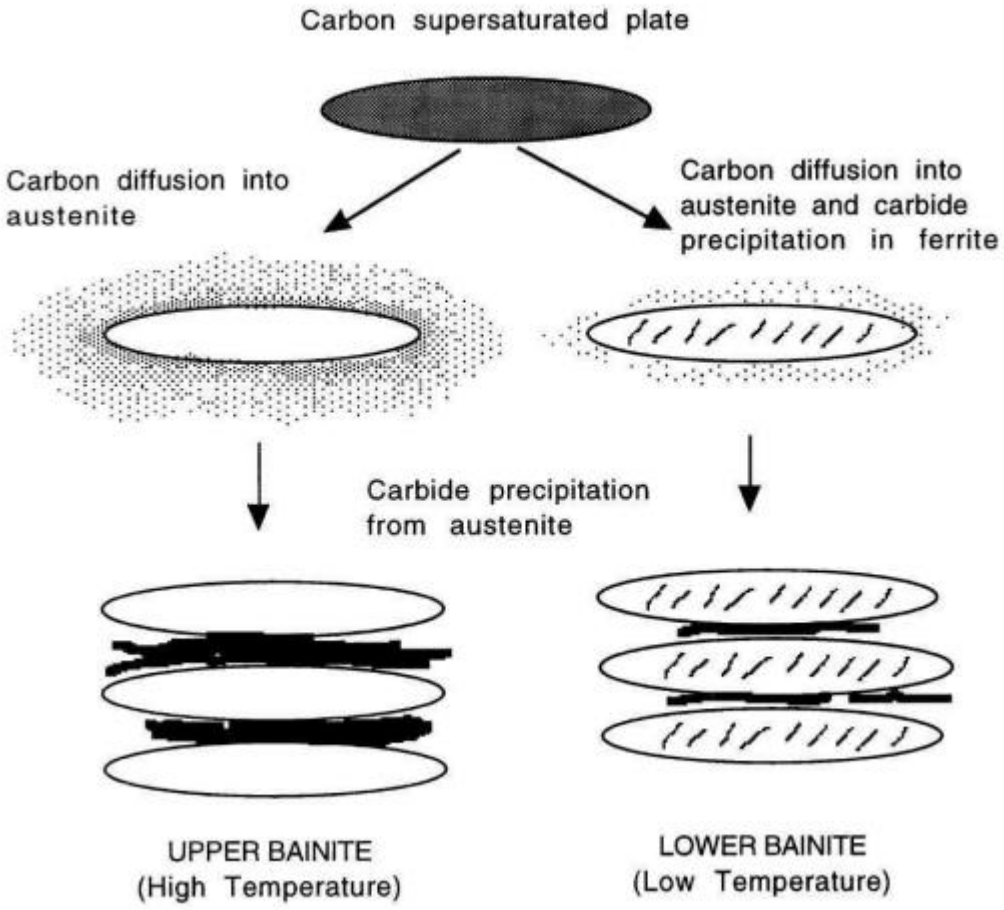

Figure 2.2: The upper and lower bainites [32].

2.2.4 Alloys Elements

Addition of alloying elements to steel, in general, either broadens the austenite field, promoting high austenite stability over a range of compositions, or diminishes the austenite field, maintaining the formation of equilibrium ferrite over a range of compositions. Thus, they have a primary role in influencing the microstructure and mechanical properties, and specifically for the steels being investigated in this thesis, nickel, molybdenum, and carbon have the biggest impact. Carbon has a significant effect on controlling cementite and various other carbides that form as well as the number and size of cementite particles. Molybdenum is essential in enhancing the level of strength, because of the rise in the precipitation of molybdenum carbides Mo_2C, which reduces the amount of cementite and therefore increases the hardness. Nickel's main role is to open the austenite phase field to improve hardenability as well as to replace carbon [36, 37, 38].

In the low alloy steels, alloying elements such as sulphur and phosphorus are added to improve the machinability. Silicon is added to remove oxygen from steel melt, and it is a stabilising element for ferrite. Chromium is considered a necessary element because it helps to increase corrosion resistance by the formation of protective oxide passive film, and also to enhance the hardenability of steel. Adding a small percentage of aluminium contributes to the stability of ferrite, as well as removing oxygen from the steel melt by forming aluminium oxide. Manganese is added to form MnS particles to improve toughness. Titanium works to control the growth of the grains in the austenite phase and has a significant influence on the welding process by controlling the coarser grain growth in the HAZ welding layer [39,40,41,42].

2.3 Steel Alloys for Nuclear Power Plants

In recent years there has been a significant worldwide increase in the reliance on nuclear power for energy generation, owing to the shutdown of many coal-fired plants. This has also led to planning of many more new build reactors. These future nuclear fission power generation plants are expected to have a lifetime in excess of 60 years to justify the huge expense of building and operating such plants. The reactor pressure vessel (RPV) is an essential element in the operation of the nuclear power plant and once installed cannot be replaced and thus is key to operational longevity [43,44]. As a rule of thumb, five major properties are required in steel alloys used for RPVs: sufficient strength, creep resistance, high fracture toughness, resistance to irradiation embrittlement, and resistance to weld cracking. The use of a high strength alloy also reduces the weight of the RPV, which decreases the total production cost of the plant and enhances the safety of large pressure vessels against earthquakes [45].

However, although it appears a straightforward process, the selection of suitable new alloys or improving the properties of the existing alloys to withstand the in-service conditions encountered by RPVs requires significant research efforts. For example, a critical point in these alloys is the balance between strength and toughness, i.e. introducing hardening mechanisms that raise the strength more than likely leads to a decline in fracture toughness of the material. In order to minimise the loss in toughness, the addition of alloying elements to have enhanced hardenability is often considered. On the other hand, these modifications may result in the deterioration of weldability in some cases [46].

Research to increase the strength and toughness of steel alloys for use in RPVs has focussed on two key areas: 1. Alloying element addition and 2. Optimisation of heat treatment. In reality, however, both of these areas have been optimised concurrently, e.g., alloying elements such as Cr and Ni, are essential for increasing the hardenability of ferritic steels [47]. Furthermore, the components made using these alloys can be enormous with wall thicknesses anywhere between 200 and 700 mm. Thus, during the quenching stage of heat treatment from the austenitic phase field the cooling rate can vary significantly from surface to mid-thickness Therefore, the microstructure generated could range from martensite or Bainite near the surface where the cooling rate is high to ferrite in the slowest cooling regions, particularly for alloys with low hardenability [48].

Over the last 30 years the steel alloy of choice for RPVs has been SA508 grade 3 or its international equivalent. However, newer generation reactor conceptual designs are indicating that the RPV wall thickness will be beyond SA508 grade 3's hardenability limit. This has led to the development of SA508 grade 4N, the N representing the addition of 2wt% Ni for improved hardenability [49]. A detailed description of both these alloys will now follow.

2.3.1 Steel Alloy 508 Grade 3

Steel Alloy 508 grade 3 (SA508 Gr.3) has been used for nuclear RPVs for more than three decades owing to its excellent combination of high toughness and strength, as well as good weldability. It also relatively lean in alloying element additions making it very cost competitive [50,51,52]. The composition of the SA508 Gr.3 alloy is Fe–0.2C–1.3Mn–0.9Ni–0.5Mo–0.2Cr–0.2Si wt. %.

The typical microstructure of SA508 Gr.3 after quality heat treatment is tempered upper Bainite [53,54]. Moreover, the strength and toughness are significantly influenced by precipitated carbides formed during initial phase transformation or during tempering, like M_2C and M_3C, which are distributed within the Bainite laths and Fe_3C formed along the lath and grain boundaries [55]. Figure 2.3 shows typical optical and the SEM images of the microstructure of SA508 Gr.3[56].

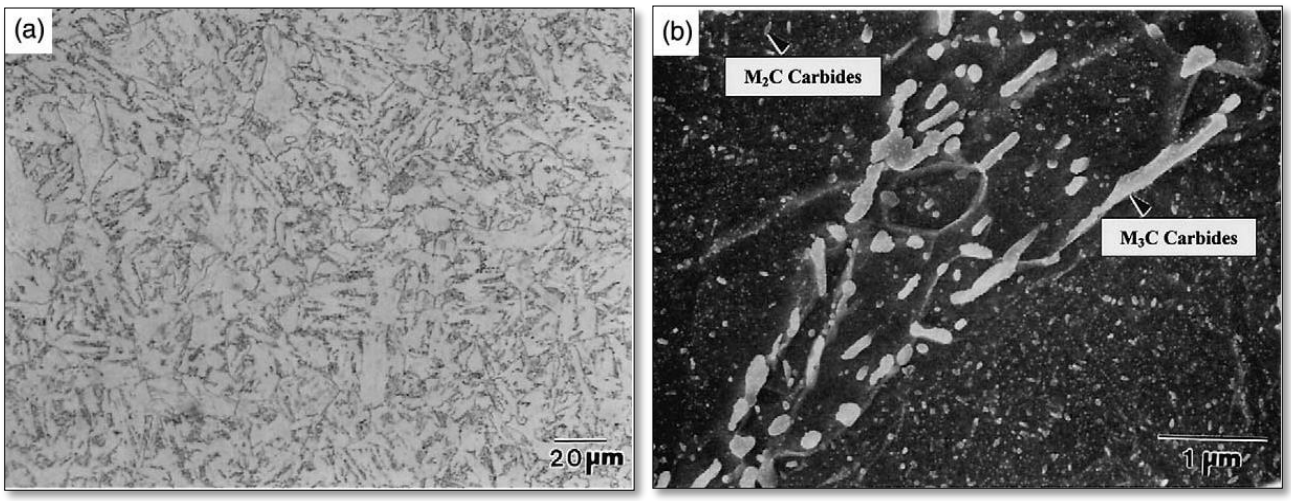

Figure 2.3: the microstructure of SA508 Gr.3 (a) optical image (b) SEM image [56].

SA508 Gr.3 is particularly sensitive to heat treatment conditions [57]. For example, Romero et al. [58] found that the coalesced plates of martensite, which have a harmful impact on toughness, are reduced by decreasing the austenite grain size. Thus, it is essential to reduce the austenite grain size heat treatment is under the grain coarsening temperature. Figure 2.4 shows the continuous cooling transformation (CCT) curve of conventional SA508 Gr.3 Cl.1 steel and SA508 Gr.3 Cl. 2 steel [59].

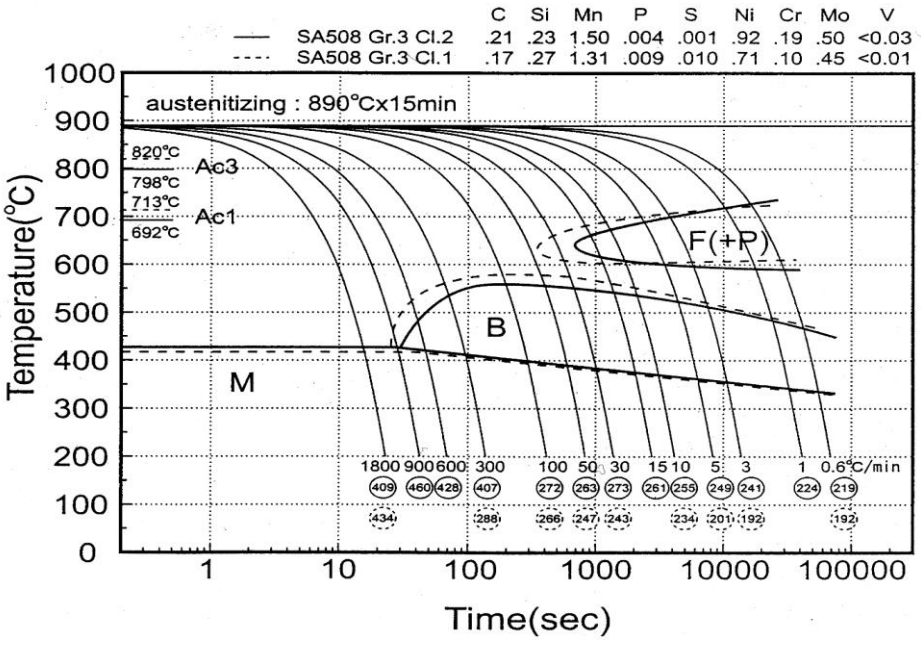

Figure 2.4: Continuous cooling transformation (CCT) curve of SA508 Gr.3 [59].

2.3.2 Steel Alloy 508 Grade 4N

Much research has focussed on developing a steel with better mechanical properties compared with SA508 Gr.3 (Mn-Ni-Mo) that can be used for nuclear power operation. These efforts have resulted in the development of SA508 Gr.4N (Ni-Cr-Mo), which has higher toughness and strength than SA508 Gr.3 [60]. SA508 Gr.4N has enhanced toughness and strength due to its composition, mainly by changing the ratio of chrome and nickel, which affects the transformation temperature to ferrite and carbides from austenite. This in turn moves the continuous cooling transformation (CCT) curve towards the right, lowering the critical cooling rate for quenching [61].

The microstructure for SA508 Gr.4N usually consists of fine and uniform martensite and lower bainite. The lower bainite has fine precipitates that are distributed uniformly inside the laths and can be easily distinguished from the surrounding regions of martensite, as shown in Figure 2.4. In Figure 2.5 the lower bainite (LB) is noted in the black line region, while the martensite (M) in the white line region [62].

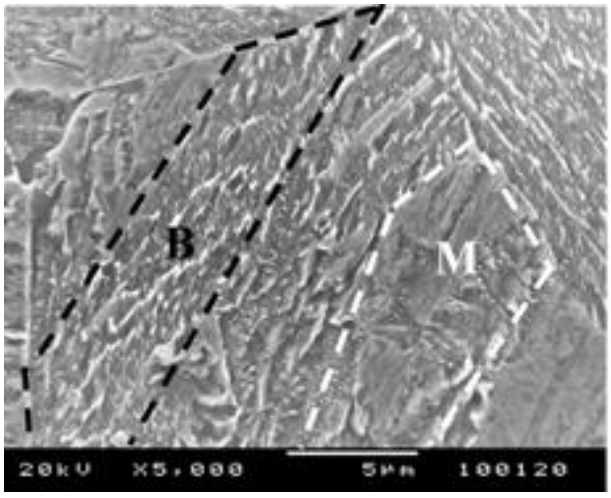

Figure 2.5: The SEM image for the microstructure of SA508 Gr.4 [62]

The major reason for improvement in strength and toughness is due to refinement of carbides. Furthermore, increasing the fraction of martensite by using fast cooling rate after austenisation and then tempering leads to further refinement of the carbides. However, the biggest advantage of the alloy is the addition of nickel, which enhances hardenability, allowing for thicker section

sizes during the quench, enabling section thicknesses in excess of 200 mm to fully meet property specifications [63,64,65]. There is, however, a significant disadvantage of Ni as it makes the materials more susceptible to irradiation embrittlement. This is further exacerbated by Cu, which must be reduced to a minimum level, which is not industrially easy owing to significant recycled material being used in the material's manufacture [66]. Figure 2.6 shows the CCT diagram for the SA508Gr.4N at 860 °C austenisation [67].

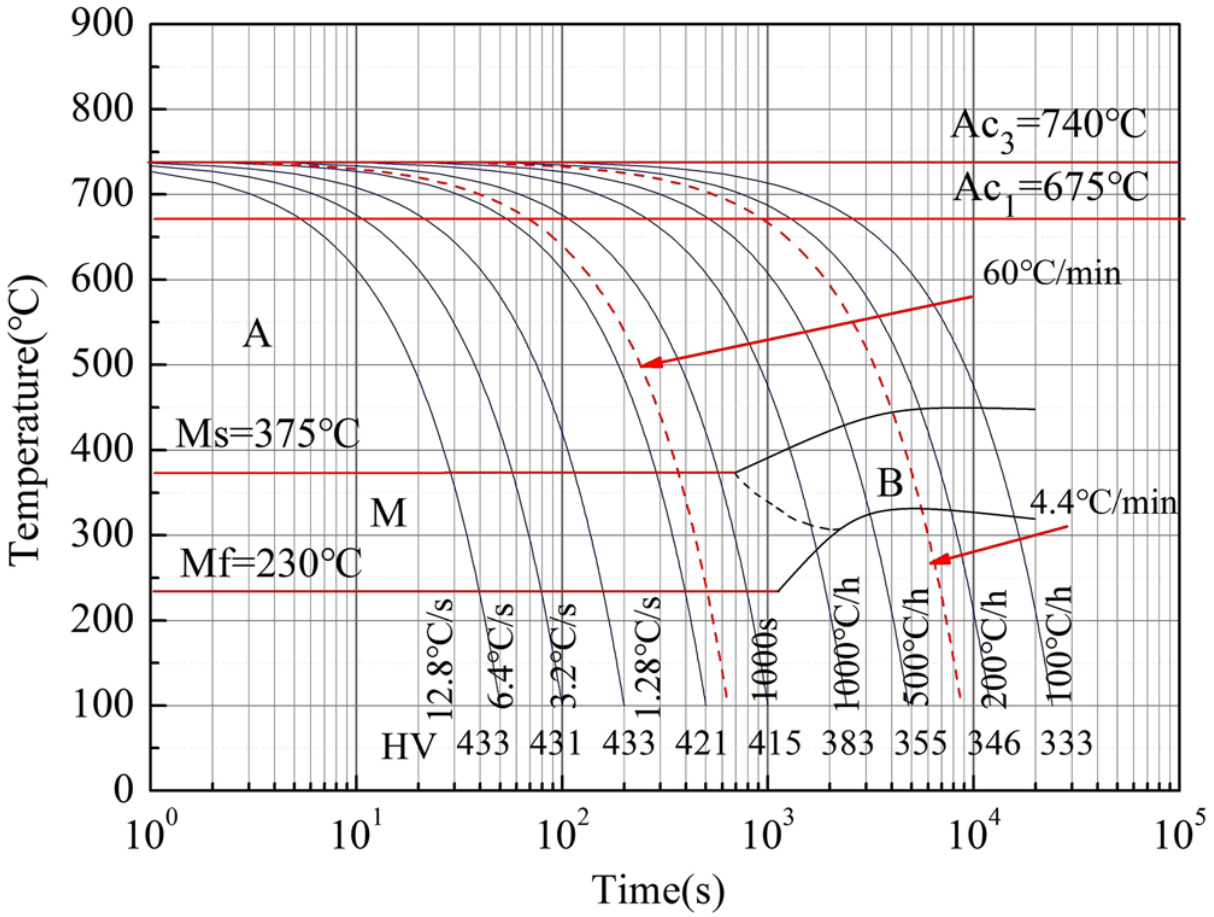

Figure 2.6: shows the CCT diagram for the SA508Gr.4N at 860 °C austenitisation [67].

2.4 Electron Beam Welding introduction

Owing to the increase in the production of nuclear energy, the development of welding techniques to be effective in joining thick sections will be necessary. Electron beam welding (EBW) because of its high-power density is the most likely candidate. EBW also delivers low

distortion and deep penetration, making it ideal for joining the thick sections, with the possibility of undertaking the process one pass, leading to significant productivity improvements [68,69].

The electron beam is generated by an electrical current which is passed into a tungsten filament inside a high vacuum chamber. This produces an electrostatic field between the negative electrode (anode) and the positive electrode (cathode) that accelerates the electrons to be two thirds the light speed, which generates the kinetic energy of the welding process. Several magnetic and electrostatic lenses with a diameter of 0.1 to 1.0 mm are then used to focus the high-speed electrons to generate the required power density, which ranges from 10^6 to 10^7 W/cm^2. A typical example of an EBW machine shown in Figure 2.7 [70].

The EBW process is characterised by high efficiency in addition to accuracy and high reliability. It is widely used in various industrial operations that need advanced welding and cutting techniques, such as the automobile and aerospace industries, also its ability to weld thick sections has allowed use in the iron and steel industry. The EBW operation is a welding process that uses a high-energy electron beam, which is different from other welding types in several features that can be summarised as follows [71,73]:

- Significant power density which is greater than 10^6 W/cm^2.
- A high welding speed minimising distortion in the fusion zone and the heat-affected zone.
- Provides high protection for the welding pool from oxidation because it is carried out inside a vacuum chamber.

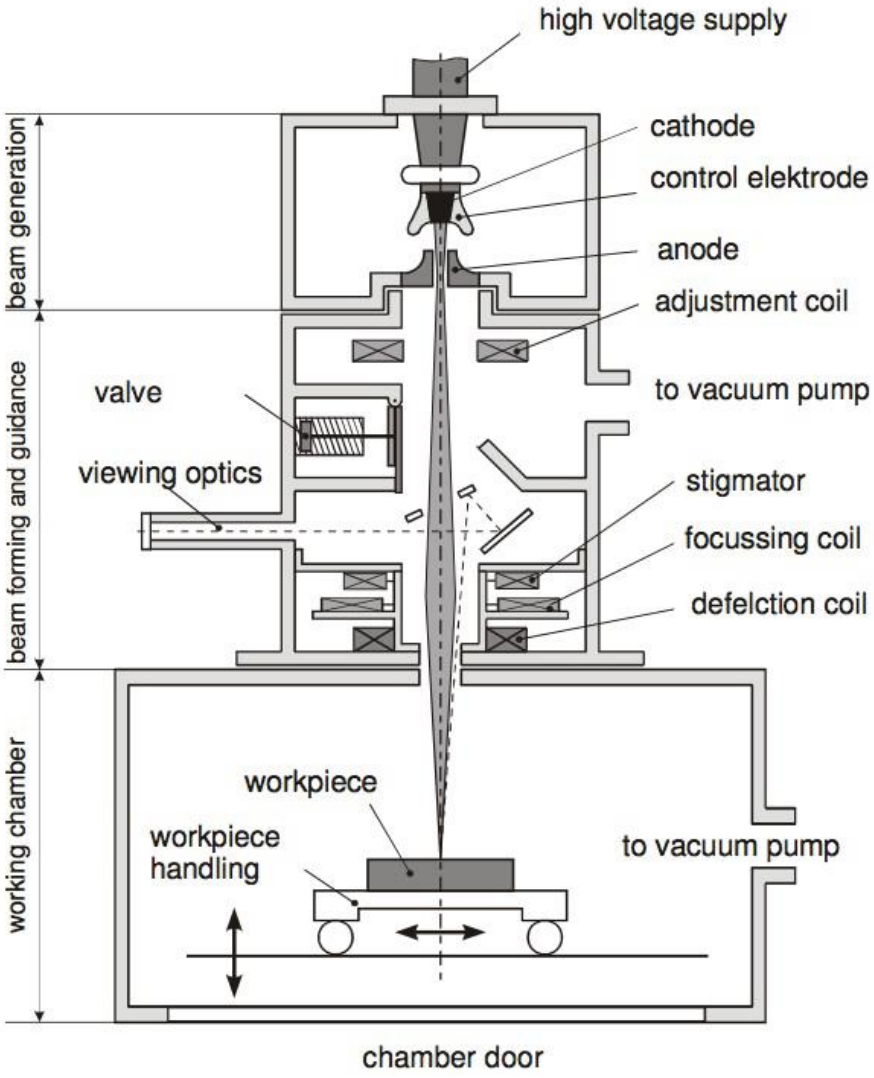

Figure 2.7: Electron Beam Welding (EBW) Machine [70].

The welding process begins by converting the kinetic energy of the electrons to thermal energy when the beam strikes the surface of the workpiece. This starts the melting process but since the electrons have low mass, there is little penetration into the sample. To get deep penetration the surface temperature must reach beyond the boiling point of metal to convert it to vapour

[72]. This gives new electrons the ability to reach deeper penetration, eventually leading to a keyhole being formed, as shown in Figure 2.8 [73].

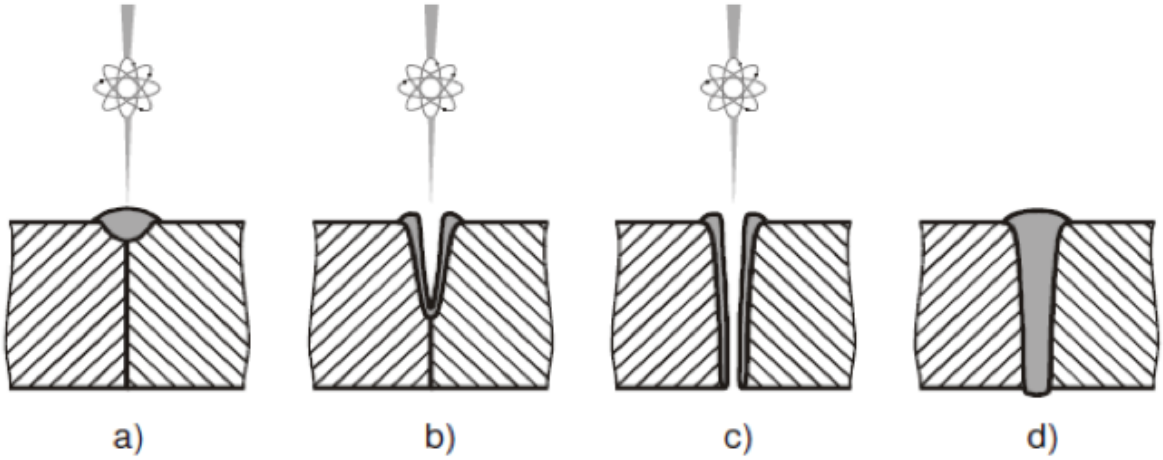

Figure 2.8: Shows the keyhole create from penetration in EBW [73].

The movement process of the molten metal occurs depending on the driving forces that resulted from the surface tension due to the difference in temperature of the keyhole walls surfaces besides, the hydrostatic forces and the pressure resulting from the evaporated atoms. The keyhole remains open due to the pressure generated by the molten metal around the vapour column with surface tension and hydrostatic pressure against the walls of the weld pool. Thus, the welding process continues. Figure 2.9 shows the keyhole and the main forces in EBW [73].

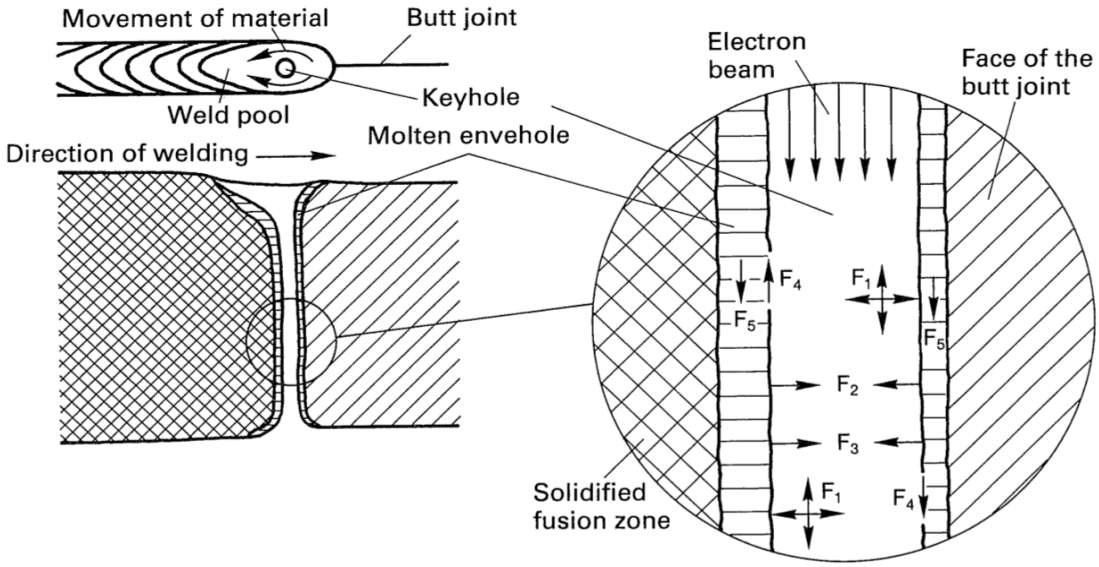

F_1 = Vapour pressure; F_2 = Force resulting from surface tension; F_3 = Hydrostatic pressure; F_4 = Frictional force from the escaping metal vapour; F_5 = Weight of the molten mantle.

Figure 2.9: Shows the keyhole and the main forces in EBW [73].

2.4.1 Reduced Pressure Electron Beam Welding

Over the past 40 years, there has been widespread development in the use of EBW. However, there has been a need to weld larger components, which are difficult to weld using traditional EBW methods owing to the fact that the vacuum chamber limits component size. It has therefore become an urgent necessity to develop an advanced process that can weld large parts at the worksite. In the last decade, The Welding Institute (TWI) have developed a new EBW technique called Reduced Pressure Electron Beam Welding (RPEBW) to weld the massive structures such as components of the reactor pressure vessel.

The traditional EBW operation has used a chamber with a high vacuum (~ 10^{-3} mbar), whilst RPEBW is carried out at a much moderate vacuum pressure (P=~1 mbar) with a mobile chamber that can move with the beam. The design of the welding device has many advantages, particularly allowing welding of large components and the use of simpler mechanical setups. There is also a significant reduction in pumping time and clean lines. The RPEBW is a desirable method to welding the RPV for according to the following points:

- The process can be managed remotely.
- The system operates automatically and can be managed by on-line seam tracking.
- The system components are not affected due to extended exposure to high radiation flux levels because the elements of the system are strongly radiative.
- The presence of monitoring systems in this process enables easy control of the quality, whether during operation or with checks performed of post-weld inspection.
- The system reduces the need for many expensive welding stations for hot cells because the welding rate is high. Thus, the desired production rate can be easily achieved.
- Minimised the need for repair due to the high welding quality, which can be repeated continuously.

All these points make RPEBW ideally suited for joining the large and thick sections [68,74]. Figure 2.10 shows an example RPEBW Machine.

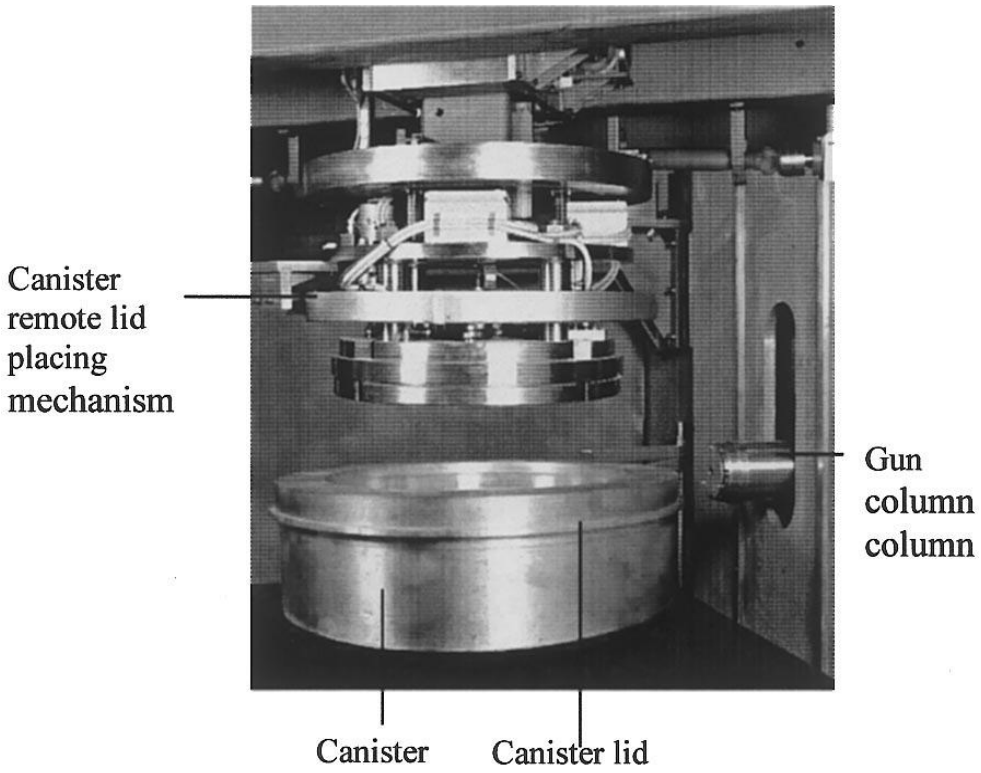

Figure 2.10: Reduce Pressure Electron Beam Welding Machine [68].

2.5 Microstructural characteristics of the welding process

The microstructure of a fusion weld usually consists of three zones: Fusion Zone (FZ), Heat Affect Zone (HAZ) and the Base Metal (BM), and they differ in terms of microstructure and mechanical specifications. The internal structure of the fusion zone appears in equiaxed and columnar structures, as shown in Figure 2.11. The formation and shape of the grains due to the solidification behaviour that takes place within the welding area depend on the parameters for the welding process, the cooling rate, the grain growth, and the thermal cycle gradient in the welding area [75].

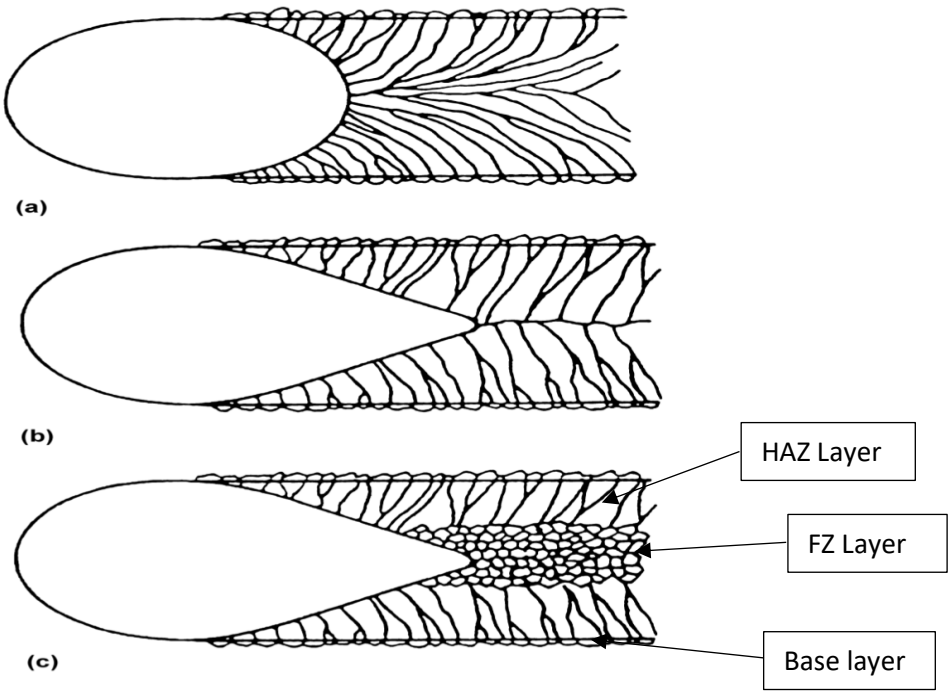

Figure 2.11: Different types of microstructure for fusion weld. (a) weld pool at low welding speed (b) weld pool shaped at high welding speed (c) weld pool shaped at higher welding speed [76].

In the melting area, the grains begin to grow vertically towards the fusion boundary, due to the thermal gradient that occurs in this direction. From the base metal, the grains grow epitaxially, and the direction of crystalline growth toward the fusion boundary is usually the <100> direction. Figure 2.12 shows schematically the growth direction. Therefore, away from the fusion boundary, competition takes place between these grains, which continue to grow in the same crystallographic direction, and the less oriented grains, as shown in Figure 2.13 [77,78]. The grains in this region will continue to grow from both sides and toward the central welding line where they will meet, as shown in Figure 2.14. Typically, defects occur during welding in

the middle line of the weld during the welding process and during the process of solidification and cooling, such as cracks, in addition to the fact that this region has impurities that result from welding, which reduces the mechanical specifications of the welding area [79,80,81].
The grains in the melting zone can display different microstructure formations that are subject to the solidification conditions. Since when the liquid cools to below the liquidus temperature, cumulative changes will occur in this region, which depends on the material system as well as the supercooling, that leads to a transformation in the microstructure morphologies of the fusion region [82,83]. Within a single weld, the solidification position can change between the centre lines and fusion boundary. The variation in welding depends on the relationship between the cooling rate and the temperature gradient, with a decrease or increase in the ratio; the solidification mode changes the structure morphologies between the dendritic and cellular. The reductions of this percentage towards the centreline lead to a strengthening of the dendritic structure in this area [84,85].

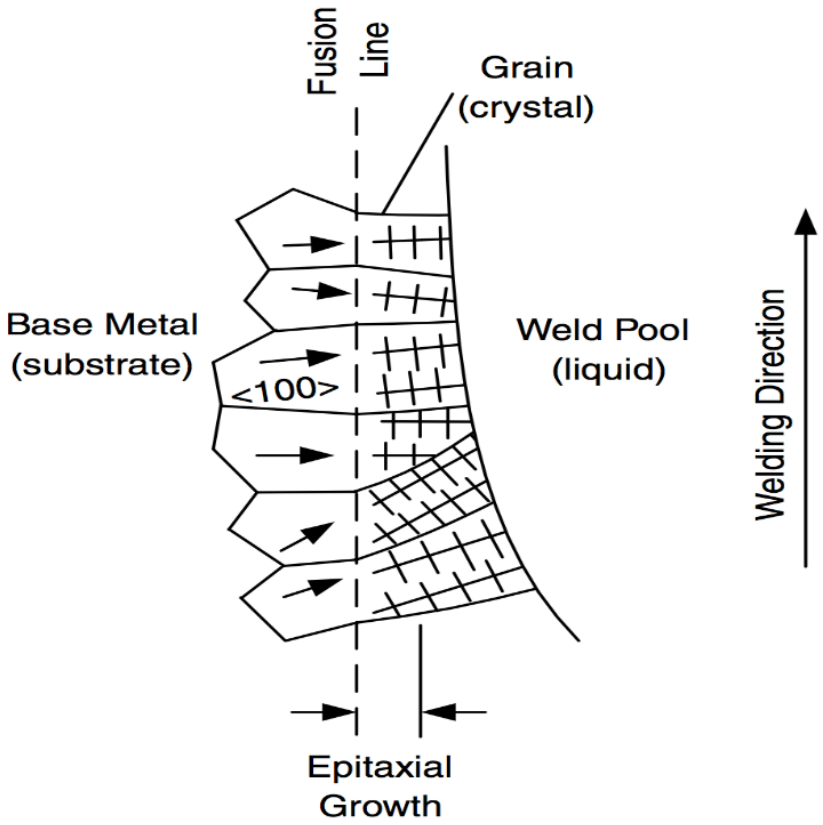

Figure 2.12: Fusion zone the epitaxial growth [75].

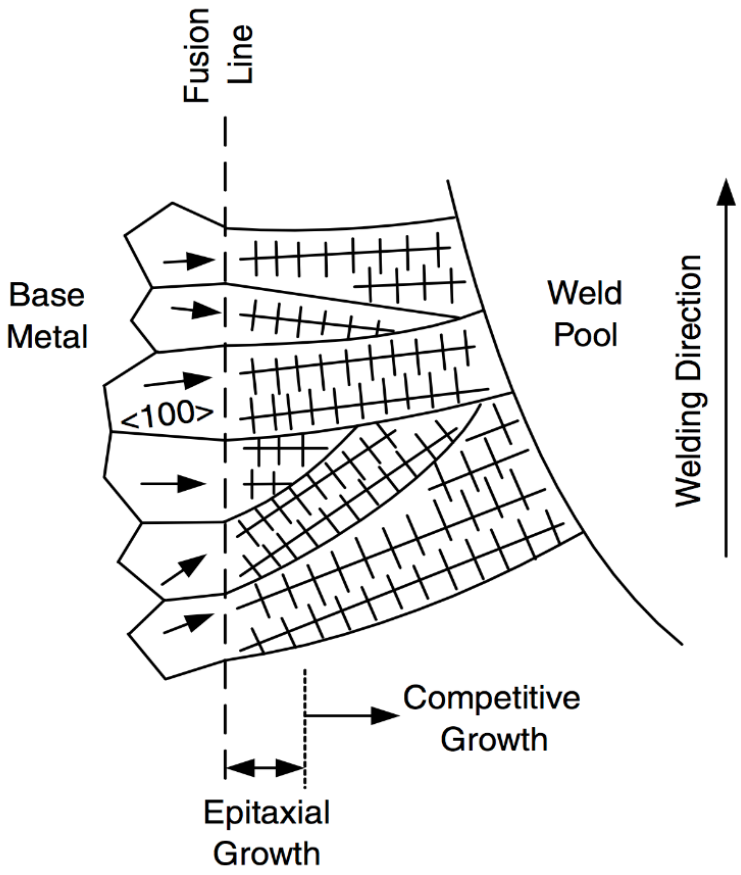

Figure 2.13: Schematic of fusion zone for competitive growth [76].

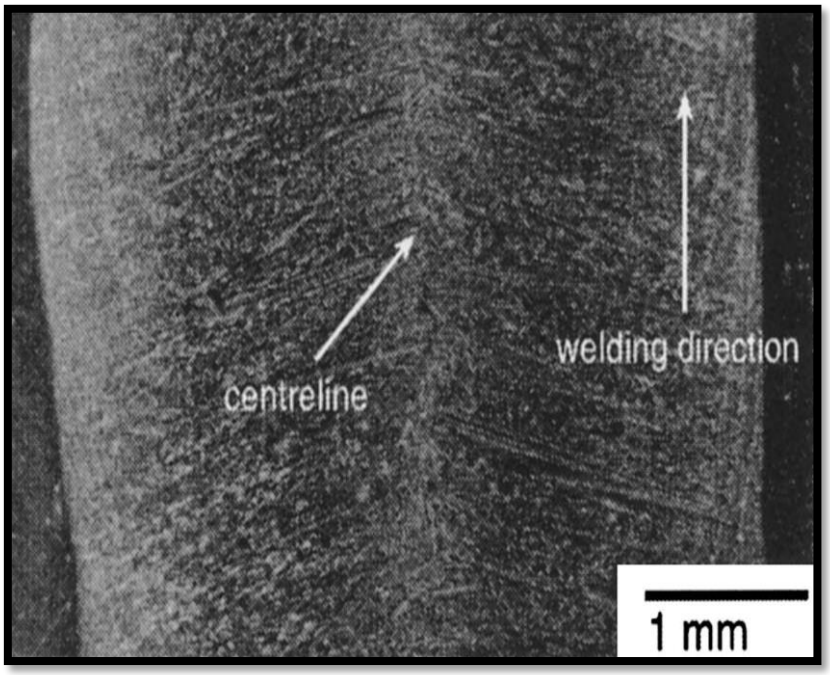

Figure 2.14: Centreline in welding solidification [80].

2.6 Heat Treatment (Quality and post heat treatment)

Heat treatment is an essential process that must be performed after the completion of the manufacturing of RPV components, to improve the microstructure and gain the desired mechanical properties [86, 87, 88]. The Quality Heat Treatment (QHT) is a term used in industry to define the last heat treatment given to the component prior to being machined to the final shape and gives the final properties of the material. It consists of an austenitisation operation then quenching in liquid by immersion or spraying it, followed by a temper to obtain the desired properties. Figure 2.15 shows the quality heat treatment operation with typical holding times and temperatures [55].

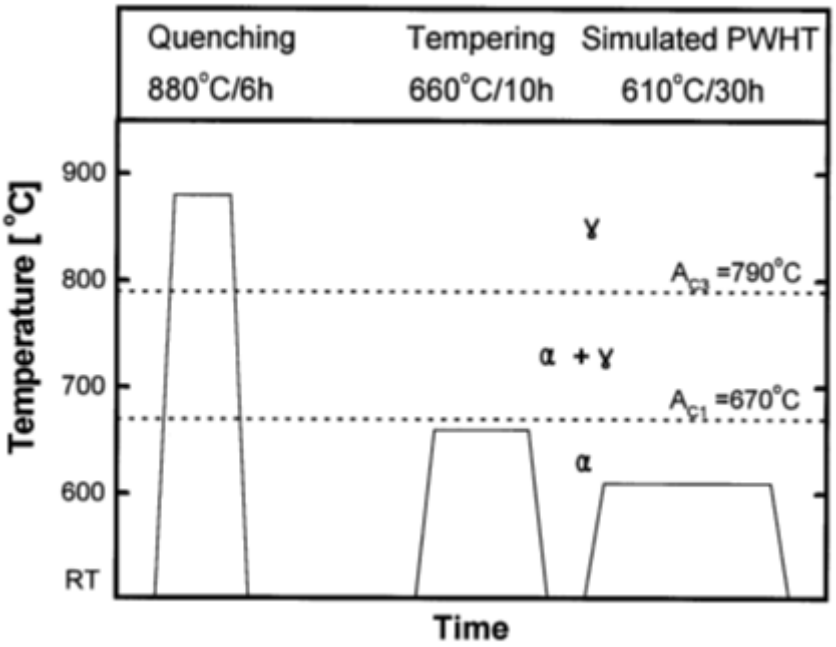

Figure 2.15: The Quality heat treatment operation [55].

After tempering, usually sub-elements are joined to produce the main component by welding. Therefore, it becomes necessary to use a post-weld heat treatment (PWHT) to treat the welding area, normally around a temperature of about 600-610℃ [89,90]. In most part, the PWHT is used to reduce residual stress, not alter microstructure, though some microstructure changes such a precipitation may occur. The wall thickness of the RPV has an essential role in determining the soaking time for the heat treatment. Especially for tempering, in industry an often-quoted number is soak time specified at 30 minutes for each 25.4mm of thickness to gain a homogeneous heat treatment. On the other hand, there are not as many hard and fast rules for

PWHT and the soaking period will depend on the experience and knowledge of the designers of the reactor. The perfect design of the heat treatment and the correct selection of chemical composition should be approved to achieve the balancing optimisation between the values of toughness and the strength. Determining it depends on several aspects as the hardenability, weldability, irradiation embrittlement and mechanical properties [91].

The welding process is considered essential when assembling the reactor, it has a significant impact on the alloy steel, the whatever mechanical specifications are high for the low carbon steel alloy, it should be affected by the welding process. The welding process dramatically affects the area near the fusion zone, which is called the heat affected zone. The changes occur in the internal structure such as the formation of martensite, and carbides participated in addition to coarsening of the grain size, which causes to a deterioration in mechanical properties, especially in toughness. Therefore, the heat treatment is considered to have a major effect in maintaining the required specifications after the welding process, which makes the operation of the nuclear reactor safe [90,92].

The HAZ zone in a single pass weld consists of different regions according to the grain size, which is dependent on the welding heat cycles. Where it can be observed that a coarse grain size occurs when the temperature is above 1100℃, while the grain size is much finer in temperatures regions experiencing between 900℃ to 1100℃ [90]. In the intercritically reheated coarse grain zone close to the fusion zone is where most of the embrittlement occurs, and this area can be enhanced by reheating it in a subsequent heating cycle. The austenite stabilises in some steels after reaustenitisation due to some alloy elements such as the carbon. With through the cooling rate, a transform occurs in these areas, and a hard structure is formed, which causes a reduction in the toughness [93].

Before post-weld heat treatment (PWHT), the microstructure of the HAZ usually consists of coarse austenite and martensite with grain size ranging from 200 to 400 μm. The large grain size is formed due to the high temperatures accompanying to the welding process, which may reach to 1350℃ [89,90].

The RPVs after welding operation need to be subjected to post-weld heat treatment to decrease and redistribute residual stresses. Thus, the leads to a rise in the toughness value which was low. The temperatures and times of PWHT are limited according to the tempering temperatures for steel alloys. Commonly the temperature is 600℃ and the holding time 30 hrs. Also, the knowledge and expertise of the company affect significantly the choice of heat treatment

conditions [94, 95, 96]. After PWHT, many transforms occur in the internal structure of the steel, as the martensite will turn into tempered martensite. The increase in the percentage of carbides from 2 to 4 vol.%, due to the increased carbide precipitation during the heat treatment. The most common carbides appear as fine Mo_2C [90]. Figure 2.16 shows the comparison between the structure of the HAZ before and after PWHT.

The microstructure of the HAZ zone changes with thermal cycles in cases where multi-part welding is used. The microstructure changes in a complex way, depending on the maximum temperature and number of welding passes, that makes testing and analysis complicated manner. The main factor in the microstructure which has a significant impact on the mechanical properties of the HAZ zone is the fraction martensite. with increasing fraction, the hardness and the strength will rise, while the toughness will decrease. When the martensite is in excess of 18 vol%, this will reduce the impact energy to around half compared to the base metal [97].

Precipitated carbides also have a significant effect in controlling the tensile strength and fracture toughness. The increase in precipitated carbides directly increases strength at the same time, decreasing the toughness. The reason for this is the hardening impact of the Mo_2C precipitation, which causes an increase in tensile properties and a decrease in the energy absorbed in the toughness [98].

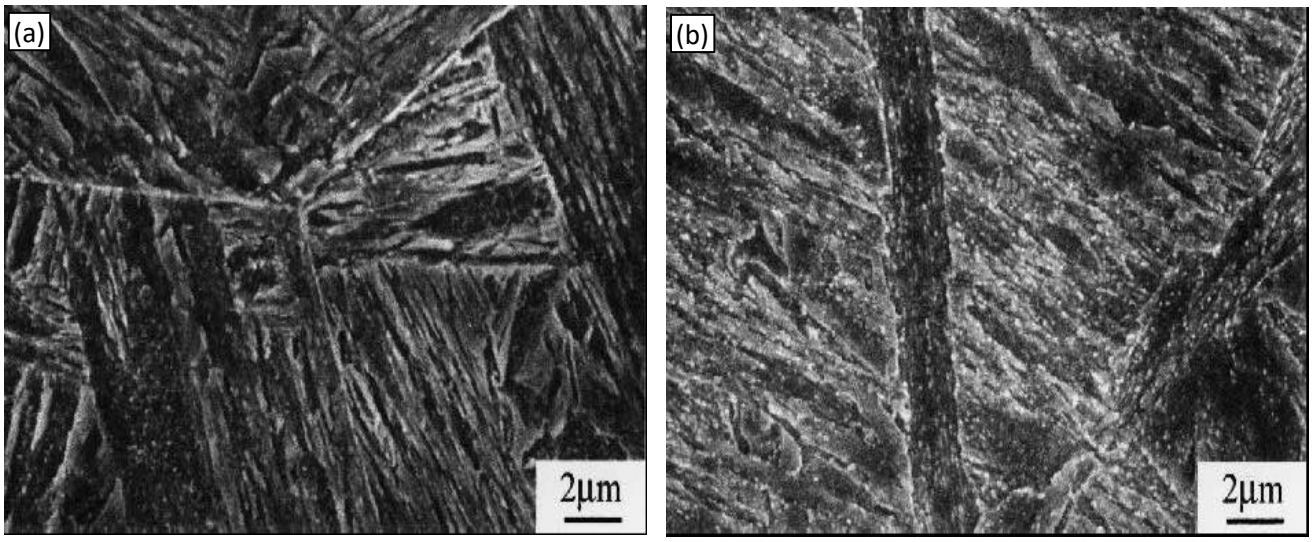

Figure 2.16: Comparison between the structures of the HAZ (a) before PWHT, (b) after PWHT [89].

2.7 Mechanical Properties of the weld

2.7.1 The Strength and Tensile Properties

Tensile testing has been used on SA 508 GR.4N to examine its general strength as well as to understand the impact of Intercritical heat treatment (IHT) on mechanical properties. In all cases the tensile strengths were higher than SA508 Gr.3. Increasing heat treatment time of the tempering heat treatment for SA508 Gr.4N indicated that the strength gradually decreases, and toughness increases with the best balance found with a tempering temperature of 650℃ and 5 hours tempering time [99]. It has been found that a microstructure having carbide precipitates has a substantial role in improving the tensile properties, with researchers confirming that fine M2C-type carbides and coarse M3C-type carbides were precipitated inside the lath, besides the along lath boundaries. Also, the fine M2C content increases more than the coarse M3C in the steel, which has a decrease in the carbon ratio with an increase in the molybdenum percentage leading to enhancement of tensile strength [41,100].

2.7.2 The Toughness and Charpy Impact Properties

The Charpy impact test commonly has been used in industries because it is simple to use, and the low cost and rapidly of the test make it desirable [101,102]. Through the analysis of the fracture caused by the Charpy impact test, it is possible to determine the ductile-brittle phase properties. Thus, it leads to study the effect of the Charpy test energy in the toughness value of the materials [103, 104]. Tempering of the RPV showed that it has a significant impact on the microstructure and mechanical properties for the steel alloy. The tempering at 650°C and holding time of more than 5 hours appeared to result in a significant deterioration in toughness with a slight increase in strength, due to the changes that occur in the martensite and austenite. Moreover, the effect of lath ferrite on softening the matrix is clearly, and the distribution of carbides which has the main impact on the toughness value [99]. Yang el at. [67] found that the microstructure has a high effect on the impact toughness of a SA508Gr.4N low alloy steel, which reveals that the martensitic structure and bainitic structure have a different impact on the mechanical properties, due to the martensitic structure consisting from more high-angle grain boundaries (HAGBs) and slight blocks. It has a positive effect and is attributed to enhance of

both toughness and strength by raising the crack propagation path. Moreover, sulphur segregation in the martensitic structure is higher than in the bainitic structure. Kim et at. [105] reported that the Charpy Impact value with fracture toughness was substantially enhanced when increasing the percentage of Ni and Cr in the SA508 Gr.4N. The Ni contents have positive effects on the toughness value due to achieve in an effective change in the grain size. In contrast, the Cr content improves the fracture toughness by influence on carbide precipitation. Li et al [100] investigated the microstructure and mechanical properties for the steel of the reactor pressure vessel (RPV) and confirmed that tempering at different temperatures from 508℃ to700℃ and holding time for 5 hours, increased in the toughness for Impact Charpy with increasing the tempering temperature from 142 to 252 J. The maximum toughness value was at 650℃.

The microstructure of low carbon steel has a significant effect to enhance the Charpy Impact toughness. The precipitates of the carbides such M_2C and M_3C inside and along the lath boundaries work to improve the toughness. This suggests that a steel with lower carbon and manganese content and increased the molybdenum percentage will have enhanced the toughness [41]. The properties for the fracture toughness transition in Charpy Impact can be improved significantly with optimisation of the chemistry ratio of alloy elements as used in the SA508 Gr.4N steels [106]. The significant factors which affect the fracture toughness before PWHT, it is the martensite fraction. When it increases, the toughness will be decreased, while the main reason which impacts on reducing the toughness after PWHT, it is the carbide, which is essential for a void initiation [107].

2.8 Stainless steels

2.8.1 Introduction

Stainless steel is all Fe based alloys which contain at least 11% chromium. When exposed to oxygen, chromium will form a layer of chromium oxide (Cr_2O_3) that enhances resistance to corrosion when exposed to acids and seawater [108,109]. The vast majority of stainless steel has an austenite crystal structure owing to the addition of nickel which stabilises the austenite to room temperature. The austenite makes the alloy have high levels of formability and relatively low strength [110]. The ability to weld is excellent for corrosion-resistant alloys of

all types of stainless steel. On the other hand, some changes in the metallurgical transformation may occur at specific temperatures that negatively affect the welding properties, such as the appearance of impurities, grain growth, or intermetallic constituents [111].

2.8.2 Types of stainless steels

The classification of stainless steels is based on metallic compositions in the microstructure of the alloys, such as ferrite, austenite and martensite. Alloy that contains more than one metallic phase, for example, 50% martensite and 50% ferrite, are classified as duplex stainless steels. There is also another classification that depends on the precipitation hardenability (PH) grades of alloys containing Ta, Al and Nb, as these alloy elements improve the hardenability of the alloy through the age-hardening heat treatment [112].

One of the most common types of stainless steel is austenitic stainless steel. It has the highest metallurgical properties, such as excellent weldability, high formability, and non-magnetic properties [113]. It has the lowest yield strength of about 210 MPa, which is equivalent to that of mild steel. It can be strengthened only through work hardening [108]. Nickel is used for the stability of austenite phase, it represents approximately 8% of the weight, among other elements are N, Cu, and C. Nitrogen and carbon improve the strength at all high and low temperatures. Table 2.1 shows the standard compositions of austenitic stainless steels [114,115]. Figure 2.17 shows the alloy elements in austenitic stainless-steel standards.

Table 0.1: Standard austenitic stainless steels Compositions [122].

Element	**Compositions range (wt%)**
Chromium	16-25
Nickel	8-20
Manganese	1-2
Silicon	0.5-3
Carbon	0.02-0.08 (>0.03 wt% designated L grades)
Molybdenum	0-2
Nitrogen	0-0.15 (usually designated with N)
Titanium and Niobium	0-0.2

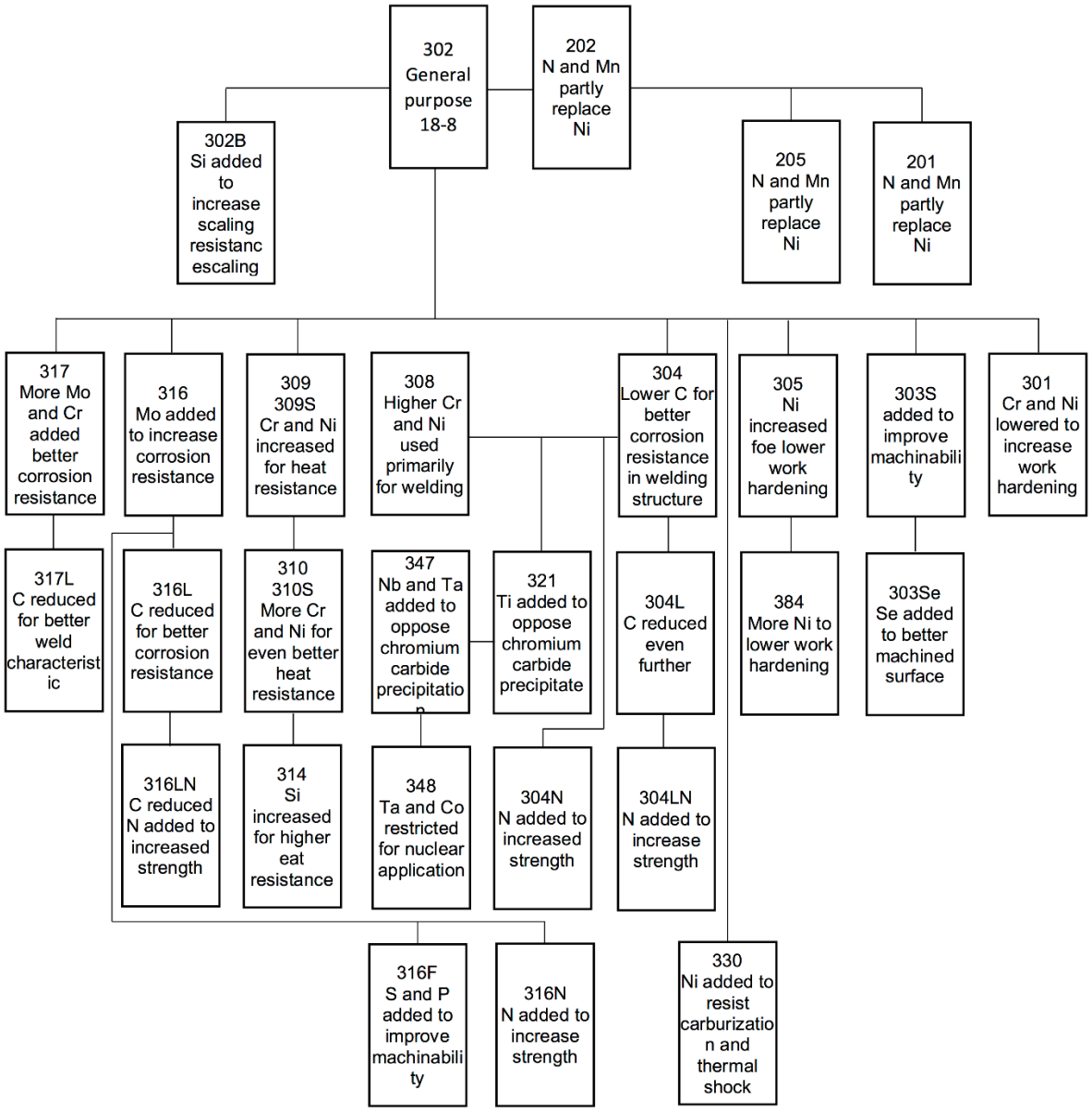

Figure 0.17: The alloy elements on austenitic stainless-steel standards [117].

2.8.3 Classification of austenitic stainless steels

A three-number system followed by some letters is sometimes used to classify stainless steel alloys, according to the American Iron and Steel Institute. Austenitic stainless steels consist of two series alloys 200 and 300, where the alloy 200 contains high levels of manganese, carbon and nitrogen. In contrast, in alloy 300, the nickel ratio is lower between the nitrogen and carbon to achieve a balance in the alloy elements [118,119]. The 300 austenitic alloys are considered

the most used with 347, 321, 316 and 304 of the "8-18" alloy type and the nominal values are 8-10 Ni and 18 Cr. The L grades are highly resistant to corrosion in aggressive media due to content the low carbon of about 0.03wt% [120,121].

The H grades contain carbon at a level of about 0.1% by weight and have an elevated application temperature that is usually higher than the standard L grades, and these alloys can be used at high temperatures [122]. The N grades have a nitrogen ratio of about 0.2wt% in the 300 series (316N, 304N), it reaches to higher levels in the alloys that have a high content of manganese and which increases the solubility of the nitrogen element in the austenite phase. Also, the high nitrogen content of austenitic stainless steels increases the strength and pitting corrosion resistance [121]. There are niobium and titanium elements in the alloys 321 and 347, and these two elements help to stabilize the alloy from the influence of the formation of chromium carbides (M23C6). These alloys are called stabilized grades [123]. At high temperatures, these elements form stable carbides with limited formation of Cr phases. The percentage of Cr in the regions at the grain boundaries is reduced due to the precipitation of chromium-rich carbides produce the structure sensitive to intergranular corrosion [124].

2.8.4 Microstructure and mechanical properties of austenitic stainless steels

One of the greatest disadvantages of using these alloys (austenitic stainless steel) in many engineering applications is the relatively low strength. The strength can be developed by using cold working. Heat treatments or phase transformations cannot increase the strength of the alloy due to the crystallization process occurring at high temperatures, this will not reduce the grain size or the transformation from the austenite phase to ferrite phase [125,126]. Moreover, martensite can be produced under especially conditions with unique heat treatments or by using cold work [127,128]. Table 2.2 demonstrates the mechanical properties of some types of austenitic stainless steels [129].

Table 2.2: The mechanical properties of some types of austenitic stainless steels [129].

Alloy	Tensile strength		Yield strength		Elongation	Reduction in area
	MPa	Ksi	MPa	Ksi	(%)	(%)
302	515	75	205	30	40	50
304	515	75	170	30	40	50
304L	480	70	205	25	40	50
308L	515	75	205	30	40	50
309	515	75	205	30	40	50
310	515	75	205	30	40	50
316	480	75	205	30	40	50
316L	515	70	170	25	40	50
317	515	75	205	30	40	50
321	515	75	205	30	40	50
330	480	70	205	30	30	-
347	515	75	205	30	40	50

In austenitic stainless steels, it is observed that the primary microstructure is the austenite phase. Therefore, alloying elements play a significant role in determining the final microstructure of the austenitic stainless-steel alloys, whether it is completely austenite or a mixture of ferrite and austenite [130]. The microstructures of the austenitic stainless steel are shown in Figure 2.18, where the austenitic steel contains for equiaxed austenite granules, as shown in Figure 2.18a. In contrast, the structure that includes a high-temperature ferrite which is called delta ferrite is shown in Figure 2.18b, delta ferrite formed during the solidification in heat treatment processing and may cause a decrease in the ductility and the toughness. Besides, this region can be suitable for the precipitation of carbides (M23C6) [110,122].

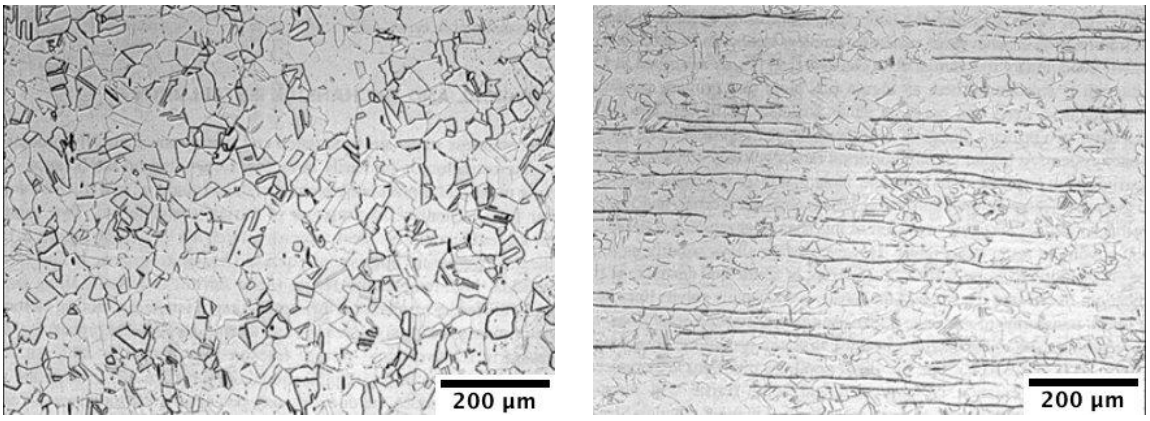

(a) (b)

Figure 0.18: The microstructure of 304 stainless steel type (a) equiaxed austenite grain (b) austenite and δ-ferrite[122].

2.9 Laser Cladding Fundamentals

Laser cladding (LC) is a processing method used for adding one material, up to thicknesses of 5mm, to the surface of a dissimilar material, with a high integrity bond line but minimal dilution of the clad layer into the substrate. In most cases the cladding is added to improve mechanical properties or improve corrosion resistance, particularly for extreme environments [131].

The main step in the LC process is the deposition of the coating layer through the injection of metal powder onto the surface of the base alloy, which is then melted and consolidated by the use of a high intensity laser beam. The deposition of the powder can be performed using two

different methods: (1) The "blown powder" method where metal powder is directed through a nozzle from which it meets a focussed laser, forming a melt pool. The substrate is then moved allowing the melt pool to solidify and a clad layer to be formed, Figure 2.19; (2) the powder is adhered onto the substrate by using suitable materials. A focused laser beam is then run over the powder, forming a local melt pool, which on removal of the laser solidifies, forming the clad layer [132].

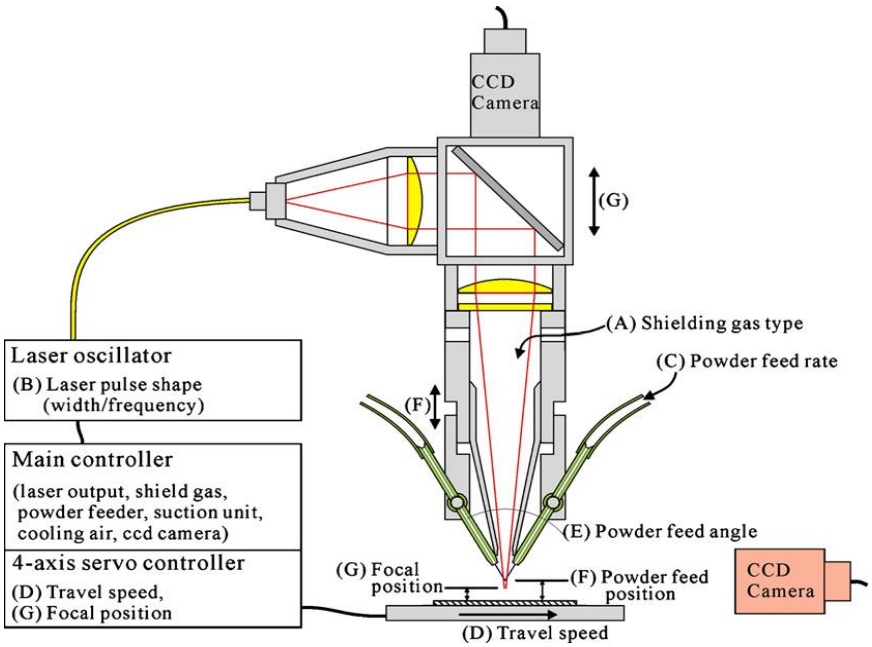

Figure 2.19: LC technique with main parameters [133].

In addition to the special chemical and physical properties of the clad layer, such as anti-oxidation, corrosion resistance, wear resistance, and increased fatigue resistance, the LC method has advantages such as:

(1) small heat affected zone in the substrate,

(2) minimal dilution between the two dissimilar materials,

(3) metallurgical bond between cladding and substrate,

(4) minimal distortion of the substrate,

(5) a relatively fine microstructure within the clad layer,

(6) minimal material loss, and

(7) integration of computer-aided design (CAD) tools with the production process.

A disadvantage of the LC process lies in the small area affected by the laser, owing to the limited size of the laser spot, restricting the cladding area produced per unit time, making the process time consuming. However, compared to the thermal spraying technique or conventional weld overlay methods, LC technology has greater precision and the cladding coatings produced exhibit higher-quality surface finish and have a higher density, i.e., significantly reduced porosity [134]. The LC method also allows for the cladding of complex geometries.

2.9.1 Laser Cladding Parameters

Successful LC is sensitive to a number of process parameters, particularly the method powder feeding, powder flow rate, laser power, and stand-off distance. The key element is managing where the laser energy is dissipated and dispersed, which is in 3 key areas: 1. uptake within the powder, 2. within the substrate, and 3. reflection from both the substrate and powder. Typically, the relationship between cladding thickness, i.e., powder flow rate, and energy required for successful cladding is directly proportional. This often limits the thickness of cladding layer that can be formed, as at some layer thickness there is not enough energy remaining to melt any of the substrate, leading to lack of bonding and the cladding layer spalls off [135].

Typically, the clad/HAZ layer of the substrate interface is the potential weakest point in a laser clad system owing to inconsistent dilution/fusion [136]. The dilution of the clad layer into the substrate depends on several factors: the thermal conductivity of the substrate material, the initial temperature of the substrate, the reflectivity of the material, the powder flow rate, and the interaction time of the powder in the beam and laser power. It was found previously that high dilution provided a favourable result on the hardness at the interface [132].

Another important factor in determining the quality of the final clad surface and clad properties is the laser path [133]. As the process requires many tracks to be generated to cover the whole surface there will be many overlap issues. Figure 2.20 shows an example of a cladding surface irregularity due to cladding overlapping [131]. Other effects include heat affecting the neighbouring clad track or causing a double heat affected zone in the substrate.

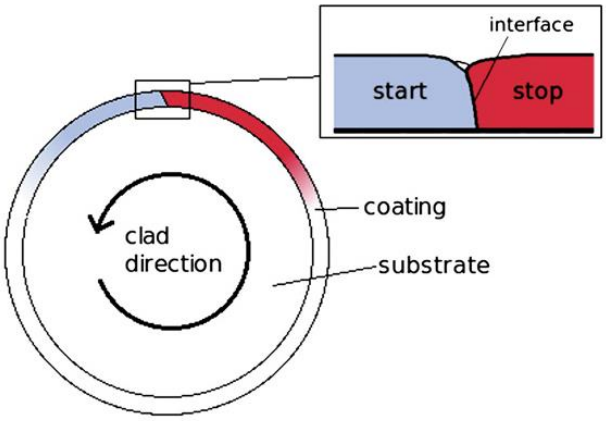

Figure 2.20: Overlapping in Start/ Stop zone in laser track [131].

2.9.2 Microstructure of Laser Cladding

Owing to the melting of dissimilar materials, the potential for the metal powder to have picked up impurities, and the high cooling rate associated with the relatively low heat input of the laser melting process, a variety of compositions, phases, and microstructural sizes can be observed in the clad layer. This, in turn, can play a significant role on the chemical and mechanical properties of the clad layer. Furthermore, due to the nature of solidification there can be defects such as porosity or solidification cracking [137].

In the case of austenitic stainless steel, which this work is focussing on, picked up alloying elements in the cladding layer can have a substantial impact. The increase of concentrations of carbon and other alloy elements generally raises hardness and can promote the formation of the ε martensitic phase, particularly under the faster cooling rates generated [138]. Furthermore, it is not uncommon to observe ferrite, which makes the cladding layer susceptible to cracking [139]. The level of ferrite formed is dependent on many parameters; the primary factors being cooling rate, chemical composition, and heat input. A post clad heat treatment can reduce the level of the ferrite, leading to superior properties.

As a general rule, the microstructure of laser cladding austenitic stainless-steel materials can be normalised to a standard microstructure, using an appropriate heat treatment. More problematic is the HAZ of the substrate adjacent to the clad material. Normally the substrate is a low alloy steel containing up to 2wt% of Ni, Cr, Mo, e.g., AISI 4340. The HAZ of such

materials will have a larger parent austenite grain size, a martensitic microstructure owing to the fast cooling rate, and possibly some carbides precipitated out because of tempering generated by neighbouring tracks. This leads to key issues of balancing laser power to ensure that high density clad layer is produced but at the same time minimising the size of the HAZ [135].

2.9.3 Mechanical Properties of Laser Cladding

To achieve a successful LC process, a range of factors must be met to obtain alloys with desired resistance to mechanical and chemical challenges. In general, wear resistance increases with increasing hardness. However, the high thermal gradients inherent in the process result in residual stress and hardness variations within the clad and HAZ. The high thermal stress concentration also produces residual stresses that may impact on the resistance to fatigue cracking and corrosion. To solve this problem, a post cladding heat treatment is used to decrease the generated stresses in the interface between the substrate and the clad material to enhance the mechanical properties. Hardness and surface-dependent properties such as oxidation, wear, corrosion, and to some extent, fatigue resistance is often irreconcilable with the required bulk properties, such as strength and stress-strain properties, or cannot be achieved simultaneously at a reasonable cost. Thus, it is possible to obtain excellent chemical and mechanical properties but at the expense of other factors. Therefore, a trade-off situation between the value and product properties is unavoidable [136].

Zeng et al. [140] mentioned that LC has a considerable effect on the mechanical properties shown through stress-strain curves. For the residual stress and the effects on the alloy, an earlier study showed that the impact of phase transformation plasticity must be taken into account. This stress is responsible for the development of microcracks. Furthermore, the various fatigue properties may be led to various thermally induced microstructures.

The addition of elements to the coating powder has a significant impact on the final mechanical properties of the result. Gao et al. [141] found that the addition of 5 wt. % Cr3C2 in Fe-based alloy powder had a substantial effect on the solidification structure of the coating. A coating with uniform microstructure was developed, and there were depressively distributed equiaxed grains and equiaxed dendrites instead of coarse dendrites. The grains become fine accompanied

with an increase in the total area of the grain boundary of the dislocation and control the plastic deformation.

2.9.4 Hardness of Laser Cladding

One of the key criteria for evaluating the reliability of the LC process is by assessing the mechanical properties of the resulting coating. The hardness of the cladding layers is of crucial importance as it provides the base alloy with required resistance to mechanical wear. There are three primary factors which impact on the value of hardness, the first grain size, second the chemical composition and third the internal stress [131]. A previous study [136] characterised alloy by coated by the LC technique and found that the clad layer was harder than the base material of 30-40%. Furthermore, the stress relief of the clad allowed the clad and HAZ areas to be 10% softer than the base material. On the contrary, Barnes et al. [142] found a remarkable rise in the hardness for the HAZ of the substrate. The formation of martensite occurs because the heating from the laser beam austinites the substrate of the component and fast self-quenching lead to formation of martensite. In the work of Lee et al. [143] It was found that high cooling rates make fine microstructures resulting in excellent mechanical properties. In another study where the microhardness of different coating layers was assessed, the rise of ferrite content and the size of grains caused significant variations in microhardness within the clad cross-section [139].

Ocelík et al. [131] examined the relationship between hardness and microstructure of Co-based alloy coated by LC with decreasing laser power during the cladding process and found that in the case of the interface between the beginning and the end (start/stop), the microstructural changes resulted in sharp changes in microhardness. It has been suggested that a re-melting approach could be used to decrease the defects in start/stop zone.

One important parameter in LC operation is the power density. Reducing the power density of the LC process below a key threshold will result in the development of an overlapping boundary zone closed to the substrate. Also, low power density will result in the formation of pores because the laser beam is too low in intensity to melt the cladding powder sufficiently. The formation of pores is undesirable as it will compromise the resistance of the cladding coating to wear and corrosion and results in lower microhardness [141], [144]. This problem may be affected by two types of factors. First, the cross-section energy distribution of the laser

beam, and second the laser irradiation blocked by the accumulation of molten powders. Accordingly, it is necessary to prevent pores formation in the cladding coating. To achieve this, the laser irradiation blocking by the accumulation of the molten powders must be solved. To fix this issue there are two ways, one is to increase the laser power, and another is to decrease the powder feed rate [145].

2.10 Overview

This review has shown that SA508 Gr.4N has much potential to replace SA508 Gr.3 in RPV applications, in particular in larger next generation nuclear power generation systems. Clearly going to larger RPVs will mean we will not be able to manufacture in one piece, leading to the requirement of fabrication. In this thesis, the use of RPEBW will be explored as a fabrication technique to generate high integrity welds, as well as be QHT following welding. This will enable a critical assessment of the technology to see it is worth investing at a larger scale for qualification purposes, which can often be at a significant cost.

The chapter presented an overview of the related literature base that has been put forward by previous researchers, including the alloys that are used in RPVs. An overview of the heat treatments and mechanical specifications such as strength, hardenability, toughness and hardness also covered. Then, followed by an analysis of electron beam welding. Moreover, the ends of the chapter included the principles and fundamentals of laser cladding.

Chapter 3/ Experimental

3.1 Steel Alloys Grade 3 and Grade 4N

Two different types of alloys have been used in this study: SA508 Gr.3 Mn-Mo-Ni low alloy steel and SA508 Gr.4N Ni-Mo-Cr low alloy steel. Both were manufactured at Sheffield Foragemasters International. Table 3.1 shows the composition for both alloys. SA 508 Gr.3 and its equivalent international designations have been the workhorse alloy for nuclear pressure vessels since the 1960s [1], while SA508 Gr.4N is a new generation alloy that is currently being assessed for its suitability in Generation IV reactors.

Table 3.1 Chemical composition of SA 508 Grade 3 & 4N used in this project

Material	C	Cr	Ni	Mn	Mo	Si	P	S	Al	Cu	V	Fe
SA508-4N	0.077	1.72	3.26	0.25	0.51	0.33	0.018	0.010	-	-	-	Bal
SA508-3	0.18	0.16	0.70	1.44	0.50	0.21	0.0049	0.0034	0.064	0.042	0.0055	Bal

Initial samples were supplied by Sheffield Forgemasters to investigate the microstructure of the two alloys. The exact processing routes of the material samples supplied were unknown. The samples were sectioned transversely by saw to small pieces with dimensions of 10 mm^3 per piece and then mounted and prepared for testing using standard micro preparation methods (grinding and polishing). Grinding was accomplished using a series of SiC abrasive papers from 280 to 1200 grit. Coarse polishing was performed using a 3 µm diamond paste using a nap-less nylon cloth. Fine polishing was performed using a 1 µm paste on a medium nap rayon cloth followed by alumina paste. The samples were then etched using a 2% Nital solution (mixed from nitric acids and ethanol) [146], Figure 3.1 shows the samples. Optical microscopy (Nikon Eclipse LV150 series light optical microscope) was used to examine the microstructure for all the samples. Vickers hardness testing was also undertaken on both samples to compare hardness.

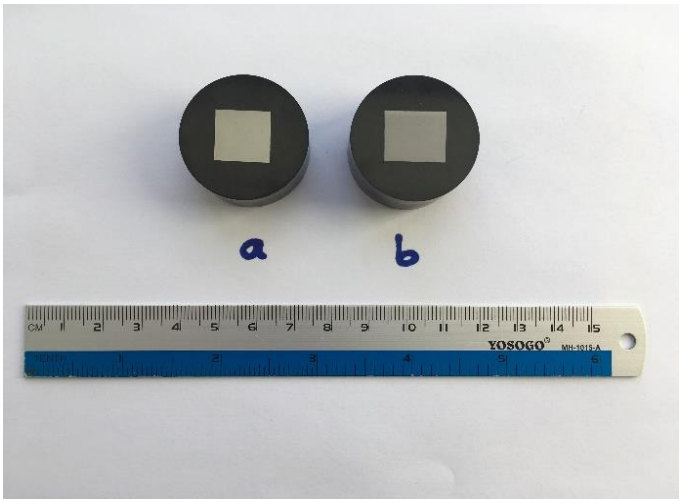

Figure 3.1: Preparation samples (a) SA508 Gr.4 (b) SA508 Gr.3

3.2 Weld Samples

As stated previously, this project aims to develop an efficient thick-walled welding process to weld the new generation RPV alloy SA508 Gr.4N to increase the thickness of the RPV wall from 150mm to be 200mm. This work was done in collaboration with The Welding Institute (TWI) using their Reduced Pressure Electron Beam Welding (RPEBW), instead of the traditional Electron Beam Welding (EBW), which operates under a fully enclosed vacuum. Work was undertaken in two stages: first RPEBW was done on 160 mm to optimise parameters and secondly, on thickness of 200mm, as shown in Figure 3.2.

Figure 3.2: The weld samples 160mm and 200mm

An initial welded specimen with 160 mm thickness was received with an X-ray radiographic image to investigate defect density and type. As seen in Figure 3.3a, there were significant defects inside the sample but there were still contiguous areas of solid weld to make this sample useful for investigating weld microstructure, for example, position A in Figure 3.3a. A slice at position A was then electrically discharged machined out, as shown in Figure 3.3b. This was then sectioned by saw to small pieces with dimensions of 40 mm length, 20 mm width, and 5 mm thickness. Note, as shown in the Chapter 4, as time progressed weld process control improved, and defect density significantly reduced. All samples were then prepared for microstructure investigation by grinding and polishing using standard methods. The grinding used abrasive papers from 280 to 1200 grit. The polishing process was accomplished using 3 µm diamond paste, 1 µm paste and finally alumina pastes for the finish polishing, using a variety of different types of clothes. Subsequently, the specimens were etched using 2% Nital solution (a mixture of nitric acid and ethanol) [146].

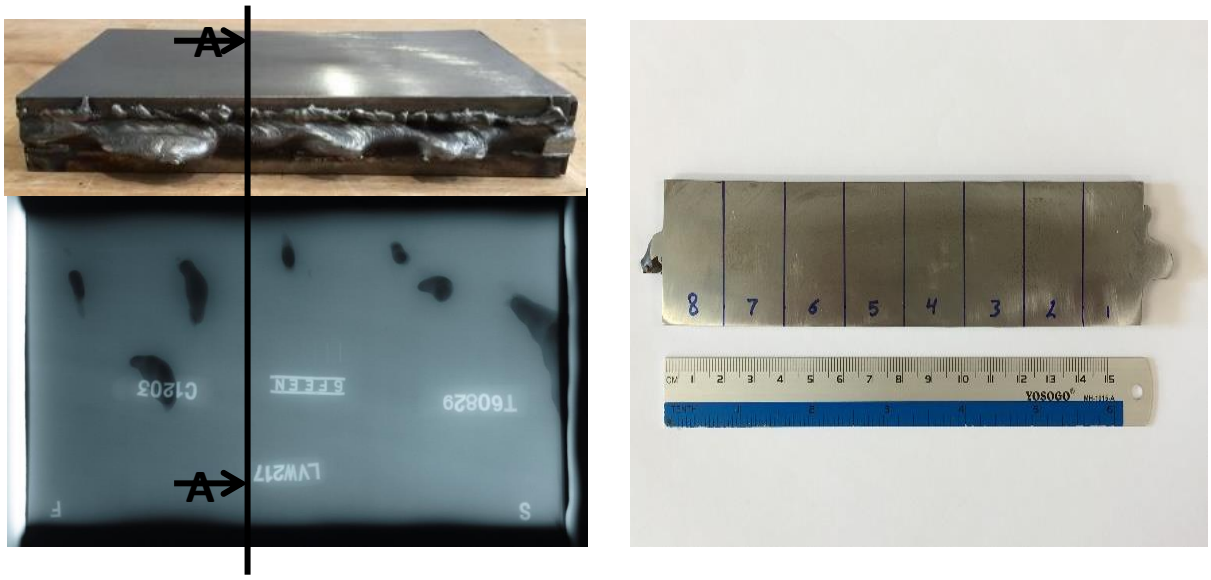

(a) (b)

Figure 3.3: (a) The weld samples 160mm with X-ray image (b) slice with small samples

3.2.1 Comparison between (PWHT) and (QHT) with as welded

The 160mm welded specimen was also used to compare two different heat treatment designs for the as-welded material, as shown in Figure 3.4. Namely: 1. post-weld heat treatment (PWHT), where the temperature reached a maximum of 565°C with a heating rate of 25°C/hr, held for 30 hours followed by cooling at 14°C/hr, and 2. quality heat treatment (QHT), the design of which consists of a two-part heat treatment, the first is austenitisation, at 860°C and holding time of 6 hours with cooling rate 25°C/min, and the second is a tempering heat treatment at a temperature 640°C with a 8 hours holding time and then furnace cooled. The heat treatment designs are schematically illustrated in Figures 3.5 and 3.6.

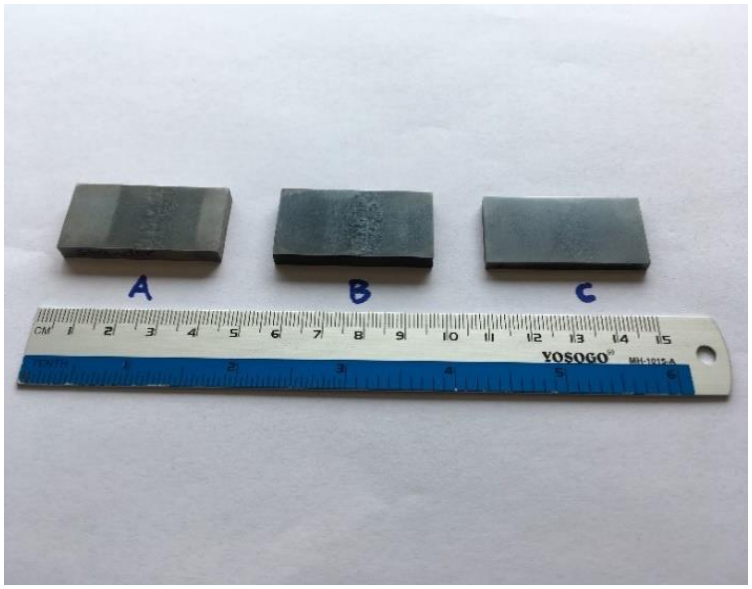

Figure 3.4: SA 508 Grade 4N; (a) as welded; (B) PWHT and (C) QHT

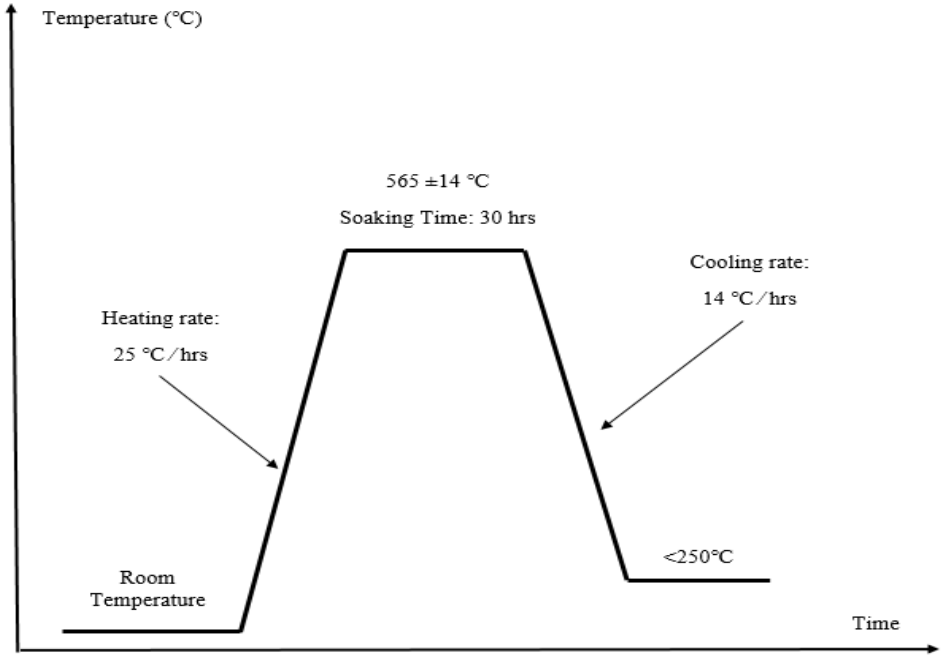

Figure 3.5: The Post Weld Heat Treatment (PWHT) Design.

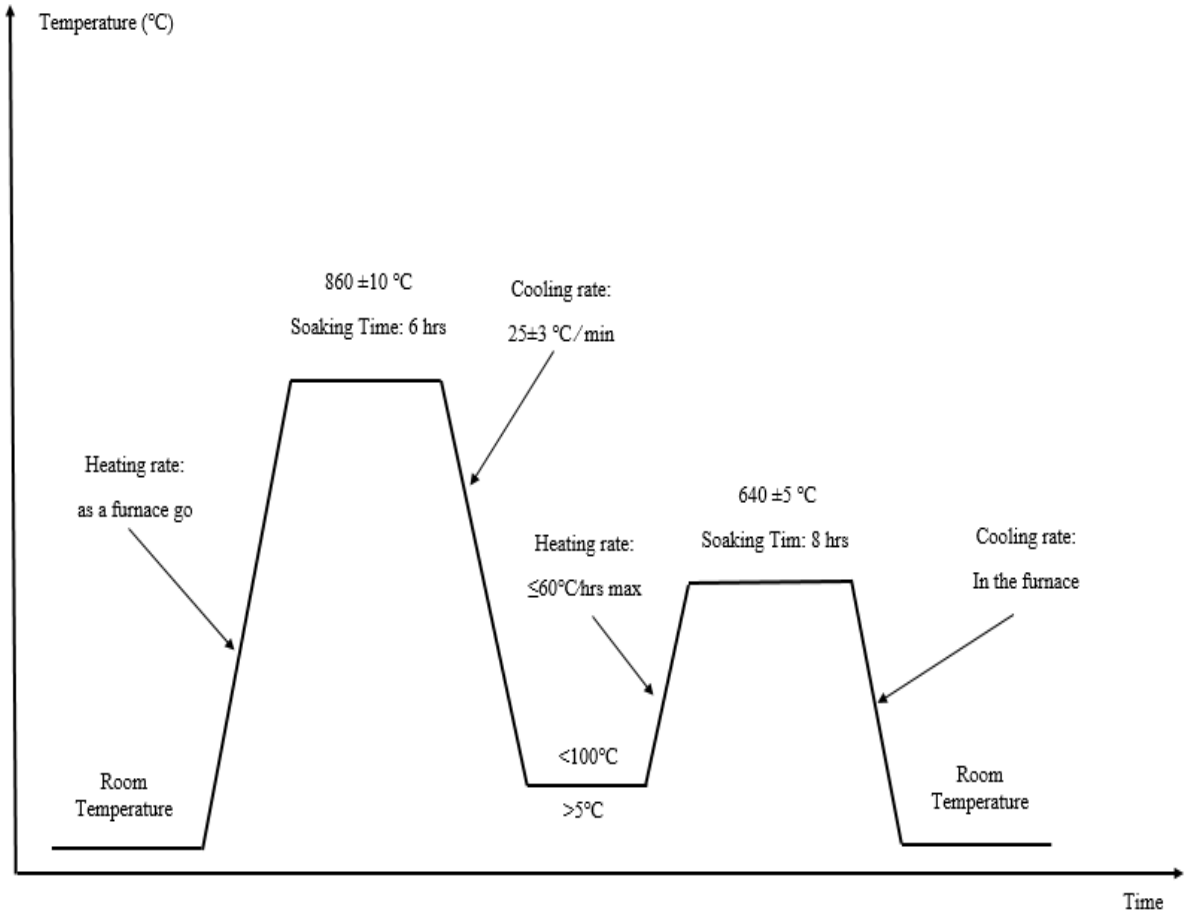

Figure 3.6: The Quality Heat Treatment (QHT) Design

The particular furnace for the heat treatment is shown in Figure 3.7, which used a digital controller to write the steps for the heat treatment operation. Moreover, the samples were also subjected to Vickers microhardness measurement, undertaken to investigate the effect of the heat treatment process on the hardness in different areas of the surface of the samples. Note, in this instance the temperature presented by the furnace was considered to be the temperature of the sample.

Figure 3.7: The furnace used in heat treatment

3.2.2 The QHT for the weld samples with different temperature

The thermomechanical compression (TMC) machine at the University of Sheffield was used to achieve more accurate QHT for the 200mm thick welded materials, as shown in Figure 3.8. Four temperatures of heat treatment were used, 860℃, 920℃, 1020℃, and 1120℃ at a holding time of 15 minutes and 25℃/min cooling rate, then tempering at 640℃ followed by air cooling, as shown in Figure 3.9. Figure 3.10 display TMC curves which miss the holding time and the curves are essential to demonstrate the cooling rate, to determine the best temperature for obtaining optimum microstructure and mechanical specifications. The samples for microstructure analysis were prepared and examined as previously explained. Figure 3.10 displays the samples.

The Thermomechanical Compression (TMC) machine is designed and produced by Servotest Ltd for the University of Sheffield. This device has a significant and precise possibility to perform several thermal processes, especially deformation processes with excellent control of the deformation parameters, including deformation temperature, also heat treatment operations.

Moreover, it is superior to control and record by the unique design of computer software to monitor the heating and cooling rates.

Figure 3.8: The thermomechanical compression machine (TMC).

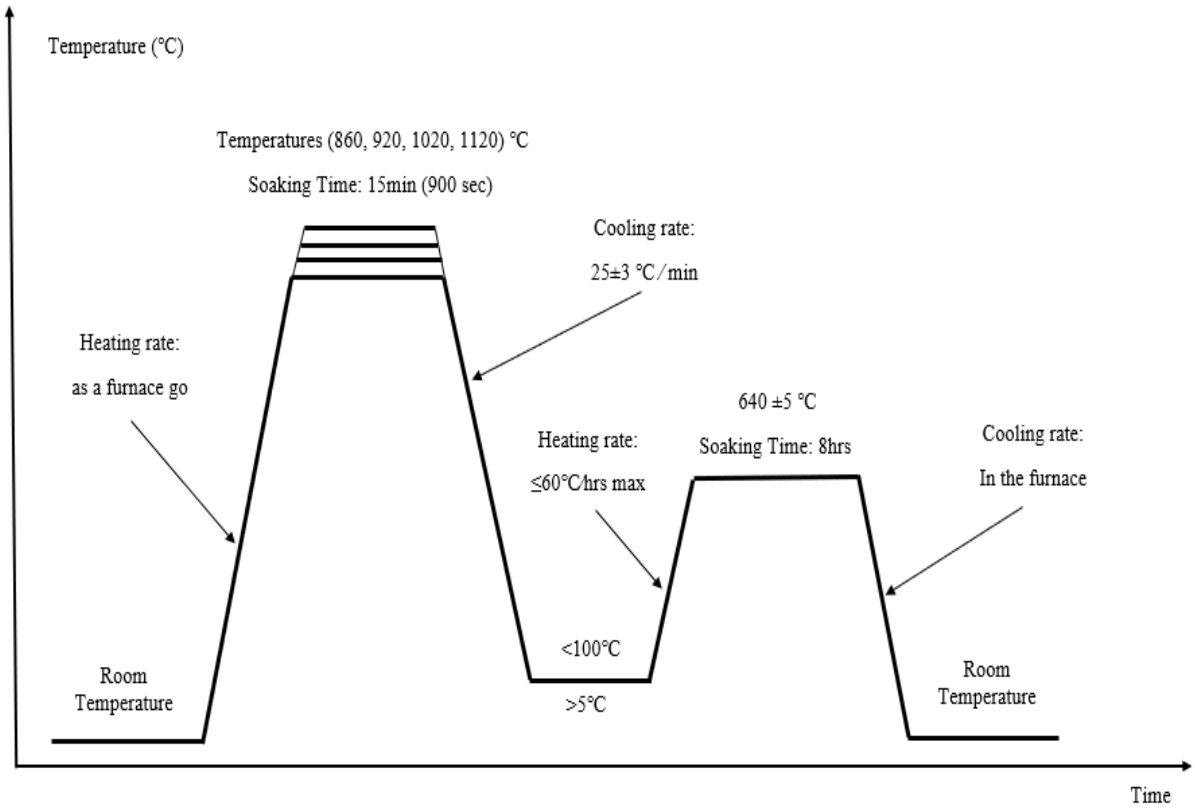

Figure 3.9: The design for different QHT temperatures.

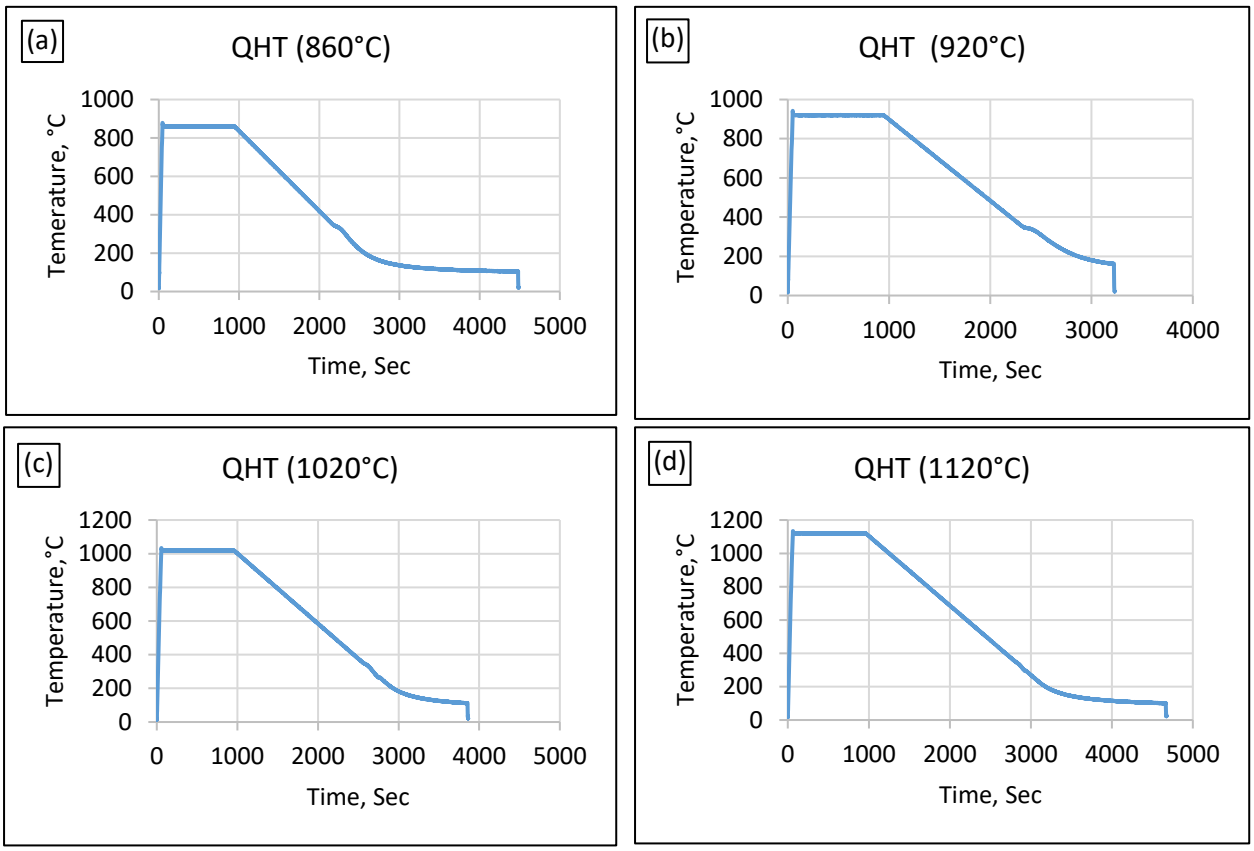

Figure 3.10: The experimental TMC temperature curves for different QHT austenisation temperatures (a) 860°C, (b) 920°C, (c) 1020°C, and (d) 1120°C.

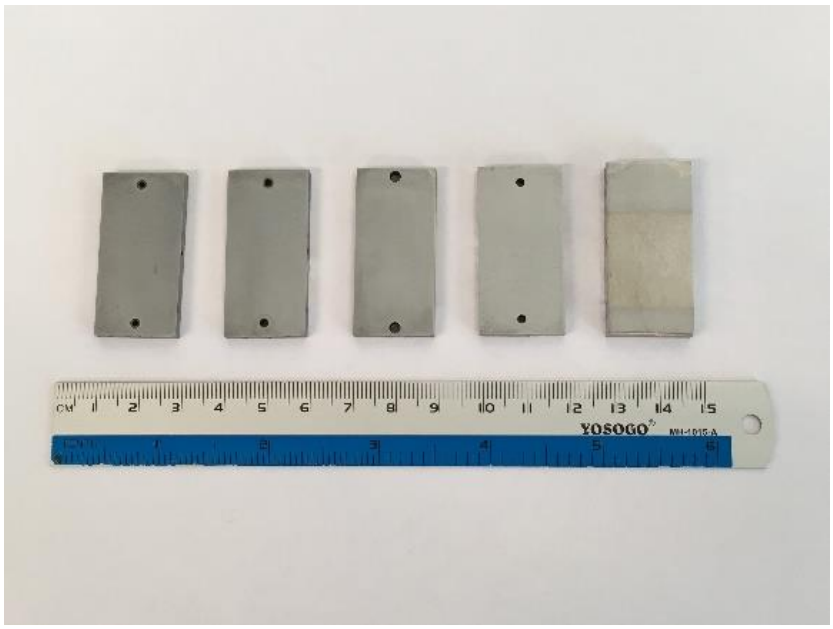

Figure 3.11: The weld samples with different QHT temperature.

3.2.3 The QHT for the weld samples with different holding times

To investigate the effect of austenisation holding time on QHT results, four different holding times at 860℃ were investigated. The holding times were 8 hours, 24 hours, 48 hours, and 96 hours, respectively, using the furnace in Figure 3.7, cooling was then done in air. This was then followed by a further austenisation at 860℃ in the TMC machine for 15 minutes followed by cooling at 25℃/min. Tempering was then undertaken at 640℃ followed by cooling inside the furnace, schematically shown in Figure 3.12 and Figure 3.13. The samples for microstructure analysis were prepared and examined as previously explained. Figure 3.14 illustrates the specimens used.

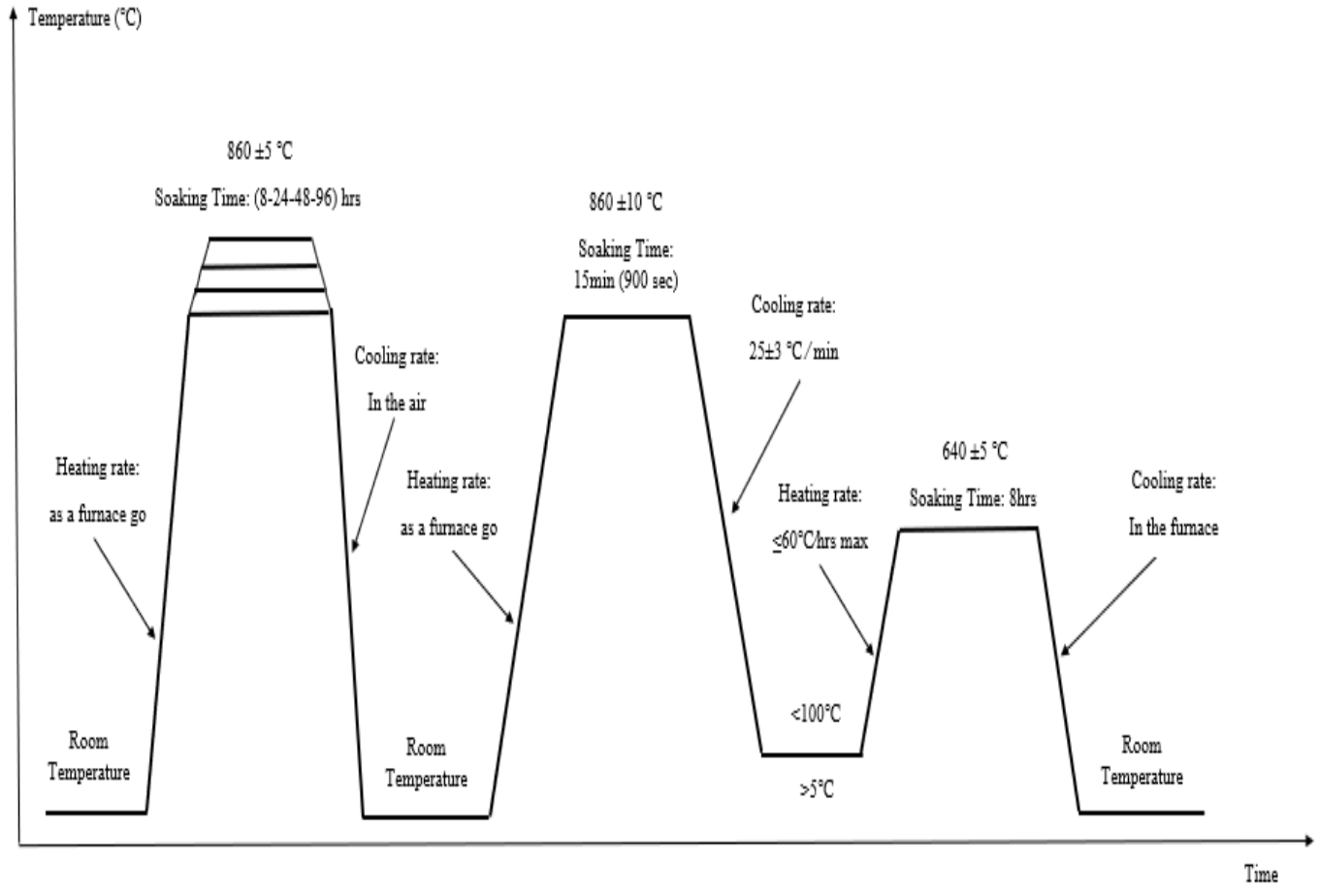

Figure 3.12: The design for different holding times QHT temperatures

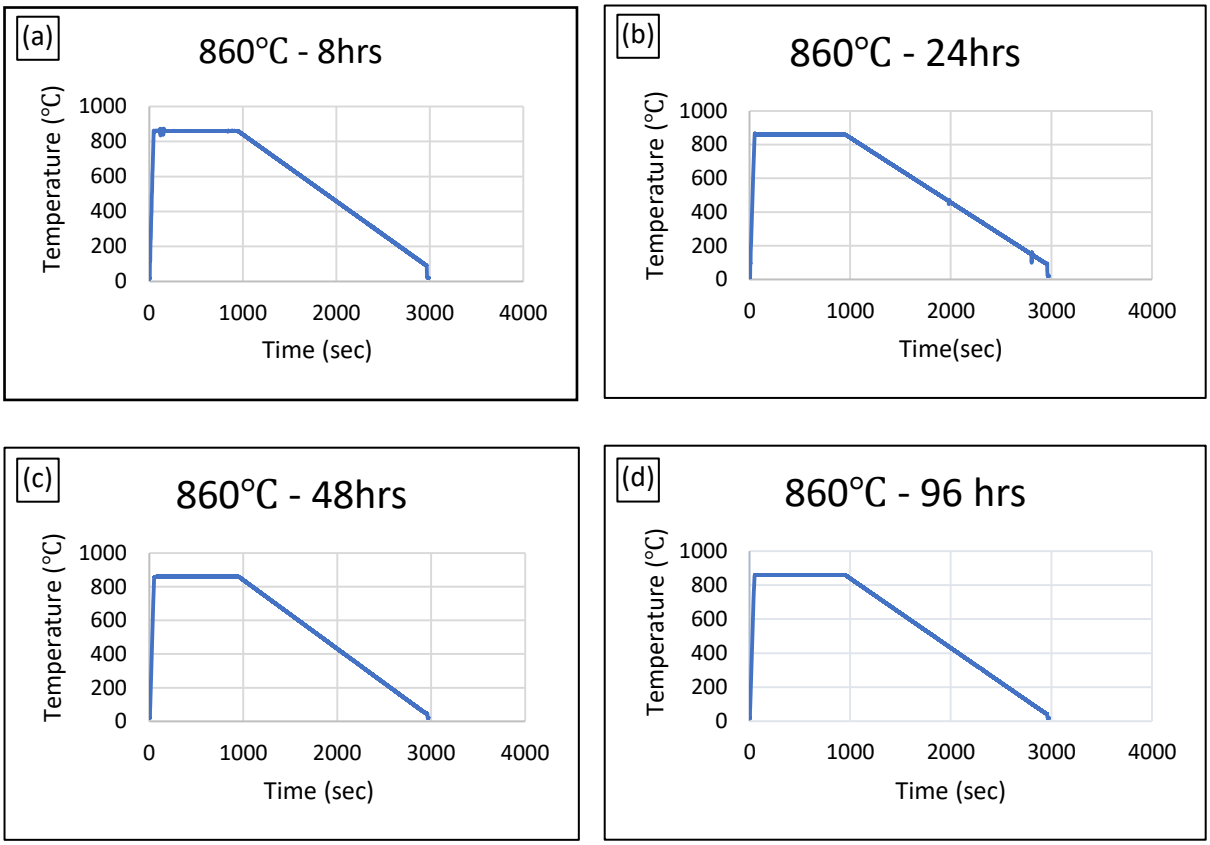

Figure 3.13: The TMC curve for different QHT temperature (a) 8 hours, (b) 24 hours, (c), and (d) 96 hours.

Figure 3.14: The weld samples with different holding times QHT temperature.

3.2.4 The Final Heat Treatment Design for the Mechanical Properties of Weld Specimens

After selecting the most appropriate temperature and hold time for QHT, a more extensive study was undertaken on the welded specimens to study the mechanical properties and to observe the extent of the impact of heat treatment design on the mechanical property specification required. The heat treatments were undertaken using the furnace in Figure 3.7 at 860℃ with the cooling rate in air, then the TMC machine at temperature 860℃ for 15 minutes with 25℃/min cooling rate. Tempering then followed at 640℃ with cooling inside the furnace. Figure 3.15 shows the final design of the QHT.

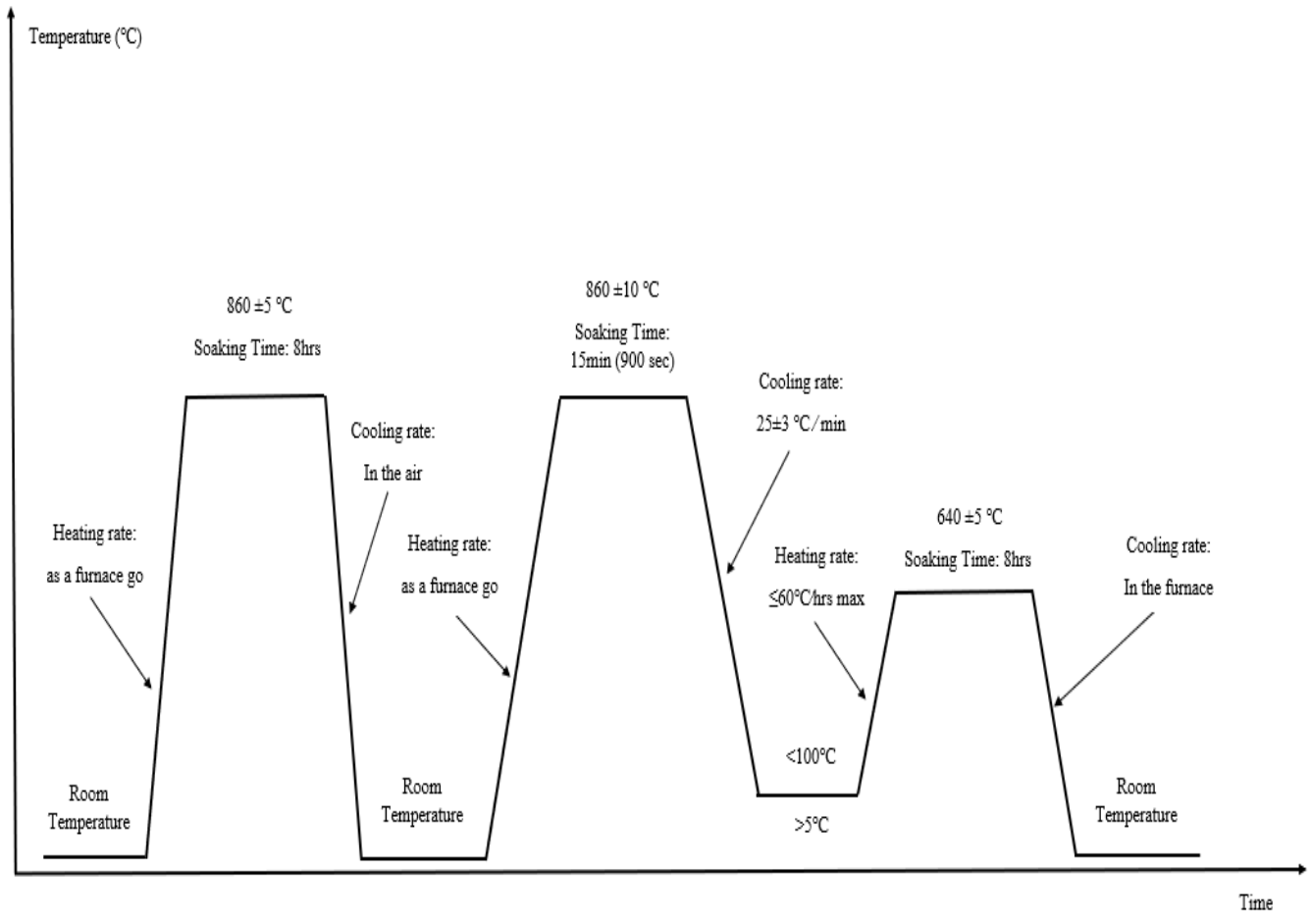

Figure 3.15: The design for the Final QHT in temperature and Hold Time.

3.3 Mechanical Properties for Weld Specimen

3.3.1 The Hardness Sample Design

All samples were subjected to Vickers hardness testing by microhardness measurement device (Struers-DuraScan made by Emco.Test) to investigate the effect of the heat treatment process on the hardness in different areas of the surface of the samples, as shown in Figure 3.16. The specimens had dimensions of 40 mm length, 20 mm width, and 5 mm in thickness with the weld direction. Figure 3.17 illustrates the temperature curve of the hardness sample in TMC machine.

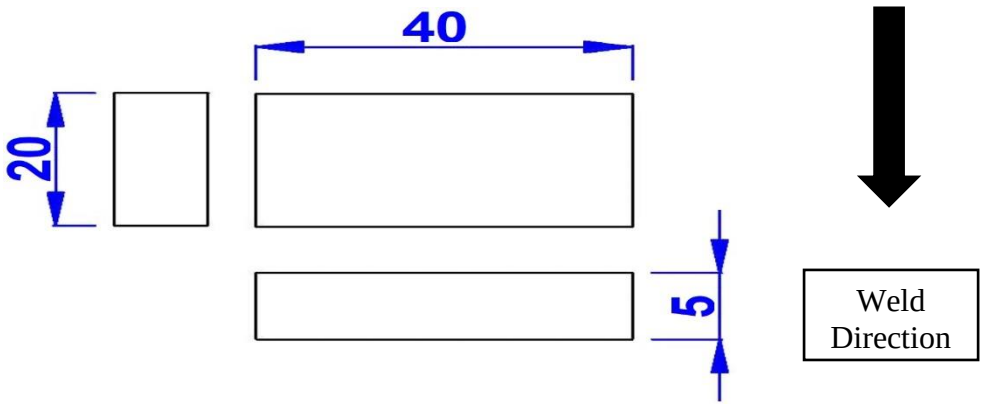

Figure 3.16: The Hardness Scheme Design (dimensions in mm)

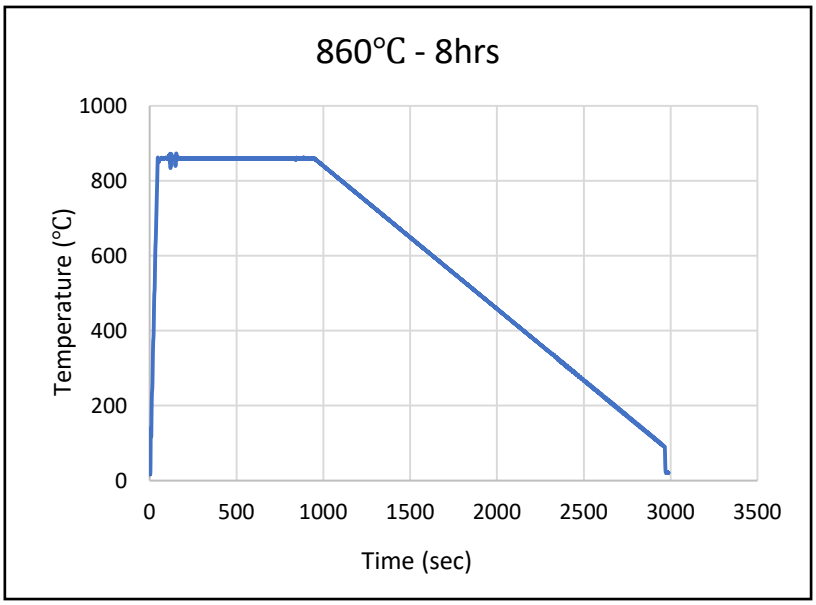

Figure 3.17: The TMC curve of QHT temperature for the hardness sample.

3.3.2 The Tensile Sample Design

The tensile specimens were designed using ASTM A370 – 14 [147], and the tensile tests were carried out at room temperature. The welding specimens were prepared by cutting using electrical discharge machining (EDM) into three samples depending on the different welding layers, the Fusion zone (FZ), Heat affect zone (HAZ), and the Base Metal (BM). The tensile samples were prepared separately for each layer after being subjected to the final QHT, as shown in Figure 3.18 and Figure 3.19. Again, the TMC was used for QHT to gain more accurate results, as shown in Figure 3.20.

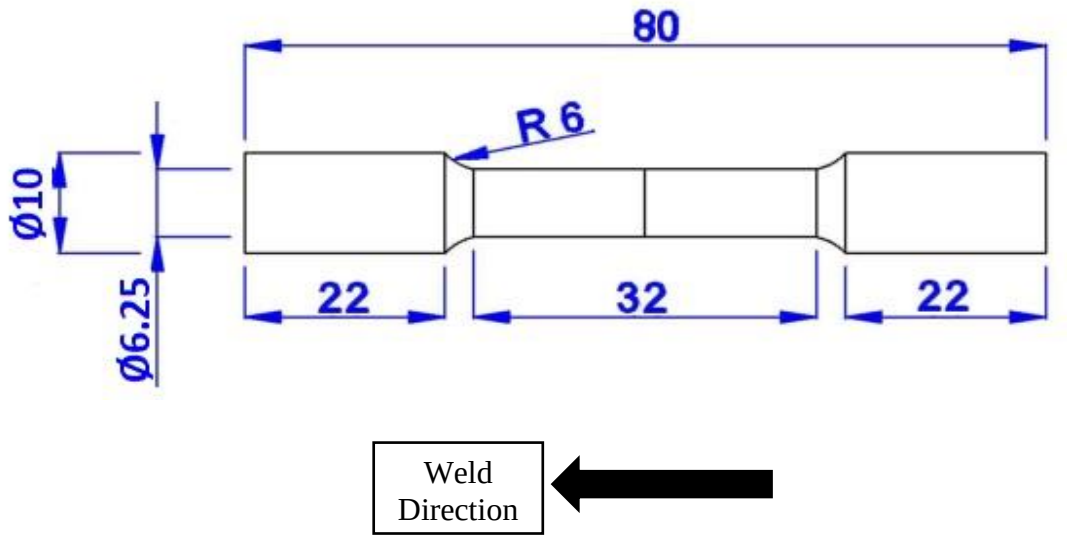

Figure 3.18: The Tensile Scheme Design

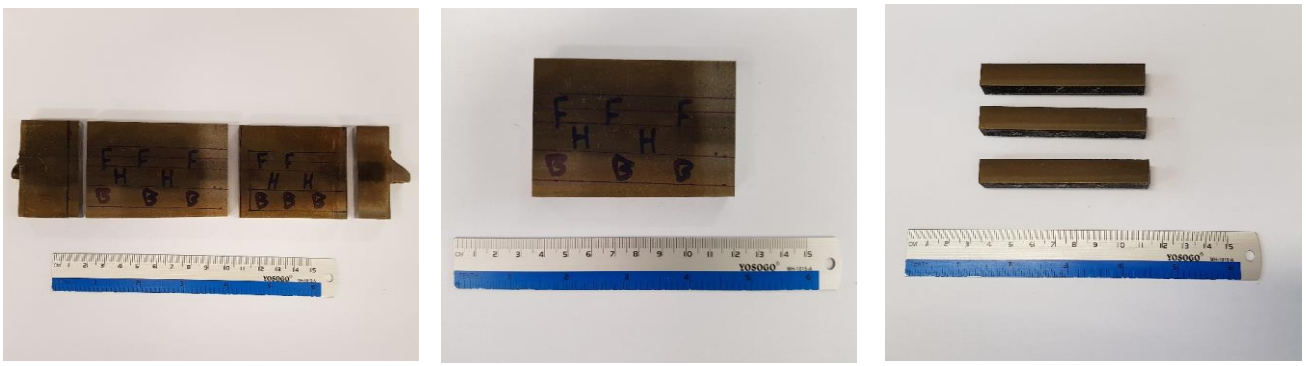

Figure 3.19: The Location for Tensile Test

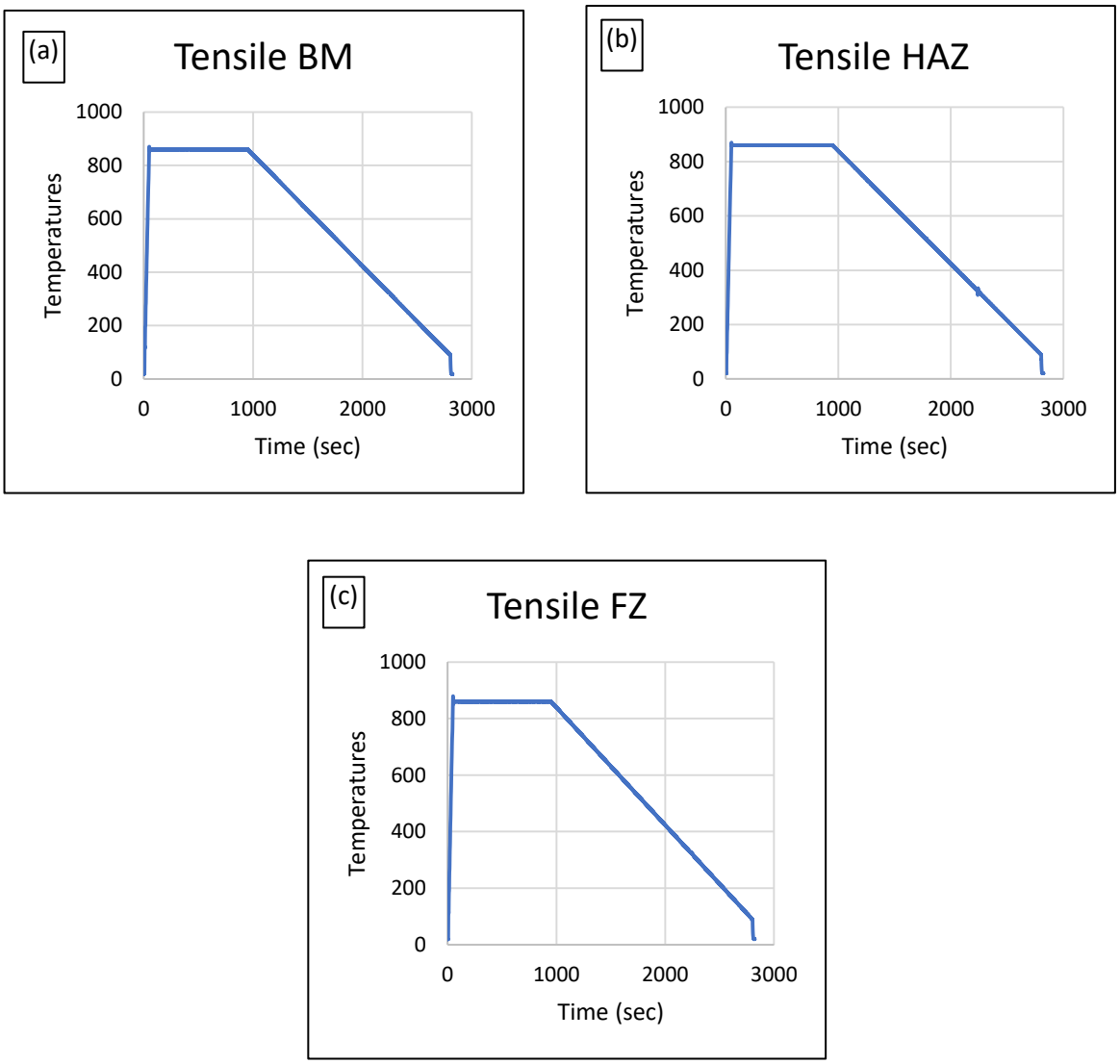

Figure 3.20: Final TMC For Tensile Test (a) Base metal, (b) Heat Affect Zone, and (c) Fusion Zone.

3.3.3 The Charpy Impact Sample Design

Charpy Impact testing was used in the as welded and QHT Specimens at -73 °C for all three locations (Base, HAZ, FZ) in the weld section. The specimens were designed according to the BS EN ISO 148-1 as shown in Figure 3.21. The samples were cut depending on the different weld layers of the weld section and subjected to the final QHT design, as shown in Figure 3.22. Each Charpy sample was heat treated separately in the TMC, as shown in Figure 3.23.

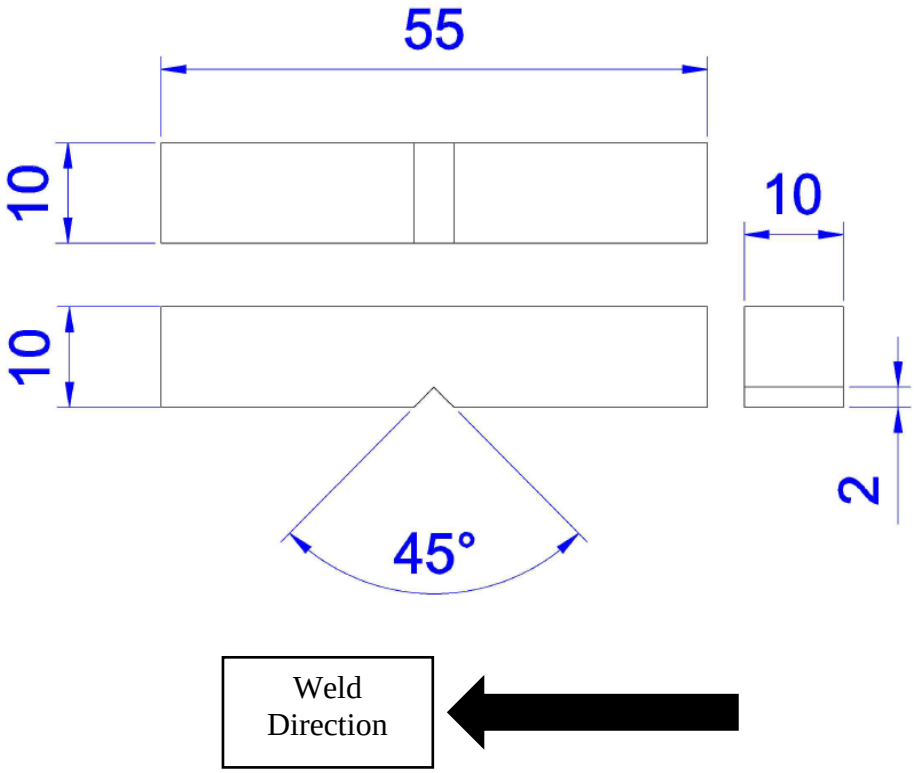

Figure 3.21: The Charpy Impact Scheme Design.

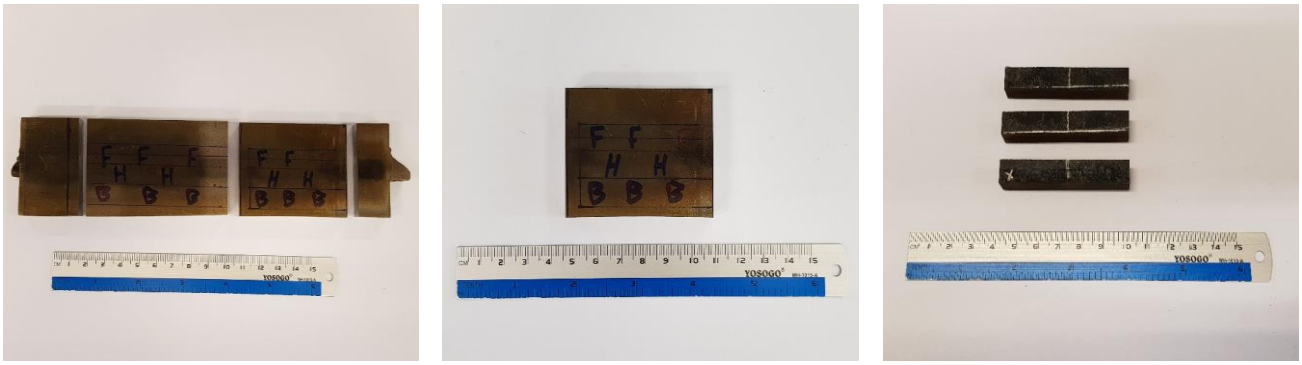

Figure 3.22: The Location for Charpy Impact Test

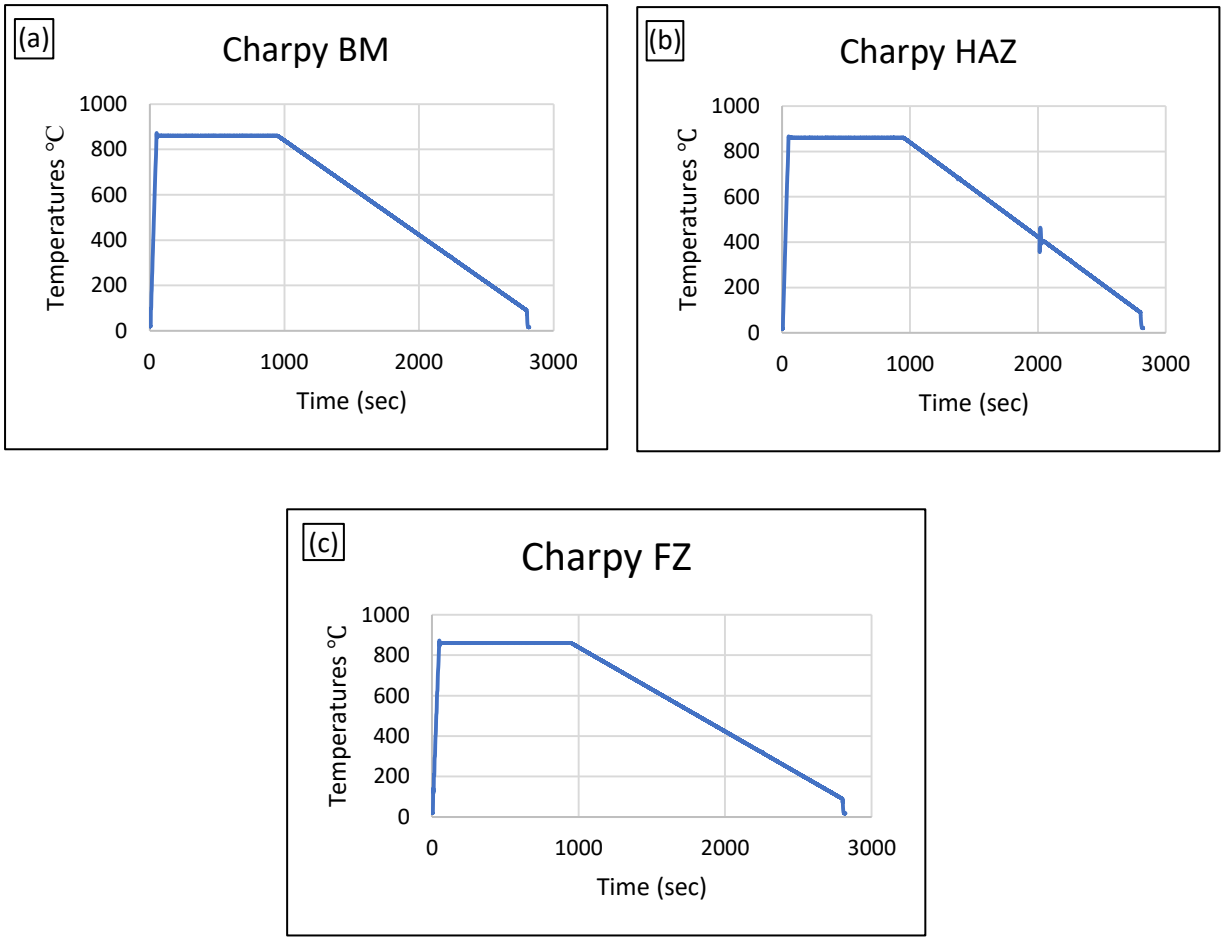

Figure 3.23: Final TMC for Charpy Impact Test (Base Metal, (b) Heat Affect Zone, and (c) Fusion Zone.

3.4 Cladding Samples

Several laser clad experiments were performed at the Nuclear Advanced Manufacturing Research Centre (NAMRC) with different parameters to identify the optimum processing parameters. SA508 Gr.4N was used as a substrate for the cladding process, the length of the track line of cladding varied between 120 mm and 125 mm, as shown in Figure 3.24. The metal used in the cladding layer was powder deposited stainless steel type 308L. Table 3.2 shows the composition for the stainless-steel type 308L powder.

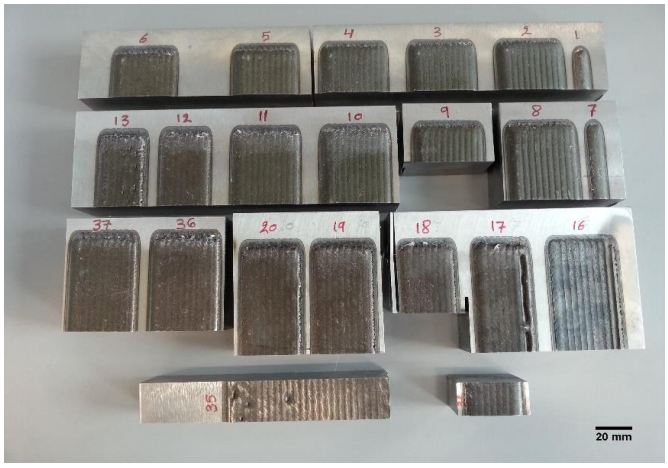

Figure 3.24: All cladded samples.

Table 3.2 chemical composition of the stainless-steel type 308L powder at on weight %.

Material	C	Cr	Ni	Mn	Mo	Si	P	S	N	Cu	B	O	Fe
Stainless steel 308L	0.01	20.4	11.0	1.39	0.01	0.51	0.002	0.005	0.036	0.01	0.01	0.034	Bal

The cladding samples were sectioned transversely by saw to small pieces with dimensions of 15 mm length, 10 mm width, and 10 mm thickness. The standard micro-preparation methods were applied to the samples to perform microstructural analysis. For etching, the samples were etched using two different types of solutions, the Nital solution with 2% percentage utilised for the steel area, while a mixture of equal amounts of acetic, nitric and hydrochloric acids was used to etch the stainless-steel area (clad layer). Figure 3.25 shows all cladding samples mounted.

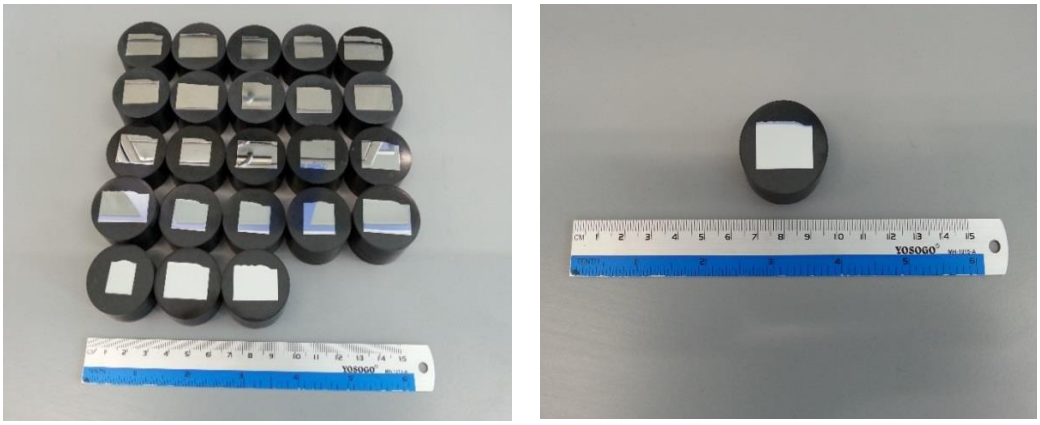

Figure 3.25: All mounted cladded samples.

3.4.1 Heat Treatment Design for Cladding Samples

3.4.2 Compression between (PWHT) and (QHT) with as welded

Two types of heat treatment have undertaken; post weld heat treatment (PWHT) at 565°C, with a heating rate of 25°C/hr and holding time of 30 hrs, followed by cooling at 14°C/hr, and the Quality Heat Treatment (QHT), the design consisting of a two-part heat treatment; the first is austenitisation, at 860°C and holding time 6 hours, and the second is a tempering heat treatment at a temperature 640°C with 8 hours holding time, as shown schematically in Figure 3.26 and Figure 3.27. The samples were subsequently prepared for microstructure analysis using the methods previously mentioned, as shown in Figure 3.28.

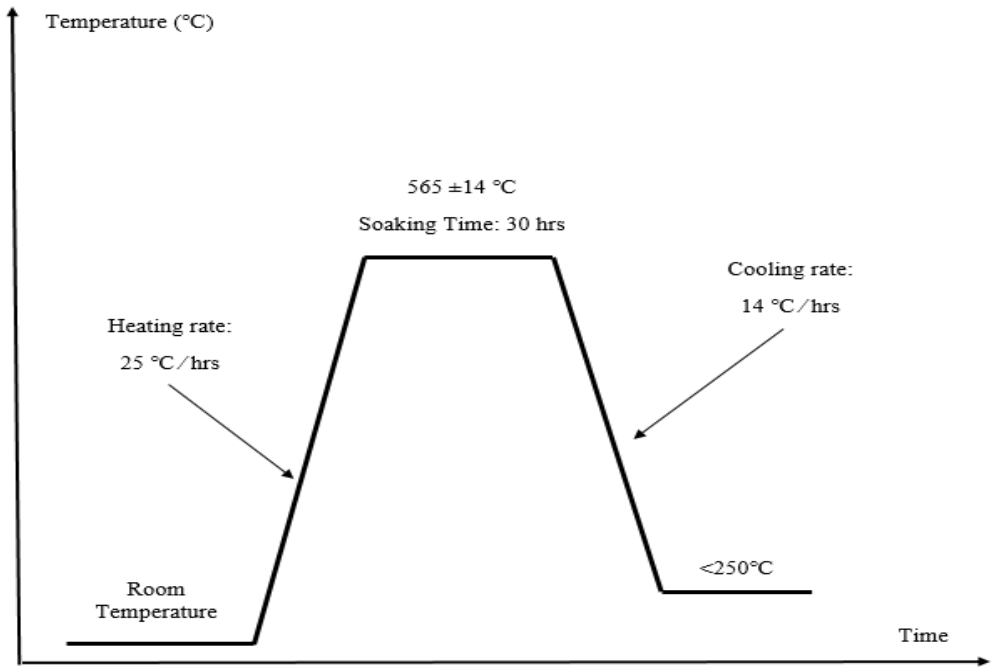

Figure 3.26: The Post Weld Heat Treatment (PWHT) Design

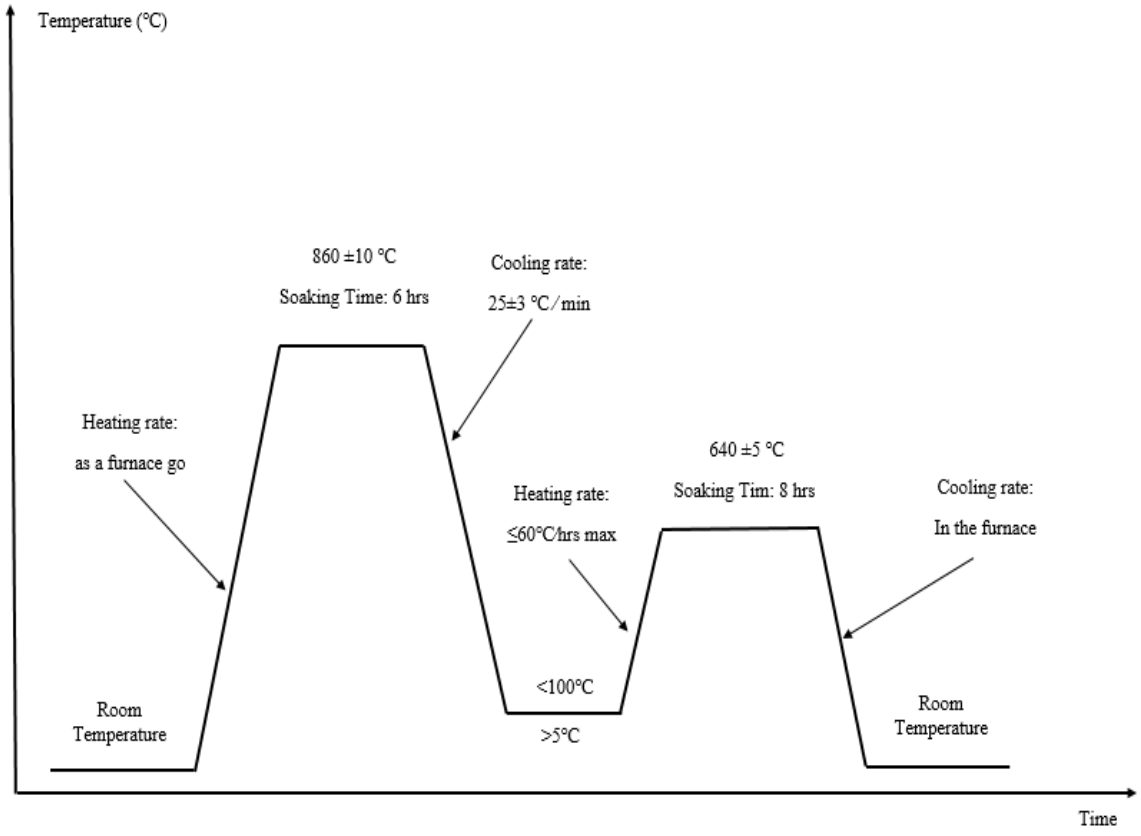

Figure 3.27: The Quality Heat Treatment (QHT) Design

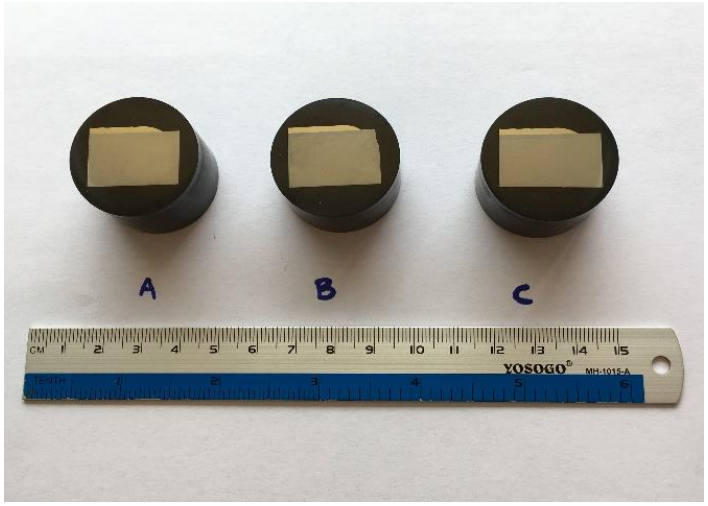

Figure 3.28: the cladding samples; (a) as welded; (B) PWHT and (C) QHT

3.4.3 The QHT for the cladding samples with different temperature

The effect of QHT temperature on the clad samples was again undertaken at four different temperatures, 860℃, 920℃, 1020℃ and 1120℃, at a holding time of 15 minutes and the cooling rate 25℃/min, then tempering at 640℃ with the cooling rate inside the furnace, as shown in Figure 3.29. The samples were mounted and prepared for etching for an examination of the microstructure, like previous specimens, as shown in Figure 3.30 and Figure 3.31.

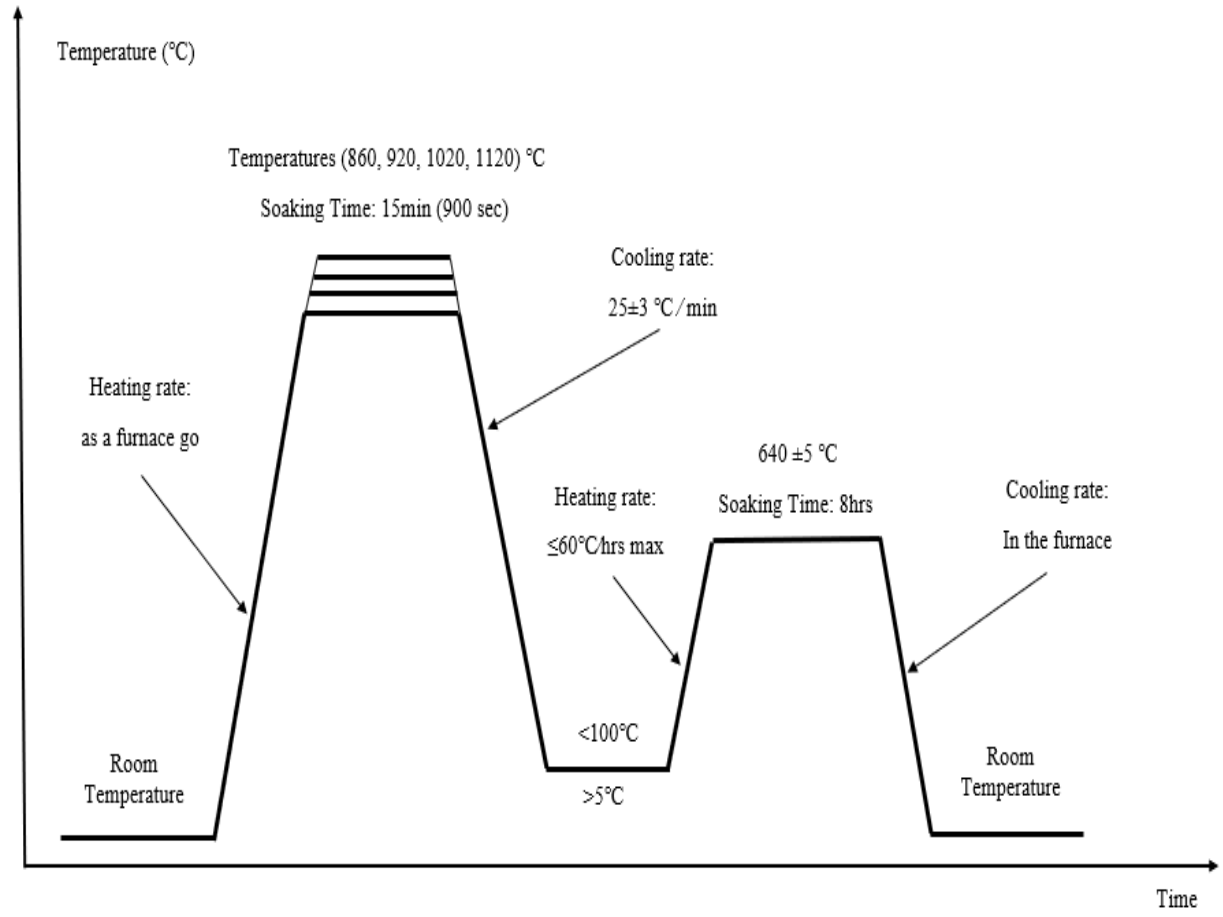

Figure 3.29: The design for different QHT temperatures.

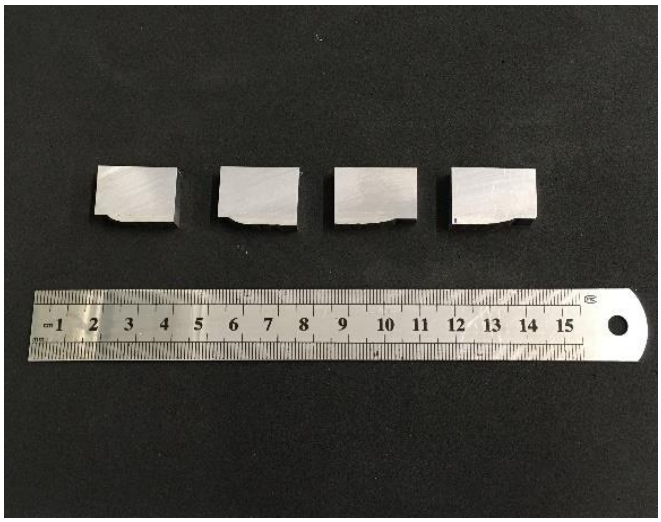

Figure 3.30: The cladding samples with different QHT temperatures.

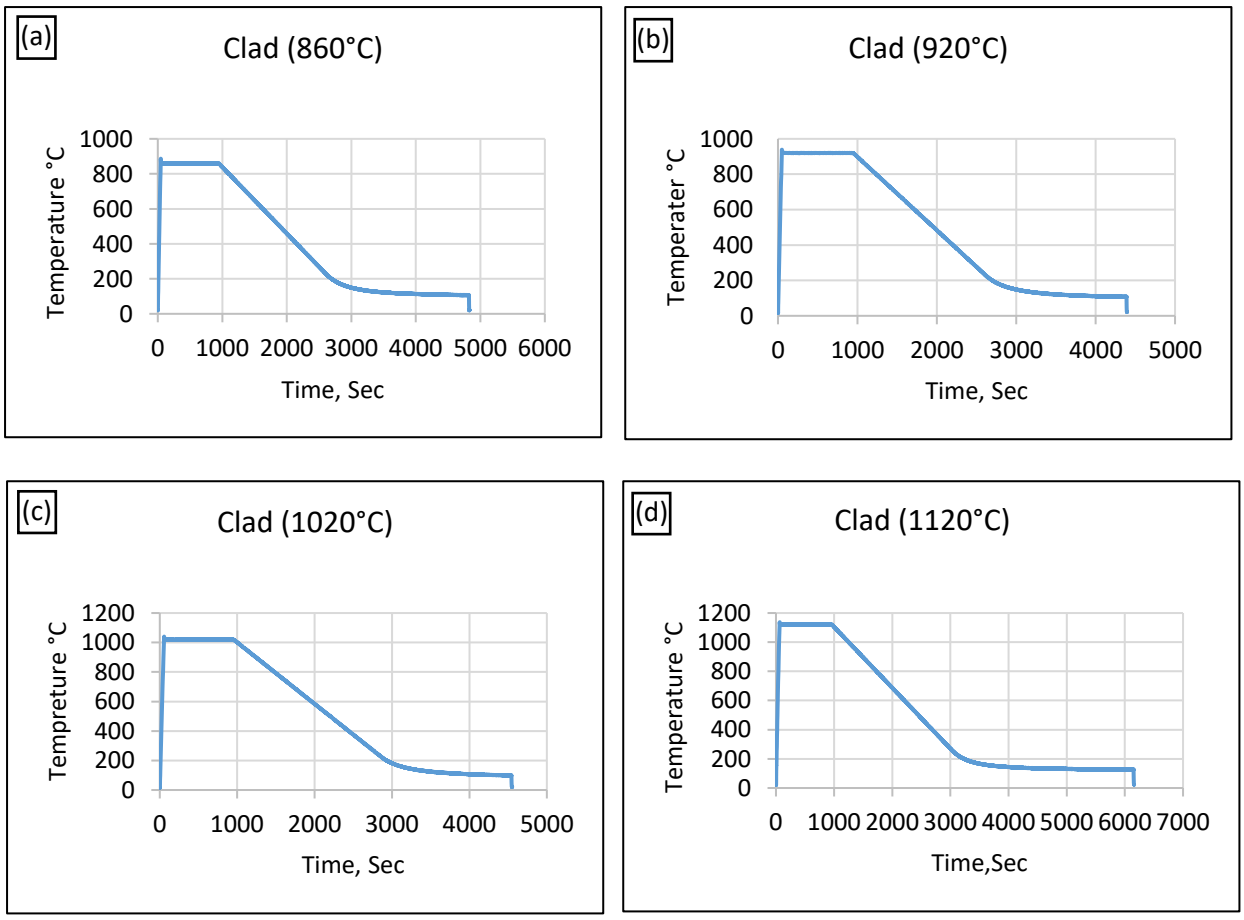

Figure 3.31: The TMC curve for different QHT temperature.

3.4.4 Microhardness for Cladding Specimens

The specimens were prepared for the microhardness test to analyse the impact of the different heat treatment on the hardness for the microstructure in diverse areas inside the cladding samples, as shown in Figure 3.32.

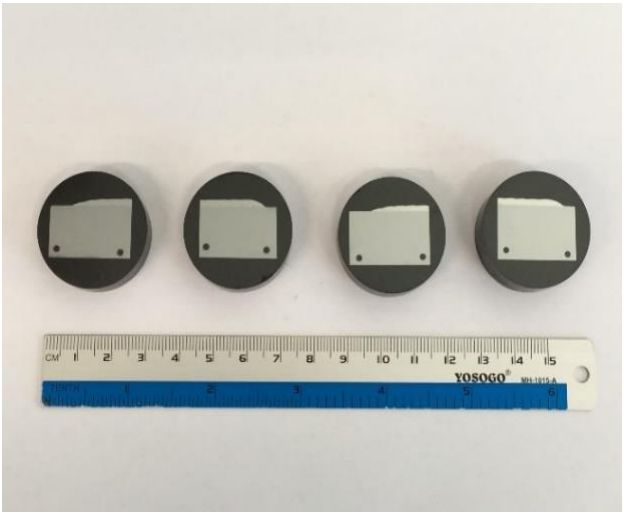

Figure 3.32: The cladding samples for microhardness test

3.4.5 Final QHT for the Cladding Specimens

The final QHT design was at 860℃ and for 8hrs holding time, exactly the same as the as-welded samples, as shown in Figure 3.34. The clad specimens were prepared to test the microstructure and mechanical properties and analyse the effect of QHT design on specifications for cladding samples in different layers; Figure 3.35 shows the clad specimens. The Thermomechanical Compression (TMC) machine was used to achieve more accurate QHT, as schematically shown in Figure 3.33.

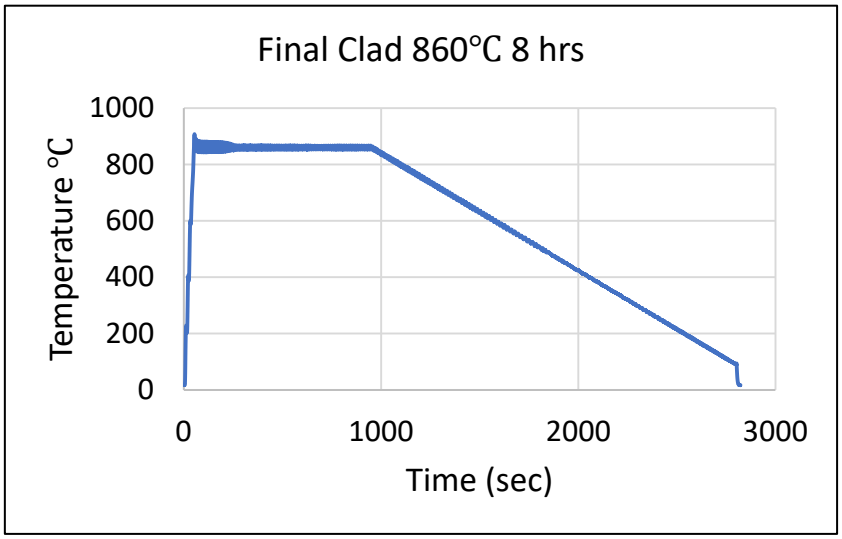

Figure 3.33: The TMC curve QHT temperature for the Final Clad sample.

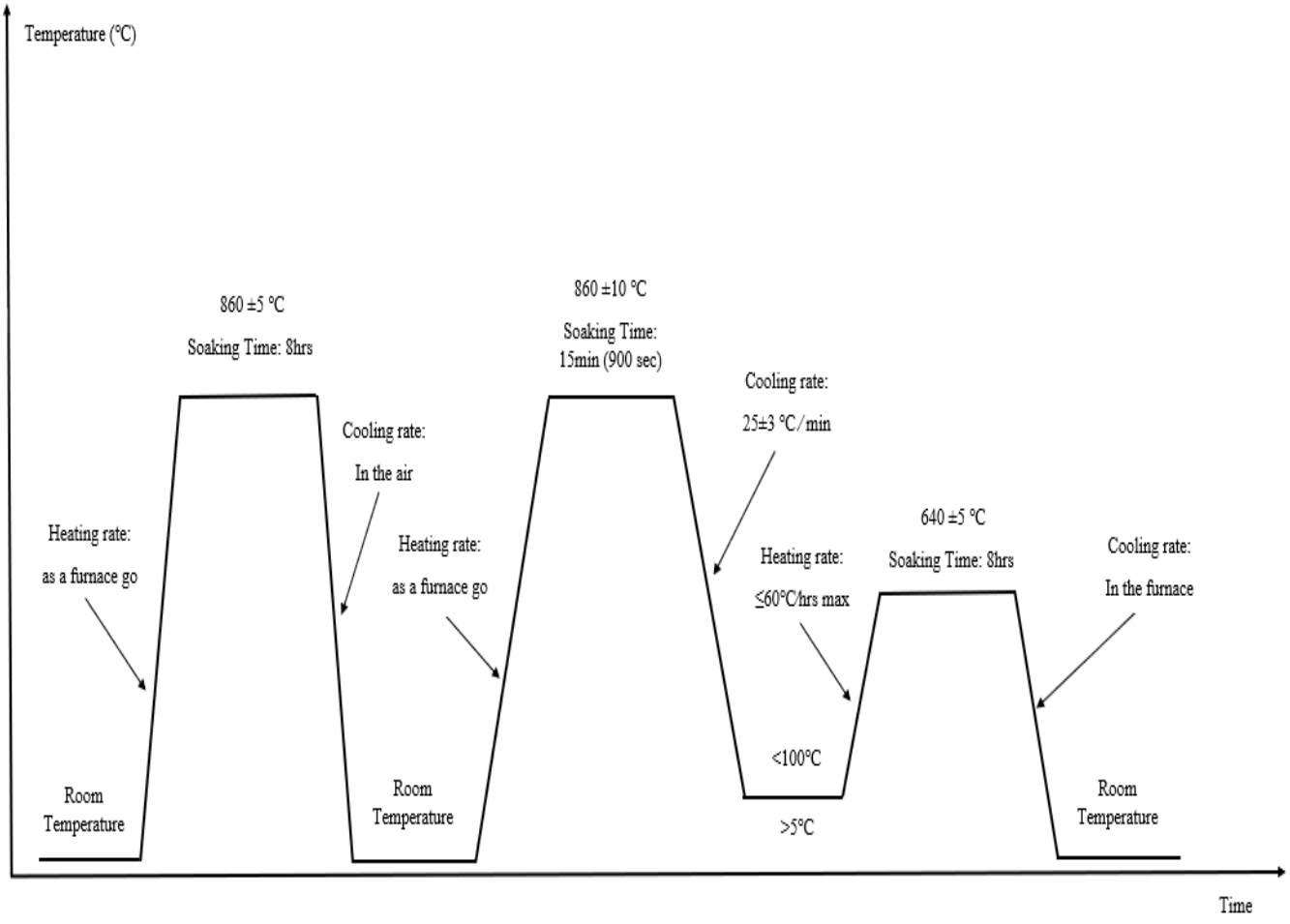

Figure 3.34: The design for the Final QHT in temperature and Hold Time.

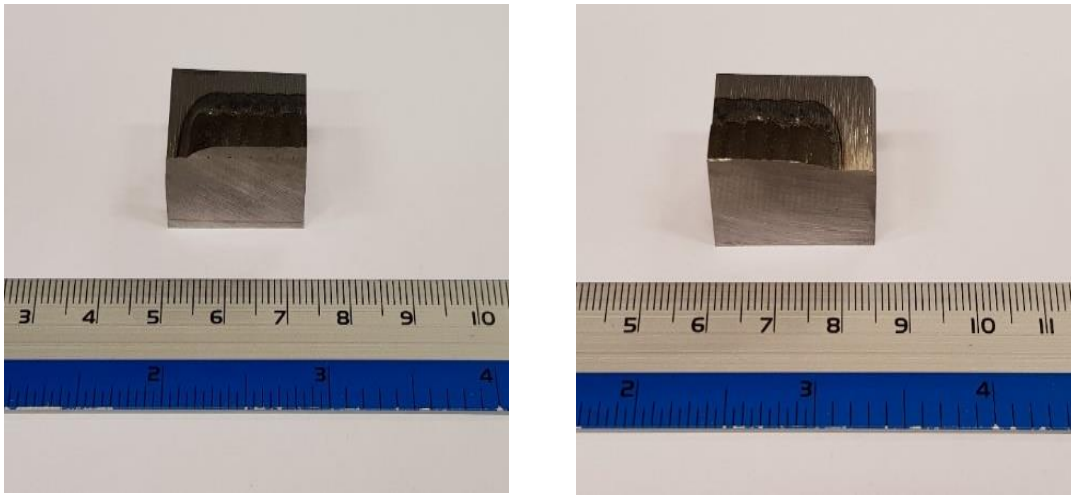

a) before QHT b) after QHT

Figure 3.35: The Final cladding samples (a) before QHT (b) after QHT

Chapter 4 / Welding Results and Discussion

4.1 Introduction

This chapter presents a basic comparison of microstructure and hardness between SA508 Grade 3 and the new generation alloy being studied here, SA508 Grade4N. This is then followed by the first analysis of as-RPEBW SA508 Grade4N and welded material that has been post weld heat treated (PWHT) under standard conditions and quality heat treated (QHT) under varying conditions undertaken in a standard furnace. To achieve more controlled QHT conditions the TMC machine at the University of Sheffield was used for investigating QHT, as it enabled controlled heating rates and cooling rates, at much greater accuracy than could be achieved in the furnace. Four different temperatures and four holding times were investigated to select the optimum QHT conditions. Based on microstructure and hardness analysis an optimum QHT was selected. Bulk as-welded material was then heat treated under these conditions and mechanically tested using hardness, tensile and Charpy impact. These data were then used to determine to what extent the QHT conditions selected succeeded in eliminating the negative effects on properties resulting from the welding process.

4.2 Comparison between SA508 Gr.3 and SA508 Gr.4N

4.2.1 Microstructures for SA508 Gr.3 and SA508 Gr.4N

To understand the differences between SA508 Grade 3 and SA508 Grade 4N in both microstructure and hardness, samples were supplied by Sheffield Forgemasters, both from unknown production runs. The microstructure of alloys using optical microscopy is shown in Figure 4.1.

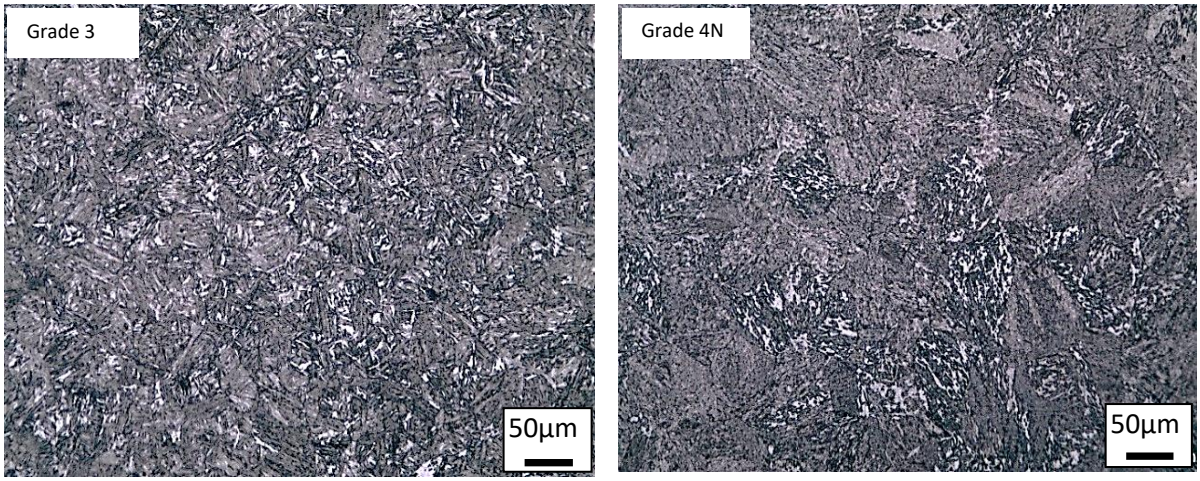

Figure 4.1: The microstructure of SA508 Gr.3 and Gr.4N

Both alloys show similar types of microstructure, i.e., mostly lath-like Bainitic packets with some evidence of pro-eutectiod ferrite (white). Interestingly, the prior austenite grain size and the Bainite packet size is significantly smaller for the as-supplied SA508 Gr.3. Lath width is also much easier to resolve in the SA508 Gr.4N, suggesting the SA508 Gr.3 also has a smaller lath width.

The presence of the ferrite is somewhat of a surprise for the SA508 Gr.4N, given that the CCT diagram presented in Chapter 2 would suggest that the cooling rate to obtain ferrite would have to be very slow, much slower than for SA508 Gr.3.

4.2.2 Hardness for SA508 Gr.3 and SA508 Gr.4N

Figure 4.2 shows the comparison between the Vickers hardness of both as-received alloys. SA508 Grade 4N had a hardness of 280 and SA508 Gr.3 had a hardness of 223. This again is a surprise given that the SA508 Gr.3 had a much finer bainite packet size and lath width, which would be expected to increase hardness, and not a significantly different volume fraction of ferrite. This would suggest that the increased levels of Ni and Cr in the SA508 Grade 4N is having a significant effect on hardness. This is most likely from increased solid solution hardening from both the Ni and Cr and possibly from increased volume fraction of chromium carbides.

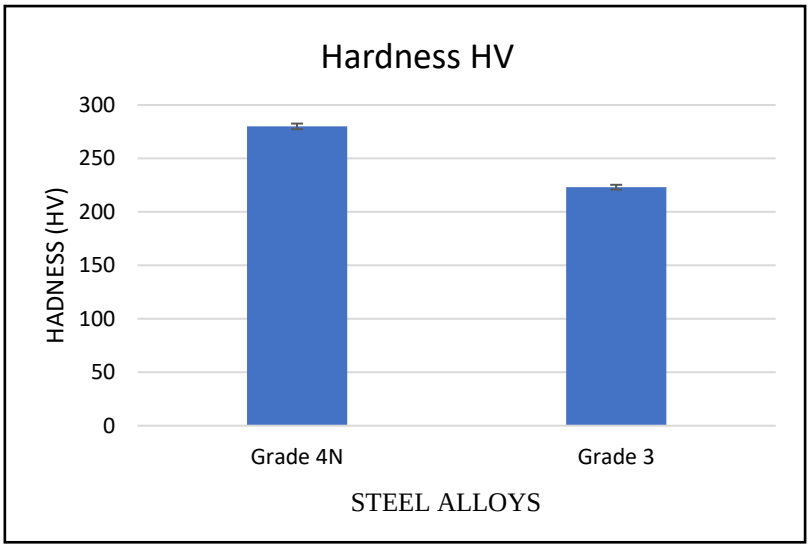

Figure 4.2: The average hardness values of SA508 Gr.3 and Gr.4N.

4.3 RPEBW SA508 Grade 4N and subsequent heat treatments

4.3. X Reduced Pressure Electron Beam Welding

Welding was undertaken on as-quenched base material that had not received post quench heat treatment. Example good quality 160 and 200 mm weld test blocks are shown in Fig.4.3 & Fig.4.4, respectively. Figs 4.3 (a) and 4.4 (a) a show the beam entrance (weld cap) side of the welds, Figs 4.3 (b) and 4.4 (b) show through-sectional slices along the length of the welds, and Figs 4.3 (c) and 4.4 (c) are radiographic inspections images. Full penetration welds were achieved throughout the length of the test blocks. In both joints, there were some cavity defects at the start and end regions of the welded samples due to weld instability (end effects), which are typical for welds in block geometry. Within the bulk of the block sample, there were no weld defects for the 160mm thick sample and only two isolated cavity defects in the 200mm thick sample. It is envisaged that with further weld development the cavity defects could be eliminated, as has already been demonstrated for 100 mm thick low alloy steel in previous studies undertaken by TWI [148]. However, it is very encouraging that with minimal parameter optimisation the only significant defects were at the root of the weld, which will be machined off after quality heat treatment and before entry into service.

Figure 4.3: 160 mm weld test block. (a) view of beam entry side of weld, (b) cross-section of weld approximately mid-plane, and (c) radiographic inspection image of the weld. S and F are the start and finish of the weld, respectively.

Figure 4.4: 200 mm weld test block. (a) view of beam entry side of weld, (b) cross-section of weld approximately mid-plane, and (c) radiographic inspection image of the weld. S and F are the start and finish of the weld, respectively.

Figure 4.5 shows optical macrographs of both welds, sectioned at locations defined by lines identified in Figures 4.5a and 4.5b. As expected from the radiographic inspection both welds at these locations are defect free with no sign of porosity or cracking. The weld fusion zone is approximately 15mm thick throughout the weld, indicating uniform heat intensity throughout the weld, which is further confirmed by the consistent size of the HAZ of approximately 15-20 mm on both sides of the weld zone.

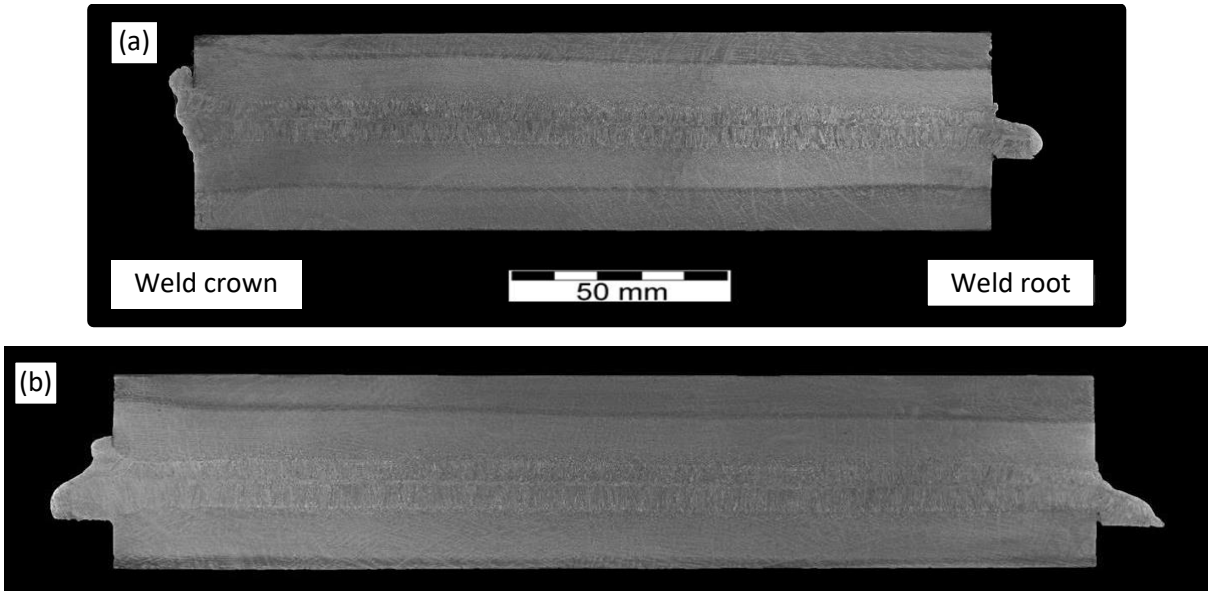

Figure 4.5: Macrographs of welds (a) 160 mm and (b) 200 mm in thickness

4.3.1 The microstructure of as a welded sample

Optical microscopy images of SA508 Grade 4N in the as-welded condition are shown in Figure 4.6. The base material, Figure 4.6(a), has a structure similar to that observed in Figure 4.1, i.e., Bainite with some evidence of ferrite. The Heat Affected Zone (HAZ), Figure 4.6(b), has Bainite with no evidence of ferrite, indicating that the cooling rate was faster than that produced the base material. The HAZ prior austenite grain size, the Bainite packet size, and Bainite lath width are all smaller than the base material, indicating that the maximum temperature reached and/or time at temperature in the austenite field was reduced compared to base material in addition to having a faster cooling rate. The fusion zone, Figure 4.6(c), consists of large columnar structure in which a clear dendritic structure is observed. It appears that the dendrites have a skeletal structure [149]. This suggests the initial dendrites formed in delta ferrite, the interdendritic regions were then carbon and alloying element rich, meaning that these regions were beyond the peritectic reaction and transformed directly from liquid to austenite. The delta ferrite then transformed to austenite with a much different chemistry than the interdendritic regions, leading to two distinct alpha-ferrite (white)/Bainite (dark) chemistries on cooling to room temperature.

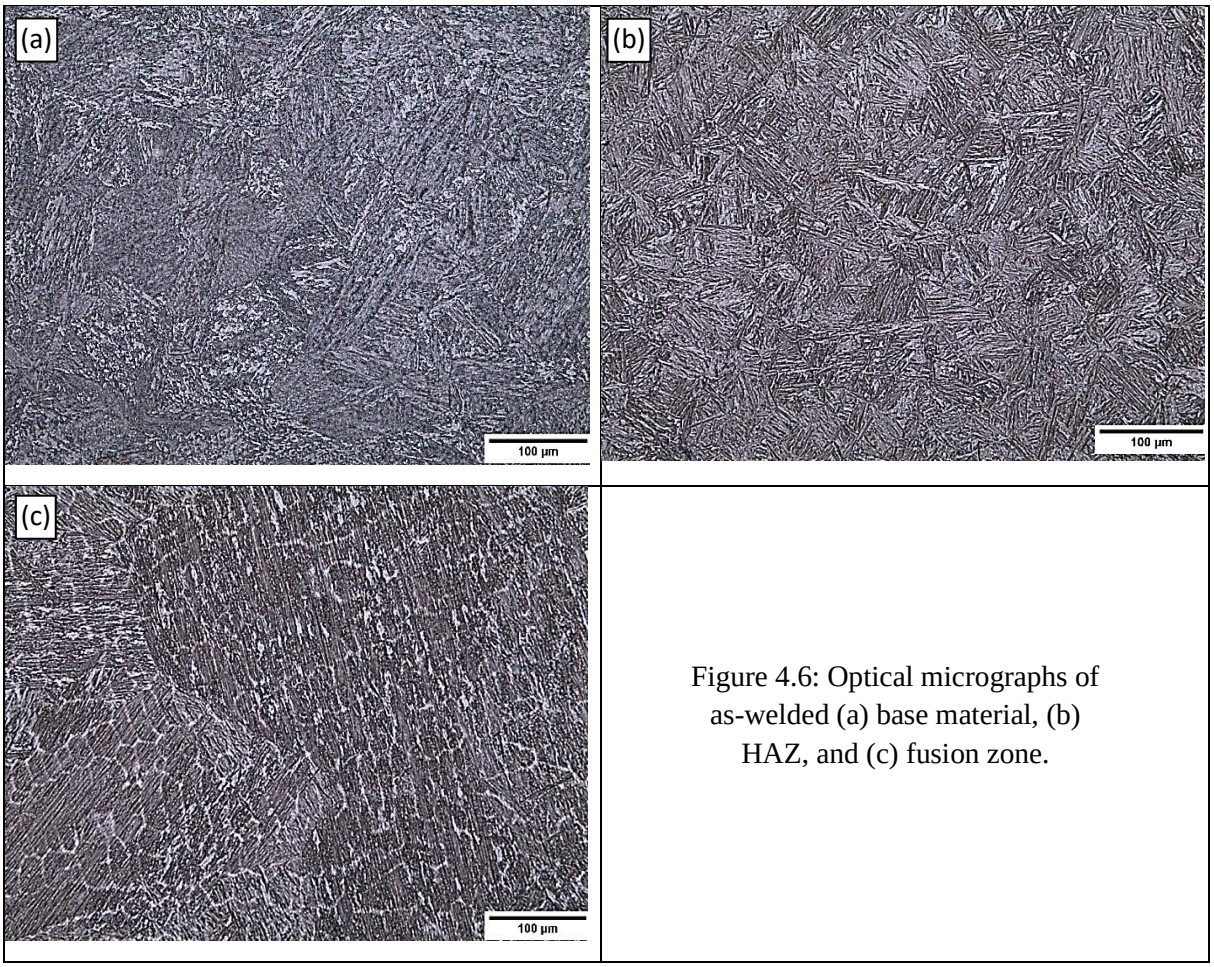

Figure 4.6: Optical micrographs of as-welded (a) base material, (b) HAZ, and (c) fusion zone.

4.3.2 The microstructure of PWHT undertaken in a furnace

Figure 4.7. Illustrates the microstructure of the base metal, Figure 4.7 (a), HAZ, Figure 4.7 (b), and fusion zone, Figure 4.7 (c), following a standard post-weld heat treatment (PWHT), i.e., heat treatment for residual stress relaxation. The BM and HAZ show similar microstructures to the as-weld material, with possibly some indication of microstructure coarsening in the HAZ. The skeletal dendrites in the fusion zone, however, appeared to have degenerated into another phase or morphology, suggesting the dendrites are high thermodynamically unstable [63].

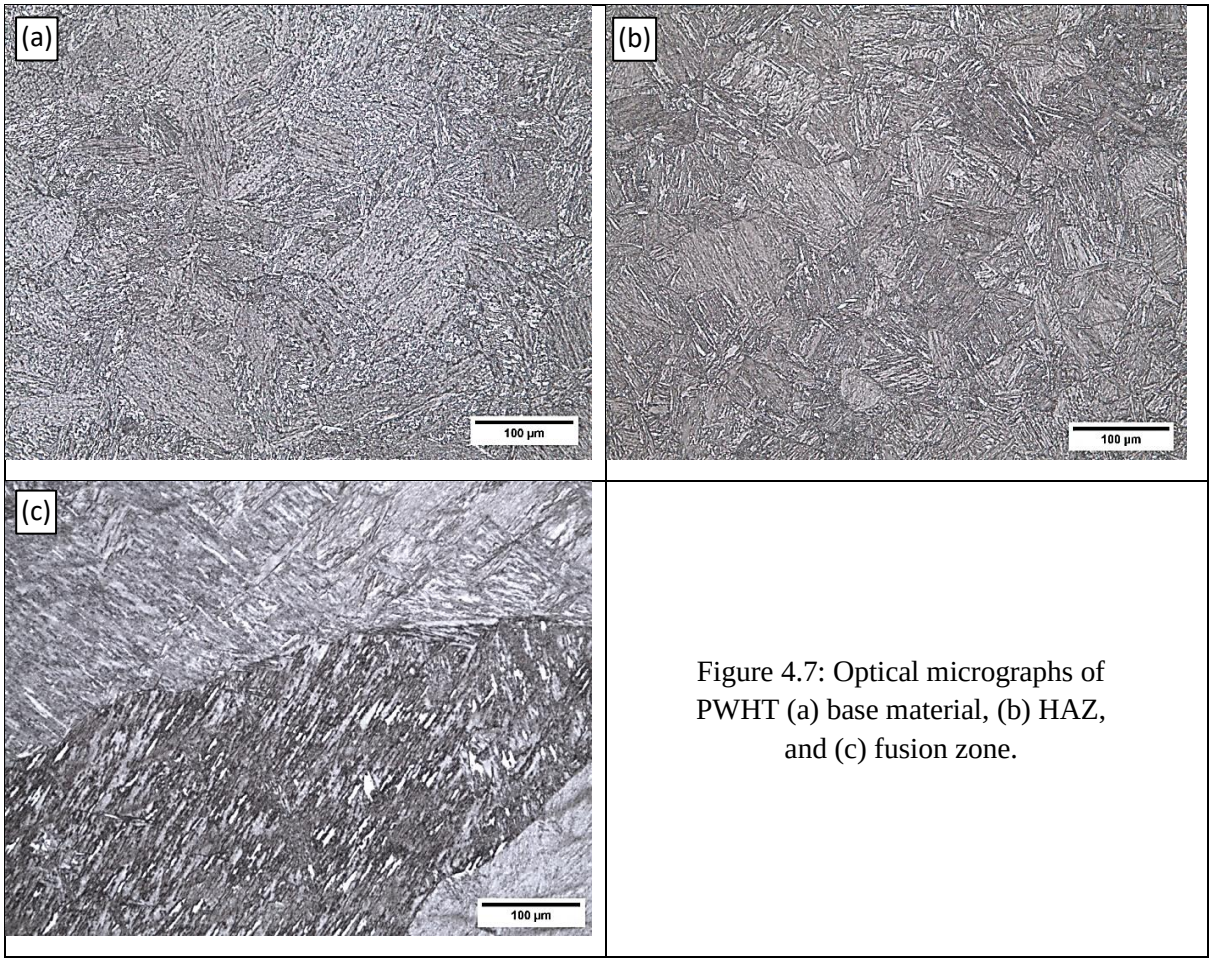

Figure 4.7: Optical micrographs of PWHT (a) base material, (b) HAZ, and (c) fusion zone.

4.3.3 The Microstructure of QHT undertaken in a furnace

Figure 4.8. Shows the microstructure of the base metal, Figure 4.8 (a), HAZ, Figure 4.8(b), and fusion zone, Figure 4.8(c) following a QHT at 860°C for 6 hours undertaken in a furnace. The three microstructures are similar in morphology, displaying a granular Bainitic microstructure. It appears, at least on the optical microscopy scale, that the QHT has wiped out the history of the Fusion Zone and HAZ and produced a microstructure close to the base metal after the standard manufacturing process. This is somewhat promising but further work is required to determine the reliability of these results, particularly looking for variation at other length scales that may influence performance in-service, such as microstructure variation at boundaries between weld zones [150].

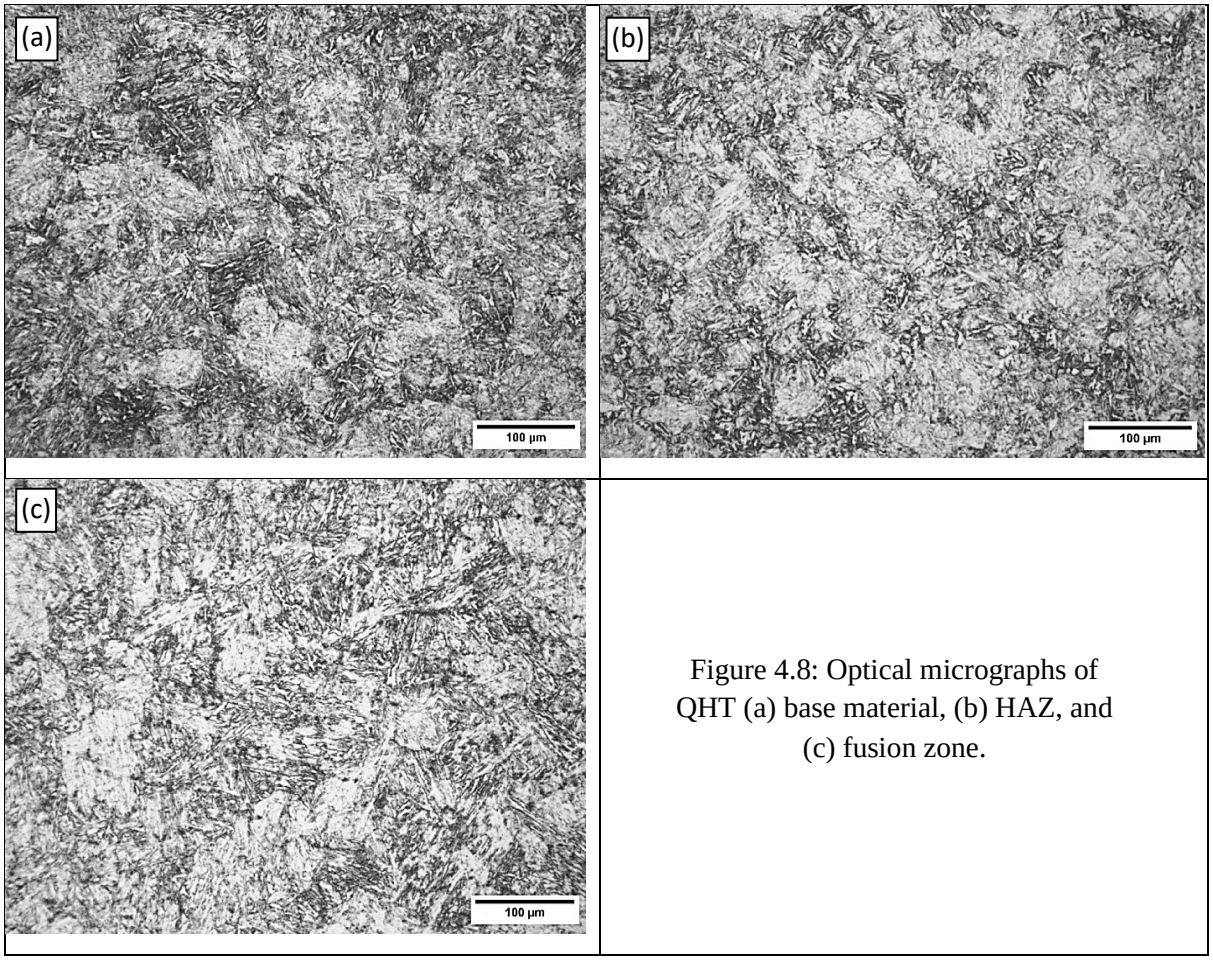

Figure 4.8: Optical micrographs of QHT (a) base material, (b) HAZ, and (c) fusion zone.

4.3.4 Hardness for the weld samples

To further investigate the impact of the different heat treatments, weld hardness testing was performed in all 3 zones of the weld for all weld types, Figure 4.9. The as-quenched base metal exhibits a hardness of 363 Hv, lower than the weld zones which have a hardness above 400 Hv, which correlates well with the finer microstructures observed in the weld zones. After PWHT the base metal hardness drops by 30 points. In contrast, the hardness of the two weld zones drops by over 100 points, again confirming the microstructure observations that the base metal was much more stable than the weld zones material, even under the relatively low temperature of the PWHT. After QHT all three hardness' were virtually the same at approximately 275 Hv, again suggesting that the QHT has performed its task of removing the effect of the welding operation [56].

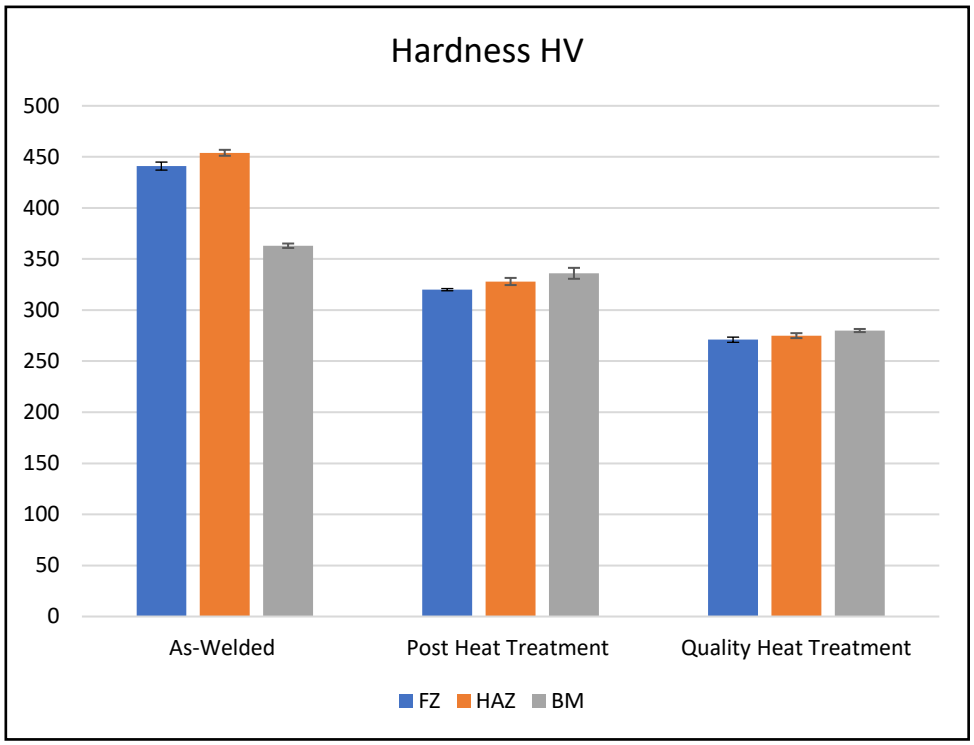

Figure 4.9: The microhardness for different types of heat treatment

4.3.5 Charpy Impact Test for 160mm weld

Charpy tests performed on the as welded and QHT samples in a regular furnace sample at -73 °C for all three layers in the weld with results are presented in Figure 4.10. As expected, the as-welded material has poor toughness, but the QHT has impact energies that are well within the known standards for this material. It is interesting to note that the highest impact energy is at the fusion zone, suggesting that the high quench rates experienced in this zone are more beneficial than the slower rates in the HAZ. Regardless, however, the results must be considered successful in removing the historical effect of the welding process [54].

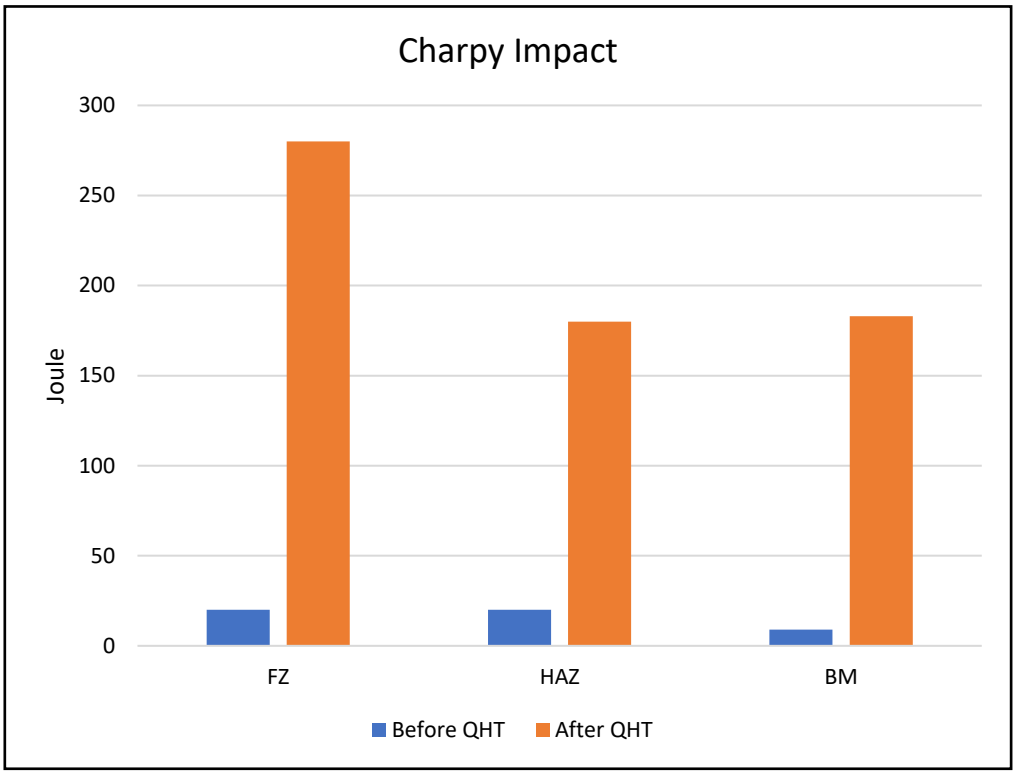

Figure 4.10: The Charpy test before and after First QHT

Figure 4.11 and Figure 4.12 shows the images of Charpy samples test before and after the QHT. Before the QHT the samples appear to be completely brittle, with a relatively flat feature free fracture surface. While the specimen after the QHT has a rough surface, which is dull and fibrous, which is associated with ductile fracture and significant energy absorption.

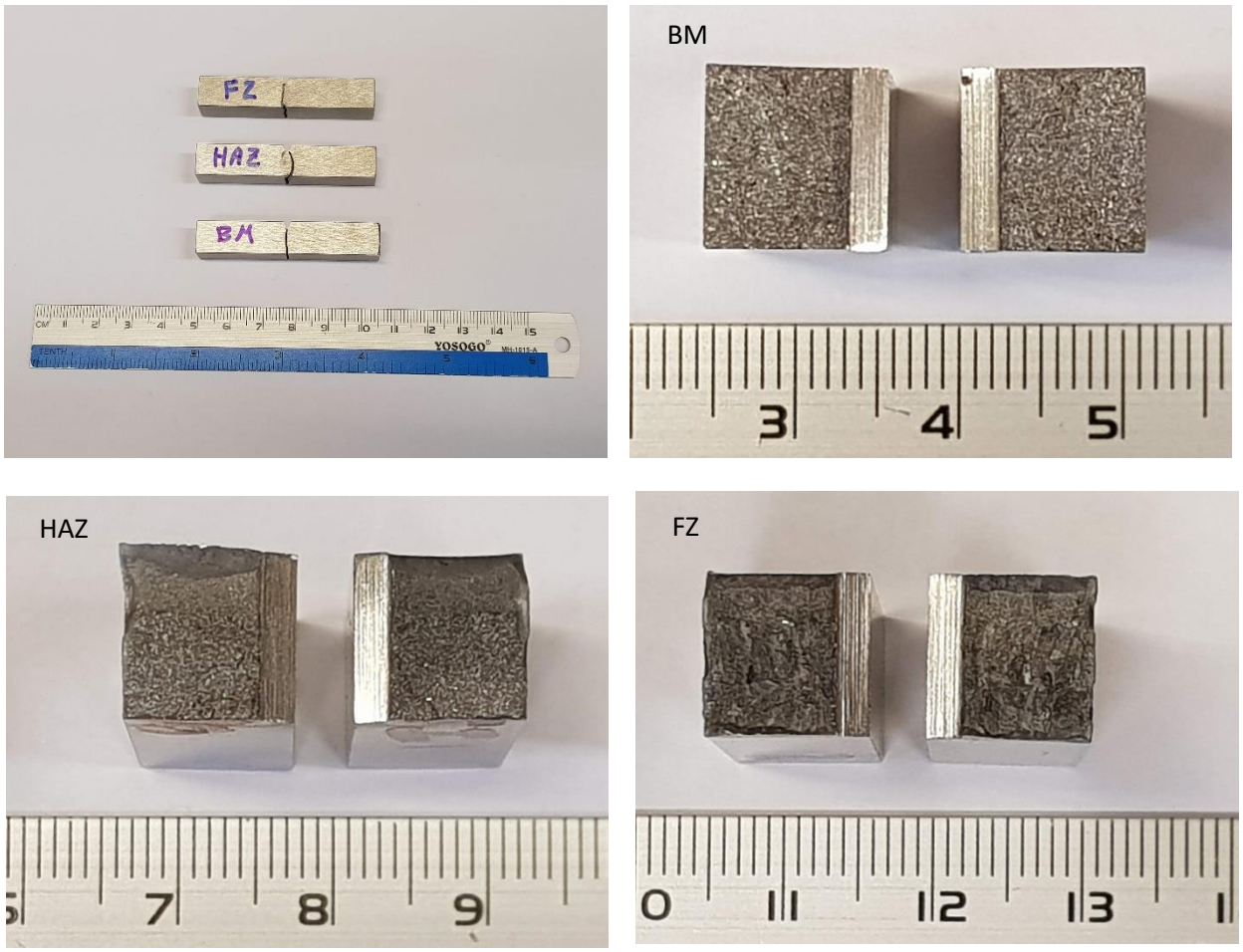

Figure 4.11: shows several images of Charpy samples test before the QHT

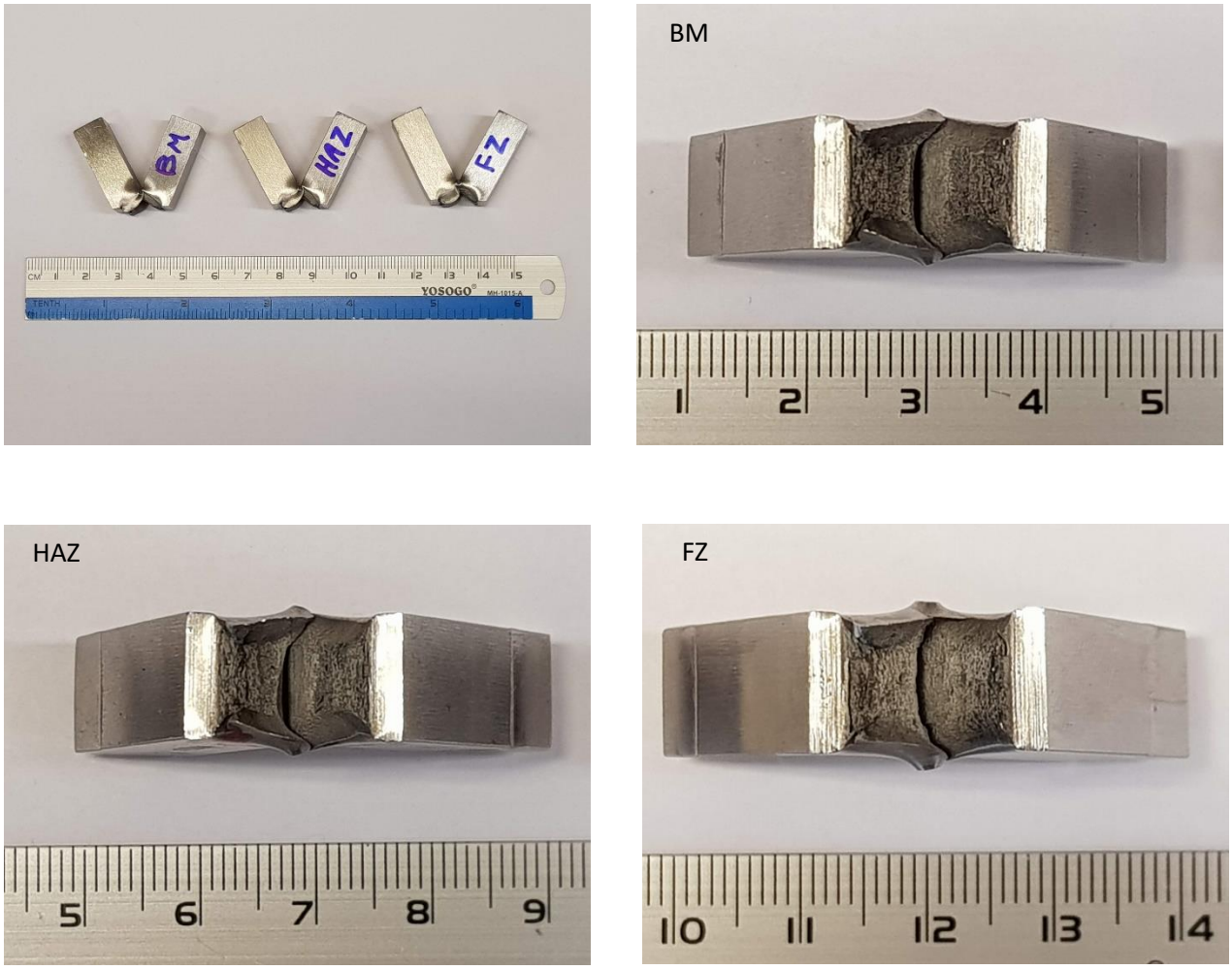

Figure 4.12: shows several images of Charpy samples test after the QHT

For further verification, the fracture in the weld samples was examined using SEM. In Figure 4.13, the three layers of the as-welded samples cleavage facets are evident throughout the fracture as well as tear ridges, all suggesting the fracture was brittle. While the fracture surfaces in Figure 4.14 shows that all layers in the welding samples appear to have the presence of dimples, suggesting the fracture is ductile.

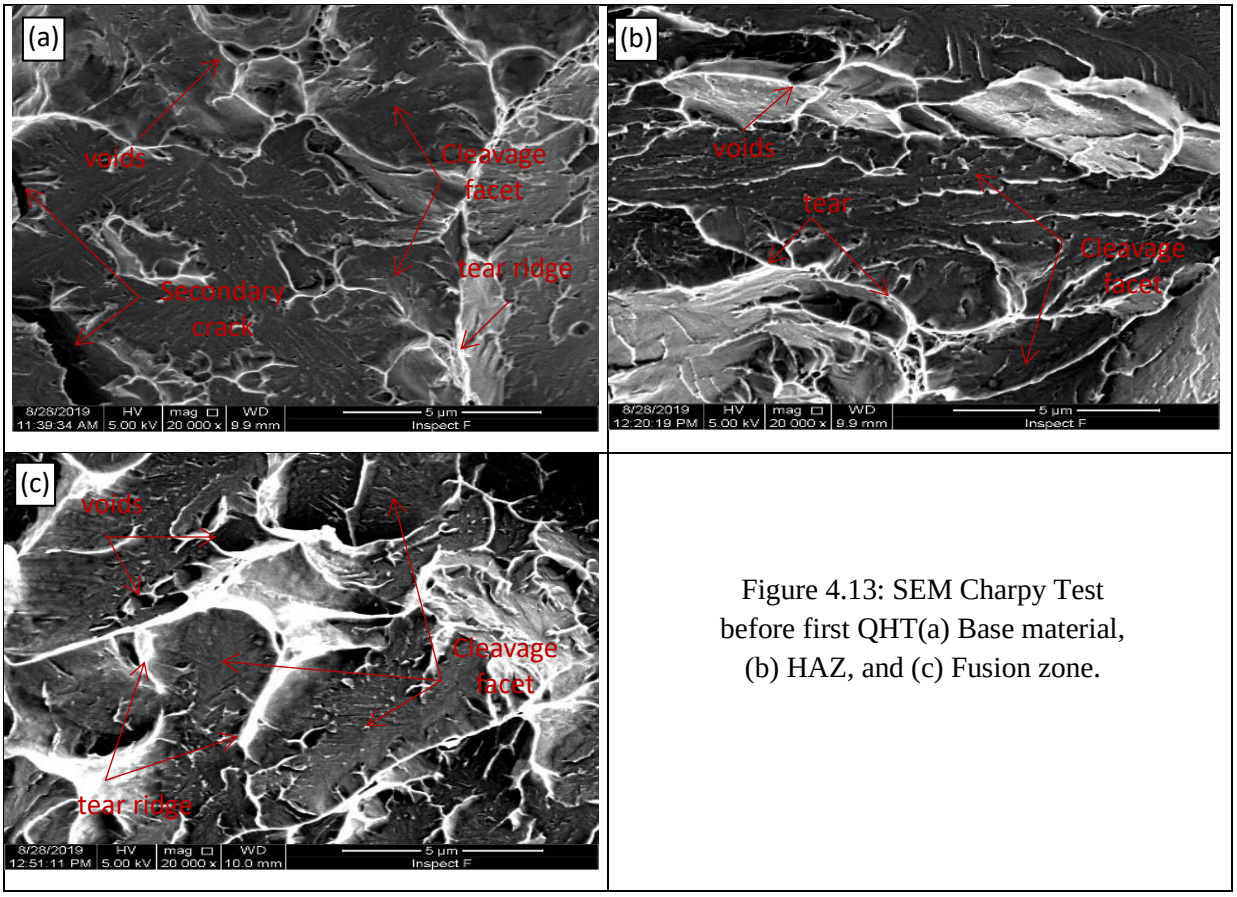

Figure 4.13: SEM Charpy Test before first QHT(a) Base material, (b) HAZ, and (c) Fusion zone.

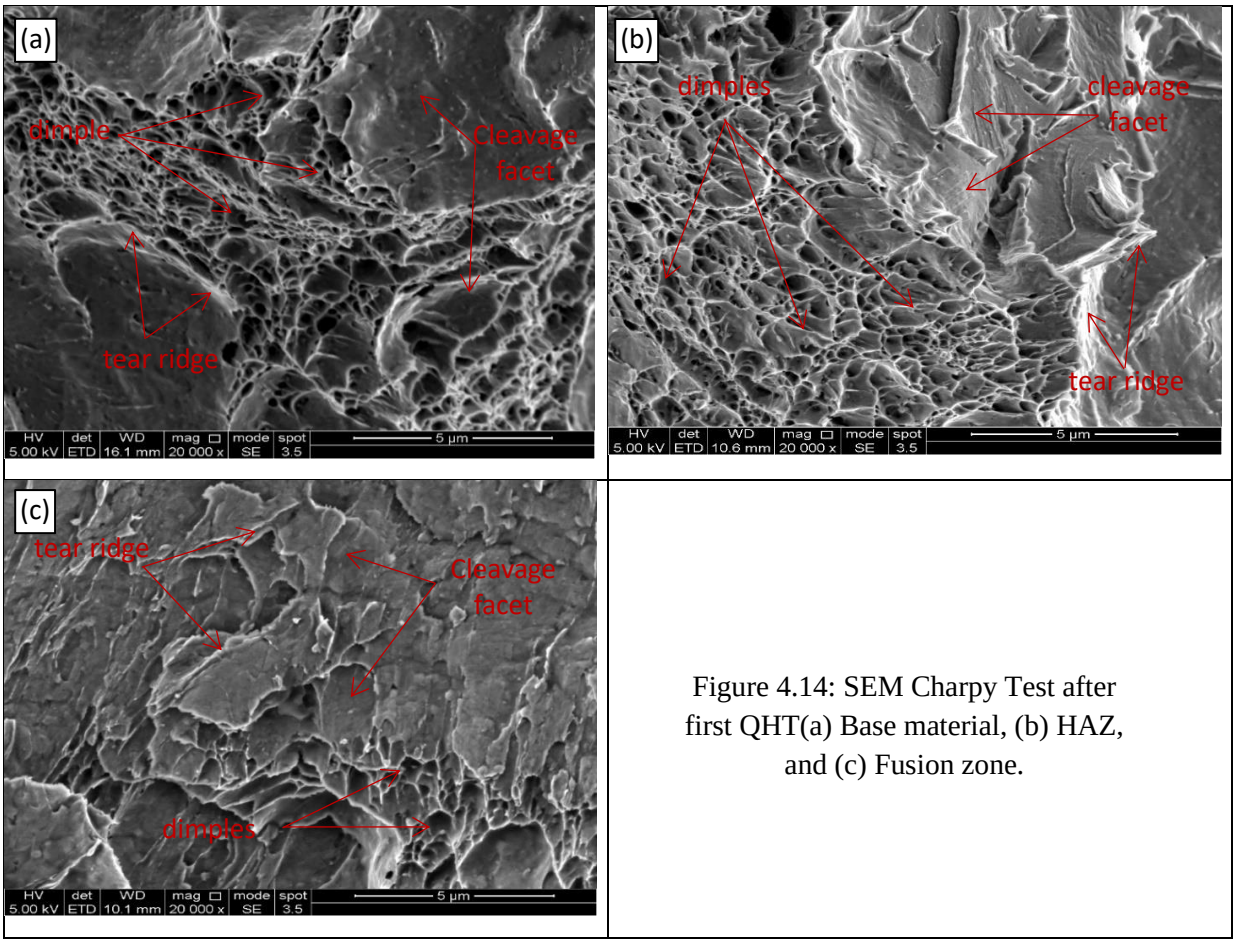

Figure 4.14: SEM Charpy Test after first QHT(a) Base material, (b) HAZ, and (c) Fusion zone.

4.4 Different temperatures of QHT for the weld samples

4.4.1 The microstructure of different temperatures of QHT for 15 minutes austenisation and cooling rate of 25 °C/min

Figure 4.15 through 4.19 illustrates the microstructure of the samples following welding and different QHT temperatures for 15 minutes. The as-welded microstructures of these materials also showed the microstructures presented in Figure 4.15, i.e. Bainite in the BM and HAZ and a skeletal cast like structure in the fusion zone. At a QHT temperature of 860℃ (Figure 4.16), the microstructure of the BM layer microstructure remained relatively stable in prior austenite grain size, Bainite packet and lath size, and the HAZ has transformed to a fully Bainitic microstructure of comparable dimensions to the BM. In the fusion zone there is also mostly Bainite with a similar microstructure size to the other regions. There is, however, some evidence of slighter coarser areas than that observed in the other regions. This would suggest that the 15 minutes hold time was not sufficient for completes carbon diffusion into these zones, suggesting on cooling they transformed to a slightly different morphology of Bainite. The 860℃ QHT, however, looks promising as there is not any evidence of significant microstructure coarsening but clearly the hold times must be much greater than 900 seconds. At 920℃ (Figure 4.17), all three weld regions are now completely Bainite but there is clearly a greater level of microstructure coarsening, slightly in austenite grain size and more significantly in Bainite lath width. In the fusion zone there is no indication of any history effect from the as-cast skeletal like microstructure. A similar pattern is also observed at a temperature of 1020℃ (Figure 4.18). At a temperature of 1120℃ (Figure 4.19) there is significant austenite grain growth.

Comparing the microstructures of the samples at different QHT temperatures and comparing them with the sample before heat treatment, it can be seen that 1120℃ needs to be rejected, as the significant austenite grain growth will have a very negative impact in impact toughness. The microstructures produced at 920℃ and 1020℃, both show significant promise as they have produced the result that is being looked for, i.e., a relatively small prior austenite grain size with a uniform Bainite microstructure and no evidence of the fusion zone microstructure. The microstructure at 860℃ also looks promising but there may be some evidence that there is not complete chemical homogeneity, which is most likely due to insufficient time at temperature. The fact that at both 920℃ and 1020℃ there was sufficient time for complete dissolution at 15 minutes suggests that diffusion rates are high, and any further time could lead

to significant grain growth. This is a problem for large components like RPVs, where the standard industry practice for heat treatment is the empirical rule of thumb of adding an hour of heat treatment time for every 25mm of section thickness. Thus, for a 200mm thick section, a heat treatment time of 8 hours would be the minimum time at temperature that would be expected. At this time, it would be expected that there would have been significant austenite grain growth at both 920℃ and 1020℃, making them impractical from a toughness point of view. This leads to a QHT temperature of 860℃ being the most practical. The only concern would be chemical homogeneity within the fusion zone. However, the fact that at 15 minutes there was no evidence of ferrite just a slightly coarsened Bainite microstructure suggests that complete diffusion will be realistic at times much not longer than 15 minutes.

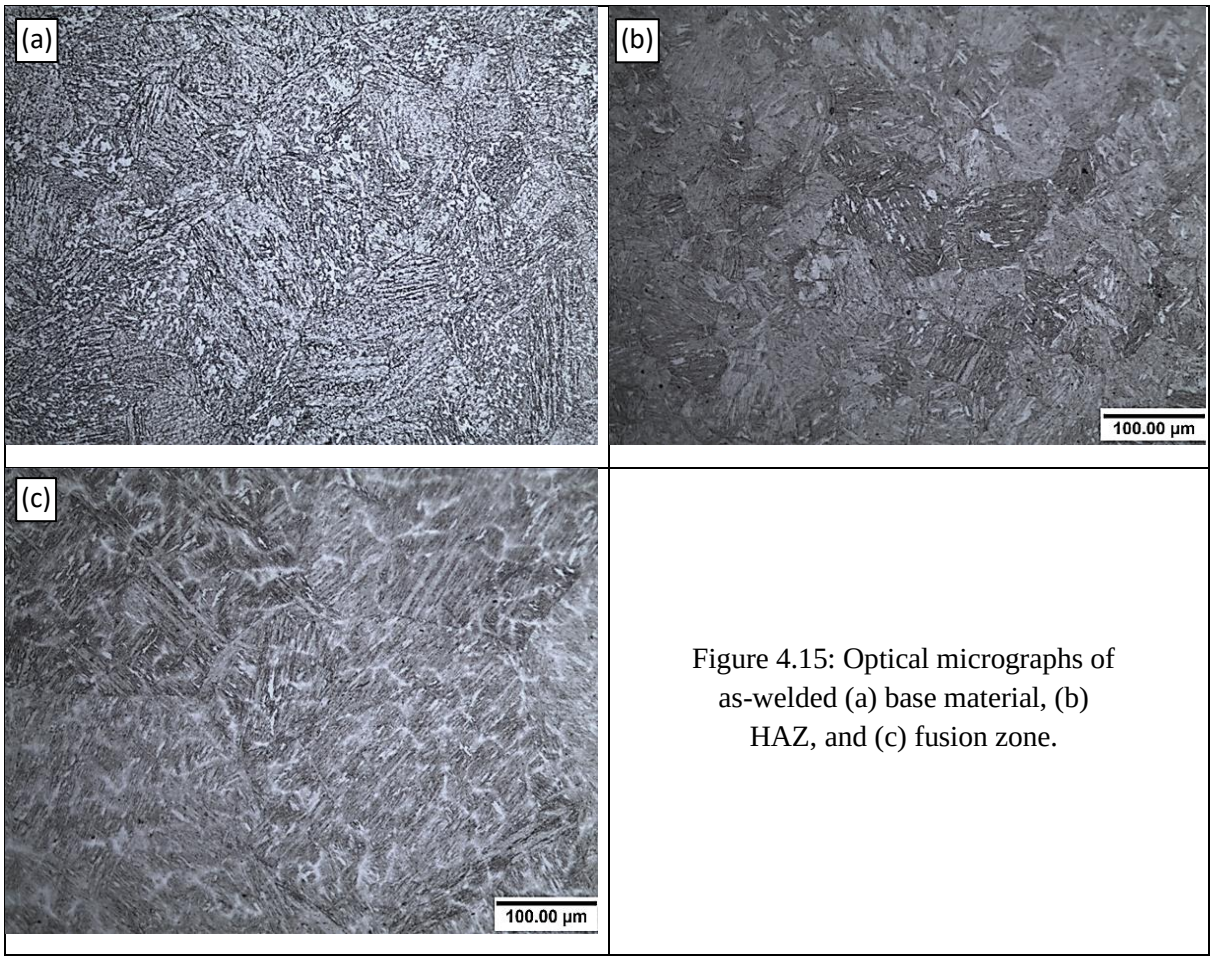

Figure 4.15: Optical micrographs of as-welded (a) base material, (b) HAZ, and (c) fusion zone.

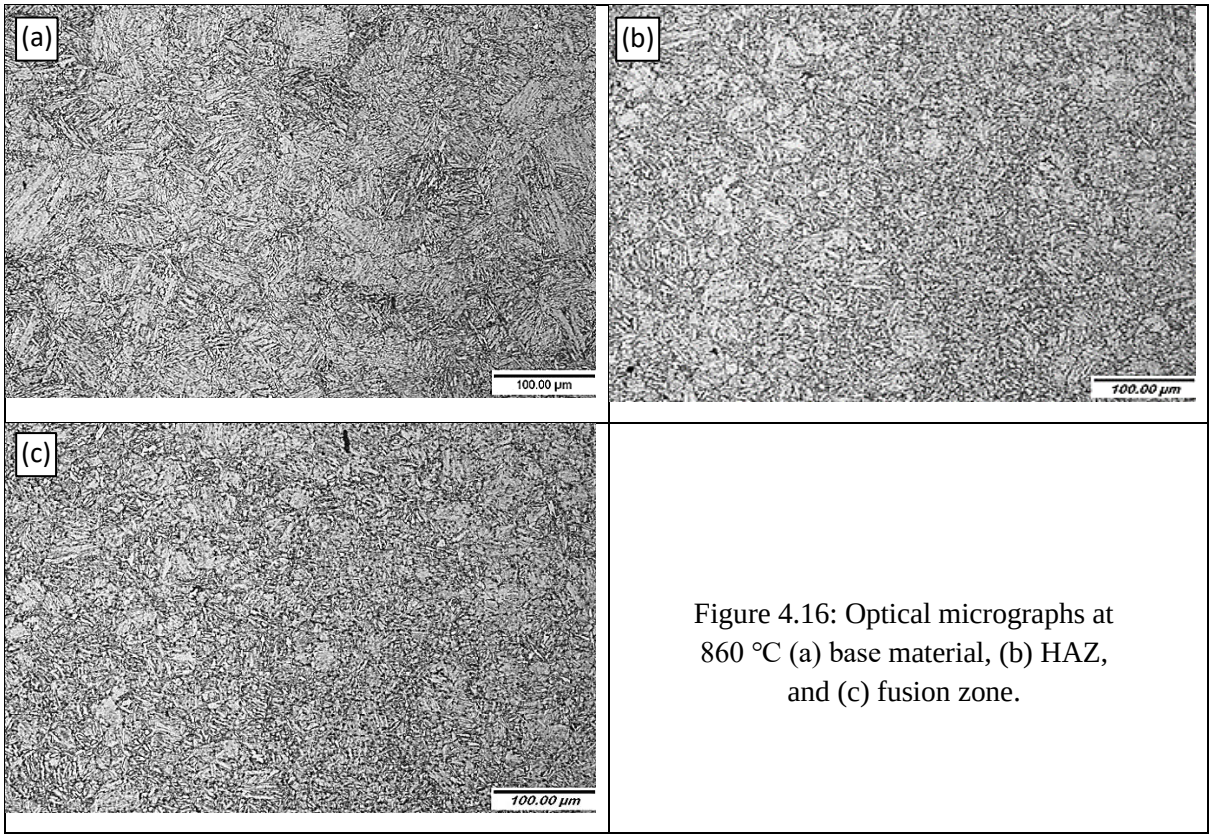

Figure 4.16: Optical micrographs at 860 ℃ (a) base material, (b) HAZ, and (c) fusion zone.

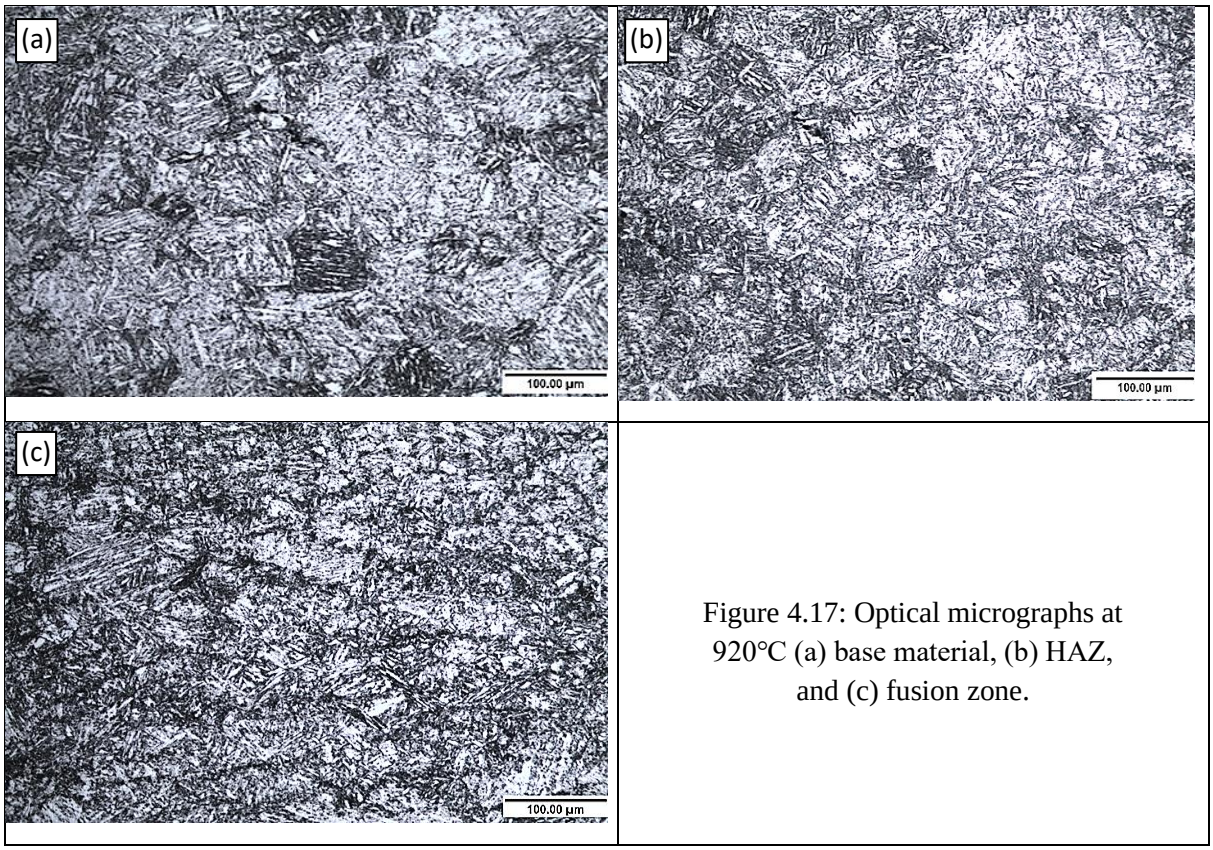

Figure 4.17: Optical micrographs at 920℃ (a) base material, (b) HAZ, and (c) fusion zone.

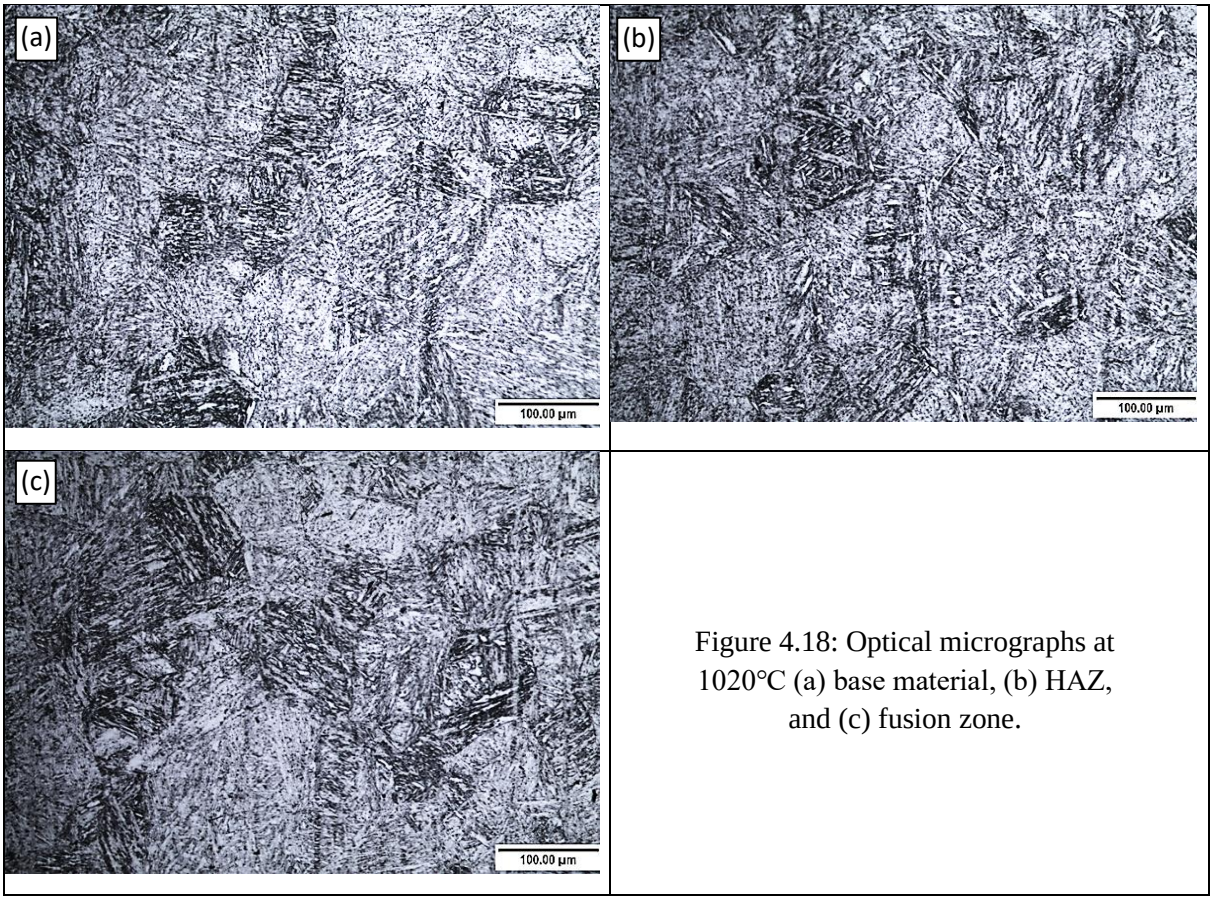

Figure 4.18: Optical micrographs at 1020℃ (a) base material, (b) HAZ, and (c) fusion zone.

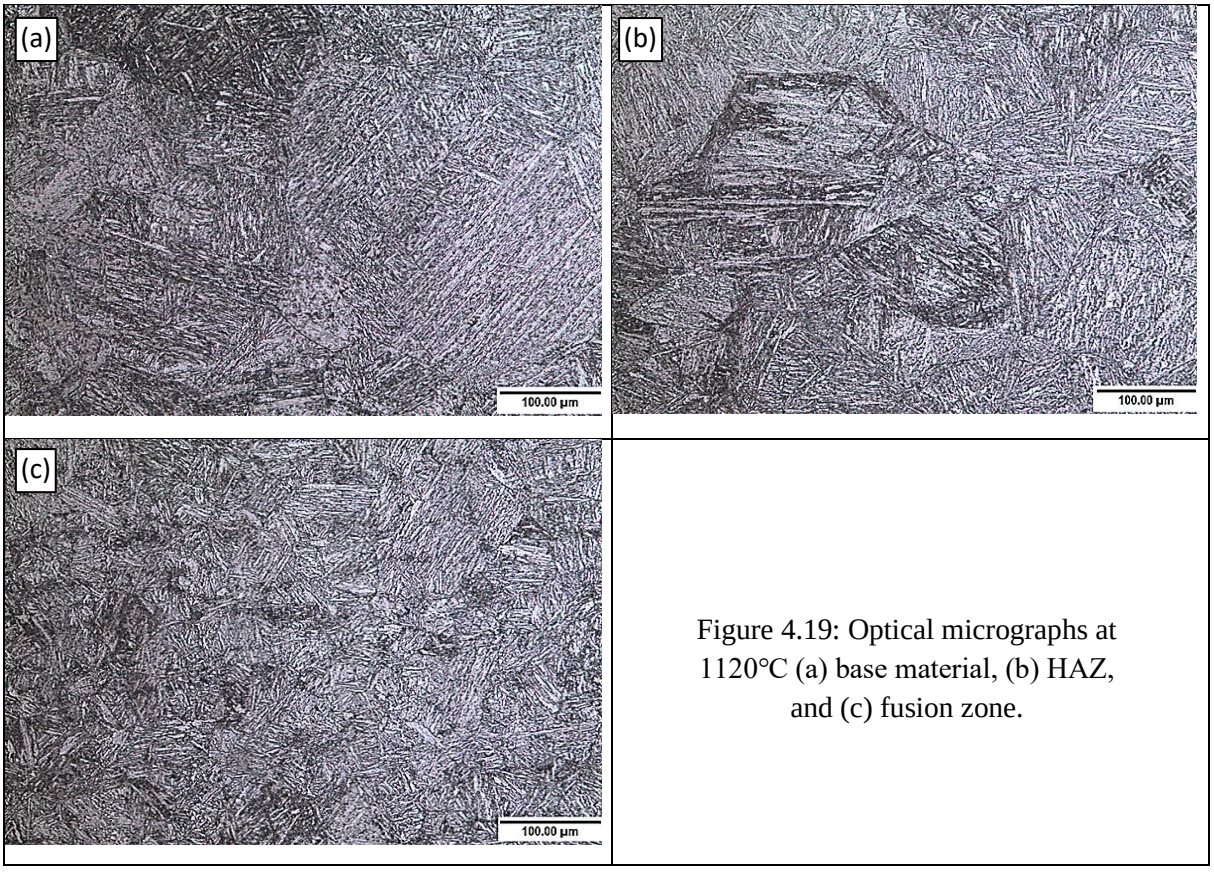

Figure 4.19: Optical micrographs at 1120℃ (a) base material, (b) HAZ, and (c) fusion zone.

4.4.2 Microhardness measurement for different temperatures

Figure 4.20 shows a comparison of the hardness between the QHT samples at different temperatures with the as-welded sample. In all QHT cases the hardness has been significantly reduced to be inside what would be expected for the specifications for this alloy. More importantly there is no significant difference in the hardness of the three different zones for any of the QHT conditions, suggesting that at least from a strength point of view the QHT at all temperatures has wiped out the effect of welding. Looking at the microstructures in Figures 4.15-19 this is not surprising, in all cases the Bainite packet size and lath width appear to be similar, which is often quoted as the key strength parameter in Bainite containing steels [67]. There is, however, a slight increase in hardness at 920°C, the origins of which are unclear. It is most likely down to an experimental anomaly, but a metallurgical origin cannot be discounted, and further work would need to be done to confirm. From the perspective of the project, if there was a metallurgical reason for the increase in hardness, this would have a negative impact on toughness, again confirming that 860°C is a better proposition for QHT.

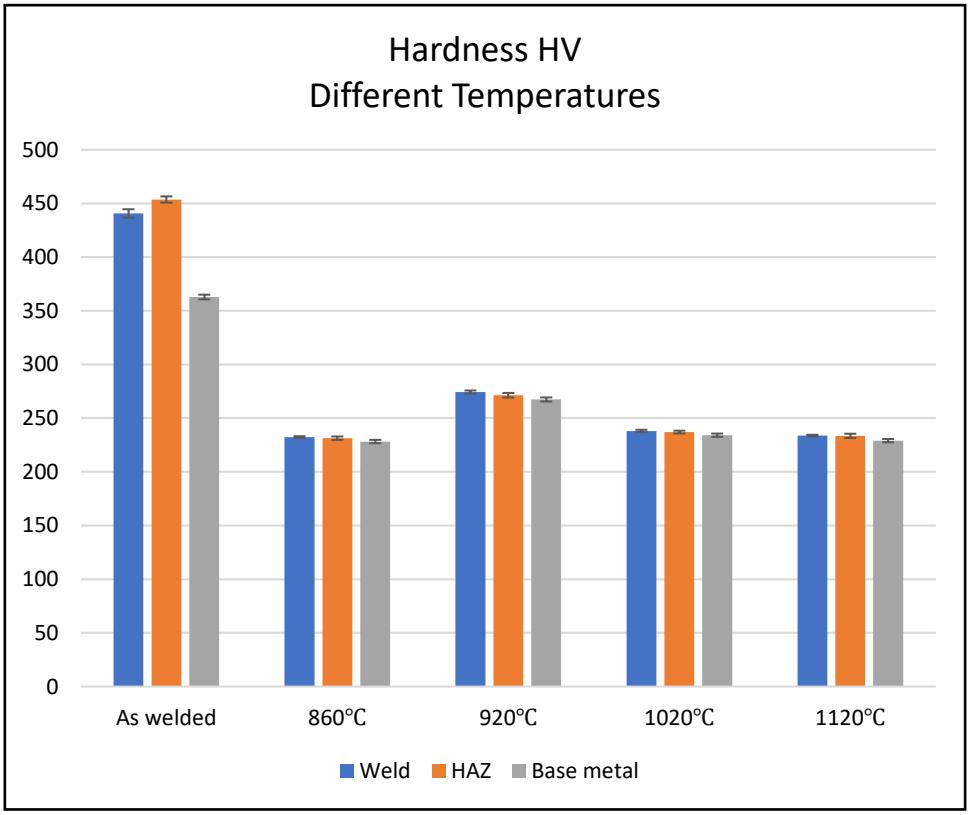

Figure 4.20: The microhardness of the different temperatures for weld Samples

4.5 Different holding time at 860°C of QHT for the weld samples

4.5.1 The microstructure of different holding time in QHT

To investigate the impact of holding time on microstructure and hardness evolution at 860°C four holding times, 8, 24, 48 and 96 hours, were investigated. Microstructures are shown from Figures 4.21 to 4.24.

Figure 4.21 shows the microstructure for all 3 weld zones for 8 hours holding time. All three layers show a similar microstructure, i.e. Bainite with a relatively fine prior austenite grain size. It is interesting to note that there is a slightly finer microstructure in the fusion zone, again suggesting the relatively nonchemical homogenous microstructure in microstructure evolution even though the phase field at 860°C should be completely austenite. The other microstructures also show a similar trend, with possibly some more evidence of coarsening in the fusion zone. Again, this points to 860°C being the ideal choice for QHT as by 8 hours the microstructure looks relatively uniform but any additional time at temperature does not lead to significant microstructure coarsening, indicating that there is a wide processing window at this temperature.

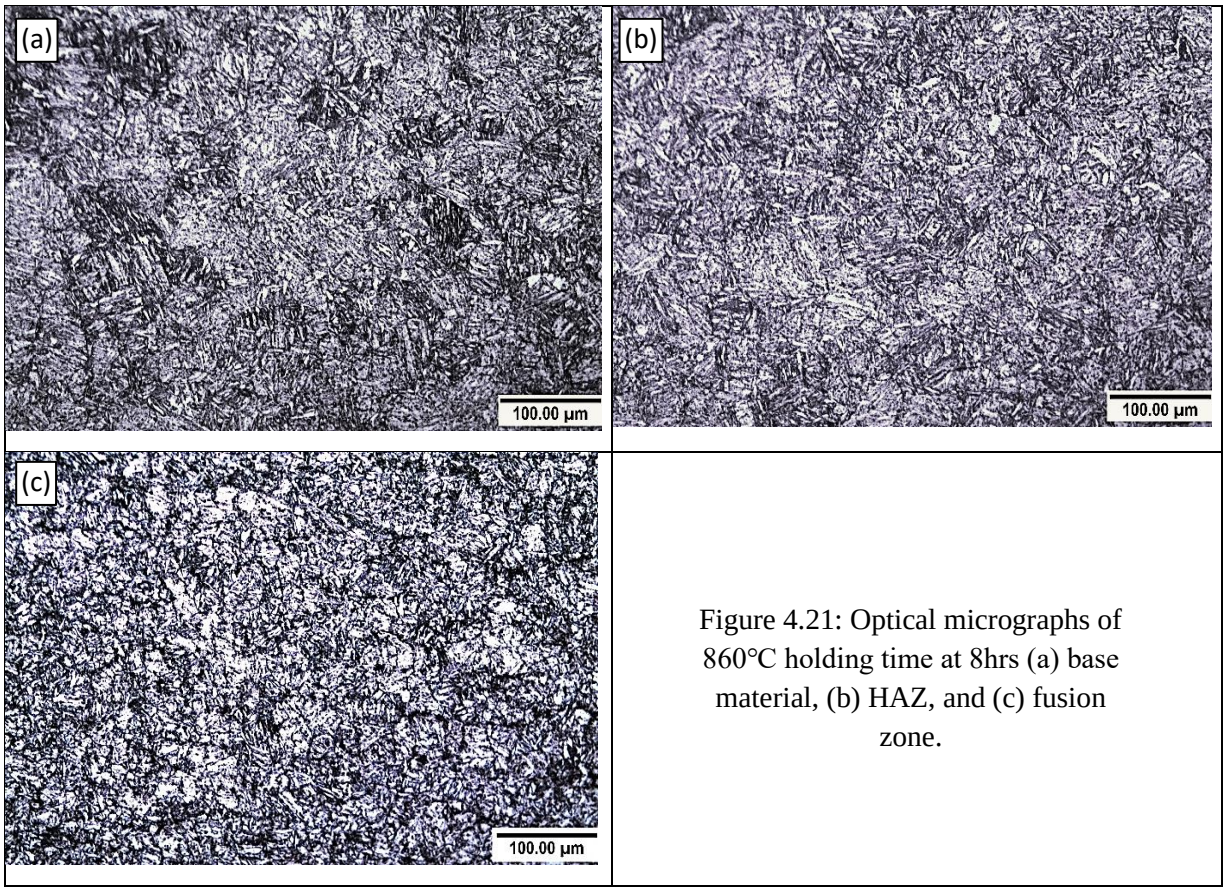

Figure 4.21: Optical micrographs of 860°C holding time at 8hrs (a) base material, (b) HAZ, and (c) fusion zone.

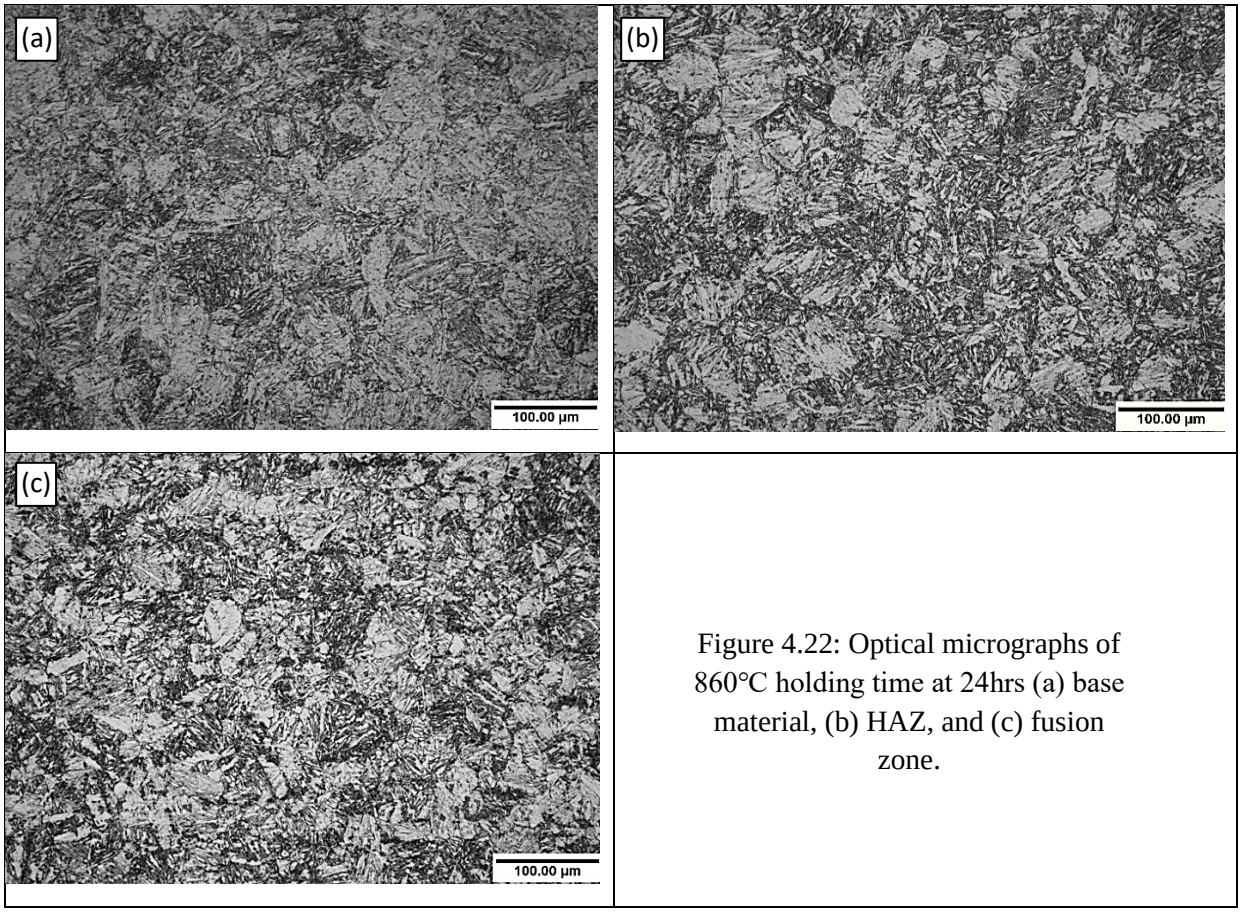

Figure 4.22: Optical micrographs of 860°C holding time at 24hrs (a) base material, (b) HAZ, and (c) fusion zone.

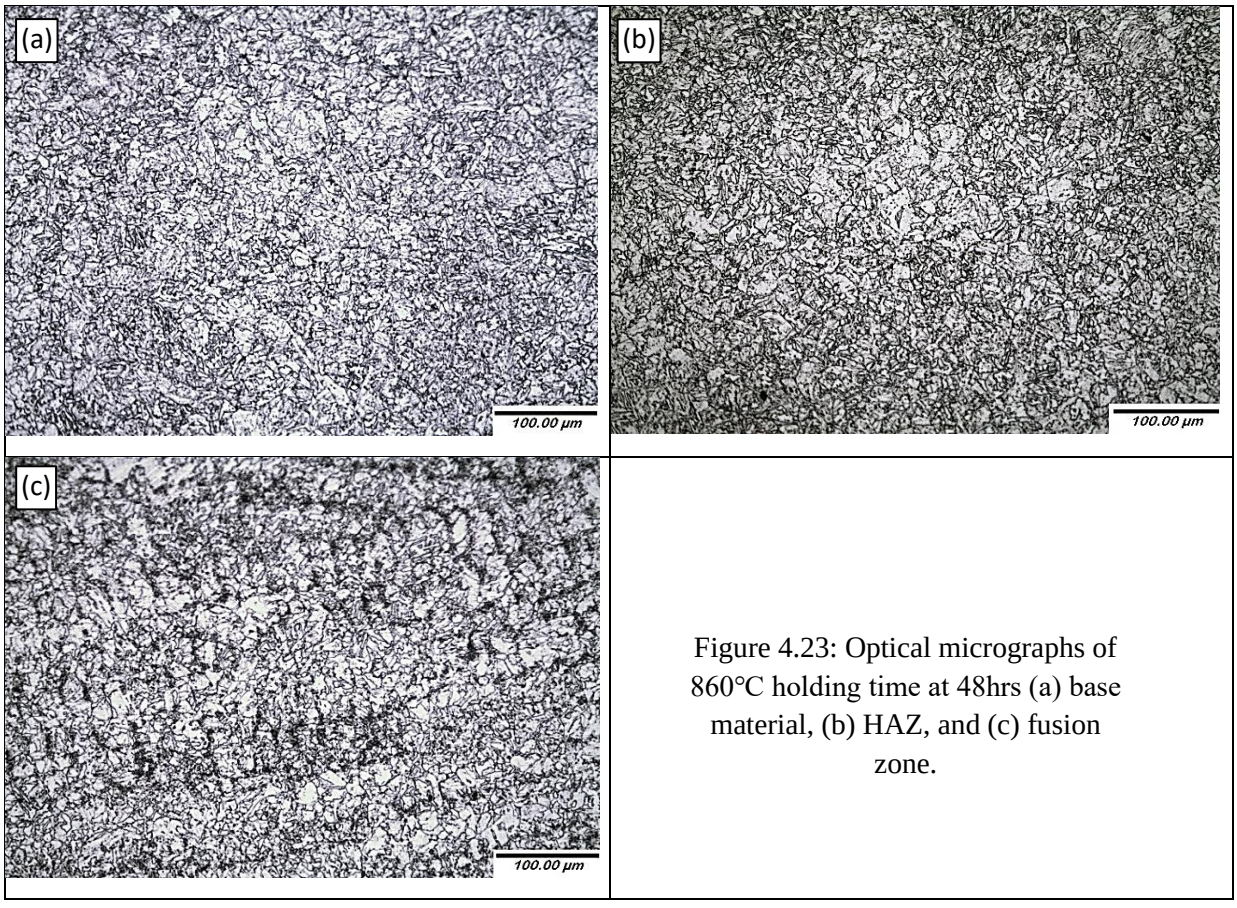

Figure 4.23: Optical micrographs of 860°C holding time at 48hrs (a) base material, (b) HAZ, and (c) fusion zone.

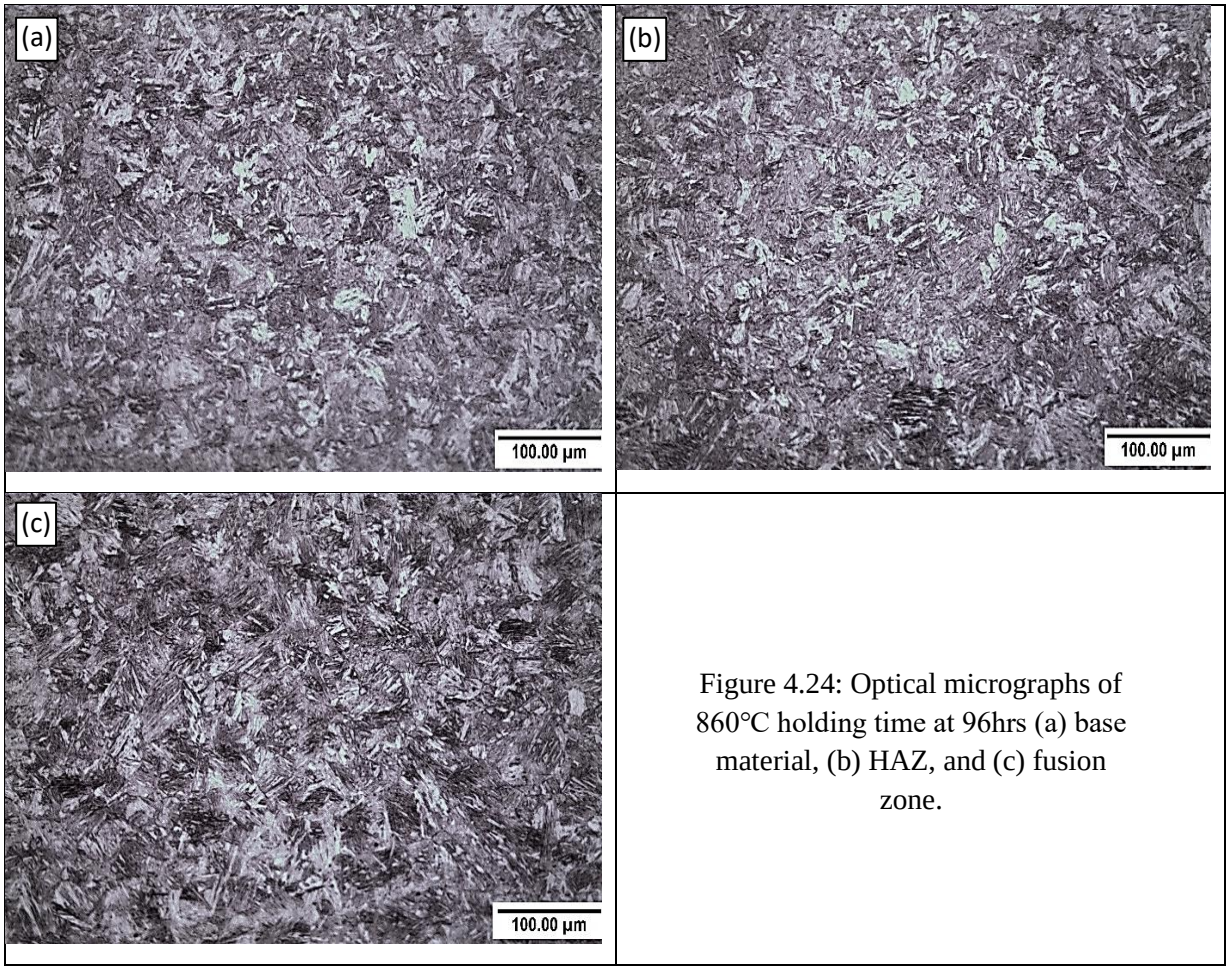

Figure 4.24: Optical micrographs of 860℃ holding time at 96hrs (a) base material, (b) HAZ, and (c) fusion zone.

Based on the CCT diagram of the SA508 Grade 4N alloy shown in Chapter 2. With a temperature of 860℃ and a cooling rate of 25 ℃/min ~ 0.42 ℃/sec, the microstructure will be Bainite with possibly some martensite, again confirming the validity of the results obtained so far.

4.5.2 Microhardness measurement for different holding times

Figure 4.25 gives the hardness values of the QHT samples at different holding times compared with the hardness value of the as-welded specimen. It can be clearly seen that the QHT has a big impact on hardness from the as-welded condition but the effect of time at temperature is negligible on the hardness, again confirming that 860℃ is an ideal choice for the QHT temperature.

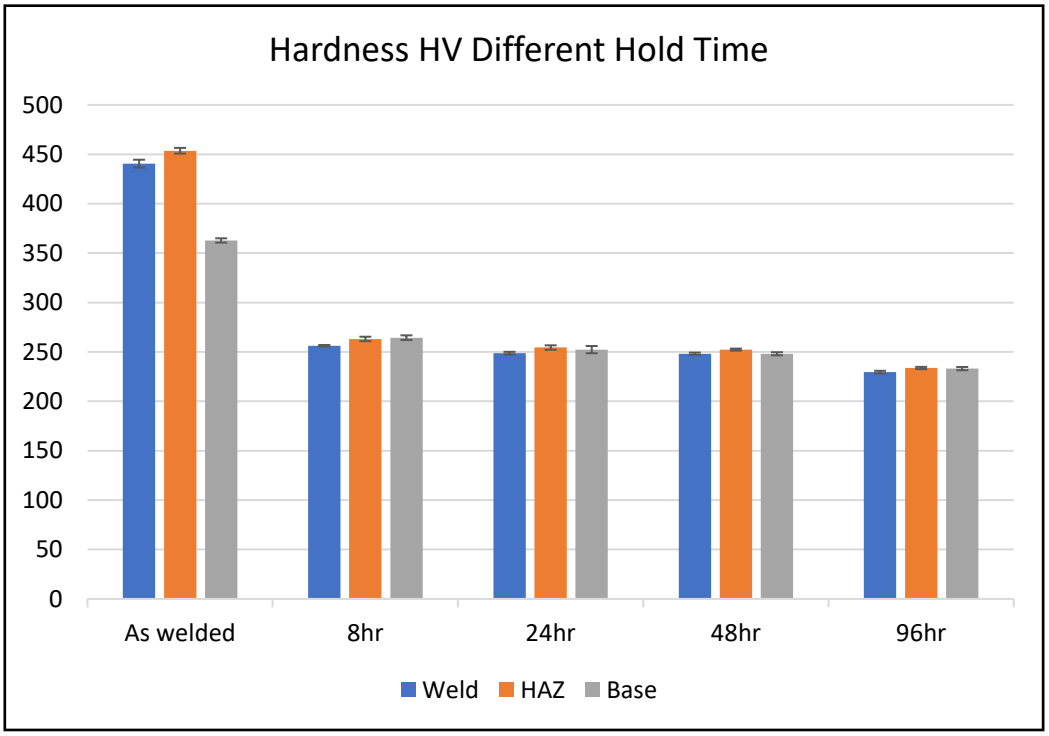

Figure 4.25: The results of the hardness test for the QHT weld samples of 860°C at different holding time.

4.6 Mechanical Properties

4.6.1 Final Microhardness

The results for Vickers microhardness results compared between as-welded specimens and the QHT weld samples at 860°C with 8hrs holding time is shown in Figure 4.26. The results revealed that the hardness value of the as-welded samples is significantly higher compared to the results of the samples after QHT. The highest hardness value in specimens before QHT was in the HAZ layer it reached 454, whereas in the layers FZ and BM it was approximately 441 and 363 respectively. The increase hardness value is the as-welded sample is due to the formation of Bainite and the residual stresses caused by the welding process. The hardness of the weld sample after QHT was decreased in all weld zones. The highest value in the BM layer, which is 264, with similar levels in the FZ and HAZ. There is a significant difference in the hardness value between the samples before and after the QHT. Its reaches 185 in the in FZ while in the HAZ and BM it was 191 and 99 respectively, suggesting that residual stress is playing a significant role. This residual stress effect is most likely high because of the thick

section nature of the weld leading to incredibly high levels of residual stress, much greater than in thin section welding. The relationship between the hardness and strength is direct, while it is reversed with the toughness. The hardness is significantly affected by heat treatment which changing the grain size, especially on the holding time and the cooling rate, that in turn effected on hardness.

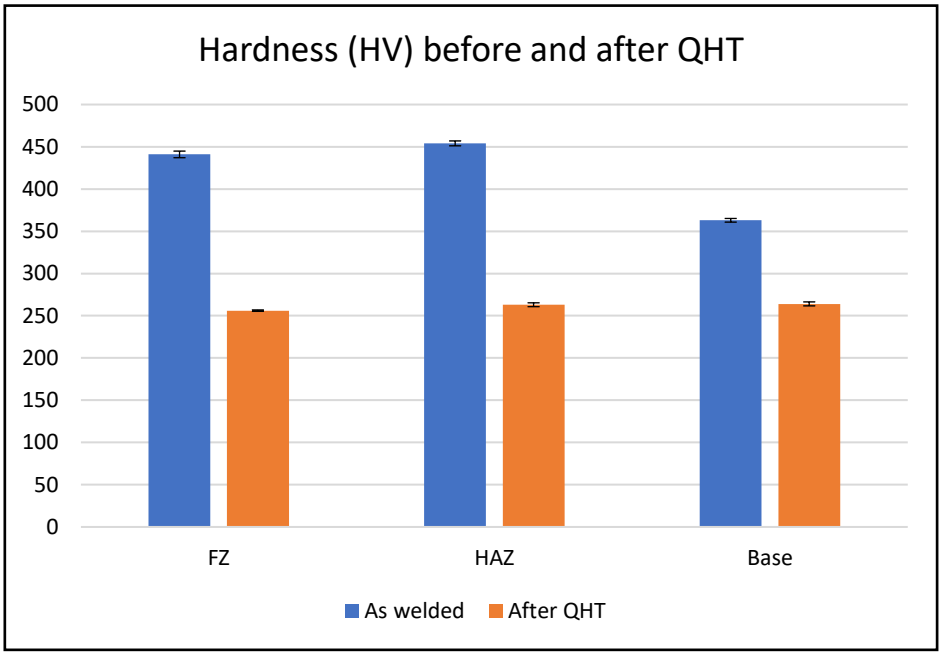

Figure 4.26: Hardness curves before and after QHT for three different weld layers

4.6.2 Tensile Test

4.6.2.1 Tensile before QHT

The tensile testing of as-welded samples was performed at room temperature, in the different sections, BM, HAZ and FZ. All specimens were loaded to failure.

In all cases, the fracture occurred in the within the gauge length, as shown in Figure 4.25. The value of ultimate tensile strength (UTS) was 865 MPa for BM, 1520 MPa for HAZ and 1280 MPa for FZ. While the yield strength (YS) was 690 MPa, 945 MPa and 860 MPa for BM, HAZ and FZ respectively. Figure 4.26 shows the stress-strain curves of the samples for each layer

of the weld, it indicates that the fracture was brittle, and the strength value is inconsistent between the three welding areas, with the HAZ having the strongest properties but the fusion zone having the lowest ductility.

(a) (b)

Figure 4.25: Tensile Samples before QHT for weld layers; a) before the test b) after the test

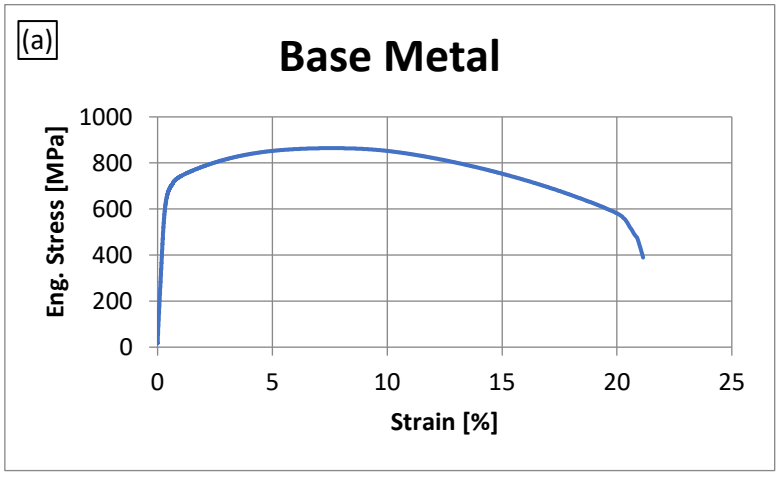

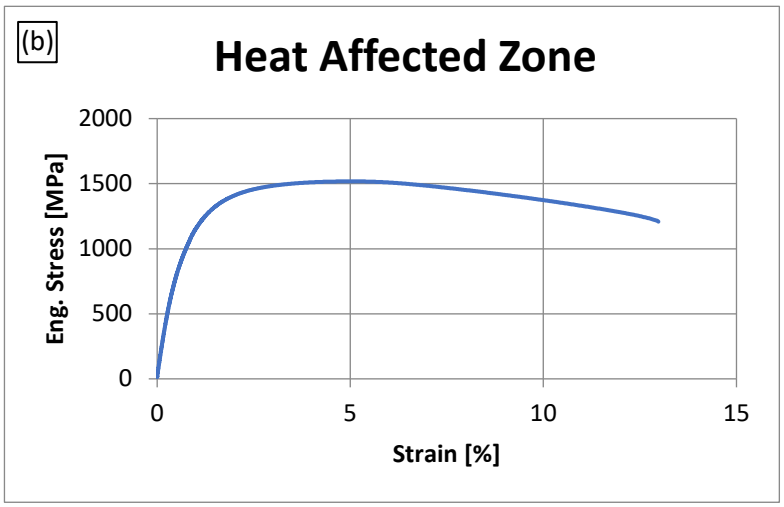

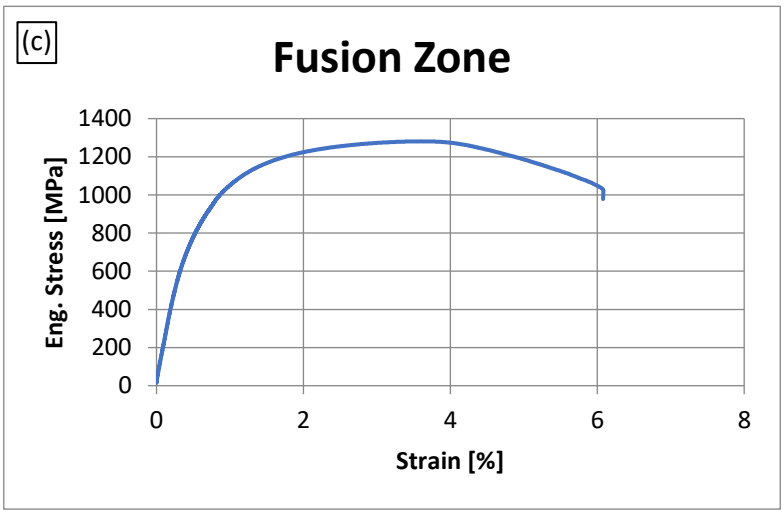

Figure 4.26: Tensile curves before QHT for three different weld layers (a) Base Metal, (b) Heat Affect Zone, (c) Fusion Zone.

4.6.2.2 Tensile after QHT

Figure 4.27 shows the fractured specimens of the QHT at 860°C for 8 hours, which has occurred within the gage length for all. The UTS value was 868 MPa for BM, 882 MPa for HAZ and 868 MPa for FZ. YS yields were 765 MPa, 772 MPa and 765 MPa for BM, HAZ and FZ respectively. All specimens show a ductility of 18% or more. Figure 4.28 illustrates the stress-strain curves of the samples for each welding zone, indicating that the fracture was ductile, and the strength value is homogeneous for all the three welding areas. The strain at failure varies quite a bit between the three curves, because it is from different regions exposed at different temperatures during the welding process, it has a slight difference in the grain size.

The rising of the percentage of molybdenum and nickel has a noticeable effect on increasing the strength of the SA 508 G4N. It supports the formation of fine carbides that has a significant impact on the microstructure and have a positive effect on the increase the strength of the alloy. Besides, the increase in chromium may not have a definite impact on the rising strength of the alloy. Because, the carbides formed by chromium do not have an orientation relationship with the matrix; also, it has a globular shape. They are distinctly different from the carbides created by the molybdenum and nickel that precipitate as a small needle-type on the grain boundary. In addition, it contributes to sub-grain refinement, which works to the solid solution strengthening, increasing the strength of the alloy [105].

Also, in the 508 G4N alloys, there is a proportion of lath martensite, which contributes to increasing the barriers to dislocation movement, in turn, gives higher strength, that enhances the mechanical properties of the alloy [151].

Figure 4.27: Tensile Samples after QHT three weld layers

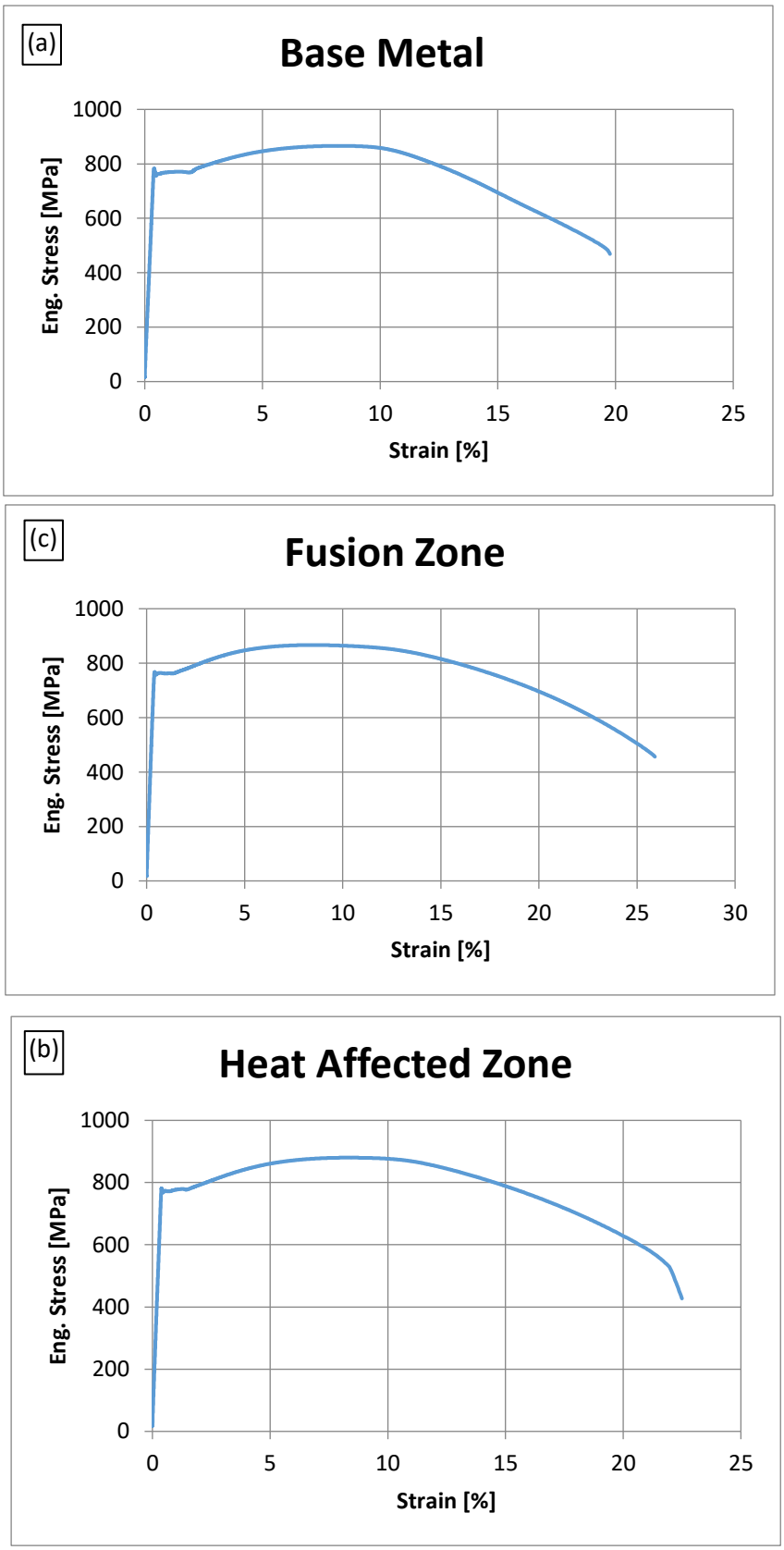

Figure 4.28: Tensile curves after QHT for three different weld layers (a) Base Metal, (B) Heat Affect Zone, (c) Fusion Zone.

4.6.2.3 Comparison of the Tensile Test on the alloys before and after Quality Heat Treatment

Figure 4.29 shows the comparison for the tensile results before and after the QHT procedure. It shows the difference in the value of the UTS and YS of the welding samples before the heat treatment has a considerable variation in the values between the three layers. As it appears that the HAZ has the highest value, almost double the value in the BM. That is due to the high-temperature effect consequent from the welding process, which led to this significant difference in tensile values between the weld layers. While it is noted that the values of UTS and YS after the QHT process was convergent. The value of UTS and YS for BM and FZ layers are similar, and they do not have a significant difference from the HAZ layer. That shows a substantial improvement in the tensile points and uniformity of the three layers of the welding area after conducting QHT. The welding should be resistant to harsh conditions which are exposed in this region when used in a reactor pressure vessel as a part of the nuclear power plant. Also, it is worth noting that the information above is not known for the mechanical test results and that this uncertainty needs to be borne in mind when analysing the mechanical test data.

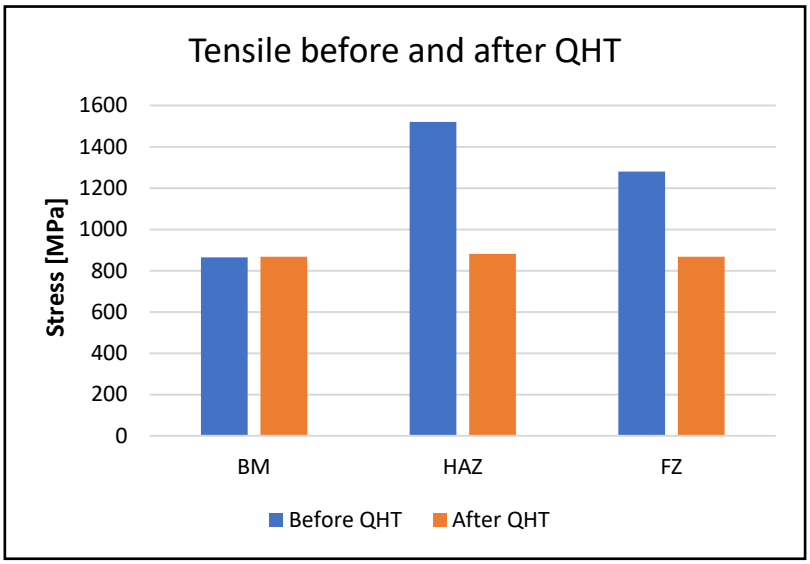

(a) Tensile curves for three different weld layers

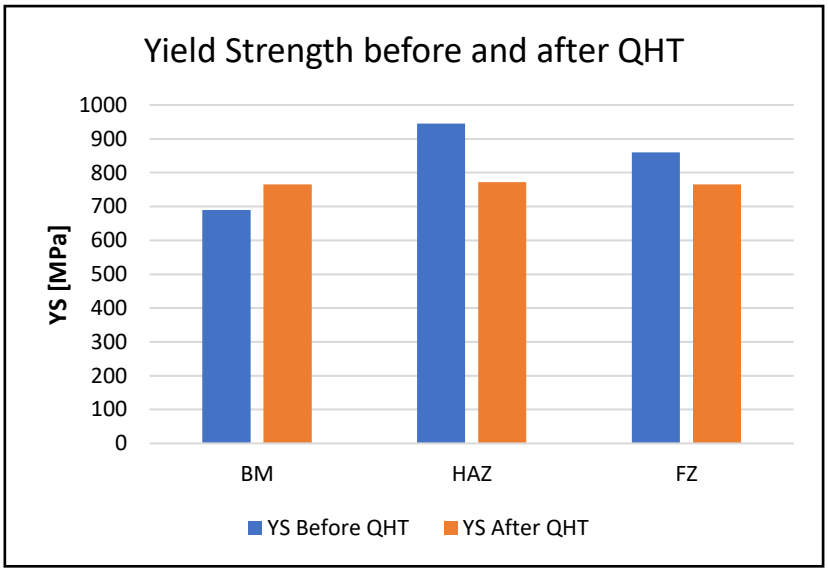

(b) YS curves for three different weld layers

Figure 4.29: (a) Tensile curves for three different weld layers, (b) YS curves for three different weld layers.

4.6.3 Charpy Impact Test for 200mm weld

Charpy impact testing was conducted at a temperature of -73°C and according to BS EN ISO 14-1:2016 specifications where the sample length was 55 mm with square section 10 mm×10mm and the angle of the notch 45° with a depth of 2 mm. The range of the weld sample was 200mm; three samples were taken from the weld surface, one specimen for each weld layer (BM, HAZ, FZ) for both tests before QHT and after it with the TMC machine. The Charpy samples were chosen for cutting in the same location of the welding samples for both tests to be more accurate, as shown in Figure 4.30.

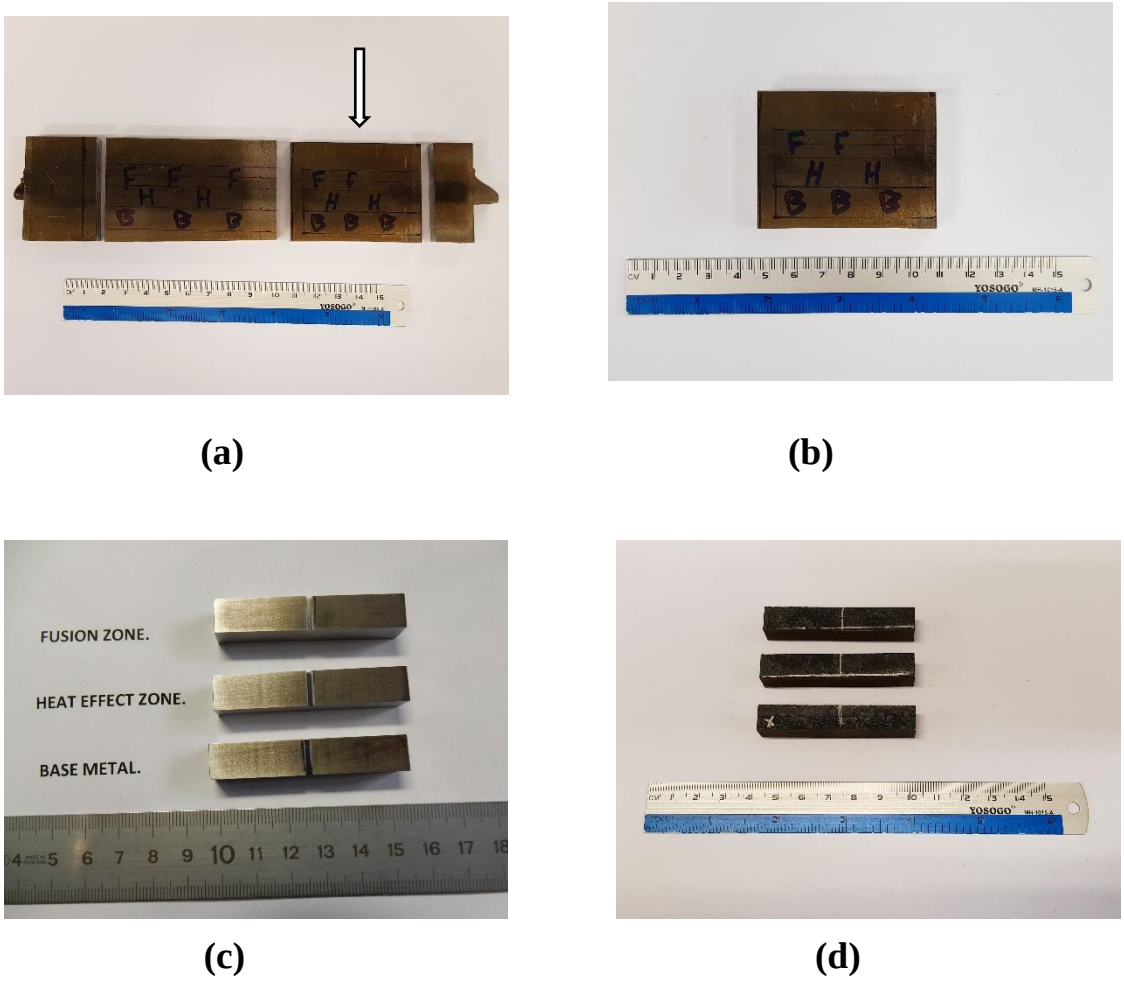

Figure 4.30: (a) location of Charpy on the weld sample (b) the weld sample for Charpy test (c) the Charpy's samples before QHT (d) the Charpy's samples after QHT

4.6.3.1 Compare the Charpy Impact Test between the alloys before and after Quality Heat Treatment

The Charpy test results show that the value of absorbed energy is significantly different before heat treatment design and after it. Figure 4.31 shows that the value of the BM layer was higher before the QHT with 130 J, which was decreased after the QHT to 115 J with a difference around 15 Joules. While, the other two welding layers, HAZ and FZ, had significantly increased in value, which was 35 and 26 before the QHT, and become 115 and 107 after the QHT. There has been a significant improvement in toughness after QHT. We notice a substantial rise in HAZ and FZ layers while reducing the absorbed energy in layer BM. The values of the three layers become very close to each other, and they are in a homogeneous state

in the welding area. In general, this causes improved toughness for the welding sample if compared with the condition before QHT. The results were identical to ASTM A508A508M.28187, which the minimum value of one specimen was 41J. Also, it is worth noting that the information above is not known for the mechanical test results and that this uncertainty needs to be borne in mind when analysing the mechanical test data.

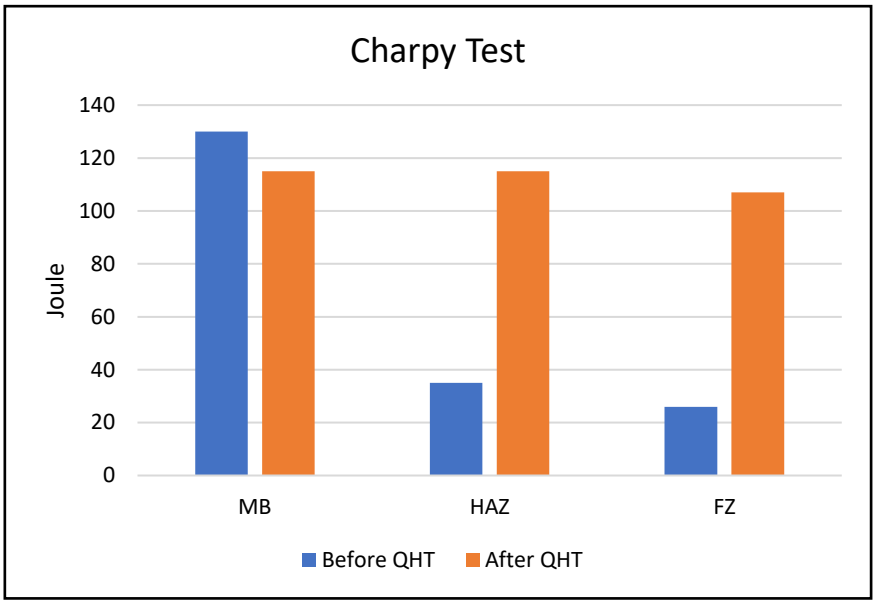

Figure 4.31: Charpy Impact curves after QHT for three different weld layers

4.6.3.2 The Charpy before QHT

Images of the Charpy samples were taken before the QHT for analysis and examination, as shown in Figure 4.32. The photos give a precise shape of the fracture area. It seems clear that the fracture appears completely separated in HAZ, and FZ layers and indicate that the fracture was brittle, while the fracture in the BM layer is not entirely separated, it suggests that the fracture is middle-ductile.

Figure 4.32: Images of the Charpy samples were taken before the QHT

SEM was used to investigate the fracture for a more accurate analysis of the results. Figure 4.33 shows the SEM micrographs of the fracture surfaces for all three welding layers. From Figure 4.33 (a) for the BM layer, the fracture presence of dimples indicates that the fracture was Middle- ductile. While the fracture in Figure (b, c) displays the cleavage facet, which suggests that the fracture was brittle.

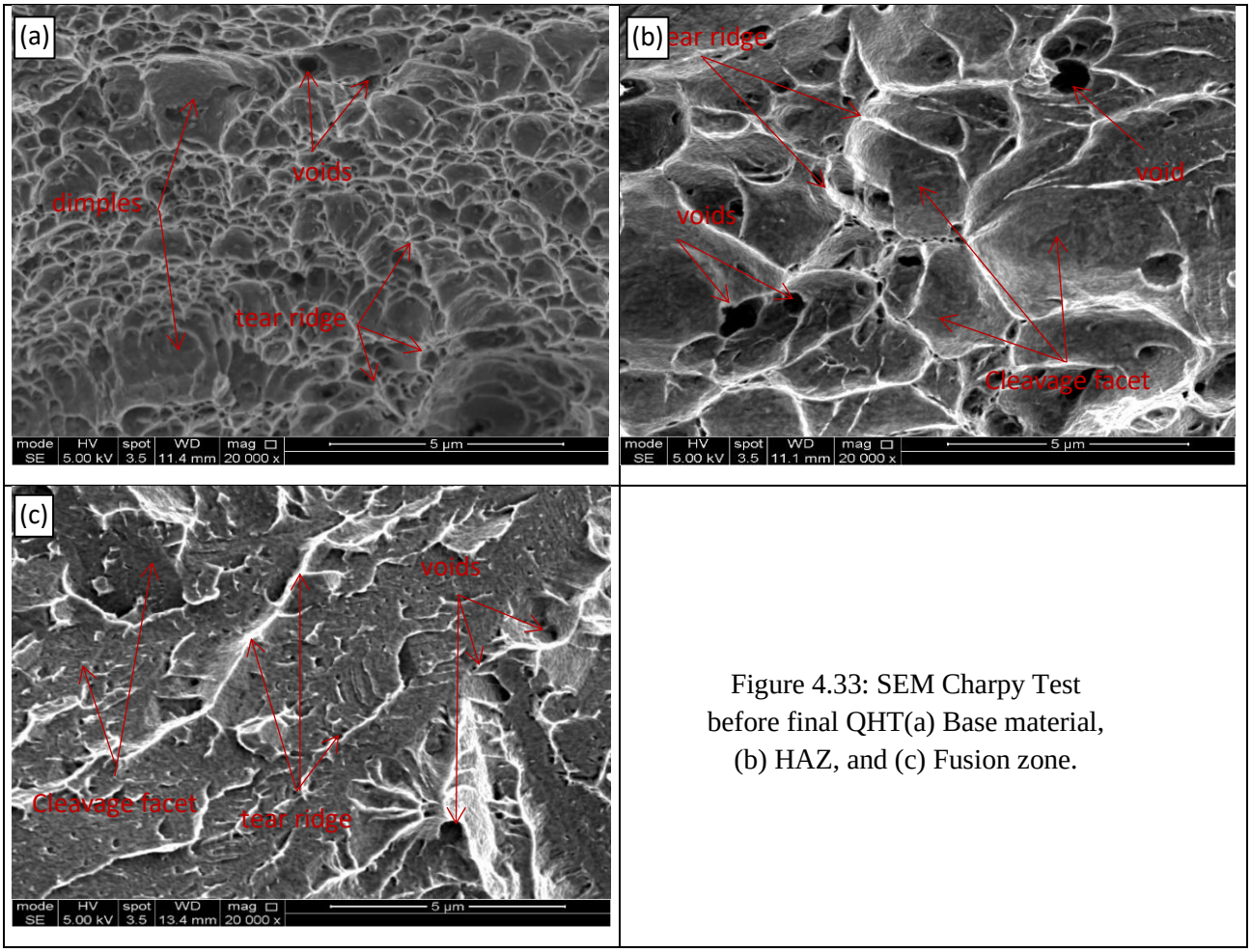

Figure 4.33: SEM Charpy Test before final QHT(a) Base material, (b) HAZ, and (c) Fusion zone.

4.6.3.3 The Charpy after QHT

Figure 4.34 illustrates the images for the Charpy test specimens after QHT. It is observed that all samples appeared to be not separated after the test, and this mostly indicates that the fracture was ductile.

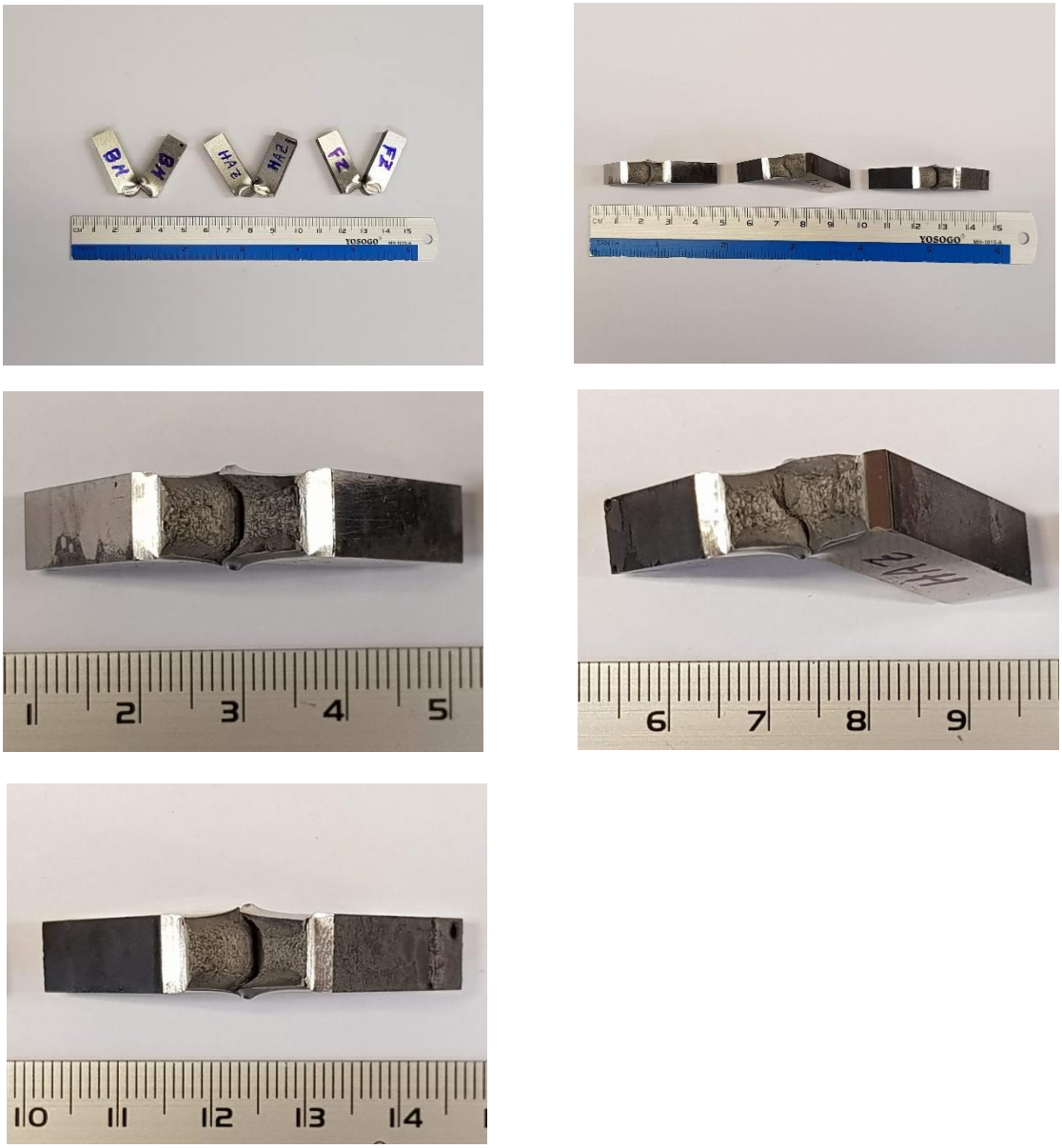

Figure 4.34: Images of the Charpy samples were taken after the QHT.

The fracture for the three welding layers was investigated by SEM. Figure 4.35 shows the fracture of the three welding layers after Quality Heat Treatment. It clearly shows dimples within the fracture area, which indicates that it was ductile.

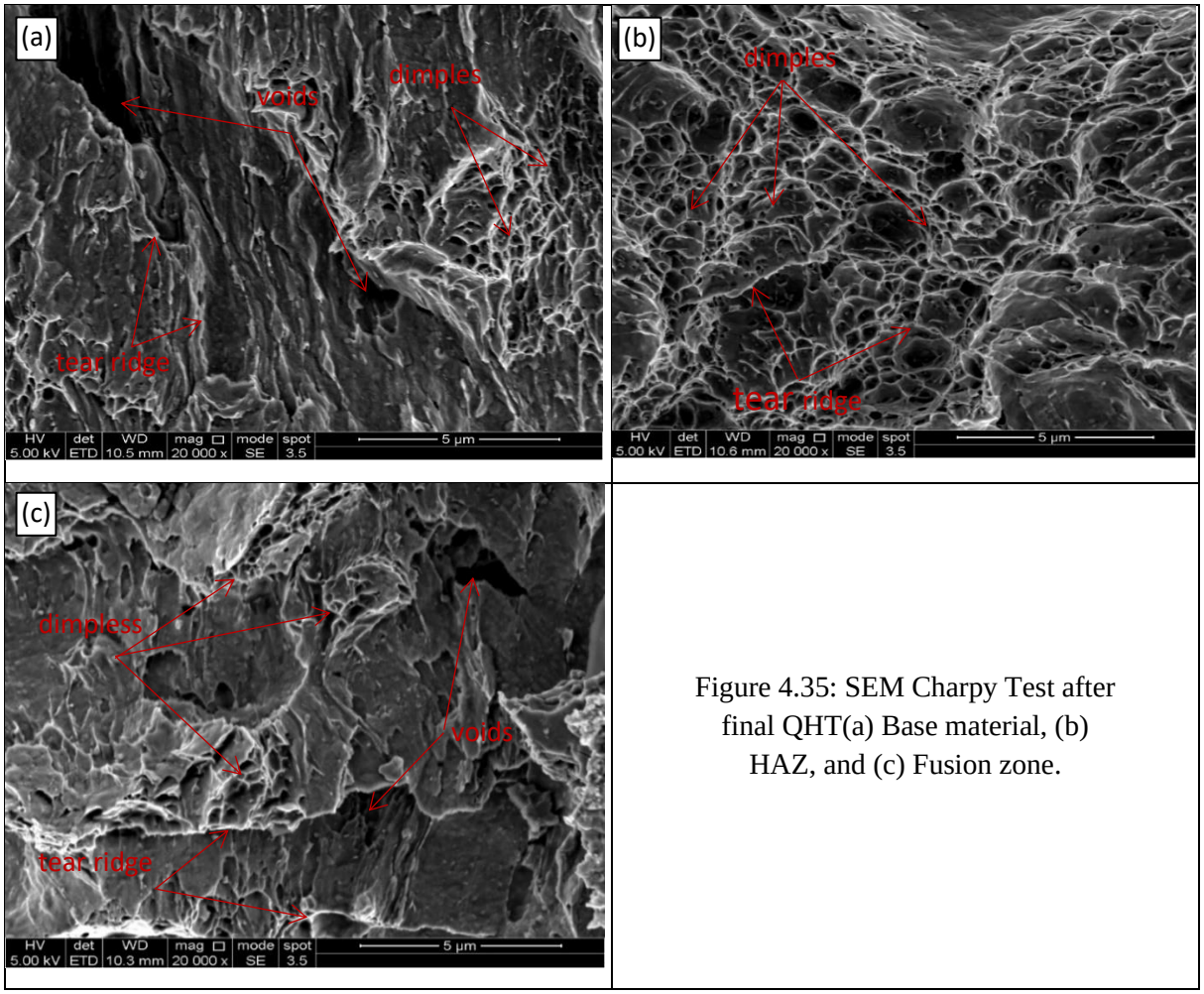

Figure 4.35: SEM Charpy Test after final QHT(a) Base material, (b) HAZ, and (c) Fusion zone.

Chapter 5 / Cladding Results and Discussion

5.1 Introduction

In this chapter, the cladding layer that protects the internal surface of the reactor pressure vessel was investigated in terms of microstructure and hardness in the as-clad condition and in the PWHT and QHT condition. The TMC machine was used to achieve accurate QHT conditions using the same temperatures as used in Chapter 4. The final design of QHT identified in Chapter 4 was then used to understand the effect of the QHT design on the cladding layers.

5.2 Cladding and HAZ Thickness

To investigate the effect of processing parameters on microstructure uniformity, porosity, and layer thickness, 23 different process variable combinations were investigated. Four samples have been selected for comparison to show the variations observed, Figures 5.1 through 5.8 and Tables 5.2 through 5.5. The difference in thickness for the clad and HAZ layers were attributed to the variations in laser power and powder feed rate. Table 5.1 shows clearly the difference in the thickness of the clad and HAZ layers for these samples. The results appear to show that the samples number two and nine have excellent specifications compared to others, due to near the defect-free clad area, while some defects such as porosities can be seen clearly in the sample number thirteen. For sample number sixteen, there is no clad layer on the substrate metal; for this reason, this sample failed.

When the laser density is not high enough, pores can be formed in the overlapping region close to the substrate. This occurrence is due to the low power density that results in incomplete melting of the cladding powder to enough level. Consequently, to prevent the formation of pores, laser power must be increased, or the power feed rate should be decreased [141].

Table 5.1: Samples specifications

Sample No.	cladding thickness	HAZ thickness	Laser power [W]	Powder feed rate [g/min]
2	1551.8 µm	1445.9 µm	5500	34
9	1594.3 µm	1317.0 µm	5000	40
13	1287.5 µm	1084.1 µm	3000	40
16	_	_	3400	40

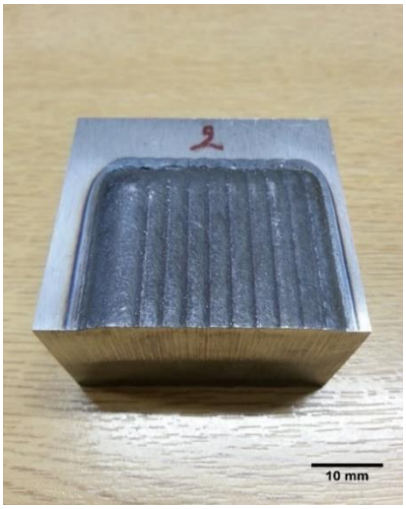

Figure 5.1: Image Sample # 2

Table 5.2 Parameters Sample # 2

NI 319 - Forgmasters cladding - Parameters							
No. of sample	Laser power [W]	Speed of cladding [mm/min]	Powder feed rate [g/min]	Carrier gas flow [l/min]	Purge gas flow [l/min]	Offset [mm]	Number of Line
2	5500	1000	34	10	20	3.2	10

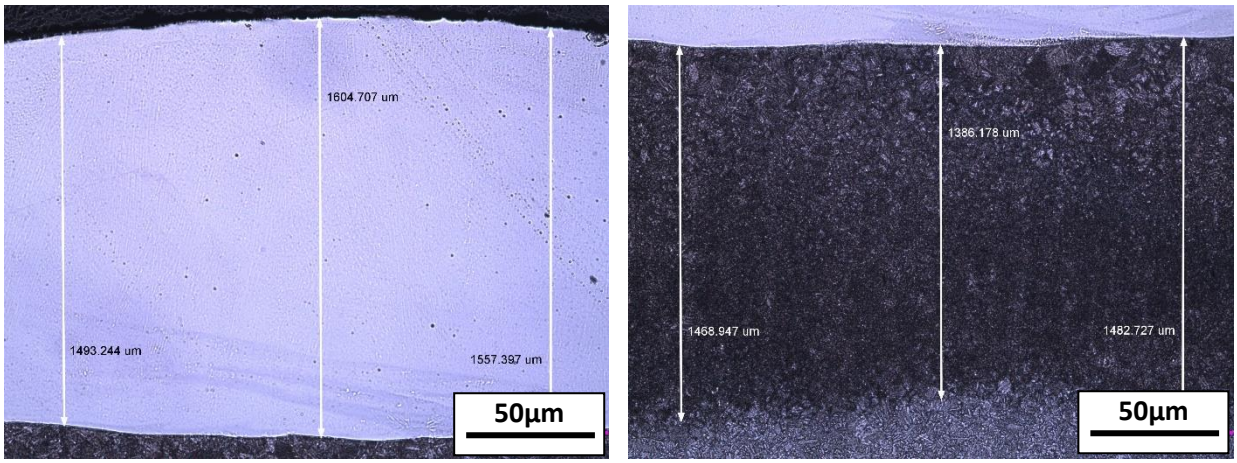

(a) Cladding Image (b) HAZ Image

Figure 5.2: Image Thickness Sample 2 (a) Cladding (b) HAZ

Average of cladding thickness No. 2= 1551.7 µm

Average of HAZ thickness No. 2= 1445.9 µm

Figure 5.3: Image Sample #9

Table 5.3 Parameters Sample #9

NI 319 - Forgmasters cladding - Parameters							
No. of sample	Laser power [W]	Speed of cladding [mm/min]	Powder feed rate [g/min]	Carrier gas flow [l/min]	Purge gas flow [l/min]	Offset [mm]	Number of Line
9	5000	1000	40	10	20	3.3	10

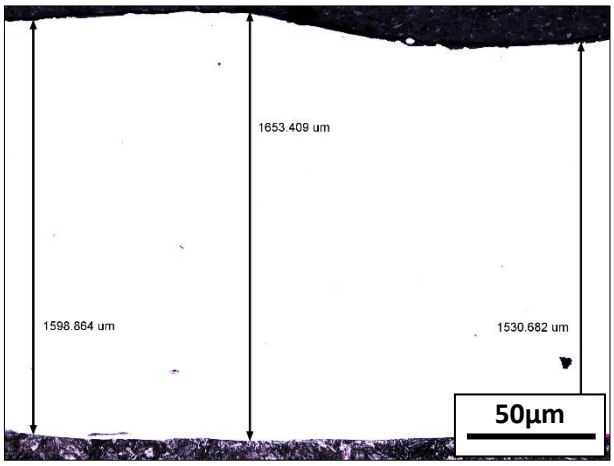

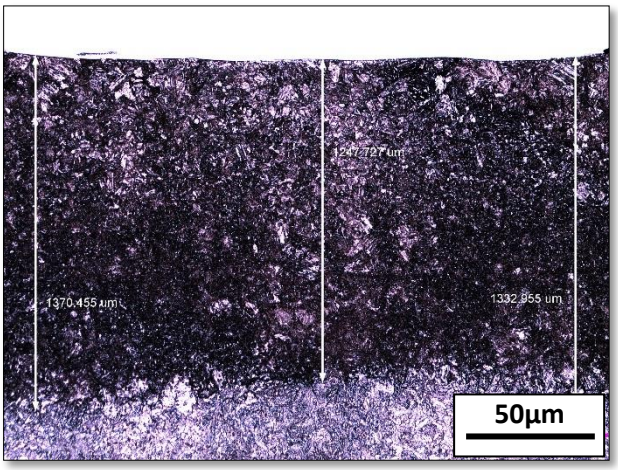

(a) Cladding Image (b) HAZ Image

Figure 5.4: Image Thickness Sample 9 (a) Cladding (b) HAZ

Average of cladding thickness No. 9= 1594.3 µm

Average of HAZ thickness No. 9= 1317.1 µm

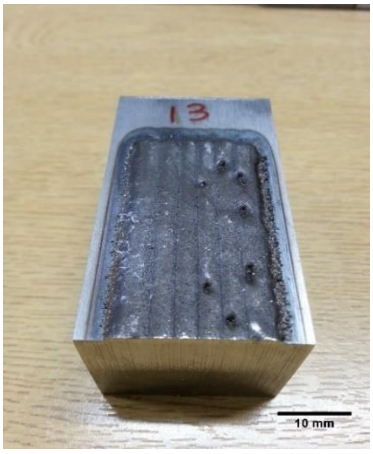

Figure 5.5: Image Sample #13

Table 5.4 Parameters Sample # 13

NI 319 - Forgmasters cladding - Parameters							
No. of sample	Laser power [W]	Speed of cladding [mm/min]	Powder feed rate [g/min]	Carrier gas flow [l/min]	Purge gas flow [l/min]	Offset [mm]	Number of Line
13	3000	1000	40	10	20	3.3	6

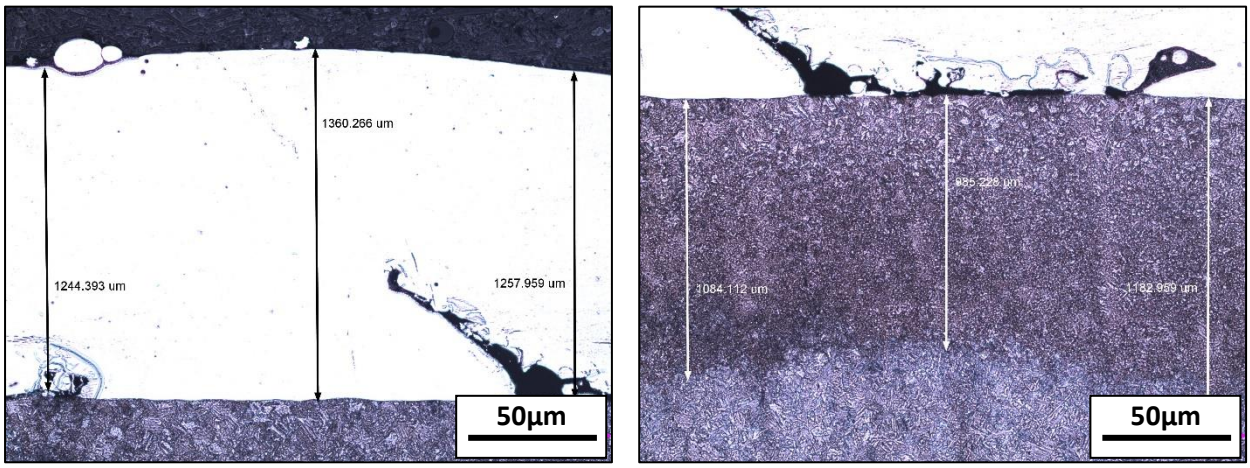

(a) Cladding Image (b) HAZ Image

Figure 5.6: Image Thickness Sample 13 (a) Cladding (b) HAZ

Average of cladding thickness No. 13= 1287.5 µm

Average of HAZ thickness No. 13= 1084.1 µm

Figure 5.7: Image Sample #16

Table 5.5 Parameters Sample # 16

NI 319 - Forgmasters cladding - Parameters							
No. of sample	Laser power [W]	Speed of cladding [mm/min]	Powder feed rate [g/min]	Carrier gas flow [l/min]	Purge gas flow [l/min]	Offset [mm]	Number of Line
16	3400	1000	40	10	20	3.3	10

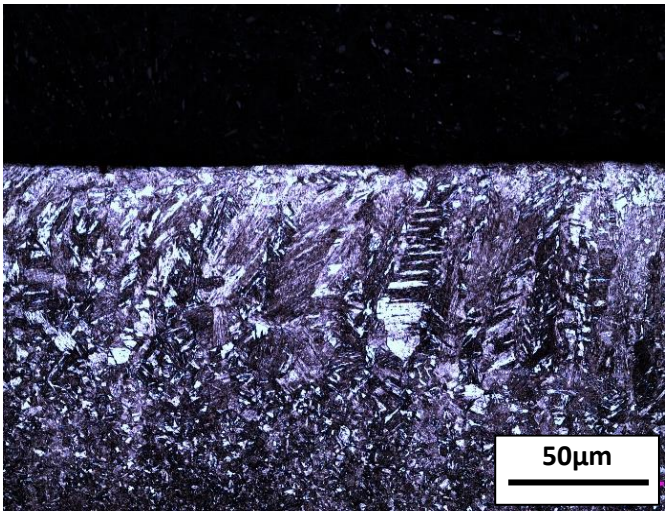

Figure 5.8: HAZ Image Sample #16

5.3.1 Microstructure of As-welded Clad Sample

First, it is essential to specify the samples used in this work, along with their properties. Figure 5.9 shows the cross-section of a clad sample. Three different layers of microstructure can be identified; the top layer, which is the clad material, while the middle layer is the HAZ of primarily the base metal and the last layer in the bottom is the base metal. The cladding material is austenitic stainless steel 308L, and the substrate material is SA508 Gr.4N. In the HAZ, the grain size is coarse, with it being most coarse adjacent to the cladding material, while the grain size is finer and smaller closer to the substrate metal [151]. The high cooling rates create grains with fine size in the microstructure, which in turn improve the mechanical properties of the alloys [150].

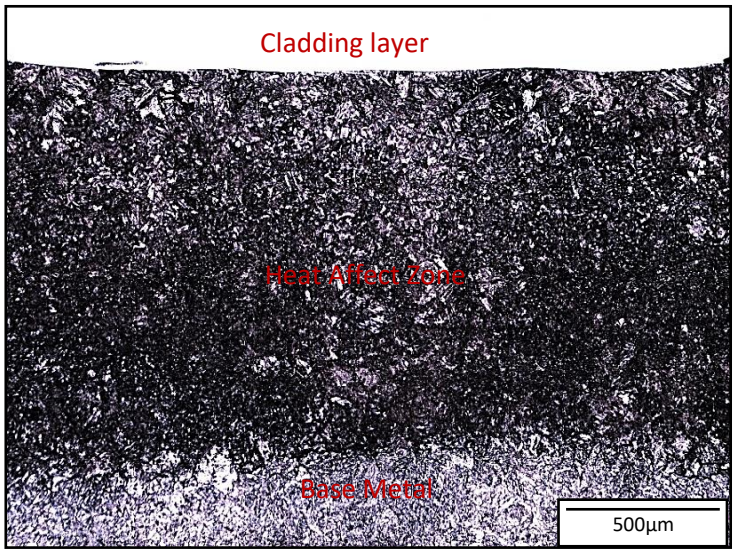

Figure 5.9: Microstructure of the HAZ and substrate metal in sample # 9.

5.3.2 Microstructure of Clad Layer

Figure 5.10. Shows the microstructure of the clad layer (Stainless steel 308L) before heat treatment, where a skeletal morphology of lacy delta ferrite (dark shapes) can be seen in a matrix of austenite (white region). The microstructure also consists of an interdendritic layer of austenite with a primary ferrite dendrite. Here there is a small amount of ferrite in the substrate close to the cladding area, which is attributed to the increased cooling rate speed in this region that prevents ferrite from transforming completely to austenite, leading to residual ferrite at room temperature [100,152,153].

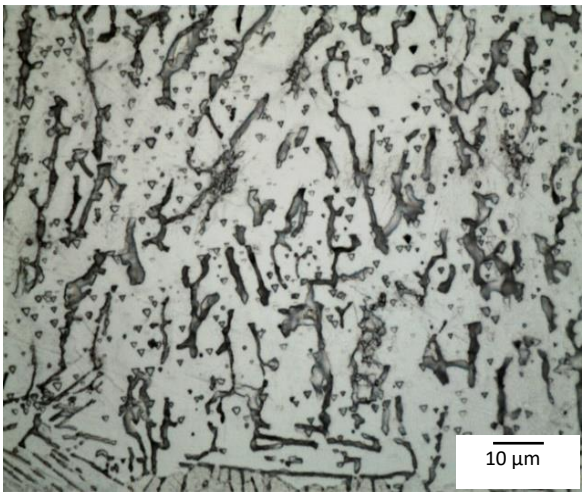

Figure 5.10: Microstructure of clad layer (stainless steel 308L).

5.3.3 The hardness for Cladding Samples

The hardness map (HV) data in Figure 5.11, shows a non-trivial impact of the cladding on the near-surface microstructure. Like the microstructure analysis, there is a clear heat-affected zone, which has a higher hardness than the base material. However, as the next line of powder is deposited, the heat-affected zones are heat affected again, and hardness was reduced. More work on the heat treatment is now required to gain the best way to change the HAZ hardness and make it of homogenous with the hardness value for all cladding layers, for that will use comparison between the PWHT and QHT processes to improve the alloy behaviour in the hardness.

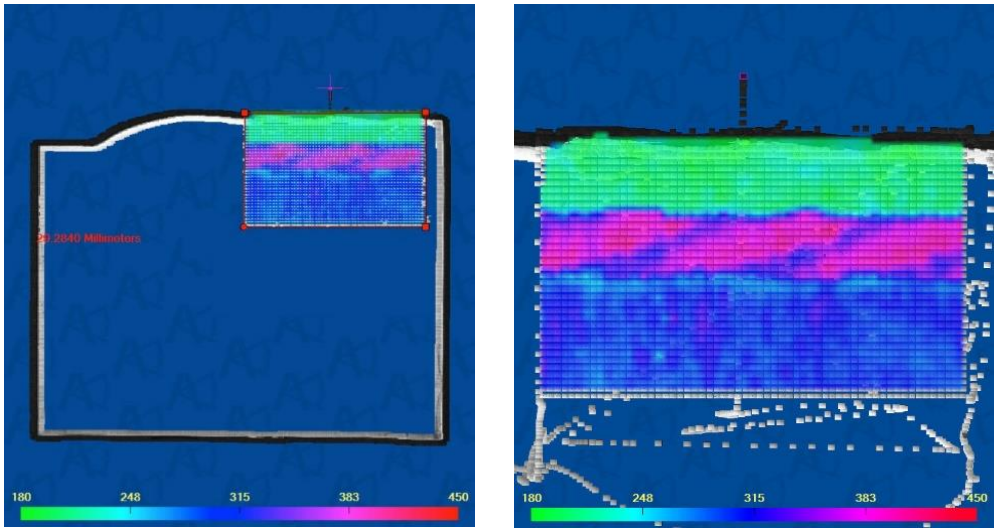

Figure 5.11: Hardness map (HV) of the cladding sample.

The grain size, internal stress and chemical composition are three essential factors that directly affect the value of local hardness [153]. Besides, the increase in ferrite content also contributes to the difference in the microhardness of the metal [107]. The hardness is related proportionally to the cladding speed, that means a higher cladding rate, produces a harder surface. That is because the increase of the cladding speed causes a decrease in the heat input per unit length of the clad layer. This will increase the cooling rate and refine the microstructure, therefore increasing the strength and hardness of clad metal [41, 99]. The high heat input from the laser cladding process raises the temperature to achieve the austenite formation temperature in the base metal adjacent to the clad region. Once the laser has passed, the bulk substrate generates a rapid cooling rate causing the transformation of the material to a martensitic structure and increased hardness, as observed [41].

5.4 Microstructure of Cladding Samples after different type of Heat Treatment

Figure 5.12 shows the microstructure of the cladding samples that were (a), as-welded (b), PWHT at 565℃ for 30-hours holding time with a cooling rate of 14℃/hr (c) QHT at 860℃- for 6-hours holding time with cooling rate 25℃/min. In the as-welded sample, the HAZ layer appears with high thickness of at least 2mm. The top area of the HAZ also has a coarser microstructure, indicating a much higher temperature was reached in the base material at the base/clad and this decreased rapidly into the substrate. The microstructure after PWHT shows that there is no significant change in the internal structure of the sample, except maybe in the upper part of the HAZ layer, which appears to have become slightly more granular. The specimen following QHT appears significantly different in the microstructure; the obvious HAZ has disappeared and the microstructure appears to be relatively homogeneous, possibly with the exception of the immediate layer next to the clad layer, where it is maybe a little coarser. The result illustrates that the QHT design is again successful and there have been no detrimental effects on microstructure evolution of the base metal or on the clad layer or their connectivity [154]. This indicates that it appears to be feasible to fabricate the RPV by welding, followed immediately by cladding, i.e. no intermediate heat treatments, and then undertake one final QHT.

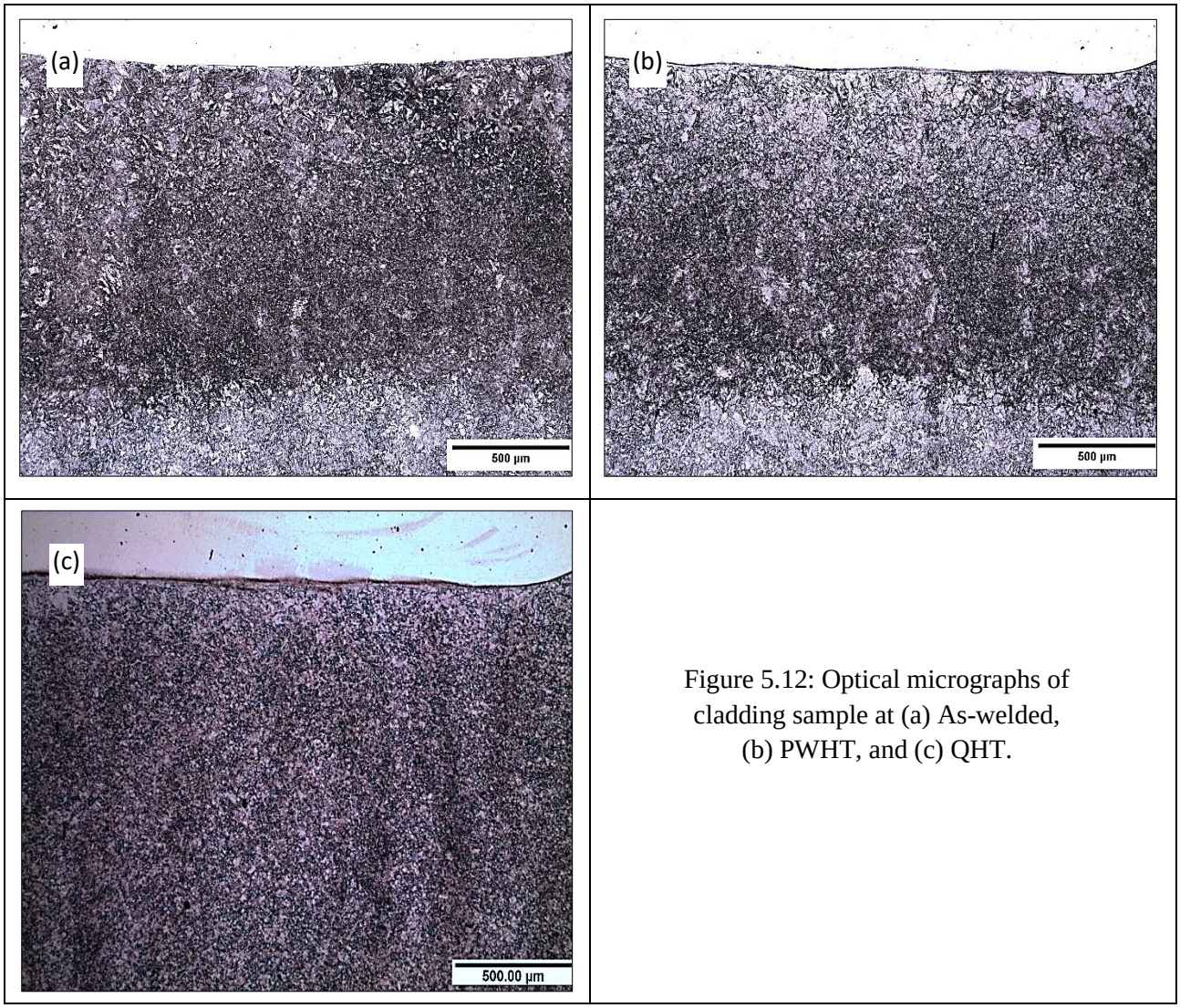

Figure 5.12: Optical micrographs of cladding sample at (a) As-welded, (b) PWHT, and (c) QHT.

5.5 Microstructure of QHT for Cladding Samples after different temperatures

Figure 5.13 shows the microstructure of the cladding samples at different QHT temperatures with a holding time 15 minutes and cooling rate of 25℃/min. The microstructure of the sample at 860℃ again consisted of fine grain size that appears to homogenous. At the temperature of 900℃, it was found that there was the beginning of growth of the grain size and the area near of the cladding layer seemed slightly larger than the grains of base metal, but still maintained a good level of consistency. At the temperature of 1020℃ grain growth is now obvious, especially in the HAZ area, where the grains seem coarser than the base metal layer. The sample

at a temperature of 1120°C, reveals a significant growth of the grain size in the HAZ Layer. This data, once again, confirms that a QHT of 860°C seems the most viable.

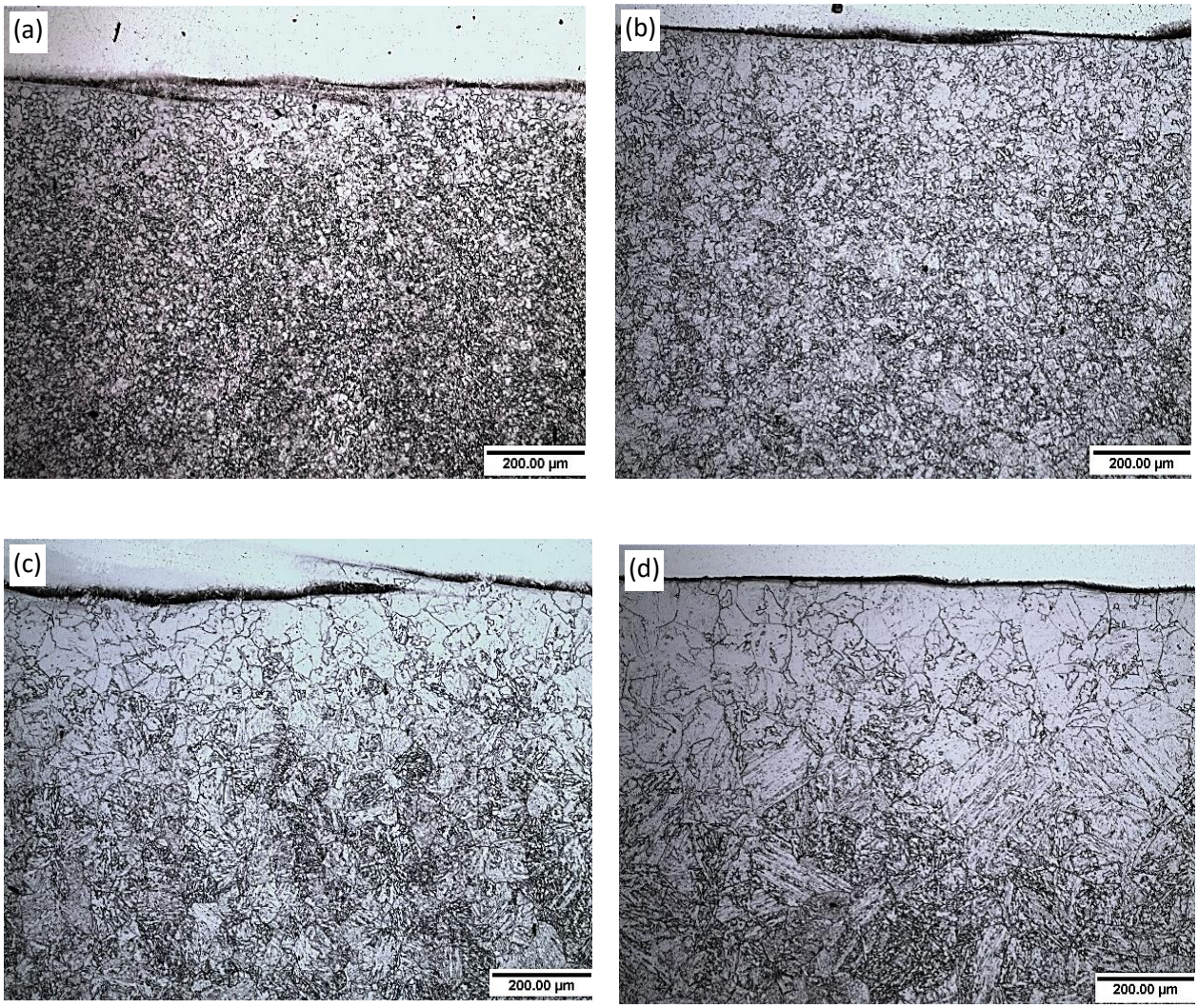

Figure 5.13: Optical micrographs of QHT for cladding sample at (a) 860°C, (b) 920°C, (c) 1020°C, (d) 1120°C

5.6 The hardness for different QHT to the clad samples

Figure 5.14 shows the hardness values (HV) of the cladding samples at different QHT temperatures reveals a slight variation in base metal hardness among samples of approximately 50 points. However, in all cases it appears that the base material hardness has become approximately uniform all the way to the clad layer, indicating the HAZ has been removed. At the best temperature for quality heat treatment, the hardness plots showed the hardness in the

specimen at a temperature of 860℃ is lower compared to the rest of the samples by approximately 25-50 points. This most likely due to the larger austenite grain size promoting the formation of martensite. This once again shows that 860℃ is the ideal temperature for QHT.

(a)860 ℃

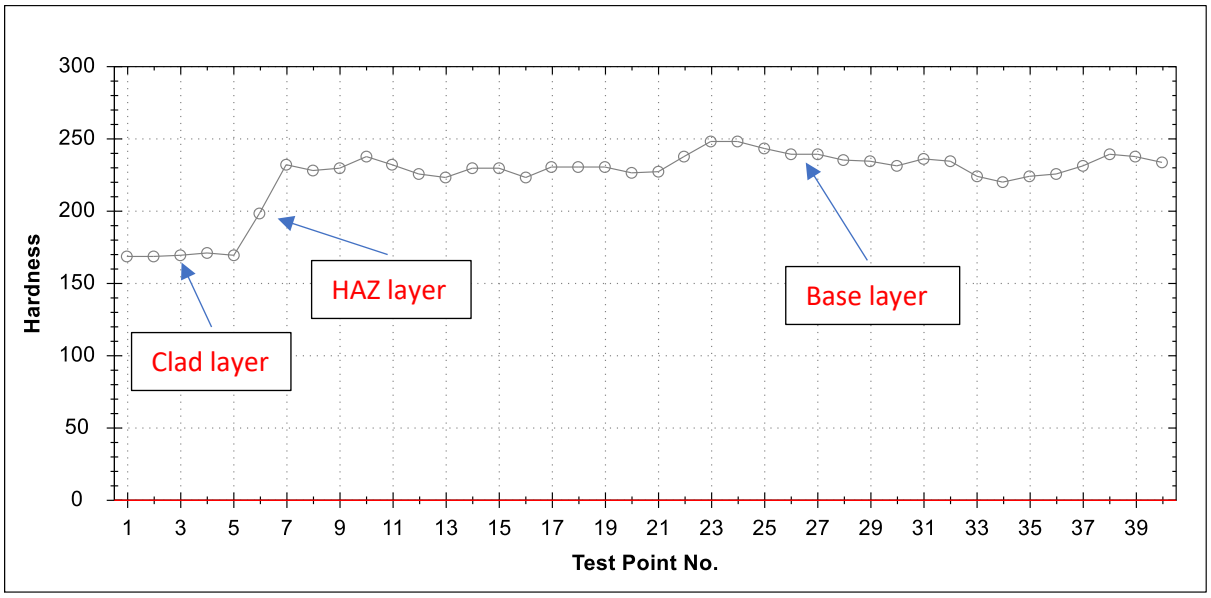

(b)920 ℃

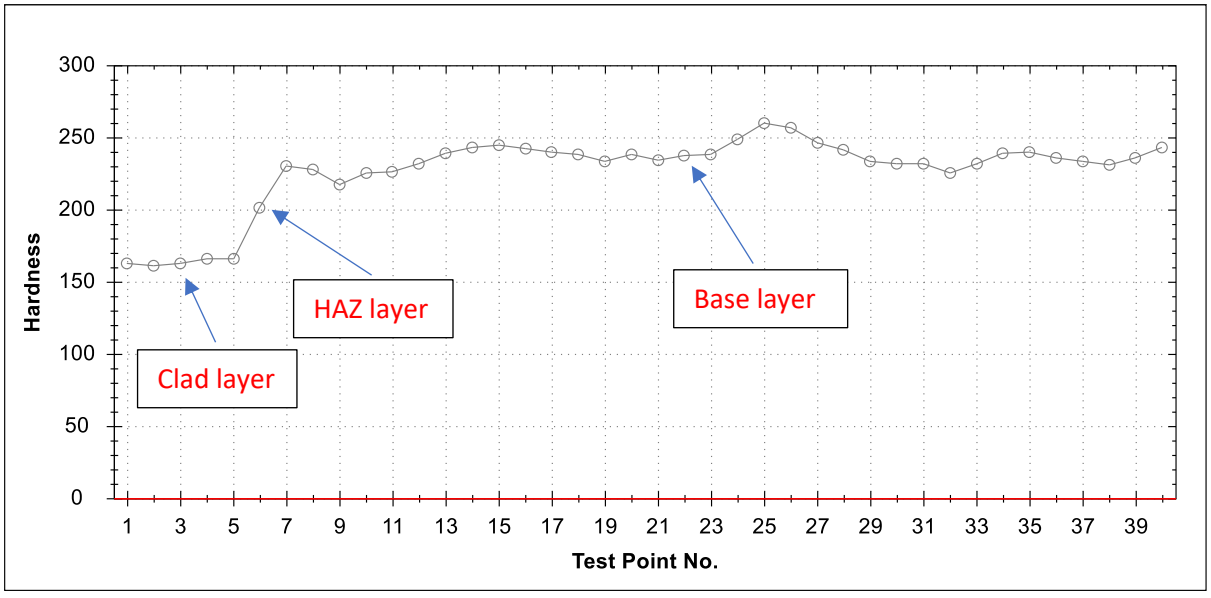

(c)1020 ℃

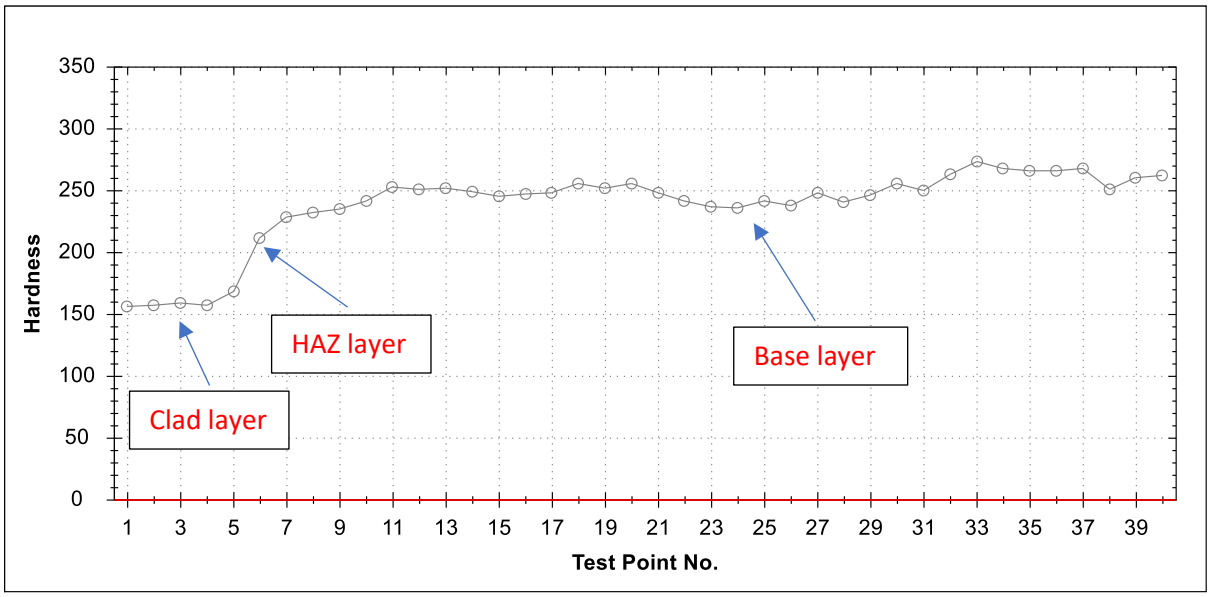

d)1120 ℃

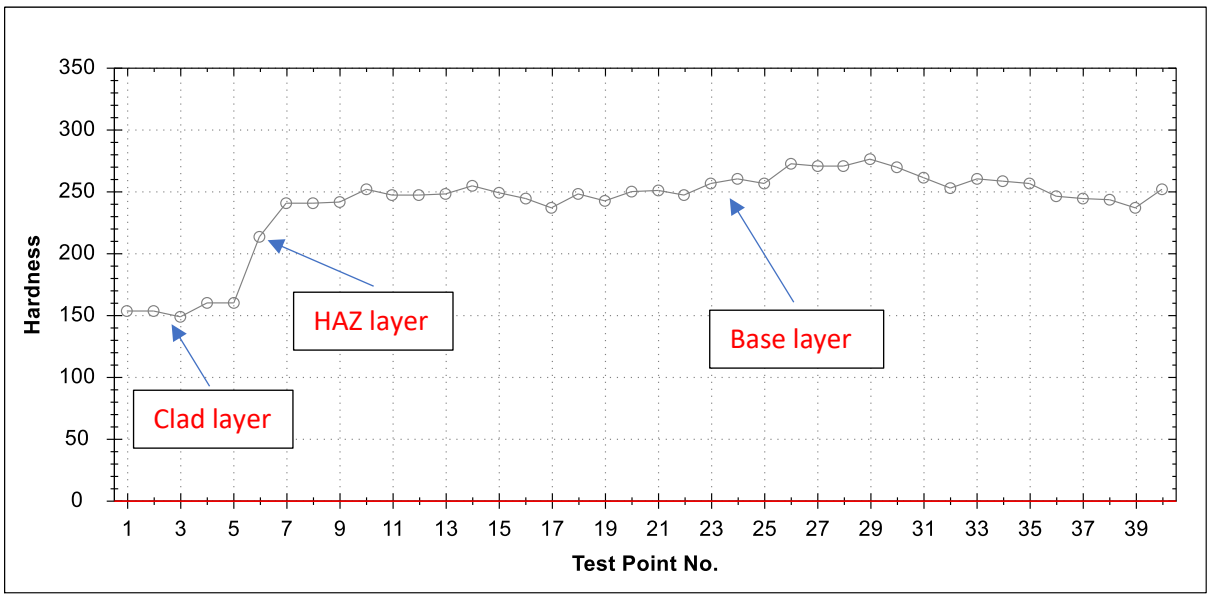

Figure 5.14: (a) hardness data after QHT at 860℃ (b) hardness data after QHT at 900℃ (c) hardness data after QHT at 1020℃ (d) hardness data after QHT at 1120℃.

5.7 Final comparison use the QHT

Figure 5.15 shows the microstructure of the clad layer (Stainless steel 308L) before heat treatment. It is composed of ferrite and austenite phases, where the ferrite morphologies consist of mainly skeletal and vermicular. When the laser cladding layers increase in the number, the content of ferrite generally increases. The grain morphology transformations depend on the grain growth rate and cooling rate. Also, decreasing the cooling rate that would increase the speed of transformation of the ferrite to the austenite, leading to a reduction of residual ferrite at room temperature [56,155].

Figure.5.15(b) shows the HAZ layer and the Base metal have distinctly different grain sizes, where it is coarser in the HAZ area, especially near the cladding layer compared to the base metal, the grain size within the HAZ is heterogeneous.

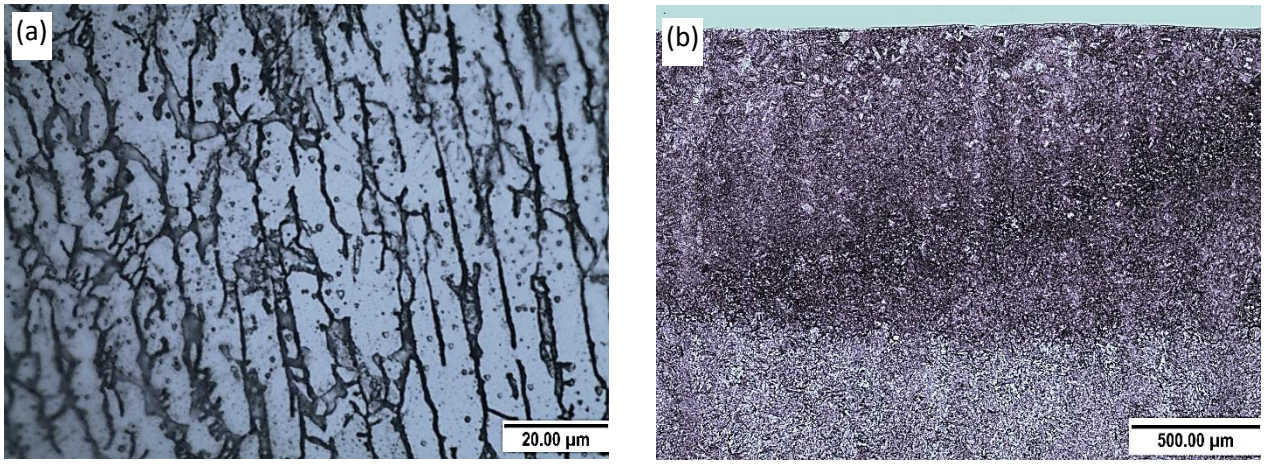

Figure 5.15: Before QHT (a) The clad layer (b) the HAZ layer

Figure 5.16 shows the cladding samples after the QHT at 860℃ and holding time of 8 hours, where there appears to be a significant improvement in all layers in the laser cladding area. The dendritic shape of the ferrite, which existed before the heat treatment in the cladding layer and has now become more equiaxed. The cooling rate plays the primary role in the distribution of the ferrite morphologies between skeletal, vermicular and lath-like. When the cooling rate fast, the ferrite is lath-like due to the limited diffusion among the austenite and ferrite. While, if the speed of the cooling is medium, the ferrite will be skeletal and vermicular because of the sufficient diffusion process [146,151,155]. Also, there has been a significant change in the grain size in all layers of the HAZ, which has become more uniform and similar to the base metal, once again confirming that the QHT has done its job without negative effects.

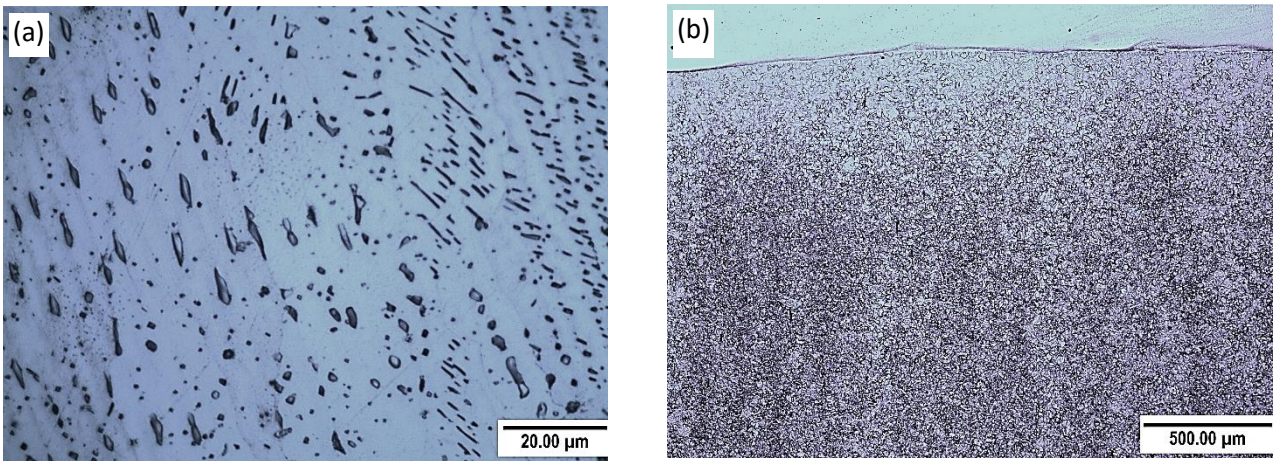

Figure 5.16: After QHT (a) The clad layer (b) the HAZ layer.

5.9 The Hardness before and after QHT by TMC

Figure 5.17 shows the images of laser cladding hardness before and after conducting the QHT where the hardness points are shown in both specimens, with forty points an appropriate distance from the edge for each specimen. Starting from the cladding layer and entering through the HAZ and the base metal to clarify the hardness values in all cladding area.

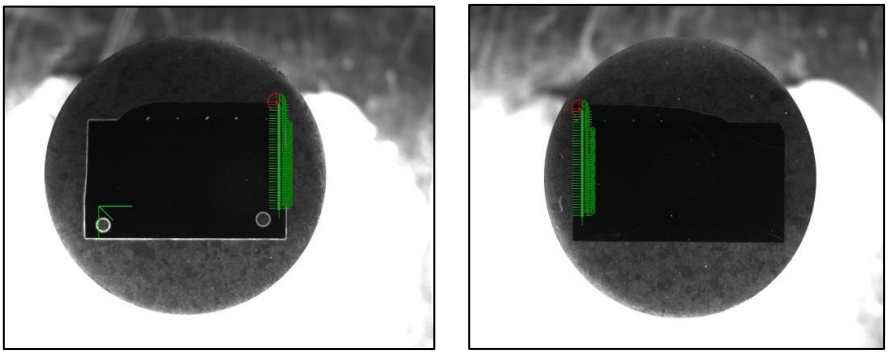

(a) (b)

Figure 5.17: (a) Image for hardness after QHT (b) Image for hardness before QHT

Figure 5.18 shows the hardness curve of the laser cladding, before and after conducting the QHT, where the chart indicates a significant difference in the hardness values among the two cases, the difference is between 50-200 HV in all cladding layers. The QHT, which was able to remove all the accumulations resulting from the laser cladding process, specifically of the HAZ layer, which had a hardness value before the heat treatment of more than 400 HV. That illustrated the QHT contributed to substantially change in each cladding area and causes the

hardness to converge, and this suggested the marked improvement in the mechanical properties of each cladding area.

The alloy elements have significant effects on the mechanical properties which the C, Ni, N, and Mn percentage lead to a decrease in the amount of ferrite and support the austenite stabilisers. While the Cr, Mo, and Si work as ferrite stabilisers and raise the amount of ferrite. The amount of ferrite is essential, as increasing it will lead to mechanical problems and reducing it will cause hot cracking. It is preferable that the percentage of ferrite is relatively low to protect the welding from corrosive environments [56,155].

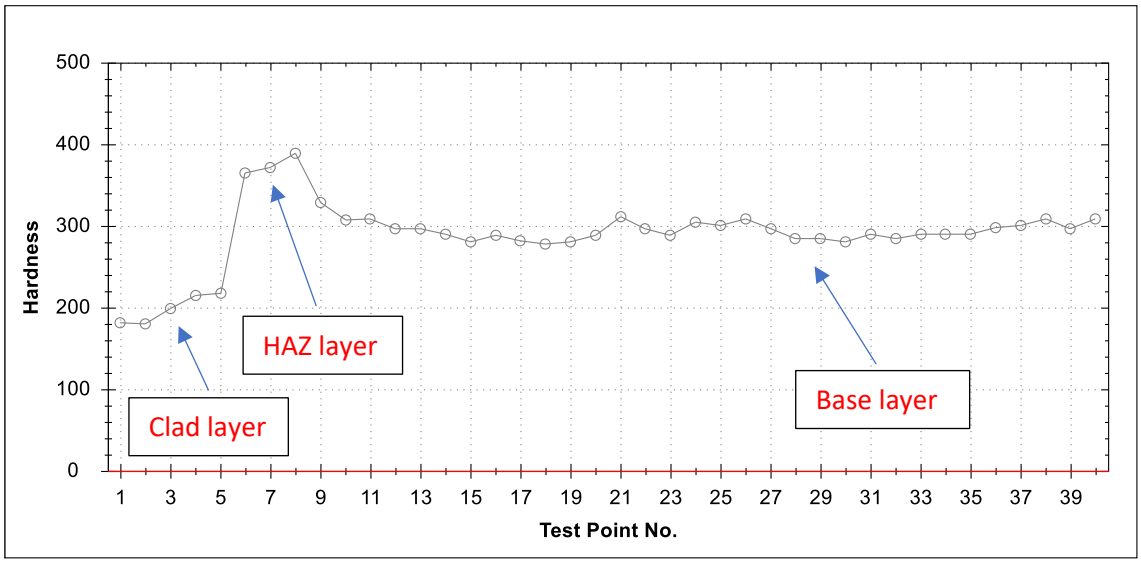

(a) Cladding hardness before QHT

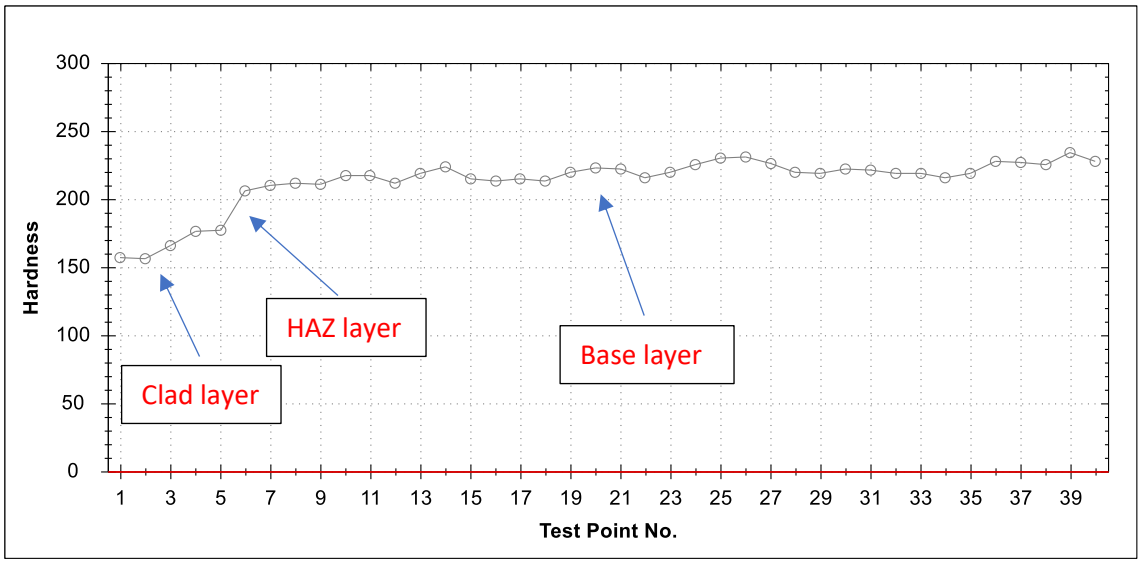

(b) Cladding hardness after QHT

Figure 5.18: (a) hardness data before QHT (b) hardness data after QHT

Chapter 6 / Conclusions

In this research, an investigation has been carried out on the reduced pressure electron beam welding of steel alloy SA508 Grade 4N with a thickness of 200 mm, and a quality heat treatment to enhance the mechanical properties and microstructure of the welding area, without having a negative impact on the base material has been designed. An equivalent study was also undertaken on the stainless-steel grade 308L cladding of SA508 Grade 4N and found that the same heat treatment also gave an excellent result. Below are the key conclusions reached after conducting this research.

6.1 The welding area in SA508 Grade 4N for RPV

- Initially, the SA508 Gr.3 & Gr.4N were compared in the as-received condition Both alloys show similar types of microstructure, i.e., mostly lath-like Bainitic packets with some evidence of pro-eutectiod ferrite. The presence of the ferrite is somewhat of a surprise for the SA508 Gr.4N, given that the CCT diagram presented in Chapter 2 would suggest that the cooling rate to obtain ferrite would have to be very slow, much slower than for SA508 Gr.3. The SA508 Grade 4N had a hardness of 280 and SA508 Gr.3 had a hardness of 223. This again is a surprise given that the SA508 Gr.3 had a much finer Bainite packet size and lath width, which would be expected to increase hardness, and not a significantly different volume fraction of ferrite. This would suggest that the increased levels of Ni and Cr in the SA508 Grade 4N is having a significant effect on hardness. This is most likely from increased solid solution hardening from both the Ni and Cr and possibly from increased volume fraction of chromium carbides.
- Thick section RPEBW was successfully undertaken on SA508 Grade 4N. In the initial sample received there was some level of porosity but sufficient contiguous material for undertaking microstructure analysis. Subsequent welds received were near defect free, indicating that the new welding technology is a viable fabrication method.
- Following welding, the base material has no structure change, i.e., Bainite with some evidence of ferrite. The Heat Affected Zone (HAZ) has Bainite with no evidence of

ferrite, indicating that the cooling rate was faster than that produced in the base material. The HAZ prior austenite grain size, Bainite packet size, and Bainite lath width are all smaller than the base material, indicating that the maximum temperature reached and/or time at temperature in the austenite field was reduced compared to base material in addition to having a faster cooling rate. The fusion zone consists of a large columnar structure in which a clear dendritic structure is observed. It appears that the dendrites have a skeletal structure. This suggested that the initial dendrites formed were delta ferrite, the interdendritic regions where then carbon and alloying element rich, meaning that these regions were beyond the peritectic reaction and transformed directly from liquid to austenite. The delta ferrite then transformed to austenite with a much different chemistry than the interdendritic regions, leading to two distinct alpha-ferrite and Bainite chemistries on cooling to room temperatures.

- The as-welded material when subjected to post weld heat treatment (PWHT) to remove residual stress showed that the base metal and HAZ had similar microstructures to the as-welded material, with possibly some indication of microstructure coarsening in the HAZ. The skeletal dendrites in the fusion zone, however, appeared to degenerate into another phase or morphology, suggesting the dendrites are highly thermodynamically unstable.

- The as-welded material when subjected to a quality heat treatment (QHT) to remove process history effects showed that the microstructures in all three weld zones are similar in morphology, displaying a Bainitic microstructure. It appeared, at least on the optical microscopy scale, that the QHT had wiped out the history of the fusion zone and HAZ and produced a microstructure close to the base metal after the standard manufacturing process.

- A detailed analysis of the optimum QHT temperature was undertaken at temperatures of 860, 920, 1020, and 1120 ℃ at a time of 900 seconds. 1120℃ was rejected as there was significant austenite grain growth will have a very negative impact on impact toughness. The microstructures produced at the other temperatures showed significant promise as they produced a relatively small prior austenite grain size with a uniform Bainite microstructure and no evidence of the fusion zone microstructure. The microstructure at 860℃ had some evidence that there was not complete chemical homogeneity, which was most likely due to insufficient time at temperature. The fact

that at both 920℃ and 1020℃ there was sufficient time for complete dissolution at 900 seconds suggested that diffusion rates are high, and any further time could lead to significant grain growth. This led to the conclusion that QHT temperature of 860℃ would be the most practical as industrial heat treatment times would be significantly longer than 900 seconds.

- Four holding times, 8, 24, 48 and 96 hours, at 860℃ were investigated to identify the optimum. All holding times produced similar microstructures in all three welding zones and there was no major evidence of significant grain growth as a function of time. This a gain pointed to 860℃ being the ideal choice for QHT as by 8 hours the microstructure looks relatively uniform but any additional time at temperature did not lead to significant microstructure coarsening, indicating that there is a wide processing window at this temperature.

- Bulk mechanical properties, tensile at room temperature and Charpy impact at -73℃, where undertaken on quality heat treated welds at 860℃ for 8 hours in all three weld zones. The UTS values for the base material, HAZ, and fusion zone were 868 MPa, 882 MPa and 868 MPa, respectively. The 0.2% proof stresses were 765 MPa, 772 MPa and 765 MPa for base metal, HAZ and fusion zone, respectively. All specimens showed a ductility of 18% or more. Charpy impact values were 115J, 115J and 107J for the base metal, HAZ and fusion zone, respectively. This indicates that the quality heat treatment chosen generates uniform properties throughout the weld ones and properties that are within the required standard.

- The results suggest the RPEBW welding technique combined with a post weld quality heat treatment for SA508 Gr.4N can produce microstructures and mechanical properties equivalent to as forged and heat-treated material. This a most promising development as it leads to the concept of fabricating structure critical components such as RPVs, which until now were thought to be only manufactured using one-piece forgings.

6.2 The laser Cladding area in SA508 Grade 4N for RPV

- Laser cladding of SS308L onto SA508 Gr.4N was successfully undertaken at the NAMRC. Optimum processing conditions were found, which produced a defect free layer at both the interface and within the clad layer.
- Three different layers of microstructure were identified in the as-clad material: the top layer, which was the clad material, a middle layer that is the HAZ of primarily the base metal and the last layer, which is the base metal. In the HAZ, the grain size was coarser than the base metal, with it being most coarse adjacent to the cladding, while the grain size became finer and smaller closer to the substrate metal. The HAZ hardness was also significantly higher than the base material indicating the cooling rate was high following deposition of the clad layer.
- The cladding samples were subjected to different types of heat treatment (PWHT, QHT) and compared with the as-welded specimen. The comparison revealed that the samples after QHT had a significant improvement in the grain size and microstructure.
- Several temperatures were used in the QHT (860, 920, 1020,1120) ℃, as previously done in the welding specimens, after comparing among the temperatures, the structure at 860℃ showed the best uniformity in grains size. The hardness value also decreased in the HAZ to a similar level as the base.
- The effect of the optimum QHT of 860℃ and holding time of 8 hours on the microstructure and hardness was also analysed. The obvious HAZ disappeared and the microstructure appeared to be relatively homogeneous, possibly with the exception of the immediate layer next to the clad layer, where is maybe a little coarser. The result illustrates that the QHT design is again successful and has no detrimental effects on microstructure evolution of the base metal or on the clad layer or their connectivity.
- The results from the clad material analysis suggest that fabricating by welding followed by cladding and then followed by QHT is a feasible manufacturing route. This would limit the number of process routes needed, thus simplifying the method of manufacture and cost.

Chapter 7 / Recommendations for future work

The current study has demonstrated that the proposed method of fabrication of RPVs using RPEBW and laser cladding is feasible, but by no means has it proven it is viable. In this chapter, a number of potential recommendations for future research are suggested that may help this promising technology see fruition.

7.1 Welding process and its effect on the microstructure and mechanical properties

- More detailed investigation of austenite grain size and transformation product at every location within the weld. in the various places along the welding line, including the crown and root of the weld. The vast majority of the analysis undertaken here was from near the centre of the weld, which may not be representative of the whole through thickness of the weld.
- Conduct tests of heat treatment that simulates the actual heat treatment the conditions feasible inside the factory on a reactor pressure vessel, including realistic heating and cooling rates.
- Undertake a detailed study of the effect of welding process parameters, such as speed, intensity and feeding on the internal structure of the welding area. This also includes characterising to which extent these parameters effect the microstructure and mechanical properties of the welding region following QHT.
- Undertake a detailed mechanical property assessment in multiple directions of the weld, e.g. weld longitudinal, weld transverse for both tensile and Charpy. This will see if there is any anisotropy of the properties, which was not investigated here.
- Undertake detailed long-term tests at the standard operating temperatures of RPVs to investigate if the historic weld material microstructure is as stable as the standard forged material.

- Undertake a detailed investigation of residual stress generated as a consequence of welding and its reduction following QHT.

7.2 Laser Cladding of the nuclear pressure vessel

- Undertake a more detailed study the effect of laser cladding process parameters, such as speed, feeding and intensity on the cladding area, which consists of the base metal and heat-affected zone.
- Undertake a detailed full-scale mechanical property assessment of the clad layer and its HAZ. Clearly, hardness looks promising after QHT but until a detailed property analysis is undertaken there is no guarantee of high structural integrity.
- The possibility of using other types of stainless steel and comparing them in terms of microstructure and mechanical properties to improve the cladding area and make it more able to protect the internal surface of the reactor pressure vessel.
- Undertake detailed long-term tests at the standard operating temperatures of RPVs to investigate if the clad material microstructure is stable.
- Undertake detailed long-term corrosion tests at the standard operating temperatures of RPVs to investigate if the clad material is as stable compared to other methods of protection.

References

1- Yvon, P., Le Flem, M., Cabet, C. and Seran, J.L., 2015. Structural materials for next generation nuclear systems: Challenges and the path forward. *Nuclear Engineering and Design*, *294*, pp.161-169.

2- Yvon, P., Le Flem, M., Cabet, C. and Seran, J.L., 2014. Structural materials challenges for next generation nuclear systems: challenges and the path forward. In Proceedings of the international workshop on new horizons in nuclear reactor thermal hydraulics and safety.

3- Zinkle, S.J., Terrani, K.A. and Snead, L.L., 2016. Motivation for utilizing new high-performance advanced materials in nuclear energy systems. *Current Opinion in Solid State and Materials Science*, *20*(6), pp.401-410.

4- Semenov, B., Dastidar, P., Kupitz, J. and Goodjohn, A., 1989. Growth projections and development trends for nuclear power. Int. At. Energy Agency Bull, 31(3), pp.6-12.

5- Server, W.L. and Nanstad, R.K., 2015. Reactor pressure vessel (RPV) design and fabrication: the case of the USA. In Irradiation Embrittlement of Reactor Pressure Vessels (RPVs) in Nuclear Power Plants (pp. 3-25). Woodhead Publishing.

6- Yang, W.J., Lee, B.S., Oh, Y.J., Huh, M.Y. and Hong, J.H., 2004. Microstructural parameters governing cleavage fracture behaviors in the ductile–brittle transition region in reactor pressure vessel steels. Materials Science and Engineering: A, 379(1-2), pp.17-26.

7- Ayres, K.R., Hurrell, P.R., Gill, C.M., Bridger, K., Burling, L.D., Punshon, C.S., Wei, L. and Bagshaw, N., 2010, January. Development of reduced pressure electron beam welding process for thick section pressure vessel welds. In ASME 2010 Pressure Vessels and Piping Division/K-PVP Conference (pp. 39-48). American Society of Mechanical Engineers Digital Collection.

8- Baufeld, B., Priest, J. and Dutilleul, T., 2018. EBW of nuclear pressure vessel steel. Elektronika ir Elektrotechnika, 53, p.136.

9- J. W. Christian, The Theory of Transformations in Metals and Alloys, Oxford: A Pergamon, 2002.

10- W. D. Callister , “Phase Diagrams,” in Material Science and Engineering An Introduction, New York, John Wiley & Sons, 2007, p. 290.

11- Reed-Hill R, Abbaschian R (1991). Physical Metallurgy Principles (3rd ed.). Boston: PWS-Kent Publishing. ISBN 978-0-534-92173-6.

12- Lambers, H.G., Tschumak, S., Maier, H.J. and Canadinc, D., 2009. Role of austenitization and pre-deformation on the kinetics of the isothermal bainitic transformation. Metallurgical and Materials Transactions A, 40(6), pp.1355-1366.

13- G. R. Speich, V. A. Demarest and R. L. Miler, "Formation of Austenite During Intercritical Annealing of Dual-Phase Steels," Metallurgical Transactions A, vol. 12, no. 8, pp. 1419-1428, 1981.

14- N. C. Law and D. V. Edmonds, "The formation of austenite in a low-alloy steel," Metallurgical and Materials Transactions A, vol. 11, no. 1, pp. 33-46, 1980.

15- C. I. Garcia and A. J. DeArdo, "Formation of austenite in 1.5 pct Mn steels," Metallurgical Transactions A, vol. 12, no. 3, pp. 521-530, 1981.

16- D. Z. Yang, E. L. Brown, D. K. Matlock and G. Krauss, "Ferrite Recrystallization and Austenite Formation in Cold-Rolled Intercritically Annealed Steel," Metallurgical Transactions A, vol. 16, pp. 1385-1392, 1985.

17- D. S. Martín, T. d. Cock, A. García-Junceda, F. G. Caballero, C. Capdevila and C. G. de Andrés, "Effect of heating rate on reaustenitisation of low carbon niobium microalloyed steel," Materials Science and Technology, vol. 24, no. 3, pp. 266-272, 2008.

18- Thewlis, G., Whiteman, J.A. and Senogles, D.J., 1997. Dynamics of austenite to ferrite phase transformation in ferrous weld metals. Materials Science and Technology, 13(3), pp.257-274.

19- Galibois, A., Krishnadev, M.R. and Dube, A., 1979. Control of grain size and sub-structure in plain carbon and high strength low alloy (HSLA) steels—the problem and the prospect. Metallurgical Transactions A, 10(8), pp.985-995.

20- Harrison, P.L. and Farrar, R.A., 1981. Influence of oxygen-rich inclusions on the $\gamma \rightarrow \alpha$ phase transformation in high-strength low-alloy (HSLA) steel weld metals. Journal of Materials Science, 16(8), pp.2218-2226.

21- Esmailian, M., 2010. The effect of cooling rate and austenite grain size on the austenite to ferrite transformation temperature and different ferrite morphologies in microalloyed steels. Iranian Journal of Materials Science and Engineering, 7(1), pp.7-14.

22- Tomita, Y., 1994. Effect of continuous-cooling transformation structure on mechanical properties of 0.4 C-Cr-Mo-Ni steel. Journal of materials science, 29(6), pp.1612-1616.

23- Esmailian, M., 2010. The effect of cooling rate and austenite grain size on the austenite to ferrite transformation temperature and different ferrite morphologies in microalloyed steels. Iranian Journal of Materials Science and Engineering, 7(1), pp.7-14.

24- Babu, S.S. and Bhadeshia, H.K.D.H., 1990. Transition from bainite to acicular ferrite in reheated Fe–Cr–C weld deposits. Materials Science and Technology, 6(10), pp.1005-1020.
25- Cui, S., Cui, Y., Wan, J., Rong, Y. and Zhang, J., 2016. Grain size dependence of the martensite morphology–a phase-field study. Computational Materials Science, 121, pp.131-142.
26- Avallone, E., Baumeister, T. and Sadegh, A., 2006. Marks' Standard Handbook for Mechanical Engineers, 11/e (pp. 64-88). New York: McGraw-Hill.
27- Guimarães, J.R.C. and Rios, P.R., 2010. Martensite start temperature and the austenite grain-size. Journal of materials science, 45(4), pp.1074-1077.
28- Ashby, M.F. and Jones, D.R., 1986. Engineering Materials 2 (with corrections edition).
29- Yang, H.S. and Bhadeshia, H.K.D.H., 2009. Austenite grain size and the martensite-start temperature. Scripta materialia, 60(7), pp.493-495.
30- Heinze, C., Pittner, A., Rethmeier, M. and Babu, S.S., 2013. Dependency of martensite start temperature on prior austenite grain size and its influence on welding-induced residual stresses. Computational materials science, 69, pp.251-260.
31- Matsuoka, Y., Iwasaki, T., Nakada, N., Tsuchiyama, T. and Takaki, S., 2013. Effect of grain size on thermal and mechanical stability of austenite in metastable austenitic stainless steel. ISIJ international, 53(7), pp.1224-1230.
32- Takahashi, M. and Bhadeshia, H.K.D.H., 1990. Model for transition from upper to lower bainite. Materials Science and Technology, 6(7), pp.592-603.
33- Babu, S.S. and Bhadeshia, H.K.D.H., 1990. Transition from bainite to acicular ferrite in reheated Fe–Cr–C weld deposits. Materials Science and Technology, 6(10), pp.1005-1020.
34- Grong, O. and Matlock, D.K., 1986. Microstructural development in mild and low-alloy steel weld metals. International Metals Reviews, 31(1), pp.27-48.
35- PA, M., Chandra, T. and CR, K., 1996. Continuous cooling transformation behaviour of microalloyed steels containing Ti, Nb, Mn and Mo. ISIJ international, 36(12), pp.1486-1493.
36- Kim, S., Lee, S., Im, Y.R., Lee, H.C., Oh, Y.J. and Hong, J.H., 2001. Effects of alloying elements on mechanical and fracture properties of base metals and simulated heat-affected zones of SA 508 steels. Metallurgical and Materials Transactions A, 32(4), pp.903-911.
37- Im, Y.R., Oh, Y.J., Lee, B.J., Hong, J.H. and Lee, H.C., 2001. Effects of carbide precipitation on the strength and Charpy impact properties of low carbon Mn–Ni–Mo bainitic steels. Journal of nuclear materials, 297(2), pp.138-148.

38- Kim, S., Im, Y.R., Lee, S., Lee, H.C., Kim, S.J. and Hong, J.H., 2004. Effects of alloying elements on fracture toughness in the transition temperature region of base metals and simulated heat-affected zones of Mn-Mo-Ni low-alloy steels. Metallurgical and Materials Transactions A, 35(7), pp.2027-2037.

39- Shibata, K., Seo, S.J., Kaga, M., Uchino, H., Sasanuma, A., Asakura, K. and Nagasaki, C., 2002. Suppression of surface hot shortness due to Cu in recycled steels. Materials Transactions, 43(3), pp.292-300.

40- Torkar, M., 2010. Effect of trace and residual elements on the hot brittleness, hot shortness and properties of 0.15-0.3% C Al-killed steels with a solidification microstructure. MATERIALI IN TEHNOLOGIJE, 44(6), pp.327-333.

41- Sharma, C.P., 2003. Engineering materials: properties and applications of metals and alloys. PHI Learning Pvt. Ltd.

42- Kuksenko, V., Pareige, C. and Pareige, P., 2013. Cr precipitation in neutron irradiated industrial purity Fe–Cr model alloys. Journal of nuclear materials, 432(1-3), pp.160-165.

43- Zinkle, S.J. and Was, G.S., 2013. Materials challenges in nuclear energy. Acta Materialia, 61(3), pp.735-758.

44- Abram, T. and Ion, S., 2008. Generation-IV nuclear power: A review of the state of the science. Energy Policy, 36(12), pp.4323-4330.

45- Murty, K.L. and Charit, I., 2008. Structural materials for Gen-IV nuclear reactors: Challenges and opportunities. Journal of Nuclear Materials, 383(1-2), pp.189-195.

46- Zinkle, S.J. and Busby, J.T., 2009. Structural materials for fission & fusion energy. Materials today, 12(11), pp.12-19.

47- Davies, L.M., 1999. A comparison of western and eastern nuclear reactor pressure vessel steels. International journal of pressure vessels and piping, 76(3), pp.163-208.

48- Tanaka, Y. and Sato, I., 2011. Development of high purity large forgings for nuclear power plants. Journal of nuclear materials, 417(1-3), pp.854-859.

49- Talamantes-Silva, J., Bates, P., Al-Bermani, S., Davies, P., Hambleton, A. and Bunney, D., 2013, July. New Challenges in the Production of Ultra Large Forgings for the Manufacturing of Pressure Vessels. In ASME 2013 Pressure Vessels and Piping Conference. American Society of Mechanical Engineers Digital Collection.

50- S. Xu, X. Q. Wu, E. H. Han, and W. Ke, “Effects of dynamic strain aging on mechanical properties of SA508 class 3 reactor pressure vessel steel,” J. Mater. Sci., vol. 44, no. 11, pp. 2882–2889, 2009.

51- S. Kim, Y.-R. Im, S. Lee, H.-C. Lee, S.-J. Kim, and J. Hong, “Effects of alloying elements on fracture toughness in the transition temperature region of base metals and simulated heat-affected zones of Mn-Mo-Ni low-alloy steels,” Metall. Mater. Trans. A, vol. 35, no. 7, pp. 2027–2037, 2004.

52- Kim, J.T., Kwon, H.K., Chang, H.S. and Park, Y.W., 1997. Improvement of impact toughness of the SA 508 class 3 steel for nuclear pressure vessel through steel-making and heat-treatment practices. Nuclear engineering and design, 174(1), pp.51-58.

53- Kim, J.T., Kwon, H.K., Kim, K.C. and Kim, J.M., 1997. Improved mechanical properties of the A 508 class 3 steel for nuclear pressure vessel through steelmaking. In Steel Forgings: Second Volume. ASTM International.

54- Marini, B., Averty, X., Wident, P., Forget, P. and Barcelo, F., 2015. Effect of the bainitic and martensitic microstructures on the hardening and embrittlement under neutron irradiation of a reactor pressure vessel steel. Journal of Nuclear Materials, 465, pp.20-27.

55- Ahn, Y.S., Kim, H.D., Byun, T.S., Oh, Y.J., Kim, G.M. and Hong, J.H., 1999. Application of intercritical heat treatment to improve toughness of SA508 Cl. 3 reactor pressure vessel steel. Nuclear Engineering and Design, 194(2-3), pp.161-177.

56- Lee, S., Kim, S., Hwang, B., Lee, B.S. and Lee, C.G., 2002. Effect of carbide distribution on the fracture toughness in the transition temperature region of an SA 508 steel. Acta materialia, 50(19), pp.4755-4762.

57- E. J. Pickering and H. K. D. H. Bhadeshia, “Macrosegregation and microstructural evolution in a pressure-vessel steel,” Metall. Mater. Trans. A Phys. Metall. Mater. Sci., vol. 45, no. 7, pp. 2983–2997, 2014.

58- Pous-Romero, H., Lonardelli, I., Cogswell, D. and Bhadeshia, H.K.D.H., 2013. Austenite grain growth in a nuclear pressure vessel steel. Materials Science and Engineering: A, 567, pp.72-79.

59- K. Suzuki, I. Kurihara, Sasaki, Y. Koyoma, and Y. Tanakaca, “Application of high strength {M}n{M}o{N}i steel to pressure vessels for nuclear power plant,” Nucl. Eng. Des., vol. 206, pp. 261–278, 2001.

60- Kim, M.C., Park, S.G., Lee, K.H. and Lee, B.S., 2015. Comparison of fracture properties in SA508 Gr. 3 and Gr. 4N high strength low alloy steels for advanced pressure vessel materials. International Journal of Pressure Vessels and Piping, 131, pp.60-66.

61- D. XIA, C. ZHOU, Y. LIU, J. WANG, C. FU, K. WANG, and M. LI, “Mechanical Properties and Corrosion Resistance of SA508-4 Low Carbon Alloy Steel,” Electrochemistry, vol. 81, no. 4, pp. 262–268, 2013.

62- Park, S.G., Lee, K.H., Min, K.D., Kim, M.C. and Lee, B.S., 2013. Characterization of phase fractions and misorientations on tempered Bainitic/Martensitic Ni-Cr-Mo low alloy RPV steel with various Ni content. Metals and Materials International, 19(1), pp.49-54.

63- B. S. Lee, M. C. Kim, J. H. Yoon, and J. H. Hong, "Characterization of high strength and high toughness Ni-Mo-Cr low alloy steels for nuclear application," Int. J. Press. Vessel. Pip., vol. 87, no. 1, pp. 74–80, 2010.

64- Lee, K.H., Kim, M.C., Lee, B.S. and Wee, D.M., 2010. Master curve characterization of the fracture toughness behavior in SA508 Gr. 4N low alloy steels. Journal of nuclear materials, 403(1-3), pp.68-74.

65- Park, S.G., Lee, K.H., Min, K.D., Kim, M.C. and Lee, B.S., 2012. Influence of the thermodynamic parameters on the temper embrittlement of SA508 Gr. 4N Ni–Cr–Mo low alloy steel with variation of Ni, Cr and Mn contents. Journal of nuclear materials, 426(1-3), pp.1-8.

66- Ko, J.L., Kim, M.C., Lee, B.S. and Kim, G.M., 2006. Microstructural changes in SA508 Gr. 4N pressure vessel steel with heat treatment conditions. Transactions of the Korean Nuclear Soc.

67- Yang, Z., Liu, Z., He, X., Qiao, S. and Xie, C., 2018. Effect of microstructure on the impact toughness and temper embrittlement of SA508Gr. 4N steel for advanced pressure vessel materials. Scientific reports, 8(1), pp.1-12.

68- Sanderson, A., Punshon, C.S. and Russell, J.D., 2000. Advanced welding processes for fusion reactor fabrication. Fusion engineering and design, 49, pp.77-87.

69- Rai, R., Palmer, T.A., Elmer, J.W. and Debroy, T., 2009. Heat transfer and fluid flow during electron beam welding of 304L stainless steel alloy. Weld. J, 88(3), pp.54-61.

70- Ahmed, N. ed., 2005. New developments in advanced welding. Elsevier.

71- Norrish, J., 2006. Advanced welding processes. Elsevier.

72- Klemens, P.G., 1976. Heat balance and flow conditions for electron beam and laser welding. Journal of Applied physics, 47(5), pp.2165-2174.

73- Schultz, H., 1993. Electron beam welding (Vol. 93). Woodhead Publishing.

74- Askeland, D.R. and Wright, W.J., 2013. Essentials of materials science & engineering. Cengage Learning.

75- Lienert, T., Siewert, T., Babu, S. and Acoff, V., 2011. Fundamentals of weld solidification. ASM Handbook 6a, pp.96-114.

76- Kou, S., 2003. Welding metallurgy. New Jersey, USA, pp.431-446.

77- Inoue, H. and Koseki, T., 2007. Clarification of solidification behaviors in austenitic stainless steels based on welding process. Nippon Steel Technical Report, 95, pp.62-70.
78- Askeland, D.R., Fulay, P.P. and Wright, W.J., 2010. The science and engineering of materials 6th edition. Thomson learning Inc, pp.232-250.
79- Hunziker, O., Dye, D. and Reed, R.C., 2000. On the formation of a centreline grain boundary during fusion welding. Acta Materialia, 48(17), pp.4191-4201.
80- Dye, D., Hunziker, O. and Reed, R.C., 2001. Numerical analysis of the weldability of superalloys. Acta materialia, 49(4), pp.683-697.
81- Cui, L., Li, X., He, D., Chen, L. and Gong, S., 2012. Effect of Nd: YAG laser welding on microstructure and hardness of an Al–Li based alloy. Materials characterization, 71, pp.95-102.
82- Kurz, W., Bezencon, C. and Gäumann, M., 2001. Columnar to equiaxed transition in solidification processing. Science and technology of advanced materials, 2(1), p.185.
83- Wang, F., Williams, S., Colegrove, P. and Antonysamy, A.A., 2013. Microstructure and mechanical properties of wire and arc additive manufactured Ti-6Al-4V. Metallurgical and materials transactions A, 44(2), pp.968-977.
84- KATO, M., MATSUDA, F. and SENDA, T., 1972. Solidification mode in aluminum weld metal. Transactions of the Japan Welding Society, 3(1), pp.69-76.
85- Hemmati, I., Ocelik, V. and De Hosson, J.T.M., 2011. Microstructural characterization of AISI 431 martensitic stainless-steel laser-deposited coatings. Journal of materials science, 46(10), pp.3405-3414.
86- Tanaka, Y. and Sato, I., 2011. Development of high purity large forgings for nuclear power plants. Journal of nuclear materials, 417(1-3), pp.854-859.
87- Debnath, K. and Singh, I., 2017. Primary and Secondary Manufacturing of Polymer Matrix Composites. CRC Press.
88- Suzuki, K., Sato, I. and Tsukada, H., 1994. Manufacturing and material properties of ultralarge size forgings for advanced BWRPV. Nuclear engineering and design, 151(2-3), pp.513-522.
89- Kim, S., Lee, S., Im, Y.R., Lee, H.C., Oh, Y.J. and Hong, J.H., 2001. Effects of alloying elements on mechanical and fracture properties of base metals and simulated heat-affected zones of SA 508 steels. Metallurgical and Materials Transactions A, 32(4), pp.903-911.
90- Kim, S., Kang, S.Y., Lee, S., Oh, S.J., Kwon, S.J., Kim, O.H. and Hong, J.H., 2000. Correlation of the microstructure and fracture toughness of the heat-affected zones of an SA 508 steel. Metallurgical and Materials Transactions A, 31(4), pp.1107-1119.

91- Hong, J.W., Kim, H.D., Ahn, Y.S., Byun, T.S. and Kuk, I.H., Korea Atomic Energy Research Institute (KAERI) and Korea Electric Power Corp, 2001. Intercritical heat treatment process for toughness improvement of SA 508 GR. 3 steel. U.S. Patent 6,264,770.

92- Kim, S., Im, Y.R., Lee, S., Lee, H.C., Kim, S.J. and Hong, J.H., 2004. Effects of alloying elements on fracture toughness in the transition temperature region of base metals and simulated heat-affected zones of Mn-Mo-Ni low-alloy steels. Metallurgical and Materials Transactions A, 35(7), pp.2027-2037.

93- Francis, J.A., Bhadeshia, H.K.D.H. and Withers, P.J., 2007. Welding residual stresses in ferritic power plant steels. Materials Science and technology, 23(9), pp.1009-1020.

94- Seifert, H.P. and Ritter, S., 2008. Corrosion fatigue crack growth behaviour of low-alloy reactor pressure vessel steels under boiling water reactor conditions. Corrosion science, 50(7), pp.1884-1899.

95- Xu, S., Wu, X.Q., Han, E.H. and Ke, W., 2009. Effects of dynamic strain aging on mechanical properties of SA508 class 3 reactor pressure vessel steel. Journal of materials science, 44(11), pp.2882-2889.

96- Fukuoka, C., Nakagawa, Y.G., Lance, J.J. and Pangborn, R.N., 1997. Conditioning monitoring by microstructural evaluation of cumulative fatigue damage. International Journal of Fatigue, 10(19), p.736.

97- Kwon, S.J., Oh, S.J., Kim, S., Lee, S. and Kim, J.H., 1998. Mössbauer analysis of heat affected zones of a SA 508 steel weld. Scripta materialia, 40(2).

98- Haverkamp, K.D., Forch, K., Piehl, K.H. and Witte, W., 1984. Effect of heat treatment and precipitation state on toughness of heavy section Mn-Mo-Ni-steel for nuclear power plants components. Nuclear engineering and design, 81(2), pp.207-217.

99- Li, C., Han, L., Yan, G., Liu, Q., Luo, X. and Gu, J., 2016. Time-dependent temper embrittlement of reactor pressure vessel steel: Correlation between microstructural evolution and mechanical properties during tempering at 650° C. Journal of Nuclear Materials, 480, pp.344-354.

100- Li, C.W., Han, L.Z., Luo, X.M., Liu, Q.D. and Gu, J.F., 2016. Effect of tempering temperature on the microstructure and mechanical properties of a reactor pressure vessel steel. Journal of Nuclear Materials, 477, pp.246-256.

101- Yu, M., Luo, Z. and Chao, Y.J., 2015. Correlations between Charpy V-notch impact energy and fracture toughness of nuclear reactor pressure vessel (RPV) steels. Engineering Fracture Mechanics, 147, pp.187-202.

102- Ghosh, A., Sahoo, S., Ghosh, M., Ghosh, R.N. and Chakrabarti, D., 2014. Effect of microstructural parameters, microtexture and matrix strain on the Charpy impact properties of low carbon HSLA steel containing MnS inclusions. Materials Science and Engineering: A, 613, pp.37-47.

103- Rossoll, A., Berdin, C., Forget, P., Prioul, C. and Marini, B., 1999. Mechanical aspects of the Charpy impact test. Nuclear engineering and design, 188(2), pp.217-229.

104- Haušild, P., Berdin, C. and Bompard, P., 2005. Prediction of cleavage fracture for a low-alloy steel in the ductile-to-brittle transition temperature range. Materials Science and Engineering: A, 391(1), pp.188-197.

105- Kim, M.C., Lee, K.H., Lee, B.S. and Kim, W.W., 2010, January. Mechanical properties of SA508 Gr. 4N model alloys as a high strength RPV Steel. In ASME 2010 Pressure Vessels and Piping Division/K-PVP Conference (pp. 143-148). American Society of Mechanical Engineers Digital Collection.

106- Lee, B.S., Kim, M.C., Yoon, J.H. and Hong, J.H., 2010. Characterization of high strength and high toughness Ni–Mo–Cr low alloy steels for nuclear application. International journal of Pressure Vessels and piping, 87(1), pp.74-80.

107- Kim, S., Kang, S.Y., Lee, S., Oh, S.J., Kwon, S.J., Kim, O.H. and Hong, J.H., 2000. Correlation of the microstructure and fracture toughness of the heat-affected zones of an SA 508 steel. Metallurgical and Materials Transactions A, 31(4), pp.1107-1119.

108- D. R. A. a. P. P. Fulay, Essentials of Materials Science and Engineering, Second ed. USA: Cengage Learning, 2010.

109- Leffler, B., 1996. Stainless steels and their properties. AvestaPolarit AB, pp.1-45.

110- Krauss, G., 2015. Steels: processing, structure, and performance. Asm International.

111- Elmesalamy, A., 2013. Narrow gap laser welding of 316L stainless steel for potential application in the manufacture of thick section nuclear components (Doctoral dissertation, The University of Manchester (United Kingdom)).

112- Callister, W.D. and Rethwisch, D.G., 2007. The structure of crystalline solids. Materials science and engineering: an intr oduction. New York: John Wiley & Sons, Inc, pp.38-79.

113- Sundgren, J.E., Bodö, P. and Lundström, I., 1986. Auger electron spectroscopic studies of the interface between human tissue and implants of titanium and stainless steel. Journal of Colloid and Interface Science, 110(1), pp.9-20.

114- Ahmed, N. ed., 2005. New developments in advanced welding. Elsevier.

115- Elmer, J.W., Allen, S.M. and Eagar, T.W., 1989. Microstructural development during solidification of stainless steel alloys. Metallurgical transactions A, 20(10), pp.2117-2131.

116- Shimada, M., Kokawa, H., Wang, Z.J., Sato, Y.S. and Karibe, I., 2002. Optimization of grain boundary character distribution for intergranular corrosion resistant 304 stainless steel by twin-induced grain boundary engineering. Acta Materialia, 50(9), pp.2331-2341.

117- J. R. Davis, Stainless Steels. USA: ASM International, 1999.

118- Borgioli, F., Galvanetto, E. and Bacci, T., 2016. Low temperature nitriding of AISI 300 and 200 series austenitic stainless steels. Vacuum, 127, pp.51-60.

119- Souza Filho, I.R., Sandim, M.J.R., Cohen, R., Nagamine, L.C.C.M., Hoffmann, J., Bolmaro, R.E. and Sandim, H.R.Z., 2016. Effects of strain-induced martensite and its reversion on the magnetic properties of AISI 201 austenitic stainless steel. Journal of Magnetism and Magnetic Materials, 419, pp.156-165.

120- Souza Filho, I.R., Sandim, M.J.R., Cohen, R., Nagamine, L.C.C.M., Hoffmann, J., Bolmaro, R.E. and Sandim, H.R.Z., 2016. Effects of strain-induced martensite and its reversion on the magnetic properties of AISI 201 austenitic stainless steel. Journal of Magnetism and Magnetic Materials, 419, pp.156-165.

121- Parvathavarthini, N., Dayal, R.K., Khatak, H.S., Shankar, V. and Shanmugam, V., 2006. Sensitization behaviour of modified 316N and 316L stainless steel weld metals after complex annealing and stress relieving cycles. Journal of nuclear materials, 355(1-3), pp.68-82.

122- Lippold, J.C., 2015. Welding metallurgy and weldability. John Wiley & Sons Incorporated.

123- Kim, J.H., Kim, S.K., Lee, C.S., Kim, M.H. and Lee, J.M., 2014. A constitutive equation for predicting the material nonlinear behavior of AISI 316L, 321, and 347 stainless steel under low-temperature conditions. International Journal of Mechanical Sciences, 87, pp.218-225.

124- Shimada, M., Kokawa, H., Wang, Z.J., Sato, Y.S. and Karibe, I., 2002. Optimization of grain boundary character distribution for intergranular corrosion resistant 304 stainless steel by twin-induced grain boundary engineering. Acta Materialia, 50(9), pp.2331-2341.

125- Yanushkevich, Z., Mogucheva, A., Tikhonova, M., Belyakov, A. and Kaibyshev, R., 2011. Structural strengthening of an austenitic stainless steel subjected to warm-to-hot working. Materials characterization, 62(4), pp.432-437.

126- Shakhova, I., Belyakov, A., Yanushkevich, Z., Tsuzaki, K. and Kaibyshev, R., 2016. On strengthening of austenitic stainless steel by large strain cold working. isij international, pp.ISIJINT-2016.

127- Tikhonova, M., Kaibyshev, R., Fang, X., Wang, W. and Belyakov, A., 2012. Grain boundary assembles developed in an austenitic stainless steel during large strain warm working. Materials characterization, 70, pp.14-20.

128- Idell, Y., Facco, G., Kulovits, A., Shankar, M.R. and Wiezorek, J.M.K., 2013. Strengthening of austenitic stainless steel by formation of nanocrystalline γ-phase through severe plastic deformation during two-dimensional linear plane-strain machining. Scripta materialia, 68(9), pp.667-670.

129- Lippold, J.C. and Kotecki, D.J., 2005. Welding metallurgy and weldability of stainless steels (p. 376).Ferrandini, P.L., Rios, C.T., Dutra, A.T., Jaime, M.A., Mei, P.R. and Caram, R., 2006. Solute segregation and microstructure of directionally solidified austenitic stainless steel. Materials Science and Engineering: A, 435, pp.139-144.

130- Ocelík, V., Eekma, M., Hemmati, I. and De Hosson, J.T.M., 2012. Elimination of Start/Stop defects in laser cladding. Surface and Coatings Technology, 206(8-9), pp.2403-2409.

131- Sexton, L., Lavin, S., Byrne, G. and Kennedy, A., 2002. Laser cladding of aerospace materials. Journal of Materials Processing Technology, 122(1), pp.63-68.

132- Lee, H.K., 2008. Effects of the cladding parameters on the deposition efficiency in pulsed Nd: YAG laser cladding. Journal of materials processing technology, 202(1-3), pp.321-327.

133- Liu, H., Wang, C., Zhang, X., Jiang, Y., Cai, C. and Tang, S., 2013. Improving the corrosion resistance and mechanical property of 45 steel surface by laser cladding with Ni60CuMoW alloy powder. Surface and Coatings Technology, 228, pp.S296-S300.

134- Xiong, Z., Chen, G.X. and Zeng, X.Y., 2009. Effects of process variables on interfacial quality of laser cladding on aeroengine blade material GH4133. Journal of materials processing technology, 209(2), pp.930-936.

135- Sun, S., Liu, Q., Brandt, M., Janardhana, M. and Clark, G., 2012. Microstructure and mechanical properties of laser cladding repair of AISI 4340 steel. In 28th international congress of the aeronautical sciences (pp. 1-9). Optimage.

136- Aghasibeig, M. and Fredriksson, H., 2012. Laser cladding of a featureless iron-based alloy. Surface and Coatings Technology, 209, pp.32-37.

137- Xu, P., Lin, C., Zhou, C. and Yi, X., 2014. Wear and corrosion resistance of laser cladding AISI 304 stainless steel/Al2O3 composite coatings. Surface and Coatings Technology, 238, pp.9-14.

138- Li, K., Li, D., Liu, D., Pei, G. and Sun, L., 2015. Microstructure evolution and mechanical properties of multiple-layer laser cladding coating of 308L stainless steel. Applied surface science, 340, pp.143-150.

139- Zeng, C., Tian, W., Liao, W.H. and Hua, L., 2013. Study of laser cladding thermal damage: A quantified microhardness method. Surface and Coatings Technology, 236, pp.309-314.

140- Gao, W., Zhao, S., Liu, F., Wang, Y., Zhou, C. and Lin, X., 2014. Effect of defocus manner on laser cladding of Fe-based alloy powder. Surface and Coatings Technology, 248, pp.54-62.

141- Barnes, S., Timms, N., Bryden, B. and Pashby, I., 2003. High power diode laser cladding. Journal of materials processing technology, 138(1-3), pp.411-416.

142- Emamian, A., Alimardani, M. and Khajepour, A., 2012. Correlation between temperature distribution and in situ formed microstructure of Fe–TiC deposited on carbon steel using laser cladding. Applied Surface Science, 258(22), pp.9025-9031.

143- Wu, X. and Hong, Y., 2001. Fe-based thick amorphous-alloy coating by laser cladding. Surface and Coatings Technology, 141(2-3), pp.141-144.

144- Kaierle, S., Barroi, A., Noelke, C., Hermsdorf, J., Overmeyer, L. and Haferkamp, H., 2012. Review on laser deposition welding: from micro to macro. Physics Procedia, 39, pp.336-345.

145- Pous-Romero, H. and Bhadeshia, H., 2014. Coalesced martensite in pressure vessel steels. Journal of Pressure Vessel Technology, 136(3).

146- American Society for Testing and Materials. Committee A-01 on Steel, Stainless Steel and Related Alloys, 2017. Standard test methods and definitions for mechanical testing of steel products. ASTM International.

147- Baufeld, B., Priest, J. and Dutilleul, T., 2018. EBW of nuclear pressure vessel steel. Elektronika ir Elektrotechnika, 53, p.136.

148- Bai, X., Wu, S. and Liaw, P.K., 2016. Influence of thermo-mechanical embrittlement processing on microstructure and mechanical behavior of a pressure vessel steel. Materials & Design, 89, pp.759-769.

149- Olabi, A.G. and Hashmi, M.S.J., 1996. The microstructure and mechanical properties of low carbon steel welded components after the application of PWHTs. Journal of materials processing technology, 56(1-4), pp.88-97.

150- Xia, D., Zhou, C., Liu, Y., Wang, J., Fu, C., Wang, K. and Li, M., 2013. Mechanical properties and corrosion resistance of SA508-4 low carbon alloy steel. Electrochemistry, 81(4), pp.262-268.

151- Park, S.G., Kim, M.C., Lee, B.S. and Wee, D.M., 2010. Correlation of the thermodynamic calculation and the experimental observation of Ni–Mo–Cr low alloy steel changing Ni, Mo, and Cr contents. Journal of nuclear materials, 407(2), pp.126-135.

152- Guo, W., Dong, S., Francis, J.A. and Li, L., 2015. Microstructure and mechanical characteristics of a laser welded joint in SA508 nuclear pressure vessel steel. Materials Science and Engineering: A, 625, pp.65-80.

153- Kryukov, A., Debarberis, L., Von Estorff, U., Gillemot, F. and Oszvald, F., 2012. Irradiation embrittlement of reactor pressure vessel steel at very high neutron fluence. Journal of nuclear materials, 422(1-3), pp.173-177.

154- Lee, B.J., Kim, H.D. and Hong, J.H., 1998. Calculation of α/γ equilibria in SA508 grade 3 steels for intercritical heat treatment. Metallurgical and Materials Transactions A, 29(5), pp.1441-1447.

Appendix - HAZ & Clad Thickness for all Samples

Table: Samples specifications.

Sample No.	Clad Thickness	HAZ Thickness	Laser power [W]	Powder feed rate [g/min]
1	931.993 µm	1476.213 µm	5500	34
3	1022.797 µm	1371.655 µm	5000	34
4	1500 µm	1298.864 µm	4500	34
5	1509.17 µm	1226.183 µm	4000	34
6	1346.591 µm	1184.091 µm	3500	34
7	990.909 µm	1460.227 µm	5500	40
8	1585.606 µm	1440.909 µm	5500	40
9	1594.318 µm	1317.046 µm	5000	40
10	1543.199 µm	1297.782 µm	4500	40
11	1509.091 µm	1132.955 µm	4000	40
12	1364.781 µm	1111.399 µm	3500	40
17	1365.909 µm	1119.318 µm	3400	40
18	1418.205 µm	1132.97 µm	3300	40
19	1371.645 µm	1092.065 µm	3200	40
20	1296.666 µm	1057.22 µm	3100	40
32	1360.227 µm	1084.091 µm	3500	40
35	1426.136 µm	1086.364 µm	3500	40
36	1427.273 µm	1057.954 µm	3650	40
37	1465.909 µm	1081.818 µm	3750	40
38	1462.5 µm	1130.682 µm	3850	40

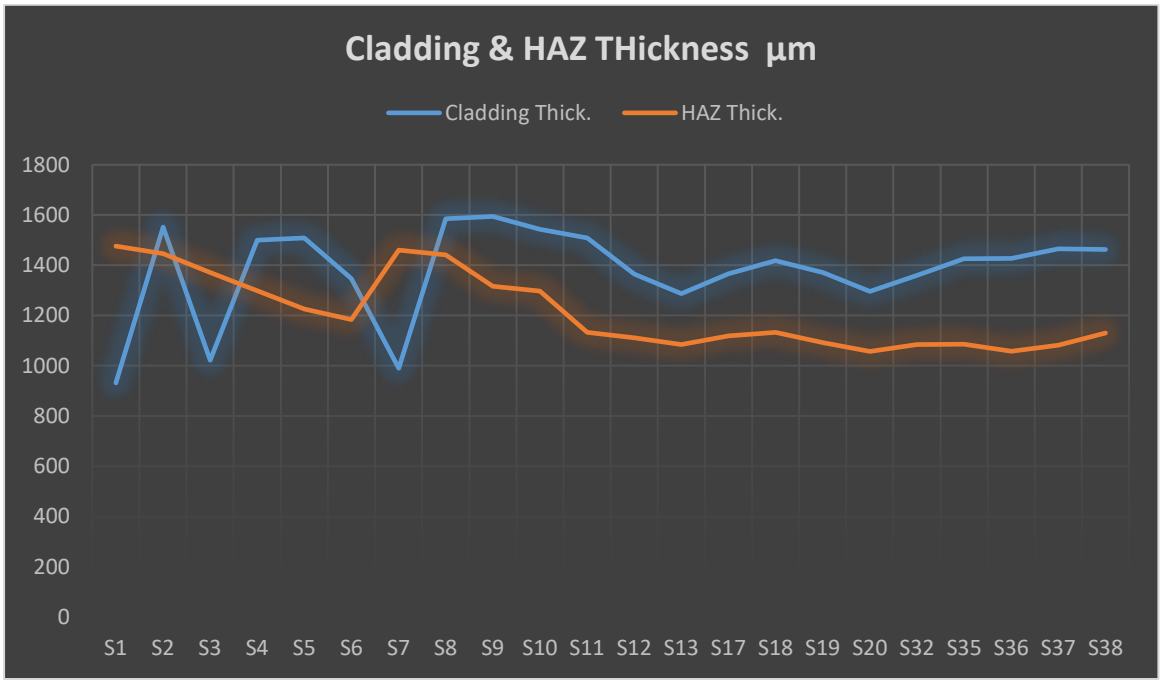

Figure: Diagram for Cladding and HAZ Thickness

Figure: Image Sample 1

Table: Parameters Sample 1

NI 319 - Forgmasters cladding - Parameters							
No. of sample	Laser power [W]	Speed of cladding [mm/min]	Powder feed rate [g/min]	Carrier gas flow [l/min]	Purge gas flow [l/min]	Offset [mm]	Number of Line
1	5500	1000	34	10	20	0.0	1

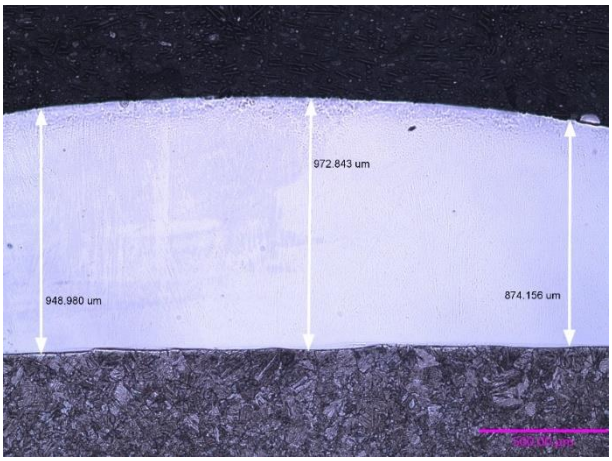

(a) Cladding Image

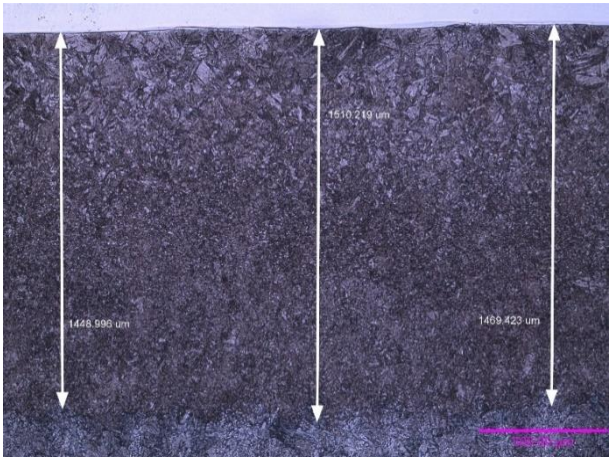

(b) HAZ Image

Figure: Image Thickness Sample 1 (a) Cladding (b) HAZ

Average of cladding thickness No. 1= 931.993 µm

Average of HAZ thickness No. 1= 1476.213 µm

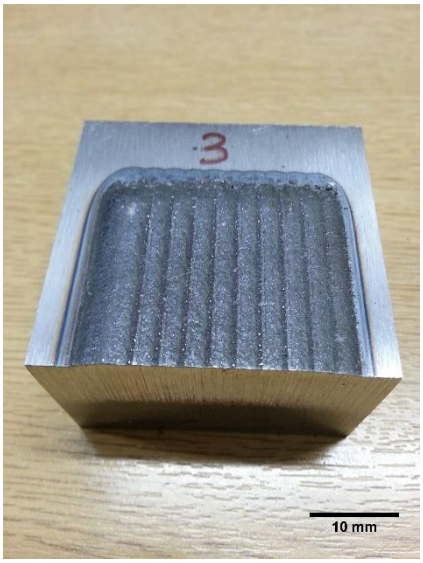

Figure: Image Sample 3

Table: Parameters Sample 3

NI 319 - Forgmasters cladding - Parameters							
No. of sample	Laser power [W]	Speed of cladding [mm/min]	Powder feed rate [g/min]	Carrier gas flow [l/min]	Purge gas flow [l/min]	Offset [mm]	Number of Line
3	5000	1000	34	10	20	3.2	10

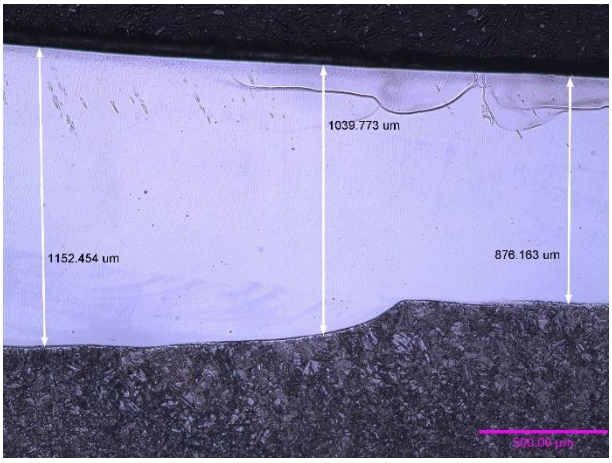

(a) Cladding Image

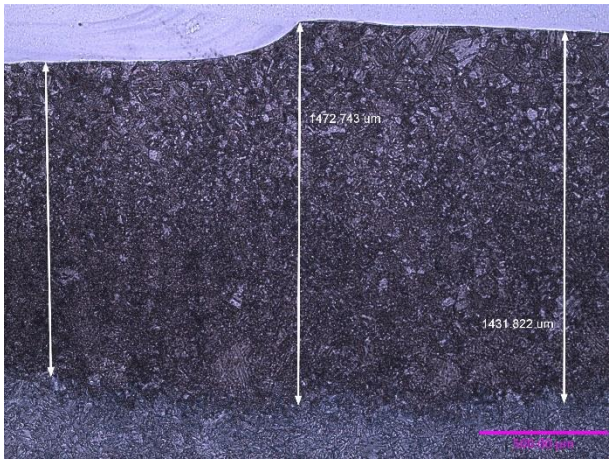

(b) HAZ Image

Figure: Image Thickness Sample 3 (a) Cladding (b) HAZ

Average of cladding thickness No. 3= 1022.797 µm

Average of HAZ thickness No. 3= 1371.655 µm

Figure: Image Sample 4

Table: Parameters Sample 4

NI 319 - Forgmasters cladding - Parameters							
No. of sample	Laser power [W]	Speed of cladding [mm/min]	Powder feed rate [g/min]	Carrier gas flow [l/min]	Purge gas flow [l/min]	Offset [mm]	Number of Line
4	4500	1000	34	10	20	3.2	10

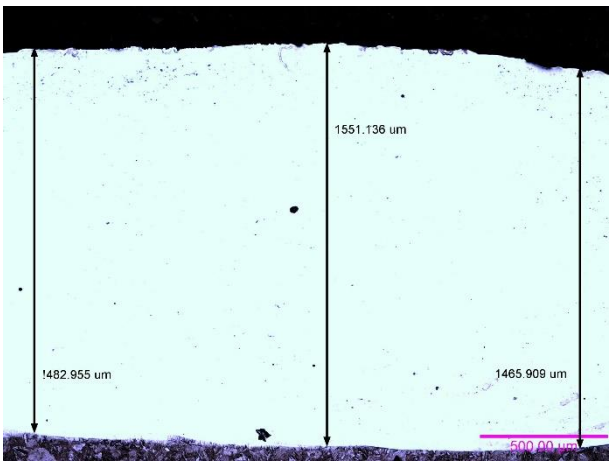

(a) Cladding Image

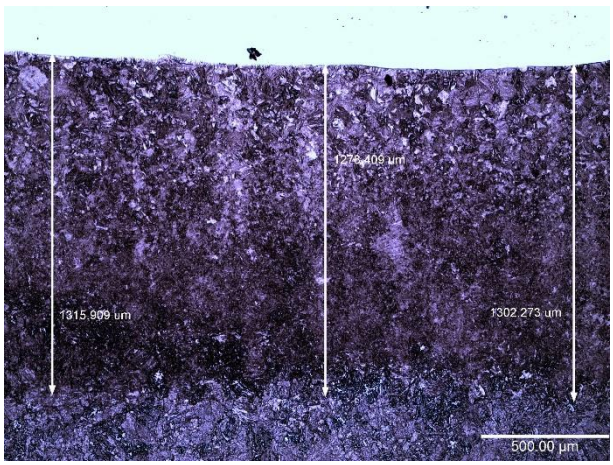

(b) HAZ Image

Figure: Image Thickness Sample 4 (a) Cladding (b) HAZ

Average of cladding thickness No. 4= 1500 µm

Average of HAZ thickness No. 4= 1298.864 µm

Figure: Image Sample 5

Table: Parameters Sample5

NI 319 - Forgmasters cladding - Parameters							
No. of sample	Laser power [W]	Speed of cladding [mm/min]	Powder feed rate [g/min]	Carrier gas flow [l/min]	Purge gas flow [l/min]	Offset [mm]	Number of Line
5	4000	1000	34	10	20	3.2	10

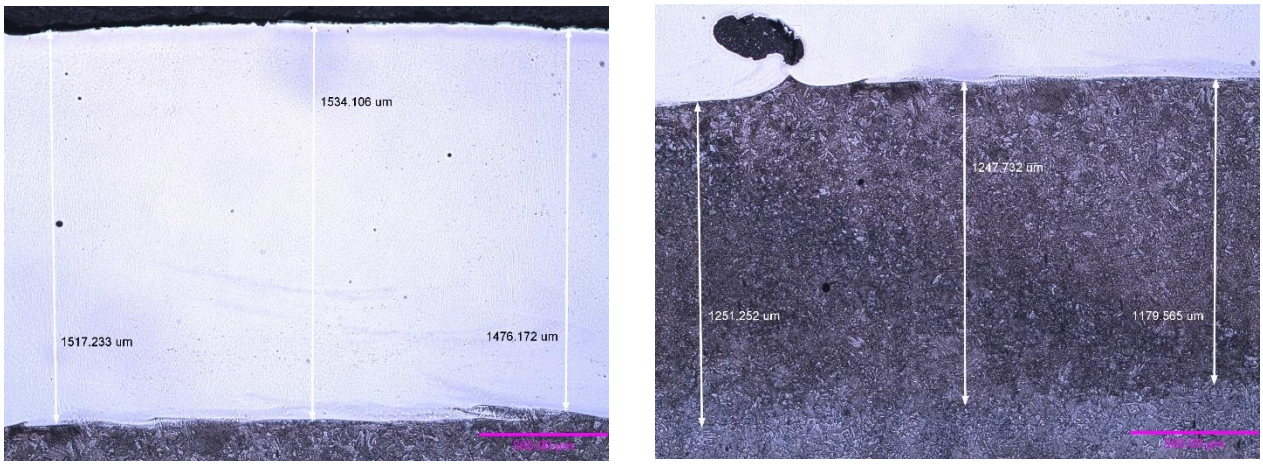

(a) Cladding Image (b) HAZ Image

Figure: Image Thickness Sample 5 (a) Cladding (b) HAZ

Average of cladding thickness No. 5= 1509.17 µm

Average of HAZ thickness No. 5= 1226.183 µm

Figure: Image Sample 6

Table: Parameters Sample 6

NI 319 - Forgmasters cladding - Parameters							
No. of sample	Laser power [W]	Speed of cladding [mm/min]	Powder feed rate [g/min]	Carrier gas flow [l/min]	Purge gas flow [l/min]	Offset [mm]	Number of Line
6	3500	1000	34	10	20	3.2	10

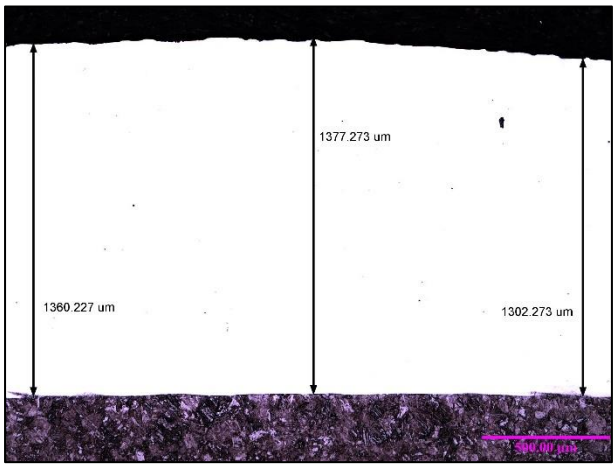

(a) Cladding Image

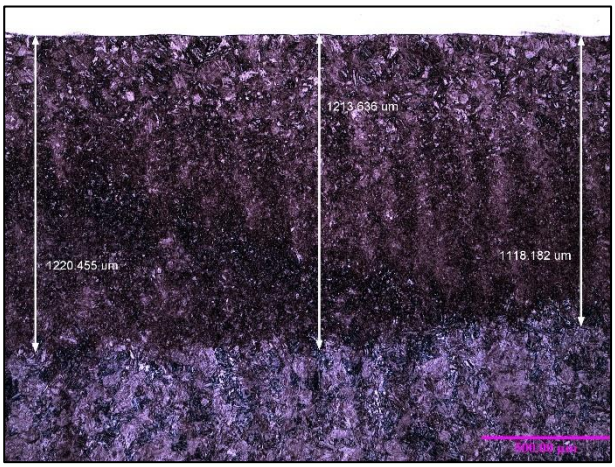

(b) HAZ Image

Figure: Image Thickness Sample 6 (a) Cladding (b) HAZ

Average of cladding thickness No. 6= 1346.591 µm

Average of HAZ thickness No. 6= 1184.091 µm

Figure: Image Sample 7

Table: Parameters Sample7

NI 319 - Forgmasters cladding - Parameters							
No. of sample	Laser power [W]	Speed of cladding [mm/min]	Powder feed rate [g/min]	Carrier gas flow [l/min]	Purge gas flow [l/min]	Offset [mm]	Number of Line
7	5500	1000	40	10	20	0.0	1

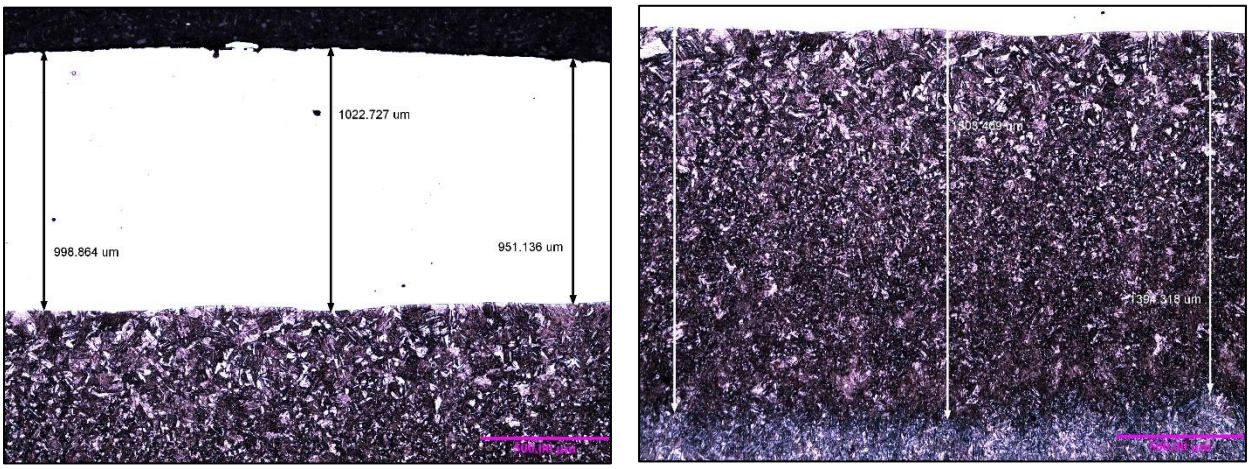

(a) Cladding Image (b) HAZ Image

Figure: Image Thickness Sample 7 (a) Cladding (b) HAZ

Average of cladding thickness No. 7= 990.909 µm

Average of HAZ thickness No. 7= 1460.227 µm

Figure: Image Sample 8

Table: Parameters Sample 8

NI 319 - Forgmasters cladding - Parameters							
No. of sample	Laser power [W]	Speed of cladding [mm/min]	Powder feed rate [g/min]	Carrier gas flow [l/min]	Purge gas flow [l/min]	Offset [mm]	Number of Line
8	5500	1000	40	10	20	3.3	10

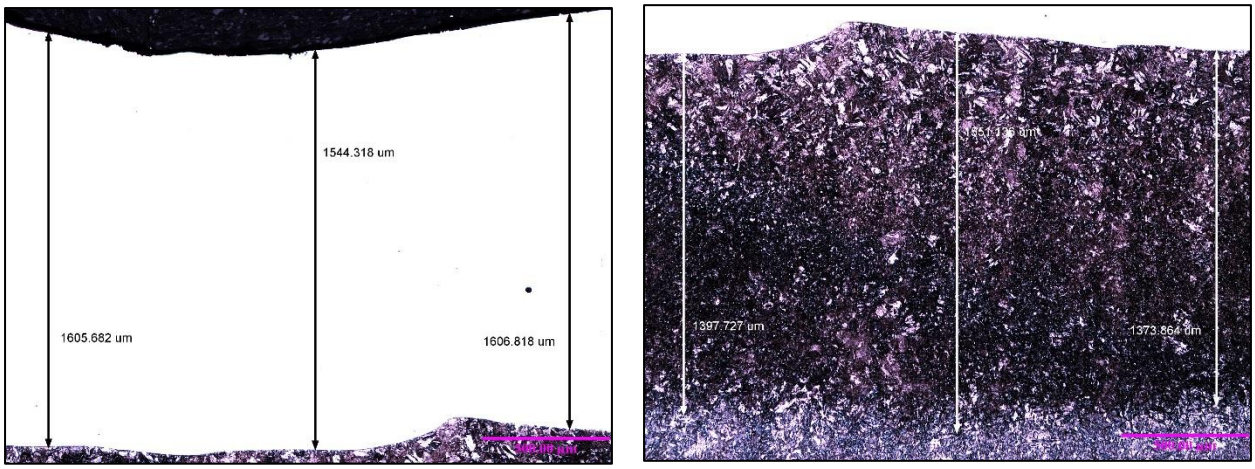

(a) Cladding Image (b) HAZ Image

Figure: Image Thickness Sample 8 (a) Cladding (b) HAZ

Average of cladding thickness No. 8=1585.606 µm

Average of HAZ thickness No. 8= 1440.909 µm

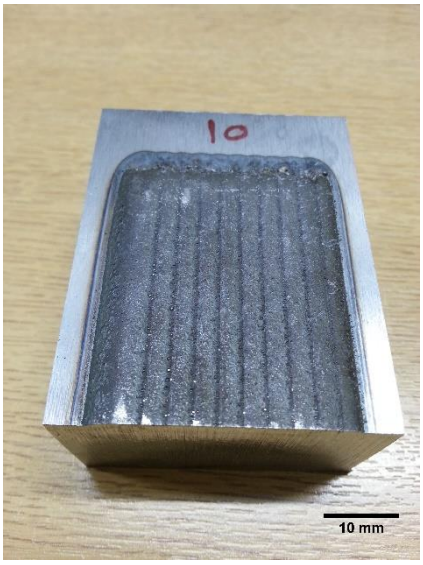

Figure: Image Sample 10

Table: Parameters Sample 10

NI 319 - Forgmasters cladding - Parameters							
No. of sample	Laser power [W]	Speed of cladding [mm/min]	Powder feed rate [g/min]	Carrier gas flow [l/min]	Purge gas flow [l/min]	Offset [mm]	Number of Line
10	4500	1000	40	10	20	3.3	10

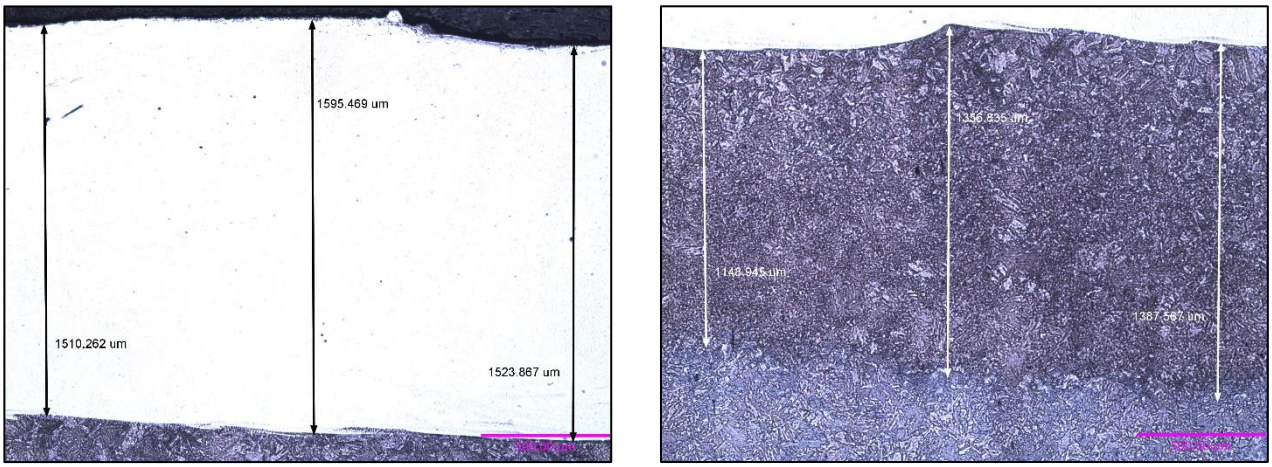

(a) Cladding Image (b) HAZ Image

Figure: Image Thickness Sample 10 (a) Cladding (b) HAZ

Average of cladding thickness No. 10= 1543.199 µm

Average of HAZ thickness No. 10= 1297.782 µm

Figure: Image Sample 11

Table: Parameters Sample 11

NI 319 - Forgmasters cladding - Parameters							
No. of sample	Laser power [W]	Speed of cladding [mm/min]	Powder feed rate [g/min]	Carrier gas flow [l/min]	Purge gas flow [l/min]	Offset [mm]	Number of Line
11	4000	1000	40	10	20	3.3	10

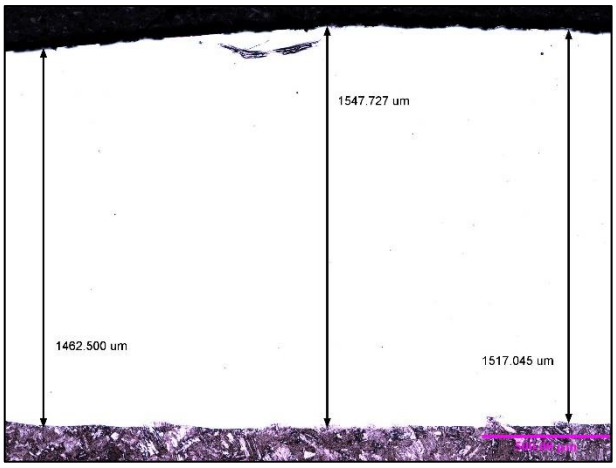

(a) Cladding Image

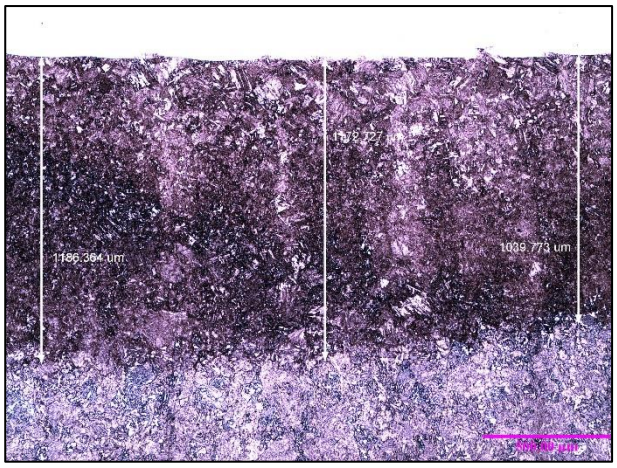

(b) HAZ Image

Figure: Image Thickness Sample 11 (a) Cladding (b) HAZ

Average of cladding thickness No. 11= 1509.091 µm

Average of HAZ thickness No. 11= 1132.955 µm

Figure: Image Sample 12

Table: Parameters Sample 12

NI 319 - Forgmasters cladding - Parameters							
No. of sample	Laser power [W]	Speed of cladding [mm/min]	Powder feed rate [g/min]	Carrier gas flow [l/min]	Purge gas flow [l/min]	Offset [mm]	Number of Line
12	3500	1000	40	10	20	3.3	12

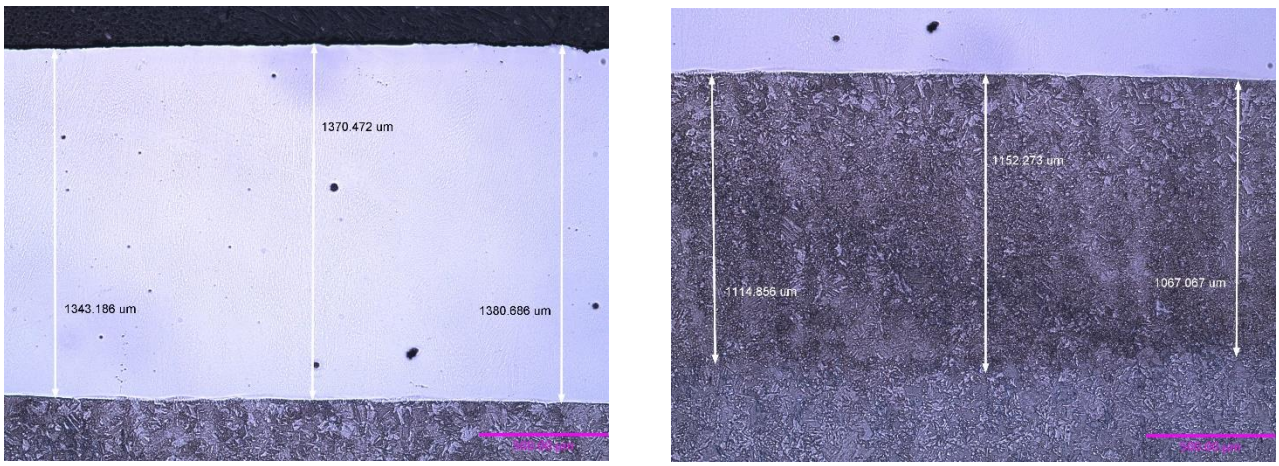

(a) Cladding Image (b) HAZ Image

Figure: Image Thickness Sample 12 (a) Cladding (b) HAZ

Average of cladding thickness No. 12= 1364.781 µm

Average of HAZ thickness No. 12= 1111.399 µm

Figure: Image Sample 17

Table: Parameters Sample 17

NI 319 - Forgmasters cladding - Parameters							
No. of sample	Laser power [W]	Speed of cladding [mm/min]	Powder feed rate [g/min]	Carrier gas flow [l/min]	Purge gas flow [l/min]	Offset [mm]	Number of Line
17	3400	1000	40	10	20	3.3	7

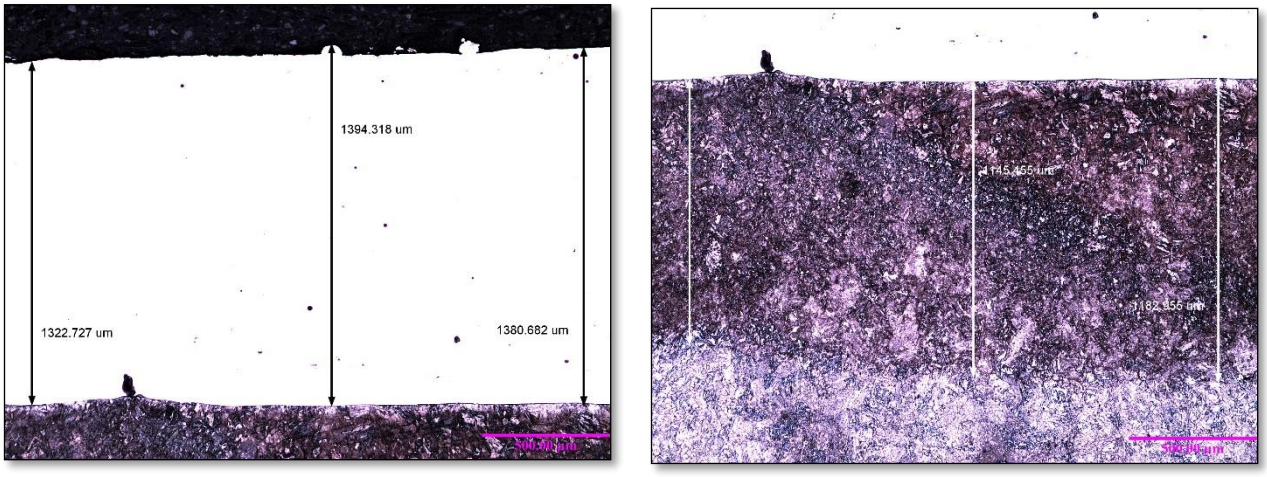

(a) Cladding Image (b) HAZ Image

Figure: Image Thickness Sample 17 (a) Cladding (b) HAZ

Average of cladding thickness No. 17= 1365.909 µm

Average of HAZ thickness No. 17= 1119.318 µm

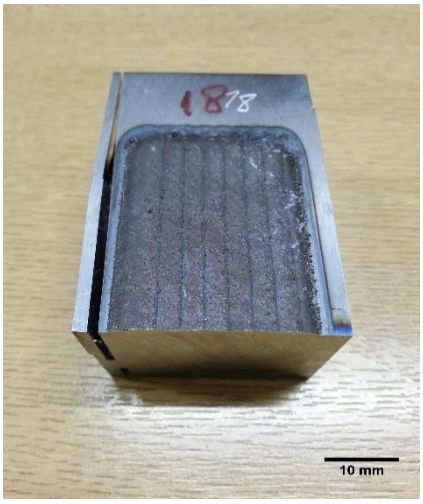

Figure: Image Sample 18

Table: Parameters Sample 18

NI 319 - Forgmasters cladding - Parameters							
No. of sample	Laser power [W]	Speed of cladding [mm/min]	Powder feed rate [g/min]	Carrier gas flow [l/min]	Purge gas flow [l/min]	Offset [mm]	Number of Line
18	3300	1000	40	10	20	3.3	8

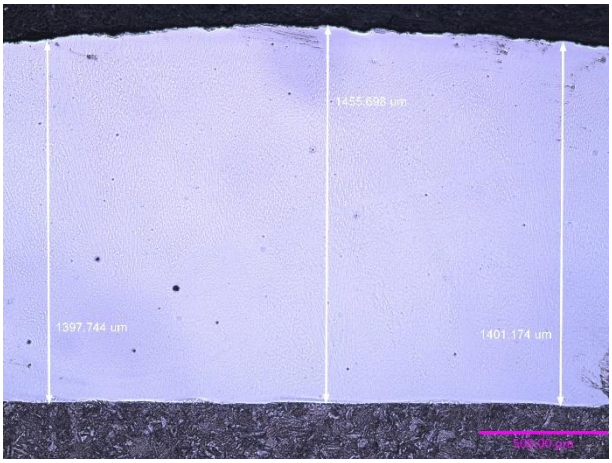

(a) Cladding Image

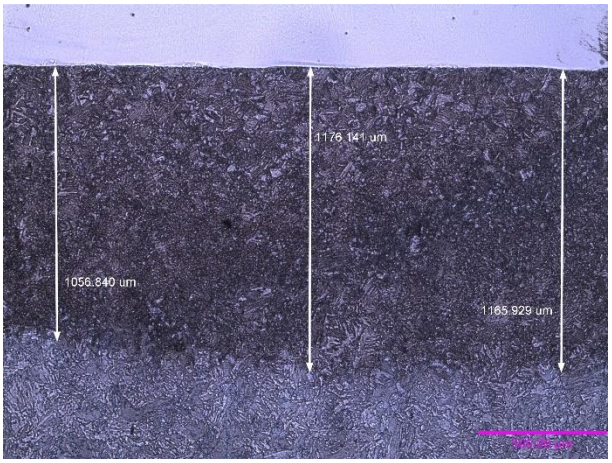

(b) HAZ Image

Figure: Image Thickness Sample 18 (a) Cladding (b) HAZ

Average of cladding thickness No. 18= 1418.205 µm

Average of HAZ thickness No. 18= 1132.97 µm

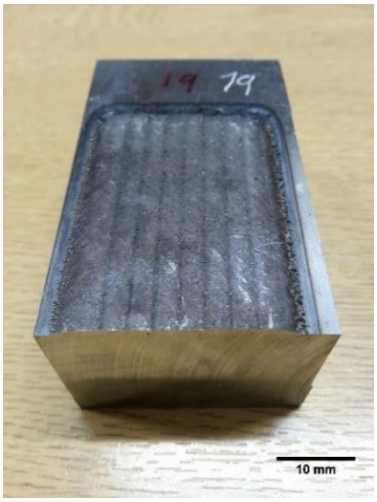

Figure: Image Sample 19

Table: Parameters Sample 19

NI 319 - Forgmasters cladding - Parameters							
No. of sample	Laser power [W]	Speed of cladding [mm/min]	Powder feed rate [g/min]	Carrier gas flow [l/min]	Purge gas flow [l/min]	Offset [mm]	Number of Line
19	3200	1000	40	10	20	3.3	8

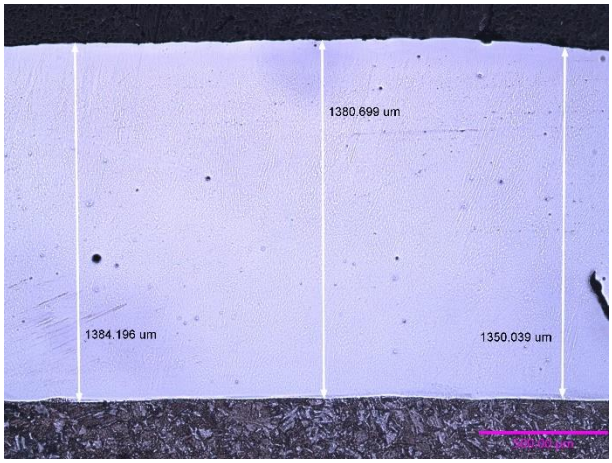

(a) Cladding Image

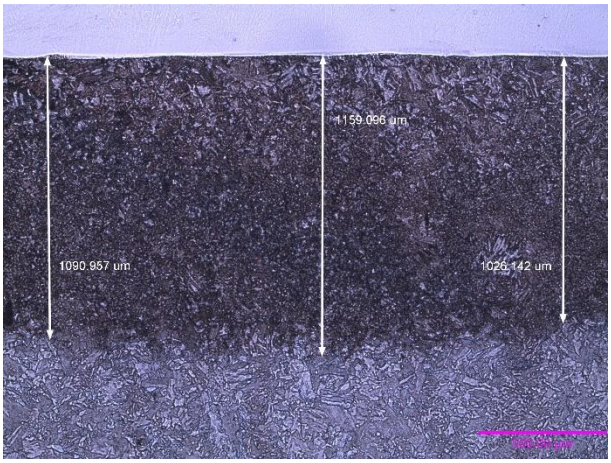

(b) HAZ Image

Figure: Image Thickness Sample 19 (a) Cladding (b) HAZ

Average of cladding thickness No. 19= 1371.645 µm

Average of HAZ thickness No. 19= 1092.065 µm

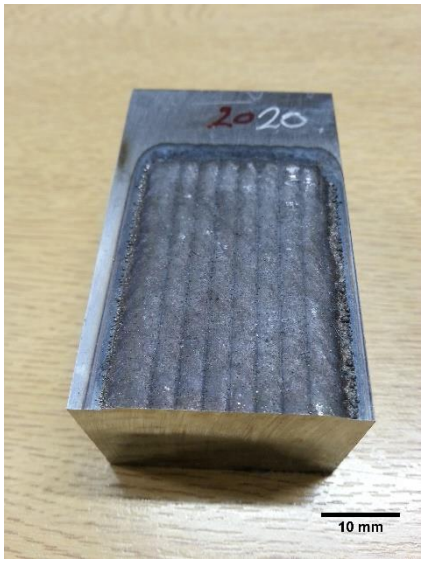

Figure: Image Sample 20

Table: Parameters Sample 20

NI 319 - Forgmasters cladding - Parameters							
No. of sample	Laser power [W]	Speed of cladding [mm/min]	Powder feed rate [g/min]	Carrier gas flow [l/min]	Purge gas flow [l/min]	Offset [mm]	Number of Line
20	3100	1000	40	10	20	3.3	8

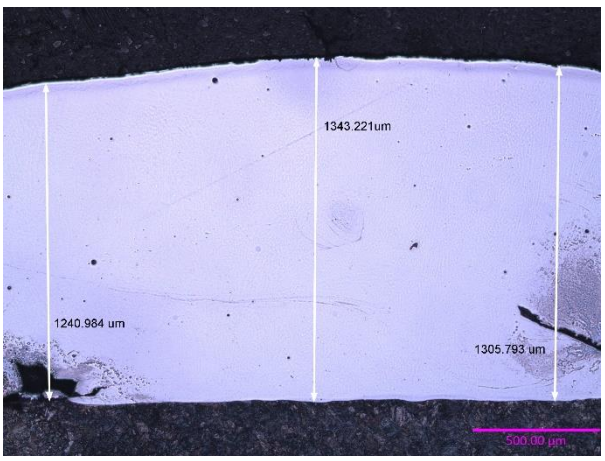

(a) Cladding Image

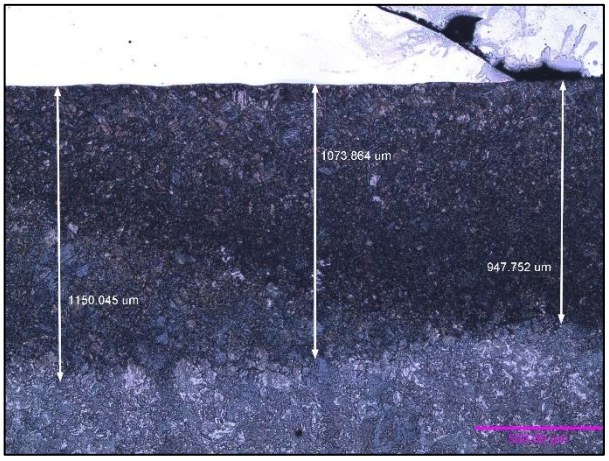

(b) HAZ Image

Figure: Image Thickness Sample 20 (a) Cladding (b) HAZ

Average of cladding thickness No. 20= 1296.666 µm

Average of HAZ thickness No. 20= 1057.22 µm

Figure: Image Sample 32

Table: Parameters Sample 32

NI 319 - Forgmasters cladding - Parameters							
No. of sample	Laser power [W]	Speed of cladding [mm/min]	Powder feed rate [g/min]	Carrier gas flow [l/min]	Purge gas flow [l/min]	Offset [mm]	Number of Line
32	3500	1000	40	10	20	3.3	8

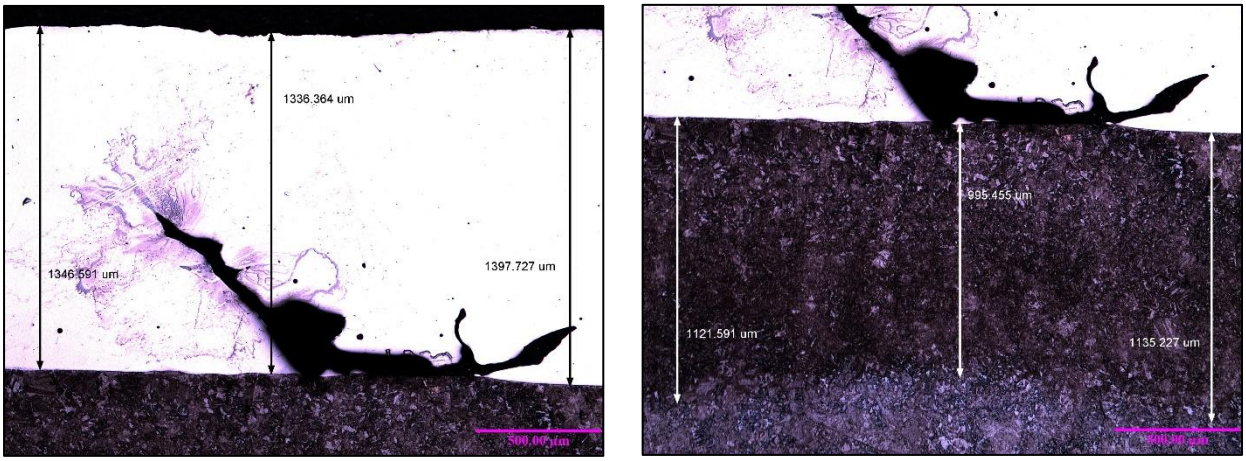

(a) Cladding Image (b) HAZ Image

Figure: Image Thickness Sample 32 (a) Cladding (b) HAZ

Average of cladding thickness No. 32= 1360.227 µm

Average of HAZ thickness No. 32= 1084.091 µm

Figure: Image Sample 35

Table: Parameters Sample 35

NI 319 - Forgmasters cladding - Parameters							
No. of sample	Laser power [W]	Speed of cladding [mm/min]	Powder feed rate [g/min]	Carrier gas flow [l/min]	Purge gas flow [l/min]	Offset [mm]	Number of Line
35	3500	1000	40	10	20	3.3	26

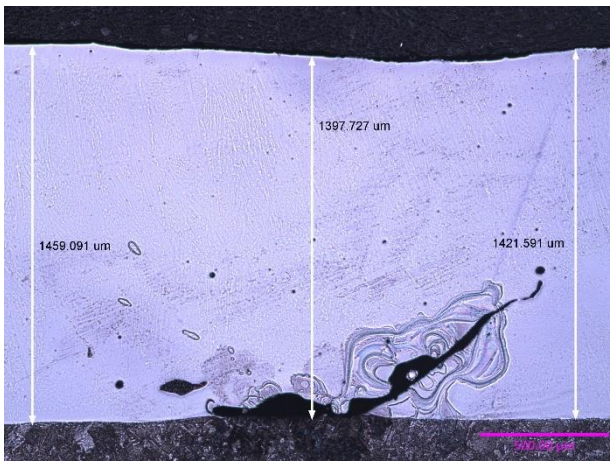

(a) Cladding Image

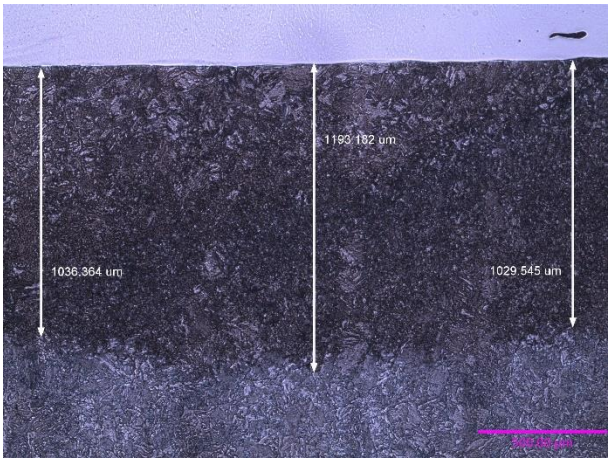

(b) HAZ Image

Figure: Image Thickness Sample 35 (a) Cladding (b) HAZ

Average of cladding thickness No. 35= 1426.136 µm

Average of HAZ thickness No. 35= 1086.364 µm

Figure: Image Sample 36

Table: Parameters Sample 36

NI 319 - Forgmasters cladding - Parameters							
No. of sample	Laser power [W]	Speed of cladding [mm/min]	Powder feed rate [g/min]	Carrier gas flow [l/min]	Purge gas flow [l/min]	Offset [mm]	Number of Line
36	3650	1000	40	10	20	3.3	10

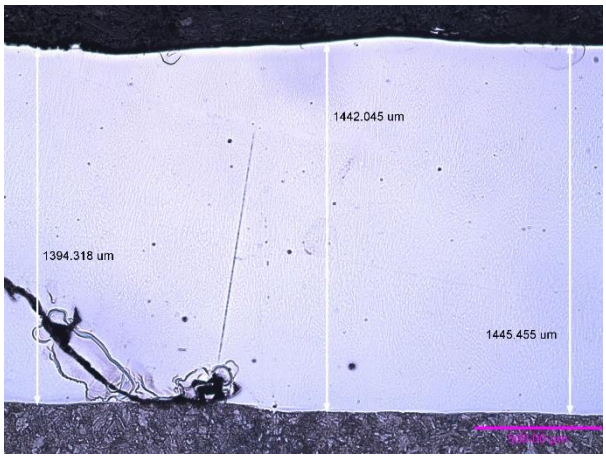

(a) Cladding Image

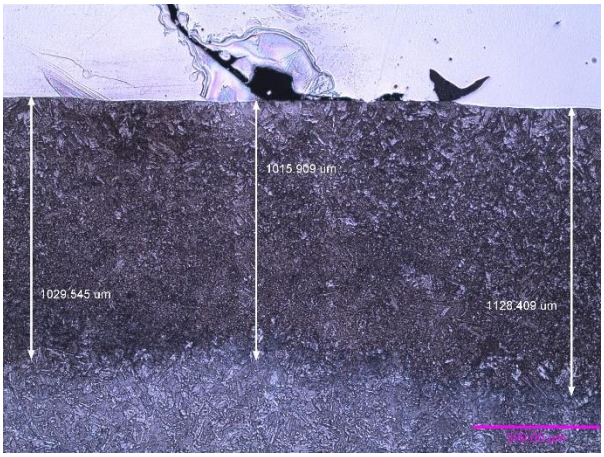

(b) HAZ Image

Figure: Image Thickness Sample 36 (a) Cladding (b) HAZ

Average of cladding thickness No. 36= 1427.273 µm

Average of HAZ thickness No. 36= 1057.954 µm

Figure: Image Sample 37

Table: Parameters Sample 37

NI 319 - Forgmasters cladding - Parameters							
No. of sample	Laser power [W]	Speed of cladding [mm/min]	Powder feed rate [g/min]	Carrier gas flow [l/min]	Purge gas flow [l/min]	Offset [mm]	Number of Line
37	3750	1000	40	10	20	3.3	10

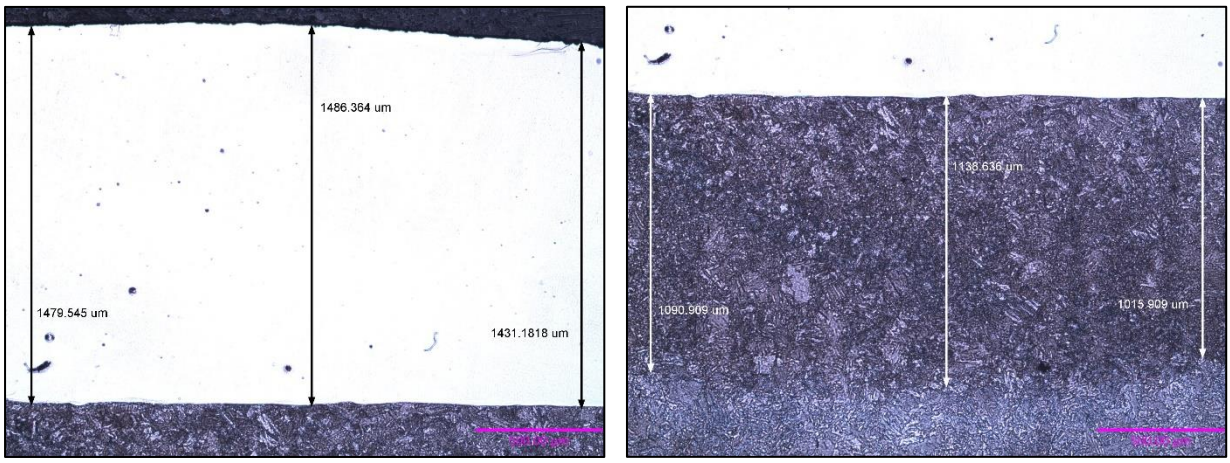

(a) Cladding Image (b) HAZ Image

Figure: Image Thickness Sample 37 (a) Cladding (b) HAZ

Average of cladding thickness No. 37= 1465.909 µm

Average of HAZ thickness No. 37= 1081.818 µm

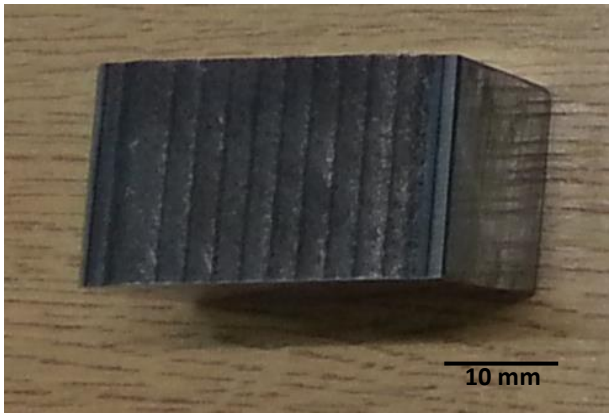

Figure: Image Sample 38

Table: Parameters Sample 38

NI 319 - Forgmasters cladding - Parameters							
No. of sample	Laser power [W]	Speed of cladding [mm/min]	Powder feed rate [g/min]	Carrier gas flow [l/min]	Purge gas flow [l/min]	Offset [mm]	Number of Line
38	3850	1000	40	10	20	3.3	10

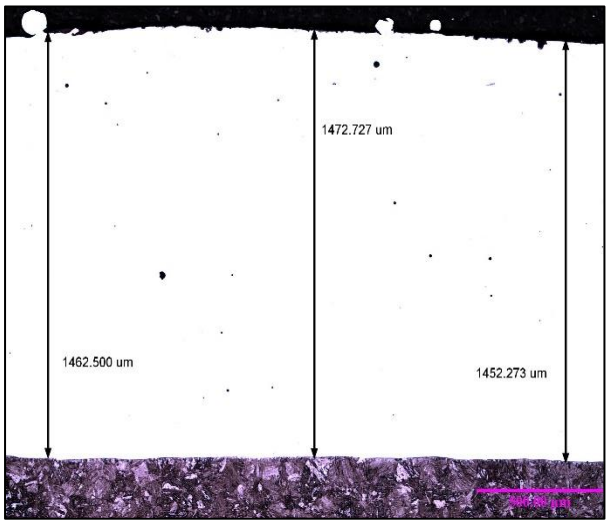

(a) Cladding Image

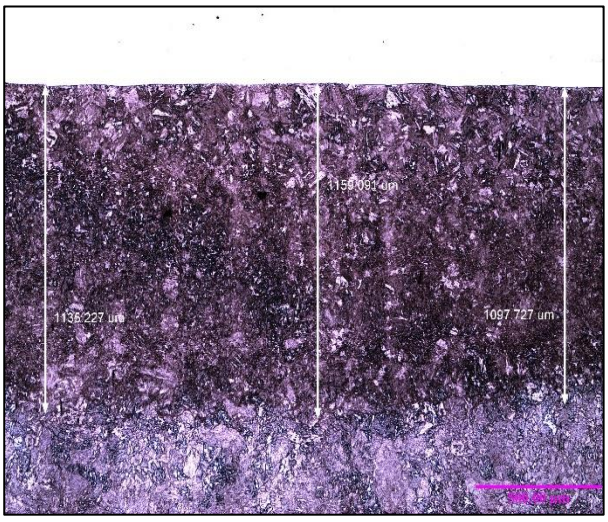

(b) HAZ Image

Figure: Image Thickness Sample 38 (a) Cladding (b) HAZ

Average of cladding thickness No. 38= 1462.5 µm

Average of HAZ thickness No. 38= 1130.682 µm